Actively Targeted Polymersomes for Tumor Imaging and Therapy

Yaohua Wei

ACTIVELY TARGETED POLYMERSOMES FOR TUMOR IMAGING AND THERAPY

Yaohua Wei

ACTIVELY TARGETED POLYMERSOMES FOR TUMOR IMAGING AND THERAPY

DISSERTATION

to obtain
the degree of doctor at the Universiteit Twente,
on the authority of the rector magnificus,
prof. dr. ir. A. Veldkamp,
on account of the decision of the Doctorate Board
to be publicly defended
on Friday 11 June 2021 at 12.45 hours

by

Yaohua Wei

born on the 4th of March, 1991
in Henan, China

This dissertation has been approved by:

Supervisors

 Prof. dr. ir. G. Storm

 Prof. dr. ir. Z. Y. Zhong

Graduation Committee:

Chair / secretary:	Prof. dr. J.L. Herek
Supervisors:	Prof. dr. ir. G. Storm
	Prof. dr. ir. Z. Y. Zhong
Committee Members:	Prof. dr. J.F.J. Engbersen
	Prof. dr. J. Prakash
	Prof. dr. J.C.M. van Hest
	Prof. dr. ir. W.E. Hennink
	Prof. dr. R.M. Schiffelers

# Table of Contents

Chapter 1

General Introduction

1.1 Nanomedicines

Nanomedicine, the application of nanotechnology for medical purpose, has attracted a great deal of attention over the past decades, particularly in the field of cancer therapy where more effective and safer diagnosis and treatment modalities are highly needed. [1, 2]. Nanomedicines promise and have shown to offer significant advantages over traditional therapeutic and diagnostic approaches in cancer therapy including enhanced efficacy and/or mitigated toxicity benefits owing to ameliorated pharmacokinetics and favorably altered tissue distribution profile (including the distribution to pathological areas) of the associated drug molecules[3]. Particulate nanomedicines have received a great deal of interest as nanomaterials for achieving above mentioned advantages. To date, quite some nanotherapeutic products are available on the market, and many more are undergoing clinical translation[4-6]. Nanoparticles applied for either therapeutic or diagnostic applications are generally well below 200 nm, and allowing drug targeting, sustained drug release, protection of fragile drugs and/or solubilization of poorly water-soluble drugs [7, 8].

1.2 Stimuli-responsive polymersomes

Polymersomes (Ps) have attracted great interest among all nanoparticles attributable to their unique cell or virus-mimicking architecture (**Scheme 1**), tunable membrane properties, and carrying capacity for hydrophilic/hydrophobic payloads (such as anticancer drugs, genes, proteins, etc.) [9, 10]. Typically, their well-defined self-assembled structure is derived from macromolecular synthetic amphiphiles, including amphiphilic diblock, triblock, graft, and dendritic copolymers [11]. Notably, Ps have an intrinsic stealthy and versatile membrane surface making them a good alternative for liposomes[12]. In addition, their outer surface can

be chemically crosslinked to further enhance their stability and circulation time in the bloodstream[13, 14].
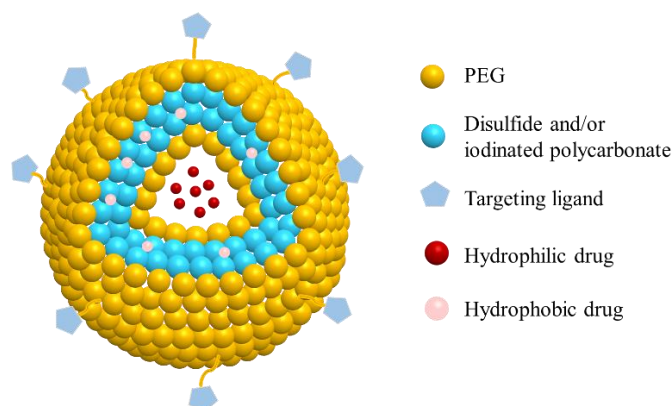
Scheme 1. Schematic structure of polymersomes

The 100-1000 fold elevated glutathione (GSH) level in the cytosol of cells (vs. the level in extracellular fluids) render GSH as an ideal and ubiquitous internal stimulus to achieve rapid intracellular destabilization efficient drug release[15-17]. Unique chemistry enabled the design of GSH-responsive nano-vehicles (including micelles, nanoparticles, polymersomes, macromolecular conjugates etc.) as novel and versatile platforms, addressing both extracellular and intracellular barriers opposing efficient targeted drug delivery[18].The disulfide shell crosslinked polymersomes (CLPs) were developed for the delivery of hydrophilic compounds, being highly stable in the circulation but showing fast drug release within target cells. The CLPs membrane ensures drug retention during blood circulation, while the disassembly of CLPs occurs in the reductive environment of the cytosol[19-22].

1.3 Actively targeted polymersomes for tumor imaging and therapy

All approved nanoparticulate nanomedicines do not expose targeting ligands and solely rely on passive targeting effects arising from altered pharmacokinetic and biodistribution profiles of the drug. Actively targeted nanomedicines are equipped with targeting ligands exposed on their surface to achieve binding to receptor molecules (over)expressed on the surface of target cells

within tumor tissue. Receptor binding of these nanoparticles provides benefits in terms of cellular internalization by receptor-mediated endocytosis and tissue retention [6]. Though antibodies, proteins or peptides have been intensively investigated and are routinely used as targeting ligands in preclinical cancer models, only a few of these targeting ligands have been used in tumor-targeted nanoformulations which moved forward to clinical trials[23].

Transferrin (**Scheme 2**) is an endogenous monomeric glycoprotein and natural ligand for the transferrin receptor (TfR), which serves to translocate iron atoms into cells[24, 25]. TfR is overexpressed on cancer cells, including the SMMC-7721 (hepatoma carcinoma), HCT-116 (colorectal cancer), MDA-MB 231 (breast cancer) cells used in this thesis research owing to aberrant iron metabolism[26-29]. Tf has been employed as targeting ligand in various nanoformulations[30-36]. Notably, Tf-targeted nanomedicines are one of the few active targeting nanomedicines which are currently under clinical evaluation [6]. For instance, MBP-426 is a liposomal oxaliplatin formulation with Tf exposed on the liposomal particle surfaces that is at the Phase 1 clinical stage in patients with advanced or metastatic solid tumors. An open-label Phase Ib/II study was used to evaluate the efficacy of MBP-426 in combination with Leucovorin and 5-FU in patients with second-line metastatic gastric, gastroesophageal junction, or esophageal adenocarcinoma[37]. CALAA-01 is an RRM2 siRNA loaded β-cyclodextrin-based targeting carrier with Tf modification evaluated in a Phase I clinical trial and an extension Phase Ib study for advanced solid tumor patients[38]. Remarkably, 21% of the treated patients had to quit from the study owing to an adverse event. The Tf-PEG-Ad conjugates have shown structural alterations and hence the Tf targeting component long term instability was proposed as the main reason for the occurrence of adverse effects[39] Hence, the long-term stability of ligand appended targeted formulation is vital to achieve clinical success and to avoid unanticipated side effects.
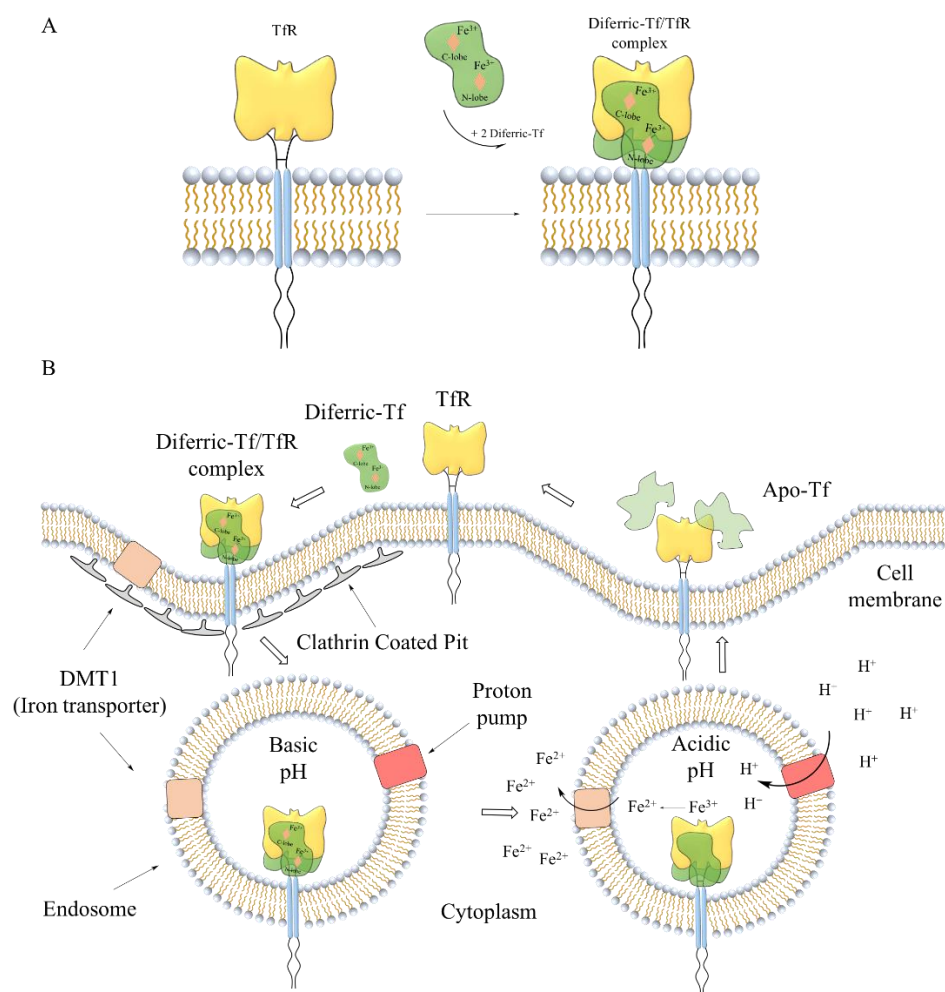
Scheme 1. Cellular uptake of iron through the Tf system via receptor-mediated endocytosis. (A) Illustration of Tf/TfR complex formation (B) Endocytosis of the diferric Tf/TfR complex occurs via clathrin-coated pits and the complex is delivered into endosomes.

In general, patients treated so far with targeted nanoparticulate systems typically benefited from reduced toxicity rather than increased efficacy as compared to the conventional treatment protocols. Actively targeted nanomedicine may bring the additional benefit of increased antitumor activity and patient survival as contributor in the enhanced therapeutic index. To achieve enhanced antitumor efficacy, actively targeted nanoparticles should 1) not release the entrapped drug while still circulating in the bloodstream, 2) should accumulate in tumor tissue, e.g. through the well-known enhanced permeability and retention (EPR) effect by taking advantage of leaky blood vessels that characterized in many solid tumors, 3) should show tumor

cell-specific uptake (or specific uptake by another target cell type within tumor tissue) and 4) should allow intracellular drug release and delivery to the proper intracellular location. It is expected that nanoparticles exposing Tf ligands on CLPs - subject of the research presented in this thesis - show fast intracellular reduction-responsive drug release.

In addition to the improvement of the therapeutic index of small molecular weight anticancer drugs, therapeutic biomacromolecules (e.g. proteins and nucleic acids) have become of increasing importance. They are characterized by very unfavorable physicochemical properties (large size, strong charge) resulting in great difficulty to cross cellular membranes to access their intracellular target site. Notably, the tumor-specific cell penetrating peptide (CPP) (sequence: RLWMRWYSPRTRAYG) developed by Matsushita et al. was reported to selectively penetrate A549 lung cancer cells *in vitro* in its free form[40]. Previously, polymersomes containing methotrexate disodium (MTX·2Na) with surface-attached CPP33 significantly improved the chemotherapeutic effect of the entrapped small molecular weight drug in case of A549 lung tumor-bearing mice[41]. CPP33-decorated polymersomes containing Granzyme B (GrB), a natural and potent apoptotic protein secrete by cytotoxic T cells and NK cells, exhibited several advantages over previously reported protein transport systems including facile fabrication, high protein encapsulation, high lung cancer cells specificity, and fast cytoplasmic protein release *in vitro*.

Recently, integration of therapeutic and diagnostic components into (nano)theranostic approaches opened the possibility to target antineoplastic and diagnostic agents into the tumor tissues simultaneously by inclusion of the therapeutic agent and the diagnostic probe in the same nanoparticles (imaging-guided drug delivery) [42-45]. X-ray computed tomography (CT) is a conventional clinical diagnostic tool, with iodine-containing compounds typically used to enhance the contrast between pathological and healthy tissues in patients[46-49]. Great interest has been given in the past few years to the development of novel nano-CT contrast agents which

are able to combine CT with various therapies and overcome the issues of conventional contrast agents, i.e. fast clearance, low target selectivity, and potential renal toxicity[50-52]. Metal nanoparticles with high atomic number exhibit an excellent X-ray attenuation coefficient, but their safety, sophisticated production process and costs limit their further clinical translation[53]. Generally, nano-sized iodinated contrast agents typically possess inadequate X-ray attenuation, which results in the need to use large doses for *in vivo* CT imaging [54, 55]. Hence, a nano-sized contrast agent should show an appropriate X-ray attenuation coefficient, good biocompatibility, prolonged circulation time and targeted imaging capacity to resolve the drawbacks of the conventional iodinated small molecules. We and others verified that disulfide crosslinked nanoparticles containing drugs show superb *in vivo* stability and accelerated intracellular drug release[56, 57]. Therefore, the introduction of disulfide chemistry in nanoparticulate theranostic agents could provide desirable features for improving both tumor diagnosis (enhanced *in vivo* stability and prolonged circulation) and therapeutics (reduction responsive drug release). Noteworthy, the pre-screening of patients for the occurrence of the EPR-mediated tumor accumulation with relevant nanoimaging probes is nowadays emerging as a key step for the successful application of targeted nanomedicines[58, 59]. Interestingly, a nano-formulation like crosslinked iodinated polymersomes (XIPs) could be used both as companion diagnostic for pre-screening and further as actual patient treatment.

1.4 Aim of the study

The aim of this thesis is to explore the potential of nanopolymersomes for the treatment and imaging of cancer.

In **Chapter 2**, transferrin (Tf), an endogenous protein that serves to translocate iron into TfR-overexpressing cells, is known as a natural ligand for TfR. Taking this particular feature, we report a Tf-functionalized, polycarbonate based polymersome containing doxorubicin (Tf-Ps-

Dox) for targeted therapy in an orthotopic SMMC-7721 hepatocellular carcinoma (HCC) model in nude mice. We report that the Tf-Ps-Dox system has attractive characteristics regarding stability, tolerability, and reduction-triggered drug release properties. Besides, the post-modification of Ps-Dox with Tf, the influence of Tf density on the targeting ability of Ps-Dox, and therapeutic efficacy of Tf-Ps-Dox towards TfR-overexpressing hepatocellular carcinoma were investigated.

In **Chapter 3**, we report for the first time that Tf-binding peptide-functionalized polymersomes (TBP-Ps), which can bound Tf and mediate targeted Dox delivery to TfR overexpressing HCT-116 colorectal cancer cells both *in vitro* and *in vivo*. The pharmacokinetics and anti-tumor therapy experiments revealed that Tf@TBP-Ps-Dox possess a prolonged circulation time and exhibited a considerably improved inhibition of HCT-116 tumor as compared to Ps-Dox. Tf-binding peptide thus provides an appealing strategy to fabricate nanomedicines targeting to TfR over-expressing malignancies.

In **Chapter 4**, siRNA (siPLK1)-loaded TBP-Ps coated with Tf showed the blood-brain barrier (BBB) crossing capacity. Biomacromolecules such as nucleic acids typically exhibit low tumor cell uptake resulting from either rapid *in vivo* degradation by nucleases or lack of cellular uptake due to their unfavorable physicochemical properties (large size, negatively charged) preventing passage of cellular membranes. Hence, we construct transferrin (Tf) bounded Ps with siPLK1 loading (Tf@TBP-Ps-siPLK1) for both BBB crossing and, subsequently tumor targeting. This transferrin-binding ligand decoration strategy is robust and has greatly simplified the production of transferrin-functionalized nanomedicines. Hence, the polymersomal siRNA with bounded Tf could provide an efficient alternative approach for brain metastases management associated with moderate toxicity.

The clinical use of protein therapeutics with intracellular targets is hampered by its *in vivo* fragility, low cell permeability and endosomal entrapment. In **Chapter 5**, we report a cell-

selective penetrating polymersomes (CPRPs) for granzyme B (GrB) orthotopic human lung tumor targeted delivery. Orthotopic A549-Luc lung tumor-bearing nude mice administered with GrB-loaded CPRPs GrB showed complete tumor growth inhibition with little body weight loss throughout the treatment period, resulting in a significantly improved survival rate.

Imaging plays a key role in the preclinical evaluation of nanomedicine-based drug delivery systems. Clinical studies provide convincing evidence on the localization of nanoparticles in tumors, albeit with fairly high levels of inter- and intraindividual variability. It is gradually becoming clear that imaging is critically important to help address this high heterogeneity in tumor accumulation of nanoparticles. In **Chapter 6**, we have designed and developed biodegradable nanopolymersomes with an ultrahigh iodine content for high-performance CT imaging *in vivo*. Their suitability for in vivo imaging of the blood pool, reticuloendothelial system and several subcutaneous malignant tumors in mice (B16 melanoma and MCF-7 human breast cancer) was evaluated in comparison with iohexol, a clinically used iodinated small molecule.

In **Chapter 7**, we investigated cRGD-functionalized disulfide-crosslinked iodine-rich polymersomes (cRGD-XIPs) loaded with doxorubicin as a novel, robust and 'smart' theranostic agent. The quality of the *in vivo* CT imaging characteristics after intravenous and intratumoral administration was evaluated in comparison with iohexol. In addition, antitumor efficacy in the subcutaneous B16 mouse model was assessed in comparison with free doxorubicin treatments, and non-targeted polymersome formulations.

Chapter 8 summarizes the results of the thesis and provides perspectives for the future development of nanomedicines based on polymersomes towards broad applications.

References

[1] A. Wicki, D. Witzigmann, V. Balasubramanian, J. Huwyler, Nanomedicine in cancer therapy: Challenges, opportunities, and clinical applications, J. Control. Release 200 (2015) 138-157.

[2] X.Y. Xu, W. Ho, X.Q. Zhang, N. Bertrand, O. Farokhzad, Cancer nanomedicine: from targeted delivery to combination therapy, Trends Mol. Med. 21 (2015) 223-232.

[3] T. Lammers, F. Kiessling, W.E. Hennink, G. Storm, Drug targeting to tumors: Principles, pitfalls and (pre-) clinical progress, J. Control. Release 161 (2012) 175-187.

[4] J.I. Hare, T. Lammers, M.B. Ashford, S. Puri, G. Storm, S.T. Barry, Challenges and strategies in anti-cancer nanomedicine development: An industry perspective, Adv. Drug Deliver. Rev. 108 (2017) 25-38.

[5] S. Hua, M.B.C. de Matos, J.M. Metselaar, G. Storm, Current Trends and Challenges in the Clinical Translation of Nanoparticulate Nanomedicines: Pathways for Translational Development and Commercialization, Front. Pharmacol. 9 (2018).

[6] R. van der Meel, L.J.C. Vehmeijer, R.J. Kok, G. Storm, E.V.B. van Gaal, Ligand-targeted particulate nanomedicines undergoing clinical evaluation: Current status, Adv. Drug Deliver. Rev. 65 (2013) 1284-1298.

[7] L. Zhang, F.X. Gu, J.M. Chan, A.Z. Wang, R.S. Langer, O.C. Farokhzad, Nanoparticles in medicine: Therapeutic applications and developments, Clin. Pharmacol. Ther. 83 (2008) 761-769.

[8] N. Kamaly, Z.Y. Xiao, P.M. Valencia, A.F. Radovic-Moreno, O.C. Farokhzad, Targeted polymeric therapeutic nanoparticles: design, development and clinical translation, Chem. Soc. Rev. 41 (2012) 2971-3010.

[9] J.S. Lee, J. Feijen, Polymersomes for drug delivery: Design, formation and characterization, J. Control. Release 161 (2012) 473-483.

[10] D.E. Discher, F. Ahmed, Polymersomes, J. Annu. Rev. Biomed. Eng. 8 (2006) 323-341.

[11] F.H. Meng, Z.Y. Zhong, J. Feijen, Stimuli-responsive polymersomes for programmed drug delivery, Biomacromolecules 10 (2009) 197-209.

[12] L.X. Zhao, N.N. Li, K.M. Wang, C.H. Shi, L.L. Zhang, Y.X. Luan, A review of polypeptide-based polymersomes, Biomaterials 35 (2014) 1284-1301.

[13] H.L. Sun, F.H. Meng, R. Cheng, C. Deng, Z.Y. Zhong, Reduction and pH dual-bioresponsive crosslinked polymersomes for efficient intracellular delivery of proteins and potent induction of cancer

cell apoptosis, Acta Biomater. 10 (2014) 2159-2168.

[14] X.R. Wang, G.H. Liu, J.M. Hu, G.Y. Zhang, S.Y. Liu, Concurrent block copolymer polymersome stabilization and bilayer permeabilization by stimuli-regulated "traceless" crosslinking, Angew. Chem. Int. Edit. 53 (2014) 3138-3142.

[15] R. Cheng, F.H. Meng, C. Deng, Z.Y. Zhong, Bioresponsive polymeric nanotherapeutics for targeted cancer chemotherapy, Nano Today 10 (2015) 656-670.

[16] F.H. Meng, W.E. Hennink, Z. Zhong, Reduction-sensitive polymers and bioconjugates for biomedical applications, Biomaterials 30 (2009) 2180-2198.

[17] R. Cheng, F. Feng, F.H. Meng, C. Deng, J. Feijen, Z.Y. Zhong, Glutathione-responsive nano-vehicles as a promising platform for targeted intracellular drug and gene delivery, J. Control. Release 152 (2011) 2-12.

[18] H.L. Sun, Y.F. Zhang, Z.Y. Zhong, Reduction-sensitive polymeric nanomedicines: An emerging multifunctional platform for targeted cancer therapy, Adv. Drug Deliver. Rev. 132 (2018) 16-32.

[19] Y. Zou, F.H. Meng, C. Deng, Z.Y. Zhong, Robust, tumor-homing and redox-sensitive polymersomal doxorubicin: A superior alternative to Doxil and Caelyx?, J. Control. Release 239 (2016) 149-158.

[20] Y. Zou, M. Zheng, W.J. Yang, F.H. Meng, K. Miyata, H.J. Kim, K. Kataoka, Z.Y. Zhong, Virus-mimicking chimaeric polymersomes boost targeted cancer siRNA therapy in vivo, Adv. Mater. 29 (2017).

[21] Y.N. Shi, Y. Jiang, J.S. Cao, W.J. Yang, J. Zhang, F.H. Meng, Z.Y. Zhong, Boosting RNAi therapy for orthotopic glioblastoma with nontoxic brain-targeting chimaeric polymersomes, J. Control. Release 292 (2018) 163-171.

[22] Y. Jiang, J. Zhang, F.H. Meng, Z.Y. Zhong, Apolipoprotein E peptide-directed chimeric polymersomes mediate an ultrahigh-efficiency targeted protein therapy for glioblastoma, Acs Nano 12 (2018) 11070-11079.

[23] J.J. Shi, P.W. Kantoff, R. Wooster, O.C. Farokhzad, Cancer nanomedicine: progress, challenges and opportunities, Nat. Rev. Cancer 17 (2017) 20-37.

[24] T.R. Daniels, E. Bernabeu, J.A. Rodriguez, S. Patel, M. Kozman, D.A. Chiappetta, E. Holler, J.Y. Ljubimova, G. Helguera, M.L. Penichet, The transferrin receptor and the targeted delivery of therapeutic agents against cancer, Bba-Gen Subjects 1820 (2012) 291-317.

[25] S. Tortorella, T.C. Karagiannis, Transferrin receptor-mediated endocytosis: a useful target for cancer therapy, J. Membrane Biol. 247 (2014) 291-307.

[26] K.L. Fan, C.Q. Cao, Y.X. Pan, D. Lu, D.L. Yang, J. Feng, L.N. Song, M.M. Liang, X.Y. Yan, Magnetoferritin nanoparticles for targeting and visualizing tumour tissues, Nat. Nanotechnol. 7 (2012) 833-U876.

[27] M.S. Muthu, R.V. Kutty, Z.T. Luo, J.P. Xie, S.S. Feng, Theranostic vitamin E TPGS micelles of transferrin conjugation for targeted co-delivery of docetaxel and ultra bright gold nanoclusters, Biomaterials 39 (2015) 234-248.

[28] T. Kang, M.Y. Jiang, D. Jiang, X.Y. Feng, J.H. Yao, Q.X. Song, H.Z. Chen, X.L. Gao, J. Chen, Enhancing glioblastoma-specific penetration by functionalization of nanoparticles with an iron-mimic peptide targeting transferrin/transferrin receptor complex, Mol. Pharm. 12 (2015) 2947-2961.

[29] H. Makwana, F. Mastrotto, J.P. Magnusson, D. Sleep, J. Hay, K.J. Nicholls, S. Allen, C. Alexander, Engineered polymer-transferrin conjugates as self-assembling targeted drug delivery systems, Biomacromolecules 18 (2017) 1532-1543.

[30] Y. Lu, Z.H. Wang, T.L. Li, H. McNally, K. Park, M. Sturek, Development and evaluation of transferrin-stabilized paclitaxel nanocrystal formulation, J. Control. Release 176 (2014) 76-85.

[31] J.Y. Yhee, S.J. Lee, S. Lee, S. Song, H.S. Min, S.W. Kang, S. Son, S.Y. Jeong, I.C. Kwon, S.H. Kim, K. Kim, Tumor-targeting transferrin nanoparticles for systemic polymerized siRNA delivery in tumor-bearing Mice, Bioconjugate Chem. 24 (2013) 1850-1860.

[32] C.H.J. Choi, C.A. Alabi, P. Webster, M.E. Davis, Mechanism of active targeting in solid tumors with transferrin-containing gold nanoparticles, P. Natl. Acad. Sci. USA 107 (2010) 1235-1240.

[33] A.J. Clark, M.E. Davis, Increased brain uptake of targeted nanoparticles by adding an acid-cleavable linkage between transferrin and the nanoparticle core, P. Natl. Acad. Sci. USA 112 (2015) 12486-12491.

[34] Y.N. Cui, Q.X. Xu, P.K.H. Chow, D.P. Wang, C.H. Wang, Transferrin-conjugated magnetic silica PLGA nanoparticles loaded with doxorubicin and paclitaxel for brain glioma treatment, Biomaterials 34 (2013) 8511-8520.

[35] H.J. Zhang, L. Hou, X.J. Jiao, Y.D. Ji, X.L. Zhu, Z.Z. Zhang, Transferrin-mediated fullerenes nanoparticles as Fe2+-dependent drug vehicles for synergistic anti-tumor efficacy, Biomaterials 37 (2015) 353-366.

[36] F.C. Lam, S.W. Morton, J. Wyckoff, T.L.V. Han, M.K. Hwang, A. Maffa, E. Balkanska-Sinclair, M.B. Yaffe, S.R. Floyd, P.T. Hammond, Enhanced efficacy of combined temozolomide and

bromodomain inhibitor therapy for gliomas using targeted nanoparticles, Nat. Commun. 9 (2018).

[37] S. Svenson, Clinical translation of nanomedicines, Curr. Opin. Solid St. M. 16 (2012) 287-294.

[38] M.E. Davis, J.E. Zuckerman, C.H.J. Choi, D. Seligson, A. Tolcher, C.A. Alabi, Y. Yen, J.D. Heidel, A. Ribas, Evidence of RNAi in humans from systemically administered siRNA via targeted nanoparticles, Nature 464 (2010) 1067-U1140.

[39] J.E. Zuckerman, I. Gritli, A. Tolcher, J.D. Heidel, D. Lim, R. Morgan, B. Chmielowski, A. Ribas, M.E. Davis, Y. Yen, Correlating animal and human phase Ia/Ib clinical data with CALAA-01, a targeted, polymer-based nanoparticle containing siRNA, P. Natl. Acad. Sci. USA 111 (2014) 11449-11454.

[40] E. Kondo, K. Saito, Y. Tashiro, K. Kamide, S. Uno, T. Furuya, M. Mashita, K. Nakajima, T. Tsumuraya, N. Kobayashi, Tumour lineage-homing cell-penetrating peptides as anticancer molecular delivery systems, Nat. Commun. 3 (2012) 951.

[41] W.J. Yang, Y.F. Xia, Y. Fang, F.H. Meng, J. Zhang, R. Cheng, C. Deng, Z.Y. Zhong, Selective cell penetrating peptide-functionalized polymersomes mediate efficient and targeted delivery of methotrexate disodium to human lung cancer in vivo, Adv. Healthc. Mater. 7 (2018).

[42] H. De Oliveira, J. Thevenot, S. Lecommandoux, Smart polymersomes for therapy and diagnosis: fast progress toward multifunctional biomimetic nanomedicines, Wiley Interdiscip. Rev. Nanomed. Nanobiotechnol. 4 (2012) 525-546.

[43] W.H. Chiang, W.C. Huang, C.W. Chang, M.Y. Shen, Z.F. Shih, Y.F. Huang, S.C. Lin, H.C. Chiu, Functionalized polymersomes with outlayered polyelectrolyte gels for potential tumor-targeted delivery of multimodal therapies and MR imaging, J. Control. Release 168 (2013) 280-288.

[44] M. Mohammadi, M. Ramezani, K. Abnous, M. Alibolandi, Biocompatible polymersomes-based cancer theranostics: Towards multifunctional nanomedicine, Int. J. Pharmaceut. 519 (2017) 287-303.

[45] C. Sanson, O. Diou, J. Thevenot, E. Ibarboure, A. Soum, A. Brulet, S. Miraux, E. Thiaudiere, S. Tan, A. Brisson, V. Dupuis, O. Sandre, S. Lecommandoux, Doxorubicin loaded magnetic polymersomes: theranostic nanocarriers for MR imaging and magneto-chemotherapy, Acs Nano 5 (2011) 1122-1140.

[46] X.F. Chen, J.B. Song, X.Y. Chen, H.H. Yang, X-ray-activated nanosystems for theranostic applications, Chem. Soc. Rev. 48 (2019) 3073-3101.

[47] Z.R. Lu, Theranostics: fusion of therapeutics and diagnostics, Pharma. Res. 31 (2014) 1355-1357.

[48] Q. Yin, F.Y. Yap, L.C. Yin, L. Ma, Q. Zhou, L.W. Dobrucki, T.M. Fan, R.C. Gaba, J.J. Cheng, Poly(iohexol) nanoparticles as contrast agents for in vivo x-ray computed tomography imaging, J. Am.

Chem. Soc. 135 (2013) 13620-13623.

[49] J.W. Lambert, Y.X. Sun, C. Stillson, Z.X. Li, R. Kumar, S.Z. Wang, P.F. FitzGerald, P.J. Bonitatibus, R.E. Colborn, J.C. Roberts, P.M. Edic, M. Marino, B.M. Yeh, An Intravascular tantalum oxide-based CT contrast agent: preclinical evaluation emulating overweight and obese patient size, Radiology 289 (2018) 103-110.

[50] Y. Dou, Y.Y. Guo, X.D. Li, X. Li, S. Wang, L. Wang, G.X. Lv, X.N. Zhang, H.J. Wang, X.Q. Gong, J. Chang, Size-tuning ionization to optimize gold nanoparticles for simultaneous enhanced CT imaging and radiotherapy, Acs Nano 10 (2016) 2536-2548.

[51] W.Y. He, K.L. Ai, L.H. Lu, Nanoparticulate X-ray CT contrast agents, Sci. China Chem. 58 (2015) 753-760.

[52] R. Meir, K. Shamalov, O. Betzer, M. Motiei, M. Horovitz-Fried, R. Yehuda, A. Popovtzer, R. Popovtzer, C.J. Cohen, Nanomedicine for cancer immunotherapy: tracking cancer-specific T-cells in vivo with gold nanoparticles and CT imaging, Acs Nano 9 (2015) 6363-6372.

[53] H. Deng, Y.Q. Zhong, M.H. Du, Q.J. Liu, Z.M. Fan, F.Y. Dai, X. Zhang, Theranostic self-assembly structure of gold nanoparticles for NIR photothermal therapy and x-ray computed tomography imaging, Theranostics 4 (2014) 904-918.

[54] H. Xu, T.Y. Ohulchanskyy, A. Yakovliev, R. Zinyuk, J. Song, L.W. Liu, J.L. Qu, Z. Yuan, Nanoliposomes co-encapsulating CT imaging contrast agent and photosensitizer for enhanced, imaging guided photodynamic therapy of cancer, Theranostics 9 (2019) 1323-1335.

[55] Y.Q. Zhu, X.X. Wang, J. Chen, J. Zhang, F.H. Meng, C. Deng, R. Cheng, J. Feijen, Z.Y. Zhong, Bioresponsive and fluorescent hyaluronic acid-iodixanol nanogels for targeted X-ray computed tomography imaging and chemotherapy of breast tumors, J. Control. Release 244 (2016) 229-239.

[56] Y. Zou, Y. Fang, H. Meng, F.H. Meng, C. Deng, J. Zhang, Z.Y. Zhong, Self-crosslinkable and intracellularly decrosslinkable biodegradable micellar nanoparticles: A robust, simple and multifunctional nanoplatform for high-efficiency targeted cancer chemotherapy, J. Control. Release 244 (2016) 326-335.

[57] D.P. Donnelly, M.G. Dowgiallo, J.P. Salisbury, K.C. Aluri, S. Iyengar, M. Chaudhari, M. Mathew, I. Miele, J.R. Auclair, S.A. Lopez, Cyclic thiosulfinates and cyclic disulfides selectively cross-link thiols while avoiding modification of lone thiols, J. Am. Chem. Soc. 140 (2018) 7377-7380.

[58] S.C. Baetke, T. Lammers, F. Kiessling, Applications of nanoparticles for diagnosis and therapy of

cancer, Brit. J. Radiol. 88 (2015).

[59] R. van der Meel, E. Sulheim, Y. Shi, F. Kiessling, W.J. Mulder, T.J.N.N. Lammers, Smart cancer nanomedicine, Nat. Nanotechnol. 14 (2019) 1007-1017.

Chapter 2

Low-Toxicity Transferrin-Guided Polymersomal Doxorubicin for Potent Chemotherapy of Orthotopic Hepatocellular Carcinoma in Vivo*

Yaohua Wei[a,b], Xiaolei Gu[a], Liang Cheng[a,c,*], Fenghua Meng[a,*], Gert Storm[b], and Zhiyuan Zhong[a,*]

[a] Biomedical Polymers Laboratory, College of Chemistry, Chemical Engineering and Materials Science, and State Key Laboratory of Radiation Medicine and Protection, Soochow University, Suzhou, 215123, P. R. China

[b] Department of Biomaterials Science and Technology, MIRA Institute for Biological Technology and Technical Medicine, University of Twente, PO Box 217, 7500AE, Enschede, The Netherlands

[c] Department of Pharmaceutics, College of Pharmaceutical Sciences, Soochow University, Suzhou, 215123, P.R. China

Abstract

Hepatocellular carcinoma (HCC) remains one of the most lethal malignancies. The current chemotherapy with typically low tumor uptake and high toxicity reveals a poor anti-HCC efficacy. Here, we report transferrin-guided polycarbonate based polymersomal doxorubicin (Tf-Ps-Dox) as a low-toxic and potent nanotherapeutics for effective treatment of transferrin receptor (TfR)-positive human liver tumor SMMC-7721 model. Tf-Ps-Dox was facilely fabricated with small size of ca. 75 nm and varying Tf densities from 2.2% to 7.0%, by post-modification of maleimide-functionalized Ps-Dox (Dox loading content of 10.6 wt.%) with thiolated transferrin. MTT assays showed that Tf-Ps-Dox had an optimal Tf surface density of 3.9%. The cellular uptake, intracellular Dox level, and anticancer efficacy of Tf-Ps-Dox to SMMC-7721 cells were inhibited by supplementing free transferrin, supporting that Tf-Ps-Dox is endocytosed via TfR. Interestingly, Tf-Ps-Dox exhibited a high accumulation of 8.5%ID/g (percent injected dose per gram of tissue) in subcutaneous SMMC-7721 tumors, which was 2 and 3-fold higher than non-targeted Ps-Dox and clinically used liposomal Dox formulation (Lipo-Dox), respectively. The median survival times of mice bearing orthotopic SMMC-7721 tumors increased from 82, 88 to 96 days when treated with Tf-Ps-Dox at Dox doses from 8, 12 to 16 mg/kg, which was significantly longer than Ps-Dox at 8 mg/kg (58 days) and Lipo-Dox at 4 mg/kg (48 days) or PBS (36 days). Notably, unlike Lipo-Dox, no body weight loss and damage to major organs could be discerned for all Tf-Ps-Dox groups, indicating that Tf-Ps-Dox caused low systemic toxicity. This transferrin-dressed polymersomal doxorubicin provides a potent and low-toxic treatment modality for human hepatocellular carcinoma.

Keywords: Transferrin; polymersomes; reduction-sensitive; targeted delivery; liver cancer

1. Introduction

Hepatocellular carcinoma (HCC) is a leading cause of cancer-related death worldwide [1]. The major clinical treatments for HCC include conventional surgery, liver transplantation, trans-arterial chemoembolization, and small kinase inhibitors [2-4]. Traditional chemotherapeutics is not effective and further associated with severe side effects as a result of poor HCC-specificity [5]. The development of HCC-targeted nanotherapeutics has been regarded as a valuable solution to HCC chemotherapy [6-18]. Antibodies and peptides were routinely used as targeting ligands for HCC treatment. For instance, CD44 antibody targeted liposomal nanoparticles were used for molecular imaging and therapy of HCC [19]. SP94 peptide decorated Pt nanocluster assembly was used to overcome cisplatin resistance for anti-HCC therapy [20]. However, none of these novel HCC-targeted nanoformulations has moved forward to clinical trials, partly due to the fact that these targeting ligands have not been validated in patients. Meanwhile, although galactosamine-PHPMA-GFLG-Dox (PK2) has been translated to the human clinical trials, the expression of asialoglycoprotein receptor (ASGP-R) on mammalian hepatocytes leads to low HCC-specificity [21].

Transferrin receptor (TfR) is overexpressed on many cancerous cells including SMMC-7721 [22], MDA-MB 231 [23], U87-MG [24], A549 cells [25] owing to abnormal iron metabolism [26]. Transferrin (Tf), an endogenous protein that serves to translocate iron into TfR-overexpressed cells, is known as a natural ligand for TfR [27]. Tf has been employed as a specific carrier for different drugs [28, 29] or targeting ligand for various nanoformulations [30-37]. Notably, several targeted nanomedicines homing to TfR are currently under clinical trials [38]. For instance, Tf-modified lipid formulation of oxaliplatin, MBP-426, from Mebiopharm has entered Phase II clinical trials for metastatic gastric, gastro esophageal junction, and esophageal adenocarcinoma [39]. Tf-targeted RRM2 siRNA formulation, CALAA-01 from Calando Pharmaceuticals, has been tested for the treatment of solid tumor patients [40, 41].

Here, we report on Tf-functionalized, polycarbonate based polymersomal Dox (Tf-Ps-Dox) for targeted therapy of orthotopic SMMC-7721 HCC in nude mice (Scheme 1). The polymersomes were prepared via co-self-assembly of biodegradable copolymer poly(ethylene glycol)-*b*-poly(trimethylene carbonate-*co*-dithiolane trimethylene carbonate) (mPEG-P(TMC-DTC), M_n = 5.0-14.8-1.9 kg/mol) and maleimide-functionalized copolymer (Mal-PEG-P(TMC-DTC), M_n =7.5-15.5-2.2 kg/mol). We reported that the Ps-Dox has outstanding stability, high tolerability, and reduction triggered drug release behavior [42]. The high stability of Ps-Dox allows facile surface conjugation with targeting ligands by post-modification method. In this study, the post-modification of Ps-Dox with Tf, the influence of Tf density on targeting ability of Ps-Dox, and the therapeutic efficacy of Tf-Ps-Dox toward TfR overexpressing hepatocellular carcinoma were investigated.
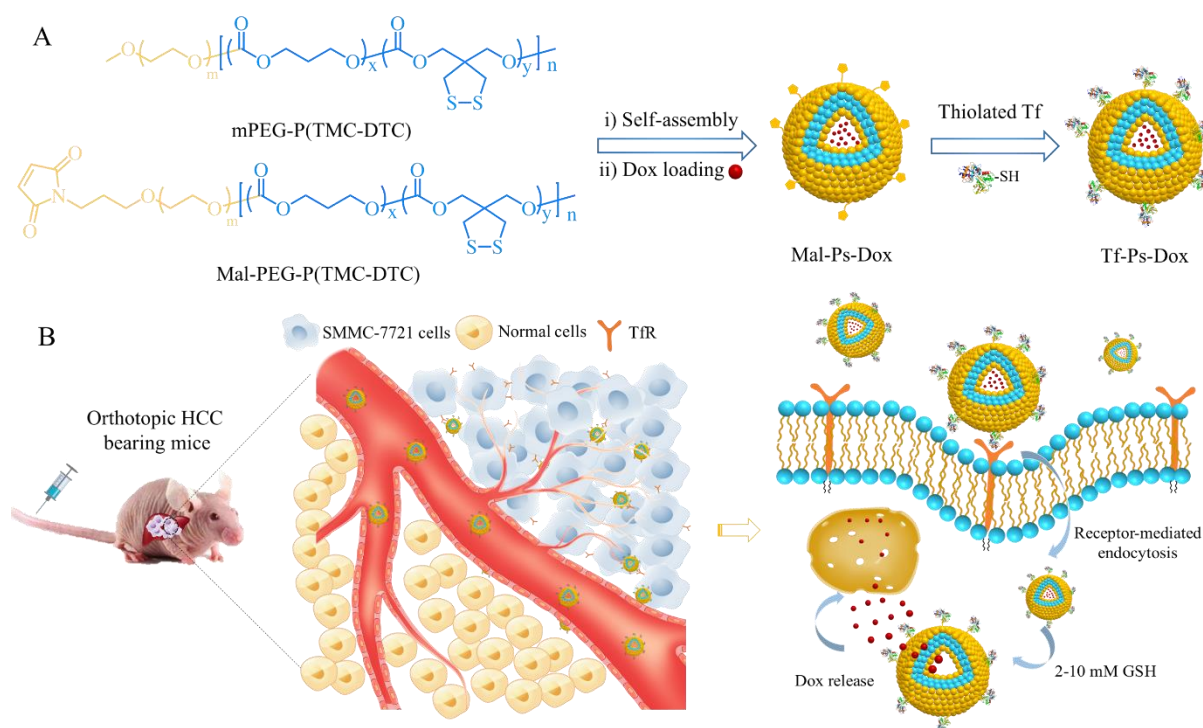
Scheme 1. Schematic illustration of the preparation of transferrin-guided, reduction-responsive and reversibly cross-linked polymersomal doxorubicin (Tf-Ps-Dox) (A), and the targeted therapy of orthotopic SMMC-7721 hepatocellular carcinoma of Tf-Ps-Dox *in vivo* (B).

2. Experimental section

2.1 Formation of maleimide-functionalized polymersomal doxorubicin (Mal-Ps-Dox)

Mal-Ps-Dox was obtained by first self-assembly of poly(ethylene glycol)-*b*-poly(trimethylene carbonate-*co*-dithiolane trimethylene carbonate) (mPEG-P(TMC-DTC)) and maleimide-functionalized copolymer Mal-PEG-P(TMC-DTC), and then active loading of Dox·HCl using a pH-gradient method [42]. In a typical example, 100 µL DMF solution of mPEG-P(TMC-DTC) and Mal-PEG-P(TMC-DTC) mixture (molar ratio = 95/5, polymer concentration = 40 mg/mL) was dropwise added into 900 µL citric acid buffer (10 mM, pH 4.0). After standing still for 1 h, the pH was adjusted to 7.8 using saturated Na_2HPO_4 solution. Then 160 µL Dox·HCl aqueous solution (5 mg/mL, theoretical drug loading content = 16.7 wt.%) was added and incubated at 37 $^{\mathrm{o}}$C for 12 h under mild stirring before 6 h dialysis (MWCO 7000 Da). During the work-up procedure thus-obtained Mal-Ps-Dox was self-crosslinked. Dox loading level was quantified using UV-Vis spectroscopy (UH5300, Hitachi, Japan) at excitation wavelength of 480 nm. Drug loading efficiency (DLE) and drug loading content (DLC) were determined using the following formula:

DLE (%) = (weight of loaded Dox/weight of Dox in feed) × 100

DLC (wt.%) = (weight of loaded Dox/total weight of polymer and Dox) × 100.

2.2 Preparation of Tf-Ps-Dox

Tf-Ps-Dox was prepared by post-modification of Mal-Ps-Dox with thiolated transferrin (Tf-SH). Tf was thiolated using 2-iminothiolanes hydrochloride (Traut's Reagent, TRC) under a nitrogen atmosphere. In brief, 22 µL TRC solution (10 mg/mL) in 10 mM HEPES (pH 8.0) containing 2 mM EDTA was added into 1 mL Tf solution (10 mg/mL) in the same media, to give a final TRC/Tf molar ratio of 10/1. The reaction proceeded at 37 $^{\mathrm{o}}$C for 1 h. The excess TRC was removed by repeated centrifugal ultrafiltration (Millipore, MWCO 10,000 Da). The extent of thiolation as determined by Ellman's assay [43] was four thiol groups per transferrin.

Then, Tf-SH was added into 1 mL freshly obtained Mal-Ps-Dox at a molar ratio of Tf-SH /Maleimide of 2/1. After reaction at 37 $^{\circ}$C for 8 h, free Tf was removed by centrifugal ultrafiltration (Millipore, MWCO 100,000Da) twice at 3000 g for 10 mins. Tf was quantified using BCA assays based on a standard curve of protein solutions of known concentrations, and the conjugation efficiency (the ratio of Tf and polymer) was then calculated.

2.3 MTT assays

Human hepatocellular carcinoma SMMC-7721 cells were seeded in a 96-well plate (5 × 10^3 cells/well) for 24 h to reach 70% confluence. 20 μL of Tf-Ps-Dox (5 μg Dox/mL) with Tf molar contents of 2.2%, 3.9%, 6.0% to 7.0% were added and incubated for 2 h. The media were substituted with fresh media and the cells were cultured further for 70 h. MTT in PBS (10 μL, 5 mg/mL) was then added to the cells for 4 h before adding 150 μL DMSO to dissolve MTT-formazan. The absorbance at 492 nm was measured using a microplate reader. The cells were co-incubated with 20-fold excess transferrin (1 mg/mL) and Tf-Ps-Dox for 2 h to verify the receptor-mediated endocytosis mechanism. Tf-Ps-Dox were used as controls.

2.4 Flow cytometry and confocal laser scanning microscopy (CLSM) studies

Flow cytometry was employed to investigate the cellular uptake of Tf-Ps-Dox. SMMC-7721 cells seeded in a 6-well plate (5×10^5 cells/well) were incubated with Tf-Ps-Dox (Tf molar contents of 2.2%, 3.9%, 6.0%, to 7.0%), Ps-Dox (10 μg DOX/mL), and PBS at 37 $^{\circ}$C for 2 h. To prove receptor-mediated endocytosis, 20-fold excess transferrin (1 mg/mL) were co-incubated with Tf-Ps-Dox. The cells following twice PBS washing were detached, centrifuged, dispersed in 500 μL PBS, and immediately measured using a BD FACS Calibur flow cytometer at FL2-channel (ex. 488 nm, em. 560 nm). For each sample, 10,000 events were collected.

For CLSM measurements, Tf-Ps-Dox was added (100 μL, 10 μg DOX/mL) to SMMC-

7721 cells seeded on coverslips in 24-well plate. After 2 h, the cells were fixed with 4% paraformaldehyde solution and the nuclei were stained with 4',6'-diamidino-2-phenylindole (DAPI) for 10 min before CLSM observation. PBS washing (×3) was applied between two steps. The inhibition experiment was conducted by adding 20-fold excess transferrin (1 mg/mL) in the culture medium. The same settings of CLSM was used for both groups. 405 Diode laser was selected for DAPI channel and the laser power was adjusted to 3%. Argon laser was selected for doxorubicin acquisition and the power was adjusted to 13%. The scan speed is 200 Hz with resolution 1024 × 1024. The PMT intensity of DAPI is 20% and 60% for doxorubicin smart gain (HyD), respectively.

2.5 Animal models

The subcutaneous and orthotopic liver tumor models in female Balb/c nude mice were established [6] by inoculating SMMC-7721 cells (1×10^6 per mouse) in 50 μL PBS containing BD Matrigel into right hind flank of 5-week-old mice, or into right upper liver lobe of 6-week-old mice, respectively. The orthotopic liver tumor was used for therapeutics studies 12 days after inoculation. Mice with subcutaneous tumor size of 200-300 mm^3 were applied for studies of biodistribution and imaging. Animals were handled under protocols approved by Soochow University Laboratory Animal Center, and the Animal Care and Use Committee of Soochow University.

2.6 *In vivo* pharmacokinetics and biodistribution of Tf-Ps-Dox

Tumor free Balb/c mice were injected with 200 μL Tf-Ps-Dox, Ps-Dox, or clinically used liposomal formulation (Lipo-Dox) at DOX dose of 4 mg/kg via tail veins (n = 3). At predetermined time points, about 20 μL blood was withdrawn from the retro-orbital sinus of mice into heparinized tubes and immediately centrifuged. The plasma was taken and incubated

overnight with 500 μL DMF containing 20 mM DTT at 25 °C. After centrifugation, Dox in the supernatant was quantified by fluorometry (Cary Eclipse, ex. 488 nm, em. 560 nm), and plotted as a function of time. The elimination half-lives and the area under the curve were derived.

In vivo targetability of Tf-Ps to subcutaneous SMMC 7721 tumor was investigated using near infrared fluorescence imaging technique. Cy5 labeled polymer was incorporated to form Tf-Ps-Cy5 and Ps-Cy5, respectively. Briefly, 200 μL Tf-Ps-Cy5 or Ps-Cy5 was *i.v.* injected into mice bearing subcutaneous SMMC-7721 tumor (1.5 μg Cy5 equiv./mouse, n = 3). The fluorescence images were acquired at varied time intervals.

2.7 Anticancer therapy of Tf-Ps-Dox in mice bearing orthotopic SMMC-7721 tumor

The mice bearing orthotopic tumor were randomly grouped (n = 6), and 200 μL Tf-Ps-Dox was injected via tail veins every four days (Dox dose: 8, 12 or 16 mg/kg, total 8 injections). Controls included PBS, Lipo-Dox (4 mg/kg) and Ps-Dox (8 mg/kg). Body weights of the mice were measured every two days and normalized to their initial weights. One mouse of each group was sacrificed on day 44, and heart, liver, spleen, lung, and kidney were taken for photograph and histological analyses (H&E staining and TUNEL staining). The survival rates, behavior changes, and liver ascites of the rest mice (n = 5) were monitored over time. Mice were also considered dead when the abdominal circumferences reached 100 mm due to liver ascites.

2.8 Statistical analysis

Difference between groups was judged using one-way ANOVA with Tukey multiple comparisons tests using Prism 7. Kaplan-Meier survival curves were analyzed by log-rank test for comparisons using Prism 7. $^*p$ <0.05 was considered significant, and $^{**}p<0.01$ and $^{***}p<0.001$ were highly significant.

3. Results and discussion

3.1 Formation of Tf-Ps-Dox

Transferrin-guided polymersomal doxorubicin (Tf-Ps-Dox) was obtained by post-modification of maleimide-functionalized polymersomal doxorubicin (Mal-Ps-Dox) with thiolated transferrin (Tf-SH) (Scheme 1A). PEG-P(TMC-DTC) was selected in this study mainly owing to its unique features including biocompatibility, robust capacity of polymersome forming and Dox loading, reduction triggered drug release, decent stability, and facile surface functionalization for cellular targeting. Tf-SH was acquired with ca. 4 thiol groups per molecule, as shown by Ellman's assays, through treating Tf with Traut's Reagent under oxygen-free conditions at 37 ºC for 1 hour. Mal-Ps-Dox was fabricated with varying Mal molar surface densities from 3% to 10% and fixed Dox theoretical loading content of 16.7 wt.%, from mPEG-P(TMC-DTC) and Mal-PEG-P(TMC-DTC), as reported previously for peptide-functionalized polymersomal doxorubicin [42, 44]. The results showed that at a Tf-SH/Mal molar ratio of 2/1, rather consistent Tf conjugation efficiencies (70% - 78%) to Mal-Ps-Dox, determined by BCA assays, were obtained (Table 1). Tf-Ps-Dox with Tf densities of 2.2%, 3.9%, 6.0%, and 7.0% were fabricated from Mal-Ps-Dox with Mal densities of 3%, 5%, 7% and 10%, respectively. Notably, all four Tf-Ps-Dox exhibited a similar Dox loading content (10.1-10.6 wt.%), small size (73-75 nm), and low polydispersity. Figure 1A presents a typical size distribution profiles of Tf-Ps-Dox. As expected, Tf-Ps-Dox was stable against extensive dilution or 10% serum (Figure S1), owing to automatic disulfide-crosslinking of the membrane during fabrication [45-47]. The release mechanism of Dox from the polymersomes could be ascribed to the enhanced permeation of polymersomal membrane resulting from the de-crosslinking of polymersomes as triggered by the intracellular reduction environment (2-10 mM GSH).

Table 1. Characterization of Tf-Ps-Dox with varying Tf surface densities (Theoretical Dox loading content = 16.7 wt.%)

| Entry	Mal molar ratio (%)	Tf surface density (%)[a]	Conjugation efficiency (%)	Size (nm)[b]	PDI[b]	DLC[c] (wt.%)	DLE[c] (%)
1	3	2.2	73	73±1	0.15	10.1	56
2	5	3.9	78	75±2	0.16	10.6	59
3	8	6.0	75	75±2	0.16	10.4	58
4	10	7.0	70	74±2	0.17	10.5	58

[a] Determined by BCA assay.
[b] Determined by DLS.
[c] Determined by UV spectroscopy.

3.2 Specific antitumor effect of Tf-Ps-Dox toward SMMC-7721 cells

SMMC-7721 cells overexpressing transferrin receptor (TfR) [22] were employed to study the targetability of Tf-Ps-Dox. Flow cytometry showed that all four Tf-Ps-Dox formulations all afforded about 2-fold higher cellular uptake than Ps-Dox (Figure 1B), signifying that Tf-Ps-Dox could target to SMMC-7721 cells and Tf surface density is not critical for cell entry. Interestingly, MTT assays revealed that the antitumor activity of Tf-Ps-Dox is, however, highly dependent on Tf density, in which Tf-Ps-Dox with a Tf density of 3.9% produced the highest inhibitory effect to the cells (Figure 1C). This is possibly due to the saturation of membrane TfR and/or too high avidity of Tf-Ps-Dox at high ligand densities to TfR. Davis et. al reported that a minimum Tf density was needed for efficient targeting in vivo [31], while too high or too low avidity of Tf to membrane TfR could lead to reduced tumor accumulation [48]. These results also indicate that Tf density has a great influence on the intracellular trafficking and/or drug release of Tf-Ps-Dox. We hereafter in later investigations selected Tf-Ps-Dox at Tf density of 3.9%, and referred it to Tf-Ps-Dox if not otherwise specified. Tf-Ps-Dox displayed a half-maximal inhibitory concentration (IC$_{50}$) toward SMMC-7721 cells of about 6.8 μg Dox equiv./mL, which though higher than free Dox, was 2 times lower than Ps-Dox (Figure 1D).

Free Dox is known to be highly toxic to cells. The high systemic toxicity greatly limits its direct application *in vivo*.
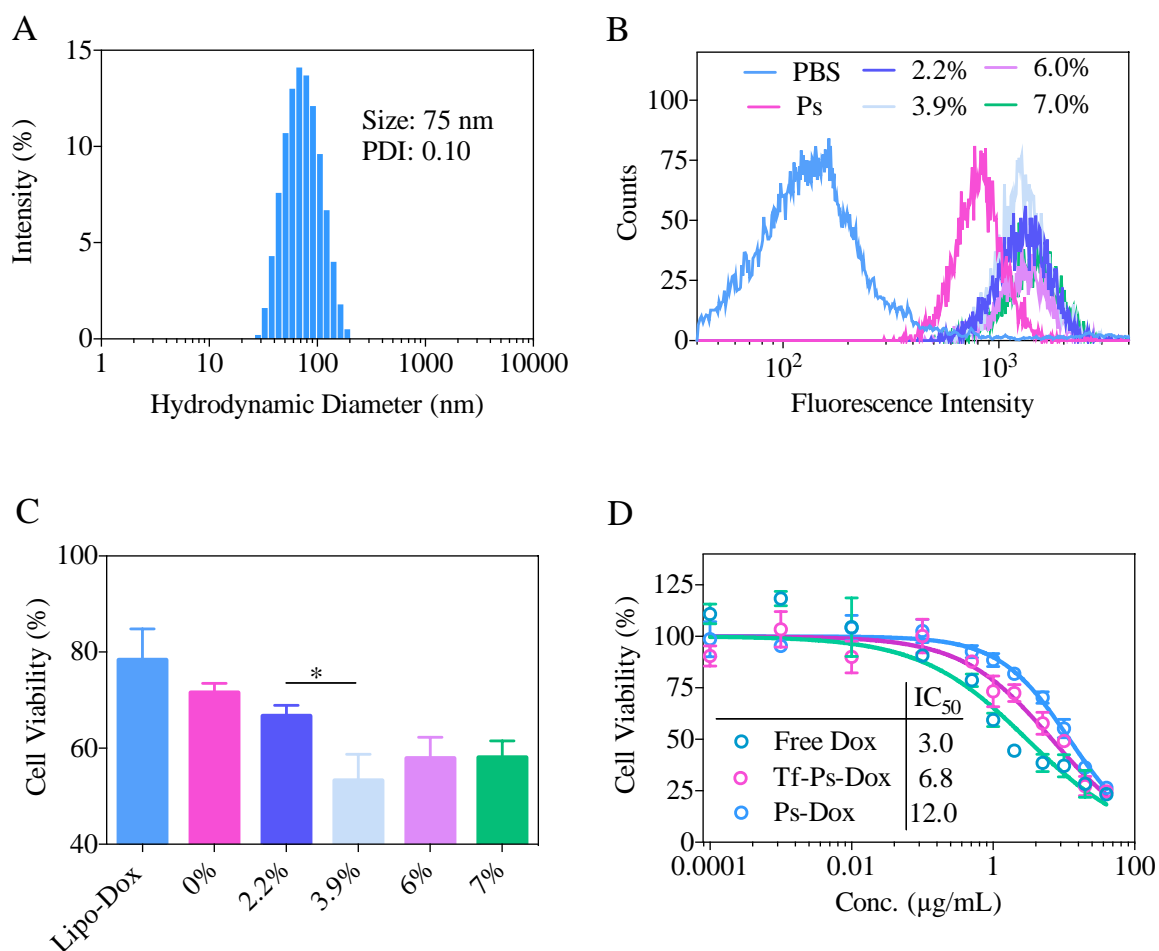
Figure 1. *In vitro* characterization of Tf-Ps-Dox. (A) Hydrodynamic size distribution. (B) Flow cytometry of SMMC-7721 cells after 2 h cultivation with Tf-Ps-Dox with varying Tf surface densities. Dox-loaded Ps and PBS were used as controls. (C) Viability of SMMC-7721 cells after 2 h incubation with Tf-Ps-Dox or Lipo-Dox (5 μg Dox/mL) and 70 h culture in fresh medium. (D) MTT assays of Tf-Ps-Dox to SMMC-7721 cells after 2 h incubation and 70 h culture in fresh medium.

To verify that Tf-Ps-Dox was taken up by SMMC-7721 cells though TfR-mediated endocytosis, we performed competitive inhibition studies by co-incubating cells with 20-fold excess free Tf. Flow cytometry showed clearly that uptake of Tf-Ps-Dox by SMMC-7721 cells was reduced to half when co-incubated with free Tf (Figure 2A), proving a TfR-mediated uptake mechanism for Tf-Ps-Dox. Accordingly, the IC_{50} of Tf-Ps-Dox was also truncated to

half by co-incubation with 20-fold excess of free Tf (Figure 2B), becoming similar to that of the non-targeted Ps-Dox. CLSM images showed that Tf-Ps-Dox treated cells had much more intense Dox fluorescence than free Tf co-cultured group (Figure 2C). All the above results support that Tf-Ps-Dox actively targets to SMMC-7721 hepatocellular carcinoma cells via TfR.
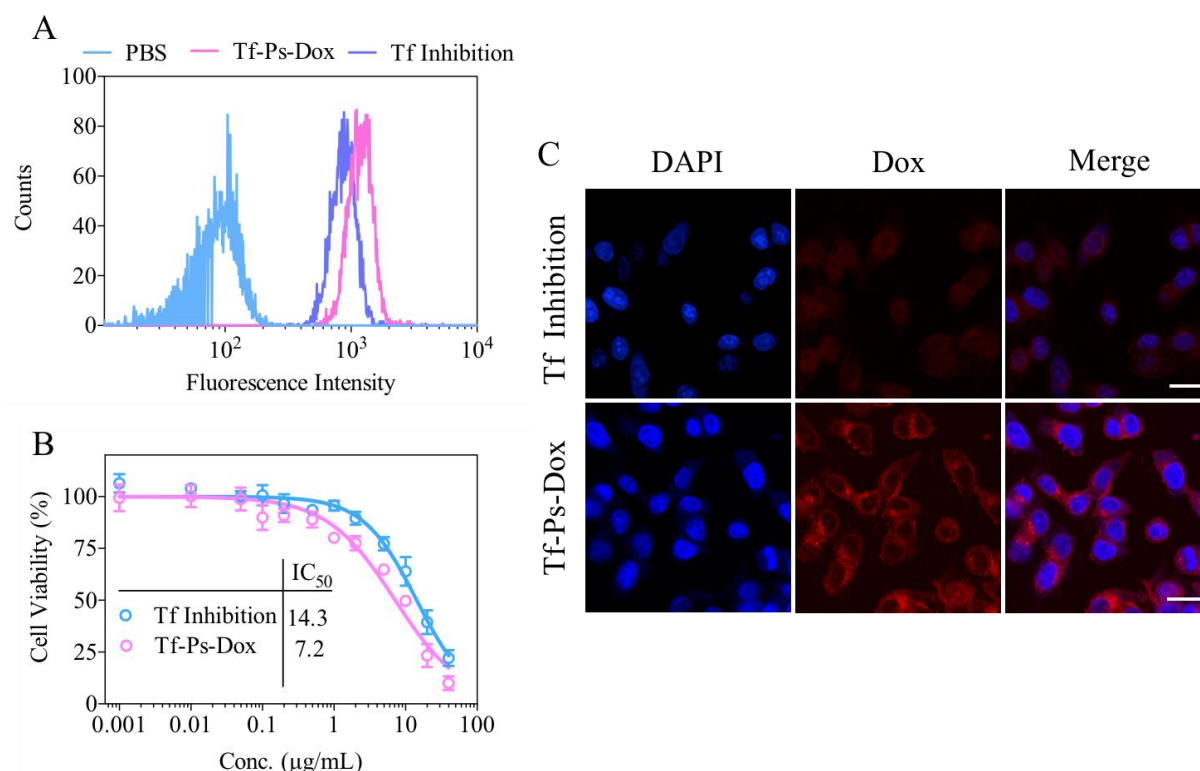

Figure 2. The inhibition of cellular uptake and cell viability of SMMC-7721 cells treated by Tf-Ps-Dox for 2 h with or without adding 20 times excess free Tf, as measured by (A) Flow cytometry, (B) MTT assays, and (C) CLSM images. Scare bar: 20 μm.

3.3 *In vivo* biodistribution and pharmacokinetics

The *in vivo* fluorescence images of subcutaneous SMMC-7721 tumors monitored over time following *i.v.* injection of Cy5-labeled blank Tf-Ps showed fast and obviously better tumor accumulation than Cy5-labeled blank Ps (non-targeted control), in which maximum Cy5 fluorescence in tumor was discerned at 6 h post-injection (Figure 3A). Then Dox contents in the tumors and major organs of mice treated by Tf-Ps-Dox at 6 h post-injection were quantified, and the tumor accumulation of 8.5% ID/g was achieved, which was respective ca. 2 or 3 times

that of Ps-Dox or Lipo-Dox, respectively (Figure 3B). This targeted tumor accumulation of the drug was higher than Dox loaded folic acid modified nanoparticles (5% ID/g) [49]. The similar enhanced tumor uptake (ca. 3-fold) was found for PTX loaded glycyrrhizin directed nanoparticles [50]. In contrast, no significant difference in Dox level was detected in the major organs for Tf-Ps-Dox and Ps-Dox. Hence, these results indicate that Tf can specifically improve the HCC accumulation of Ps-Dox.
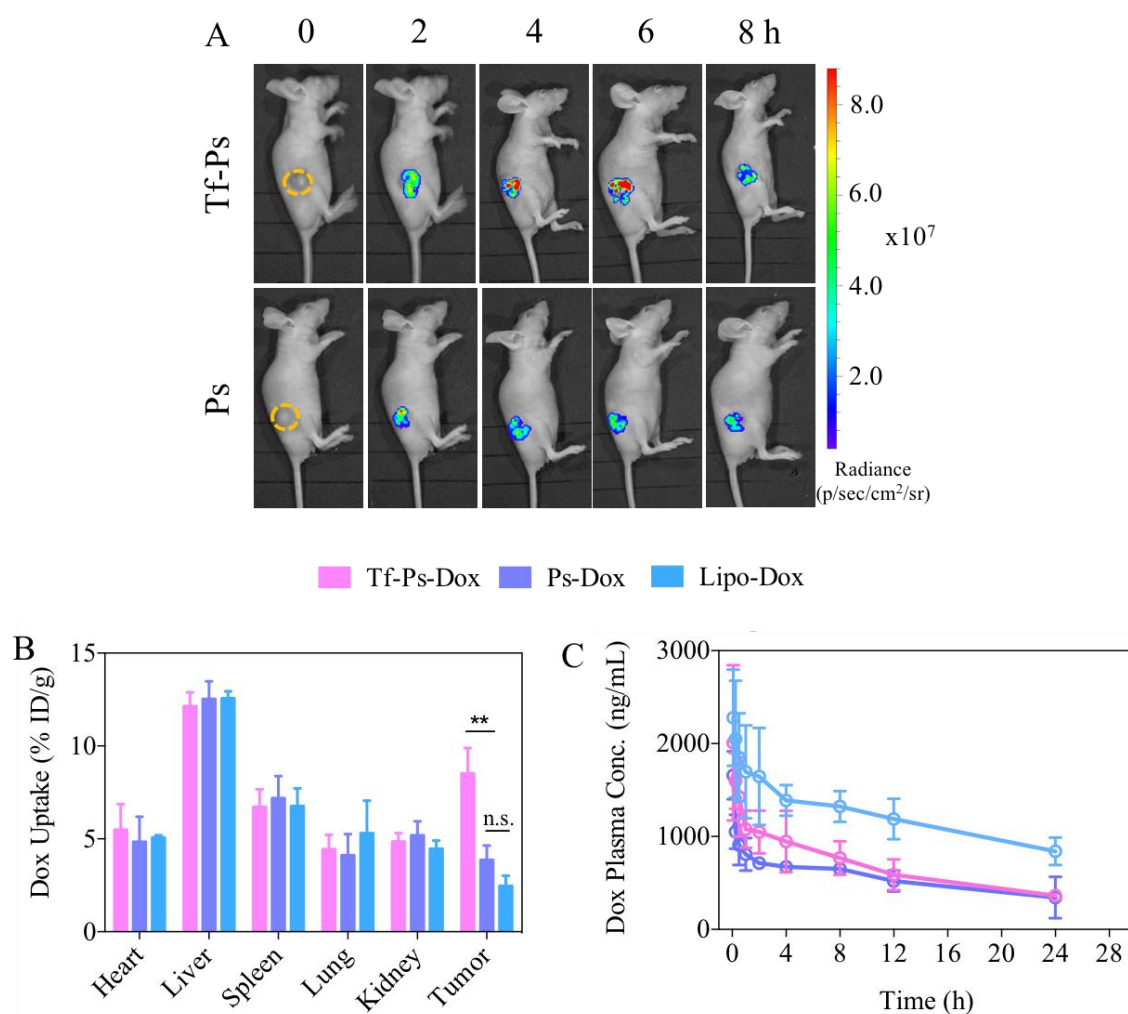

Figure 3. *In vivo* imaging, biodistribution and pharmacokinetics studies. (A) NIR images of mice bearing SMMC-7721 tumor at various time points after iv injection of Cy5-labeled Tf-Ps or Ps. (B) *In vivo* biodistribution of Dox in SMMC-7721 tumor-bearing mice treated by Tf-Ps-Dox (Dox dose: 10 mg/kg) at 6 h post injection. (C) Pharmacokinetics of Tf-Ps-Dox in Balb/c mice (Dox dose: 4 mg/kg). One-way Anova and Tukey multiple comparisons tests, **$p < 0.01$.

We further investigated the pharmacokinetics of Tf-Ps-Dox in Balb/c mice. It was showed that Tf-Ps-Dox could circulate long in mice and had an elimination half-life was 8.7 h, which was comparable to that of non-targeted Ps-Dox (8.2 h), but shorter than Lipo-Dox (16.9 h, Figure 3C). The results prove that Tf-Ps-Dox indeed has admirable *in vivo* stability, and that the Tf-functionalization does not shorten their blood circulation.

3.4 Therapy of mice with orthotopic SMMC-7721 tumor

These tumor-bearing mice received only PBS developed severe liver ascites starting from 26 days post tumor inoculation and abnormal increase of body weights (Figure 4A). The mice became apathetic and weak over time. These results indicate successful establishment of orthotopic SMMC-7721 tumor in the liver. During the treatment, the mice were judged dead if body weight loss was over 15% as compared to the original weight or the abdominal circumference exceeded 100 mm. All PBS-treated mice died within 42 days (Figure 4B). In sharp contrast, the mice received Tf-Ps-Dox treatment at varying doses from 8, 12, to 16 mg/kg every 4 days (8 injections in total) were mostly without liver ascites in 40 days, in which the increase of body weights was largely inhibited (Figure 4A). The non-targeted Ps-Dox group revealed, though some antitumor effect, apparently more liver ascites and body weight increase than Tf-Ps-Dox. Considering the injection frequency and the total dose of Dox, Lipo-Dox at 8 mg/kg was not studied for comparison owing to serious side effects [51]. Lipo-Dox (4 mg/kg) was selected as control instead. However, it also caused systematic toxicity over repeated intravenous injection, including significant body weight loss (Figure 4A) and pronounced hand-food syndrome (HFS) of the mice. Similarly, Webster et. al reported that galactosylated chitosan triptolide nanoparticles treated mice with orthotopic HCC only revealed slight body weight change, in contrast to an obvious weight loss of the non-targeted group resulting from severe

side effects and significant body weight increase of PBS group [52]. As shown in the survival curves, Lipo-Dox treatment to the mice did not improve the survival rate as compared to PBS group (Figure 4B). The survival rate was, however, significantly improved by treating with Ps-Dox or Tf-Ps-Dox at 8 mg/kg, in which the median survival times were 58 and 82 days, respectively. In addition, the median survival times could be further increased to 88 and 96 days by increasing the dose of Tf-Ps-Dox to 12 and 16 mg/kg, respectively. Of note, 1 out of 5 mice receiving Tf-Ps-Dox (16 mg/kg) revealed complete regression (CR). This median survival time was much longer than that of 5-fluorouracil nanoparticle treated mice with orthotopic SMMC-7721 tumor (35 days) [53].
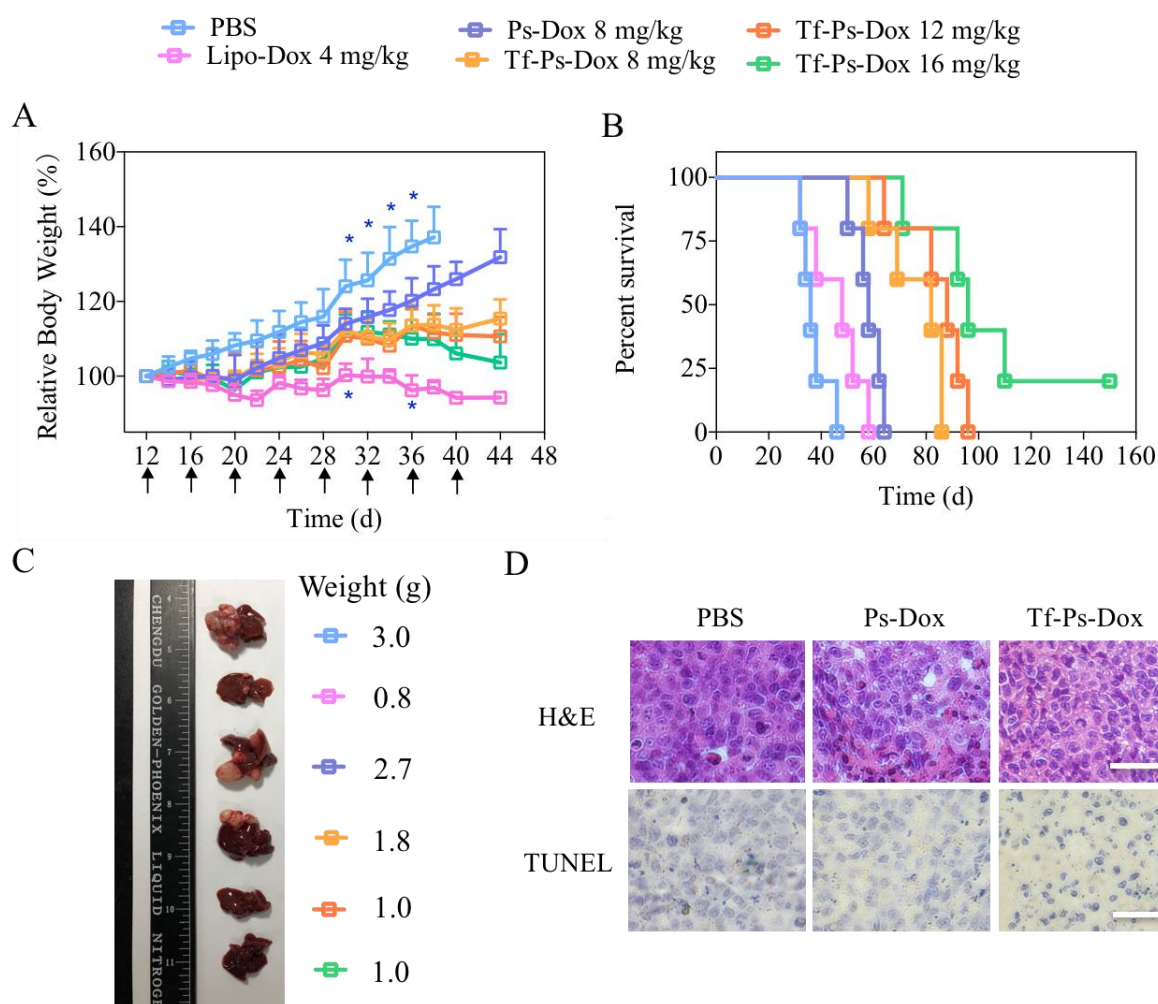
Figure 4. *In vivo* antitumor activity of Tf-Ps-Dox in orthotopic SMMC-7721 tumor bearing mice (n = 6) with drug administration every 4 days (total 8 injections). (A) Relative body weight changes. (B)

Survival curves. Statistical analysis (Kaplan-Meier analysis, log-rank test): Ps-Dox (8 mg/kg) *vs* PBS: **p <0.01; Lipo-Dox (4 mg/kg) *vs* PBS: n.s.; Ps-Dox (8 mg/kg) *vs* Lipo-Dox (4 mg/kg): n.s.; Tf-Ps-Dox (8 mg/kg) *vs* Lipo-Dox (4 mg/kg) and Ps-Dox (8 mg/kg): **p <0.01; Tf-Ps-Dox (16 mg/kg) *vs* Tf-Ps-Dox (8 mg/kg): *p <0.05. (C) The photograph of livers excised on 44 d. (D) The images of H&E and TUNEL stained tumor slices from mice treated with PBS, Ps-Dox (8 mg/kg), or Tf-Ps-Dox (8 mg/kg). Scale bar: 50 μm.
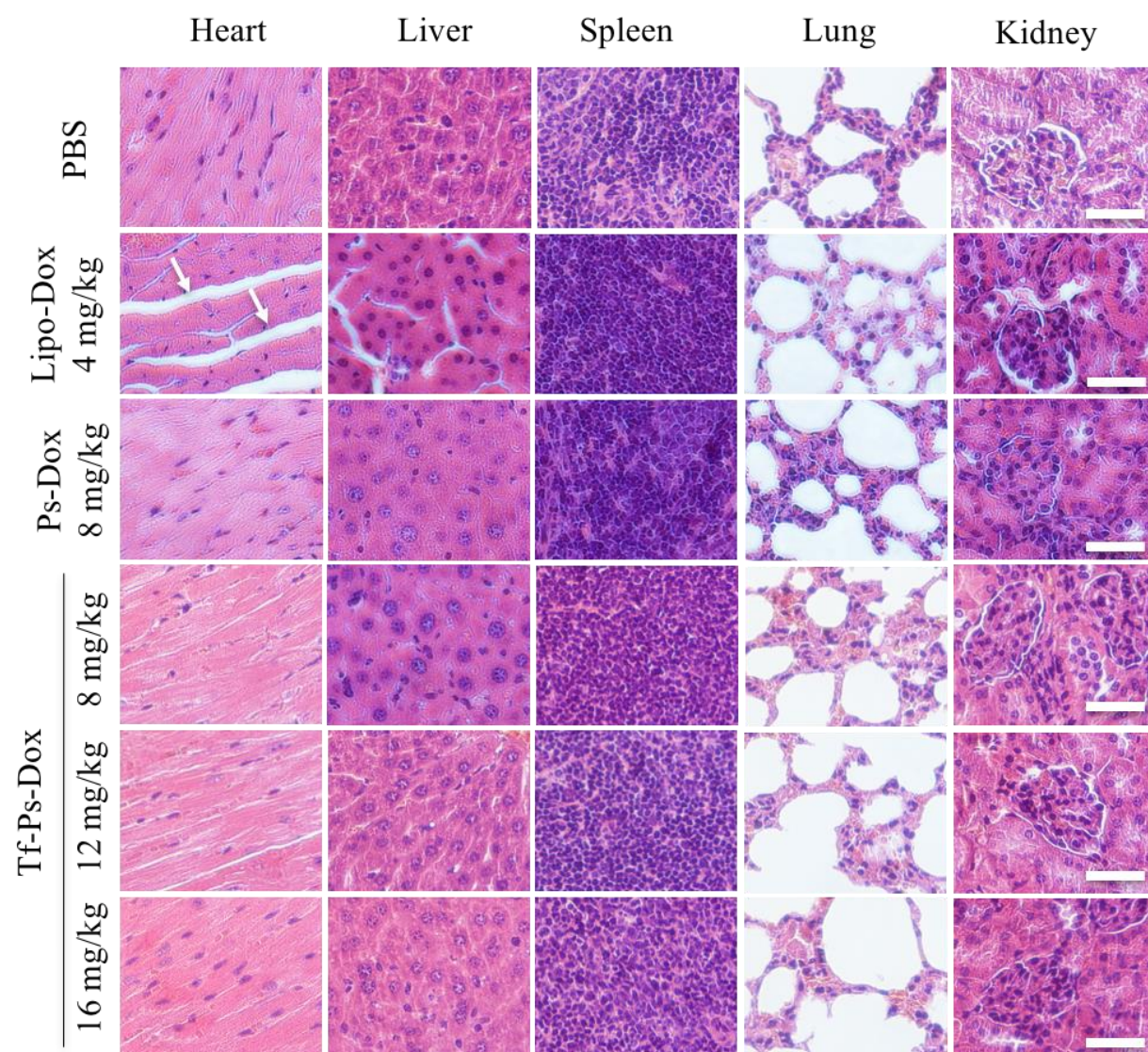
Figure 5. H&E stained heart, liver, spleen, lung, and kidney sections excised from mice after different treatments (400 ×). Scale bar: 50 μm.

Figure 4C shows the *ex-vivo* photographs of livers excised from different treatment groups on day 44. At 8 mg/kg, Tf-Ps-Dox induced apparently better tumor suppression than Ps-Dox. Notably, the mice treated with Tf-Ps-Dox at 12 and 16 mg/kg bare significantly fewer tumorous spots in the livers. The histological assays of H&E or TUNEL stained slices of orthotopic liver tumors displayed distinct differences between PBS, Ps-Dox and Tf-Ps-Dox groups. From TUNEL assays, Tf-Ps-Dox group showed significant decrease of tumor burden and increase of tumor apoptosis compared with PBS group (Fig 4D). While in H&E stained tumor slices, Tf-Ps-Dox treated tumors displayed much more nuclear-lysis, incomplete cell membrane, and cell shrinkage than Ps-Dox group, in contrast to PBS group. In addition, H&E slices of the major organs exhibited that Tf-Ps-Dox instigated no obvious side effects to normal organs (Figure 5, Figure S2). However, Lipo-Dox caused damage not only to the liver but also to the heart tissue. For instance, after repeated injection of Lipo-Dox, the liver tissue structure became incomplete, the liver plate was not arranged neatly, and some hepatocyte nuclear vacuolar degeneration occurred (Figure S3). In addition, abnormal shape and arrangement was found in cardiomyocytes.

4. Conclusion

We have established that transferrin-guided polymersomal doxorubicin (Tf-Ps-Dox) can be easily fabricated with controlled transferrin density, small size and high drug loading via ligand post-modification strategy. Functionalization of Ps-Dox with 3.9% Tf brings about better uptake and specific antitumor effect toward transferrin receptor over-expressed human SMMC-7721 cells. *In vivo* experiments reveal that Tf-Ps-Dox can actively target to orthotopic SMMC-7721 tumor in mice, leading to 2-3 times better tumor accumulation and significantly improved survival time compared with non-targeted Ps-Dox and clinically viable liposomal Dox formulation (Lipo-Dox). Particularly, Tf-Ps-Dox at doses of 8 to 16 mg/kg brings visibly lesser

systemic toxicity than Lipo-Dox at 4 mg/kg. Transferrin-guided polymersomal doxorubicin has appeared to be appealing for targeted hepatocellular carcinoma chemotherapy.

Acknowledgements

References

[1] B. Njei, Y. Rotman, I. Ditah, J.K. Lim, Emerging Trends in Hepatocellular Carcinoma Incidence and Mortality, Hepatology 61 (2015) 191-199.

[2] A. Fomer, M. Gilabert, J. Bruix, J.L. Raoul, Treatment of intermediate-stage hepatocellular carcinoma, Nat. Rev. Clin. Oncol. 11 (2014) 525-535.

[3] N.K. Mohamed, M.A. Hamad, M.Z.E. Hafez, K.L. Wooley, M. Elsabahy, Nanomedicine in management of hepatocellular carcinoma: Challenges and opportunities, Int. J. Cancer 140 (2017) 1475-1484.

[4] A. Lamprecht, Nanomedicines in gastroenterology and hepatology, Nat. Rev. Gastroenterol. Hepatol. 12 (2015) 195-204.

[5] Y.D. Livney, Y.G. Assaraf, Rationally designed nanovehicles to overcome cancer chemoresistance, Adv. Drug Delivery Rev. 65 (2013) 1716-1730.

[6] Y. Fang, W.J. Yang, L. Cheng, F.H. Meng, J. Zhang, Z.Y. Zhong, EGFR-targeted multifunctional polymersomal doxorubicin induces selective and potent suppression of orthotopic human liver cancer in vivo, Acta Biomater. 64 (2017) 323-333.

[7] D.Y. Gao, T.T. Lin, Y.C. Sung, Y.C. Liu, W.H. Chiang, C.C. Chang, J.Y. Liu, Y.C. Chen, CXCR4-targeted lipid-coated PLGA nanoparticles deliver sorafenib and overcome acquired drug resistance in liver cancer, Biomaterials 67 (2015) 194-203.

[8] J. Gao, H.W. Chen, Y.S. Yu, J.J. Song, H. Song, X. Su, W. Li, X. Tong, W.Z. Qian, H. Wang, J.X. Dai, Y.J. Guo, Inhibition of hepatocellular carcinoma growth using immunoliposomes for co-delivery of adriamycin and ribonucleotide reductase M2 siRNA, Biomaterials 34 (2013) 10084-10098.

[9] J. Gao, Y.S. Yu, Y.Y. Zhang, J.J. Song, H.W. Chen, W. Li, W.Z. Qian, L. Deng, G. Kou, J.M. Chen, Y.J. Guo, EGFR-specific PEGylated immunoliposomes for active siRNA delivery in hepatocellular carcinoma, Biomaterials 33 (2012) 270-282.

[10] T.P. Guan, W.T. Shang, H. Li, X. Yang, C.H. Fang, J. Tian, K. Wang, From Detection to Resection: Photoacoustic Tomography and Surgery Guidance with Indocyanine Green Loaded Gold Nanorod@liposome Core-Shell Nanoparticles in Liver Cancer, Bioconjug. Chem. 28 (2017) 1221-1228.

[11] Y.K. Kim, A. Minai-Tehrani, J.H. Lee, C.S. Cho, M.H. Cho, H.L. Jiang, Therapeutic efficiency of folated poly(ethylene glycol)-chitosan-graft-polyethylenimine-Pdcd4 complexes in H-ras12V mice with liver cancer, Int. J. Nanomedicine 8 (2013) 1489-1498.

[12] X.B. Ma, H. Hui, Y.S. Jin, D. Dong, X.L. Liang, X. Yang, K. Tan, Z.F. Dai, Z. Cheng, J. Tian, Enhanced immunotherapy of SM5-1 in hepatocellular carcinoma by conjugating with gold nanoparticles and its in vivo bioluminescence tomographic evaluation, Biomaterials 87 (2016) 46-56.

[13] D. Shao, J. Li, X. Zheng, Y. Pan, Z. Wang, M. Zhang, Q.X. Chen, W.F. Dong, L. Chen, Janus "nano-bullets" for magnetic targeting liver cancer chemotherapy, Biomaterials 100 (2016) 118-133.

[14] B. Singh, Y. Jang, S. Maharjan, H.J. Kim, A.Y. Lee, S. Kim, N. Gankhuyag, M.S. Yang, Y.J. Choi, M.H. Cho, C.S. Cho, Combination therapy with doxorubicin-loaded galactosylated poly(ethyleneglycol)-lithocholic acid to suppress the tumor growth in an orthotopic mouse model of liver cancer, Biomaterials 116 (2017) 130-144.

[15] L.F. Tan, S.P. Wang, K. Xu, T.L. Liu, P. Liang, M. Niu, C.H. Fu, H.B. Shao, J. Yu, T.C. Ma, X.L. Ren, H. Li, J.P. Dou, J. Ren, X.W. Meng, Layered MoS2 Hollow Spheres for Highly-Efficient Photothermal Therapy of Rabbit Liver Orthotopic Transplantation Tumors, Small 12 (2016) 2046-2055.

[16] J. Wang, Z.H. Zhang, X. Wang, W. Wu, X.Q. Jiang, Size- and pathotropism-driven targeting and washout-resistant effects of boronic acid-rich protein nanoparticles for liver cancer regression, J. Control. Release 168 (2013) 1-9.

[17] H.J. Zhang, N. Patel, S. Ding, J. Xiong, P.P. Wu, Theranostics for hepatocellular carcinoma with Fe3O4@ZnO nanocomposites, Biomater. Sci. 4 (2016) 288-298.

[18] X.X. Zhang, S.Y. Guo, R. Fan, M.R. Yu, F.F. Li, C.L. Zhu, Y. Gan, Dual-functional liposome for tumor targeting and overcoming multidrug resistance in hepatocellular carcinoma cells, Biomaterials 33 (2012) 7103-7114.

[19] L.N. Wang, W.J. Su, Z. Liu, M.Q. Zhou, S. Chen, Y.A. Chen, D. Lu, Y.H. Liu, Y. Fan, Y.Z. Zheng, Z.C. Han, D.L. Kong, J.C. Wu, R. Xiang, Z.J. Li, CD44 antibody-targeted liposomal nanoparticles for molecular imaging and therapy of hepatocellular carcinoma, Biomaterials 33 (2012) 5107-5114.

[20] H.P. Xia, F.Y. Li, W. Park, S.F. Wang, Y. Jang, Y. Du, S. Baik, S. Cho, T. Kang, D.H. Kim, D.S. Ling, K.M. Hui, T. Hyeon, pH-Sensitive Pt Nanocluster Assembly Overcomes Cisplatin Resistance and

Heterogeneous Stemness of Hepatocellular Carcinoma, ACS Central Sci. 2 (2016) 802-811.

[21] J.L. Lv, H.L. Sun, Y. Zou, F.H. Meng, A.A. Dias, M. Hendriks, J. Feijen, Z.Y. Zhong, Reductively degradable alpha-amino acid-based poly(ester amide)-graft-galactose copolymers: facile synthesis, self-assembly, and hepatoma-targeting doxorubicin delivery, Biomater. Sci. 3 (2015) 1134-1146.

[22] K.L. Fan, C.Q. Cao, Y.X. Pan, D. Lu, D.L. Yang, J. Feng, L.N. Song, M.M. Liang, X.Y. Yan, Magnetoferritin nanoparticles for targeting and visualizing tumour tissues, Nat. Nanotechnol. 7 (2012) 459-464.

[23] M.S. Muthu, R.V. Kutty, Z.T. Luo, J.P. Xie, S.S. Feng, Theranostic vitamin E TPGS micelles of transferrin conjugation for targeted co-delivery of docetaxel and ultra bright gold nanoclusters, Biomaterials 39 (2015) 234-248.

[24] T. Kang, M.Y. Jiang, D. Jiang, X.Y. Feng, J.H. Yao, Q.X. Song, H.Z. Chen, X.L. Gao, J. Chen, Enhancing Glioblastoma-Specific Penetration by Functionalization of Nanoparticles with an Iron-Mimic Peptide Targeting Transferrin/Transferrin Receptor Complex, Mol. Pharm. 12 (2015) 2947-2961.

[25] H. Makwana, F. Mastrotto, J.P. Magnusson, D. Sleep, J. Hay, K.J. Nicholls, S. Allen, C. Alexander, Engineered Polymer-Transferrin Conjugates as Self-Assembling Targeted Drug Delivery Systems, Biomacromolecules 18 (2017) 1532-1543.

[26] K.B. Johnsen, T. Moos, Revisiting nanoparticle technology for blood-brain barrier transport: Unfolding at the endothelial gate improves the fate of transferrin receptor-targeted liposomes, J. Control. Release 222 (2016) 32-46.

[27] S. Tortorella, T.C. Karagiannis, Transferrin Receptor-Mediated Endocytosis: A Useful Target for Cancer Therapy, J. Membr. Biol. 247 (2014) 291-307.

[28] T.C. Karagiannis, P.N. Lobachevsky, B.K.Y. Leung, J.M. White, R.F. Martin, Receptor-mediated DNA-targeted photoimmunotherapy, Cancer Res. 66 (2006) 10548-10552.

[29] M. Szwed, A. Matusiak, A. Laroche-Clary, J. Robert, I. Marszalek, Z. Jozwiak, Transferrin as a drug carrier: Cytotoxicity, cellular uptake and transport kinetics of doxorubicin transferrin conjugate in the human leukemia cells, Toxicol. In Vitro 28 (2014) 187-197.

[30] S. Bae, K. Ma, T.H. Kim, E.S. Lee, K.T. Oh, E.S. Park, K.C. Lee, Y.S. Youn, Doxorubicin-loaded human serum albumin nanoparticles surface-modified with TNF-related apoptosis-inducing ligand and

transferrin for targeting multiple tumor types, Biomaterials 33 (2012) 1536-1546.

[31] C.H.J. Choi, C.A. Alabi, P. Webster, M.E. Davis, Mechanism of active targeting in solid tumors with transferrin-containing gold nanoparticles, Proc. Natl. Acad. Sci. U. S. A. 107 (2010) 1235-1240.

[32] A.J. Clark, M.E. Davis, Increased brain uptake of targeted nanoparticles by adding an acid-cleavable linkage between transferrin and the nanoparticle core, Proc. Natl. Acad. Sci. U. S. A. 112 (2015) 12486-12491.

[33] Y.N. Cui, Q.X. Xu, P.K.H. Chow, D.P. Wang, C.H. Wang, Transferrin-conjugated magnetic silica PLGA nanoparticles loaded with doxorubicin and paclitaxel for brain glioma treatment, Biomaterials 34 (2013) 8511-8520.

[34] J. Wang, S.M. Tian, R.A. Petros, M.E. Napier, J.M. DeSimone, The Complex Role of Multivalency in Nanoparticles Targeting the Transferrin Receptor for Cancer Therapies, J. Am. Chem. Soc. 132 (2010) 11306-11313.

[35] Z.G. Yang, B. Yu, J. Zhu, X.M. Huang, J. Xie, S.L. Xu, X.J. Yang, X.M. Wang, B.C. Yung, L.J. Lee, R.J. Lee, L.S. Teng, A microfluidic method to synthesize transferrin-lipid nanoparticles loaded with siRNA LOR-1284 for therapy of acute myeloid leukemia, Nanoscale 6 (2014) 9742-9751.

[36] H.J. Zhang, L. Hou, X.J. Jiao, Y.D. Ji, X.L. Zhu, Z.Z. Zhang, Transferrin-mediated fullerenes nanoparticles as Fe2+-dependent drug vehicles for synergistic anti-tumor efficacy, Biomaterials 37 (2015) 353-366.

[37] F.C. Lam, S.W. Morton, J. Wyckoff, T.L.V. Han, M.K. Hwang, A. Maffa, E. Balkanska-Sinclair, M.B. Yaffe, S.R. Floyd, P.T. Hammond, Enhanced efficacy of combined temozolomide and bromodomain inhibitor therapy for gliomas using targeted nanoparticles, Nat. Commun. 9 (2018) 11.

[38] R. van der Meel, L.J.C. Vehmeijer, R.J. Kok, G. Storm, E.V.B. van Gaal, Ligand-targeted particulate nanomedicines undergoing clinical evaluation: Current status, Adv. Drug Delivery Rev. 65 (2013) 1284-1298.

[39] R. Suzuki, T. Takizawa, Y. Kuwata, M. Mutoh, N. Ishiguro, N. Utoguchi, A. Shinohara, M. Eriguchi, H. Yanagie, K. Maruyama, Effective anti-tumor activity of oxaliplatin encapsulated in transferrin-PEG-liposome, Int. J. Pharm. 346 (2008) 143-150.

[40] M.E. Davis, J.E. Zuckerman, C.H.J. Choi, D. Seligson, A. Tolcher, C.A. Alabi, Y. Yen, J.D. Heidel,

A. Ribas, Evidence of RNAi in humans from systemically administered siRNA via targeted nanoparticles, Nature 464 (2010) 1067-1070.

[41] N.C. Bellocq, S.H. Pun, G.S. Jensen, M.E. Davis, Transferrin-containing, cyclodextrin polymer-based particles for tumor-targeted gene delivery, Bioconjug. Chem. 14 (2003) 1122-1132.

[42] Y. Zou, F.H. Meng, C. Deng, Z.Y. Zhong, Robust, tumor-homing and redox-sensitive polymersomal doxorubicin: A superior alternative to Doxil and Caelyx?, J. Control. Release 239 (2016) 149-158.

[43] G.L. Ellman, A COLORIMETRIC METHOD FOR DETERMINING LOW CONCENTRATIONS OF MERCAPTANS, Arch. Biochem. Biophys. 74 (1958) 443-450.

[44] N. Zhang, Y.F. Xia, Y. Zou, W.J. Yang, J. Zhang, Z.Y. Zhong, F.H. Meng, ATN-161 Peptide Functionalized Reversibly Cross-Linked Polymersomes Mediate Targeted Doxorubicin Delivery into Melanoma-Bearing C57BL/6 Mice, Mol. Pharm. 14 (2017) 2538-2547.

[45] W.J. Yang, Y. Zou, F.H. Meng, J. Zhang, R. Cheng, C. Deng, Z.Y. Zhong, Efficient and Targeted Suppression of Human Lung Tumor Xenografts in Mice with Methotrexate Sodium Encapsulated in All-Function-in-One Chimeric Polymersomes, Adv. Mater. 28 (2016) 8234-8239.

[46] Y. Jiang, J. Zhang, F. Meng, Z. Zhong, Apolipoprotein E Peptide-Directed Chimeric Polymersomes Mediate an Ultrahigh-Efficiency Targeted Protein Therapy for Glioblastoma, ACS Nano 12 (2018) 11070-11079.

[47] W.J. Yang, Y.H. Wei, L. Yang, J. Zhang, Z.Y. Zhong, G. Storm, F.H. Meng, Granzyme B-loaded, cell-selective penetrating and reduction-responsive polymersomes effectively inhibit progression of orthotopic human lung tumor in vivo, J. Control. Release 290 (2018) 141-149.

[48] D.T. Wiley, P. Webster, A. Gale, M.E. Davis, Transcytosis and brain uptake of transferrin-containing nanoparticles by tuning avidity to transferrin receptor, Proc. Natl. Acad. Sci. U. S. A. 110 (2013) 8662-8667.

[49] J.J. Wu, C. Tang, C.H. Yin, Co-delivery of doxorubicin and interleukin-2 via chitosan based nanoparticles for enhanced antitumor efficacy, Acta Biomater. 47 (2017) 81-90.

[50] L.L. Shi, C. Tang, C.H. Yin, Glycyrrhizin-modified O-carboxymethyl chitosan nanoparticles as drug vehicles targeting hepatocellular carcinoma, Biomaterials 33 (2012) 7594-7604.

[51] Y. Zou, Y.F. Xia, F.H. Meng, J. Zhang, Z.Y. Zhong, GE11-Directed Functional Polymersomal

Doxorubicin as an Advanced Alternative to Clinical Liposomal Formulation for Ovarian Cancer Treatment, Mol. Pharm. 15 (2018) 3664-3671.

[52] Y.Q. Zhang, Y. Shen, M.M. Liao, X. Mao, G.J. Mi, C. You, Q.Y. Guo, W.J. Li, X.Y. Wang, N. Lin, T.J. Webster, Galactosylated chitosan triptolide nanoparticles for overcoming hepatocellular carcinoma: Enhanced therapeutic efficacy, low toxicity, and validated network regulatory mechanisms, Nanomed.-Nanotechnol. Biol. Med. 15 (2019) 86-97.

[53] M.R. Cheng, B. He, T. Wan, W.P. Zhu, J. Han, B.B. Zha, H.X. Chen, F.X. Yang, Q. Li, W. Wang, H.Z. Xu, T. Ye, 5-Fluorouracil Nanoparticles Inhibit Hepatocellular Carcinoma via Activation of the p53 Pathway in the Orthotopic Transplant Mouse Model, PLoS ONE 7 (2012) e47115.
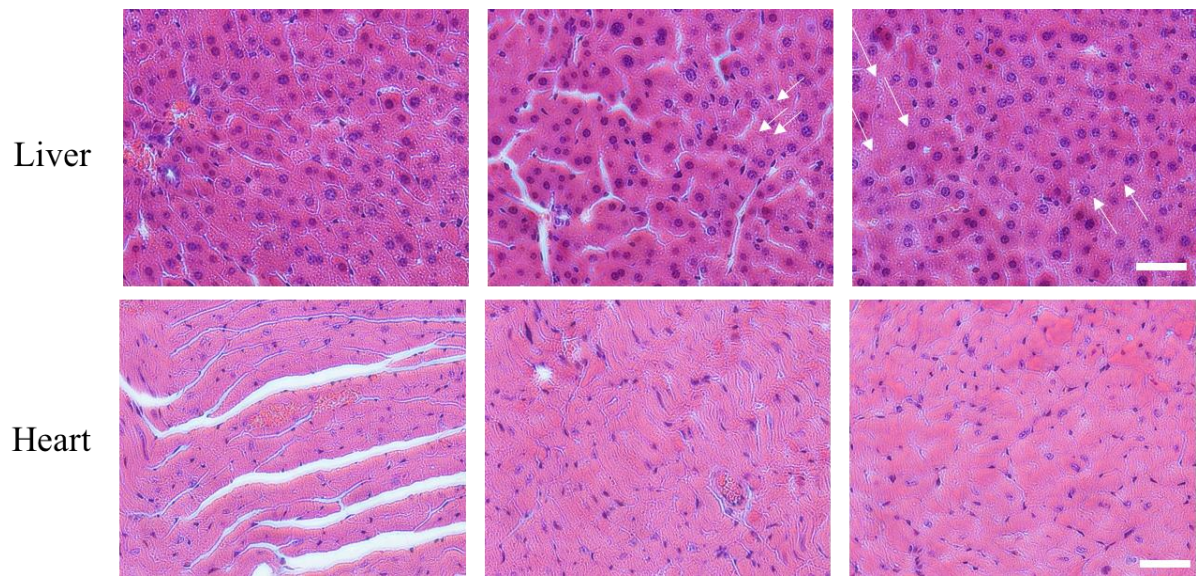
Supplementary Data
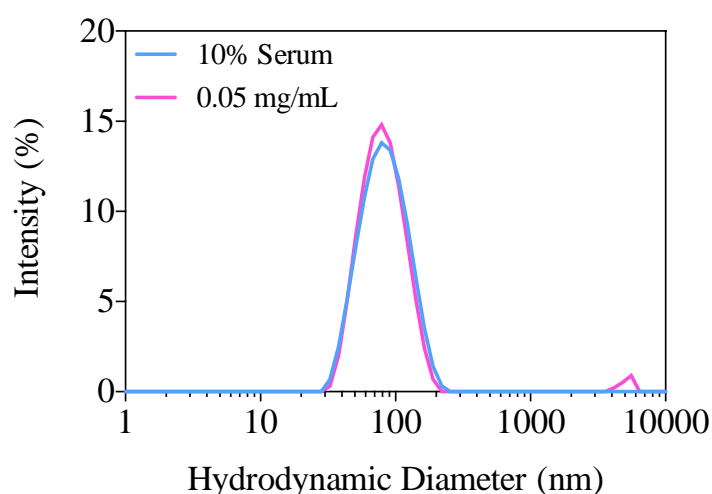
Figure S1. Colloidal stability of Tf-Ps-Dox against extensive dilution (final concentration of 0.05 mg/mL) and 10% serum after 24 h incubation determined by DLS.
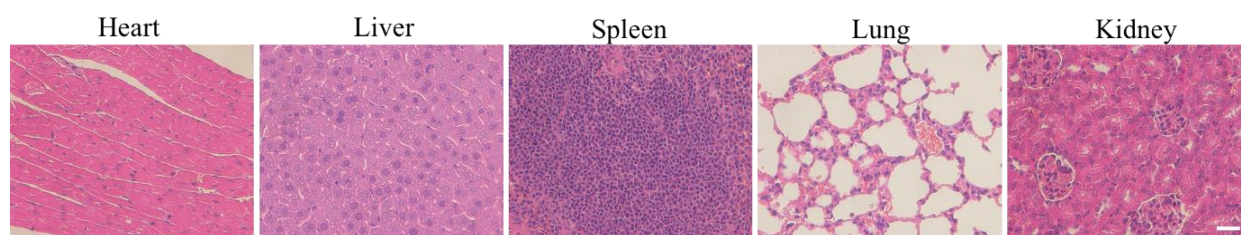
Figure S2. H&E stained slices of major organs of healthy Balb/c mice. Scale bar: 50 μm

Figure S3. H&E staining of liver and heart slices of Lipo-Dox treated mice. Arrows indicated the damages. Scale bars: 50 μm.

Chapter 3

Transferrin-Binding Peptide Functionalized Polymersomes Mediate Targeted Doxorubicin Delivery to Colorectal Cancer In Vivo*

Yaohua Wei[a,b], Xiaolei Gu[a], Yinping Sun[a], Fenghua Meng[a,]*, Gert Storm[b], and Zhiyuan Zhong [a,]*

[a] Biomedical Polymers Laboratory, College of Chemistry, Chemical Engineering and Materials Science, and State Key Laboratory of Radiation Medicine and Protection, Soochow University, Suzhou, 215123, P. R. China

[b] Department of Biomaterials Science and Technology, MIRA Institute for Biological Technology and Technical Medicine, University of Twente, PO Box 217, 7500AE, Enschede, The Netherlands

Abstract

Transferrin receptor (TfR) is a promising target validated in the clinical trials for managing various malignancies. Transferrin (Tf) and single chain antibody fragment can target TfR and are typically conjugated to nanomedicines via post-modification, which poses a formidable challenge for production. Here, we report that the polymersomes functionalized with a Tf-binding peptide CGGGHKYLRW (TBP-Ps) can selectively and stably bind Tf and subsequently mediate targeted doxorubicin (Dox) delivery to TfR over-expressing HCT-116 colorectal cancer cells *in vitro* and *in vivo*. The Tf surface density of the polymersomes could be controlled by the surface content of TBP. Interestingly, modifying Dox-loaded TBP-Ps with Tf led to greatly increased cellular uptake and inhibitory effect of HCT-116 cells. Tf-coated TBP-Ps demonstrated rapid accumulation in the tumor xenografts in nude mice following *i.v.* injection. More importantly, Dox-loaded Ps with Tf coating significantly enhanced the antitumor efficacy in mice bearing HCT-116 tumor compared to polymersomes without Tf coating. Tf-binding peptide provides an appealing strategy in formulating Tf-targeted nanomedicines.

Keywords: Transferrin; polymersomes; targeted delivery; colorectal cancer; chemotherapy

1. Introduction

Targeted nanomedicines are considered as a future treatment modality for cancers[1-4]. To accomplish targeted delivery, researchers have decorated nanomedicines with different ligands ranging from peptides[5, 6], antibodies[7] and antibody fragments[8], glycoproteins[9-11], to folic acid[12, 13]. In spite of intensive investigations, few actively targeted nanomedicines have come to the stage of clinical translation[14-16]. Notably, several targeted nano-formulations homing to transferrin receptor (TfR) have been approved for clinical trials[17-19]. TfR over-expresses on highly proliferative cancer cells[10, 12, 20]. Transferrin (Tf) and single-chain antibody fragment (ScFv) against TfR have been selected as ligands for TfR targeting[21-25]. For example, Davis *et al.* described that Tf-conjugated cyclodextrin polymer-based nanoparticles exhibited enhanced transfection of K562 leukemia cells as compared to the non-targeted ones[26], and in a phase I clinical trial targeted delivery of siRNA to patients with solid tumor[27]. Chang *et al.* reported that liposomes modified with ScFv to the TfR could mediate targeted delivery of wild-type p53 gene to metastatic pancreatic tumor model[22]. The results of phase I clinical trial revealed the accumulation of p53 gene in advanced solid tumor patients, low adverse effects, and stable disease[28]. However, the conjugation of large-sized ligands like Tf and ScFv to nanomedicines via post-modification may pose a production challenge. For instance, the thiol/maleimide reaction routinely used for post-modification with proteins encounters problems including difficulty in precise thiolation of the proteins and the inter-crosslinking between proteins resulting from multi-functionality, thus compromising the targeting efficacy *in vitro* and *in vivo*.

In contrast to large glycoproteins and antibody fragments, peptides with a short sequence and easy handling enable functionalization of nanomedicines via pre-modification[29]. Various peptides have been screened as antibody alternatives for targeted tumor therapy in the past years[30-35]. Nevertheless, to date, only BIND-014, a docetaxel nanoformulation decorated

with prostate-specific membrane antigen-targeting peptide, has reached clinical assessments[36]. The slow development of peptide-targeted nanomedicines is likely due to the fact that peptides are not as specific and effective as antibodies for *in vivo* targeting. Interestingly, Signore *et al.* reported that CGGGHKYLRW as a Tf-binding peptide (TBP) showed a high specificity and affinity to Tf[37]. TBP following plasma incubation could promote TfR-mediated cellular uptake of gold nanoparticles.

Here, we report for the first time that Tf-binding peptide-functionalized polymersomes (TBP-Ps) loaded with doxorubicin hydrochloride (TBP-Ps-Dox) following Tf absorption *in situ* mediate targeted Dox delivery to TfR over-expressing HCT-116 colorectal cancer cells *in vitro* and *in vivo* (**Scheme 1**). Several reports demonstrated that colorectal cancers over-express TfR[38, 39]. We previously reported that the disulfide-crosslinked polymersome is a promising substitute to liposome for Dox delivery[40-43]. Interestingly, TBP-Ps-Dox following Tf absorption (Tf@TBP-Ps-Dox) revealed greatly enhanced cellular uptake and antitumor effect in HCT-116 cells over Ps-Dox. The pharmacokinetics and anti-tumor therapy experiments revealed that Tf@TBP-Ps-Dox possess a long circulation time and exhibited a considerably improved inhibition of HCT-116 tumor as compared to Ps-Dox. Tf-binding peptide thus provides an appealing strategy to fabricate nanomedicines targeting to TfR over-expressing malignancies.
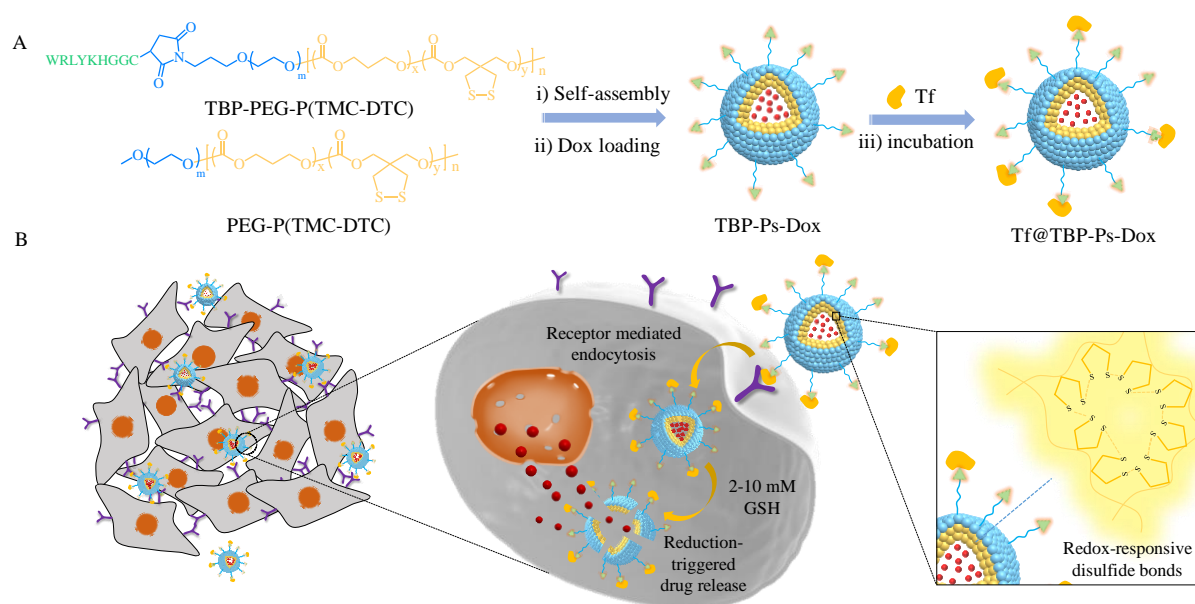
Scheme 1. (A) Schematic of facile fabrication of transferrin-coated polymersomal doxorubicin via a transferrin-binding peptide (TBP), CGGGHKYLRW. (i) TBP-functionalized polymersomes (TBP-Ps) are assembled from PEG-P(TMC-DTC) and TBP-PEG-P(TMC-DTC); (ii) Efficient Dox loading into TBP-Ps gives TBP-Ps-Dox via a pH-gradient method; and (iii) incubation with transferrin yields transferrin-coated polymersomal doxorubicin (Tf@TBP-Ps-Dox). (B) Tf@TBP-Ps-Dox can not only increase the accumulation and retention in transferrin receptor over-expressing HCT-116 colorectal tumor cells but also enhance the cellular uptake compared to Ps-Dox, leading to enhanced efficacy of targeted therapy of colorectal cancer in vivo.

2. Experimental methods

2.1 Synthesis of TBP-PEG-P(TMC-DTC)

Poly(ethylene glycol)-*b*-poly(trimethylene carbonate-co-dithiolane trimethylene carbonate) (mPEG-P(TMC-DTC)) and maleimide functionalized copolymer Mal-PEG-P(TMC-DTC) were produced according to our previous report (Table S1)[40]. Then Mal-PEG-P(TMC-DTC) (200 mg, 8.2 μmol) was added under stirring to 1.5 mL TBP (CGGGHKYLRW, 19.2 mg, 16.4 μmol) solution in N, N-dimethlyformamide (DMF). The reaction proceeded at 37 °C for 24 h, followed by intensive dialysis (MWCO 3500) against 100 mL DMF (×3) and 100 mL DCM

(×2) at room temperature (rt) with solvent replacement each hour. TBP-PEG-P(TMC-DTC) was then purified by precipitation in 30-fold cold diethyl ether, filtration and vacuum drying. Yield: 92%. BCA assay was used to determine the conjugation efficiency of TBP as described[44]. The conjugation efficiency was ca. 95%.

2.2 Fabrication of TBP-Ps-Dox and Tf@TBP-Ps-Dox

Transferrin binding peptide functionalized polymersomes (TBP-Ps) were co-assembled from TBP-PEG-P(TMC-DTC) and mPEG-P(TMC-DTC). The pH-gradient method was used to obtain doxorubicin hydrochloride (Dox·HCl) loaded polymersomes (TBP-Ps-Dox)[41]. In a typical example, 100 μL DMF solution (40 mg/mL) of mPEG-P(TMC-DTC) and TBP-PEG-P(TMC-DTC) (weight ratio: 4/1) was added into 900 μL citrate buffer (pH 4.0, 10 mM) under stirring. Saturated Na_2HPO_4 solution was used to adjust the pH to 7.8 after 1 h incubation. To reach a theoretical drug loading content of 16.7 wt.%, 160 μL Dox·HCl in deionized solution (5 mg/mL) was added dropwise, and incubated at 37 $^{\circ}$C for 12 h before purification by passing G-25 column using phosphate buffer (PB, 10 mM, pH 7.4) as an eluent. The polymersomes were collected and concentrated by repeated ultrafiltration (MWCO 10,000 Da, 2600 ×g, 10 min, rt). By manipulating the molar ratio of the two copolymers, TBP-Ps-Dox with different surface densities of TBP were produced. Size, size distribution and zeta potential were measured. The DOX loading was quantified using UV-Vis spectroscopy (Ex. 480 nm)[40].

Tf@TBP-Ps was obtained by incubating TBP-Ps with Tf (containing) solutions. Typically, 1 mL TBP-Ps with TBP molar surface density of 8.6%, 17.2%, and 25.8% referring to the copolymers (4 mg/mL) was incubated 1 hour with 13.4, 26.8, and 40.2 μM Tf (corresponding to a TBP/Tf molar ratio of 1/1), respectively, followed by 2 times ultrafiltration using ultrafiltration centrifugal tubes (MWCO 100,000 Da, 2600 ×g, 10 min, rt). BCA assay was used to determine the Tf surface contents. The influence of the incubation time of TBP-Ps with Tf

solution at blood concentration (2 mg/mL) on the final Tf surface contents were also investigated. The size and zeta potential of TBP-Ps-Dox before and after Tf coating was measured.

2.3 Determination of Tf binding stability of Tf@TBP-Ps using ^{125}I labelling

To evaluate the stability of Tf binding to TBP-Ps, Tf was labeled with radioactive [125]I . Briefly, into 200 μL of Tf solution in PBS (10 mg/mL) was added 200 μCi of Na[125]I and 10 μL chloramine-T (10 mg/mL) under constant stirring at room temperature. After 10 min, the ^{125}I-Tf was purified by ultrafiltration (MWCO 10,000 Da, 3000 rpm, 20 mins) to remove free Na[125]I. The final radioactivity of ^{125}I-Tf was measured using gamma counter (GC-1500, USTC ZONKIA, China), and the efficiency of radio labelling was calculated to be ca. 100%. Next, ^{125}I-Tf/Tf (1/10 mol/mol) was incubated with TBP-Ps for 1 h at predetermined ratios to yield ^{125}I-Tf loaded polymersomes (^{125}I-Tf@TBP-Ps), and the unbound Tf or ^{125}I-Tf was removed by repeated ultrafiltration until no radioactivity could be detected in the filtrate. To determine the Tf binding stability to TBP-Ps, 100 μL of ^{125}I-Tf@TBP-Ps was incubated with 400 μL PBS, PB solution containing 20-fold excess Tf, human serum, or mouse whole blood for 24 h before ultrafiltration. The radioactivity of purified ^{125}I-Tf@TBP-Ps was measured and was compared to their original radioactivity before the treatments.

2.4 *In vitro* cytotoxicity of Tf@TBP-Ps-Dox and blank Tf@TBP-Ps

The studies were conducted using TfR-overexpressing HCT-116 colorectal cancer cells. In brief, the cells seeded in a 96 well plate (3×10^3 cells/well) for 24 h were added 20 μL of Tf@TBP-Ps-Dox (5 μg Dox/mL) with varied TBP molar surface densities (0, 8.6%, 17.2%, or 25.8 mol.%). The medium was replaced after 2 h incubation prior to another 70 h incubation. Then 3-(4,5-dimethythiazol-2-yl)-2,5-diphenyltetrazoliumbromide (MTT) was added (10 μL,

5 mg/mL) for 4 h. The culture media were discarded, and 150 μL DMSO was incubated for 10 min. The absorbance at 492 nm of each well was acquired, and the cell viability (%) was obtained by comparing the absorbance of the cells treated with PBS only.

The cytotoxicity of Tf@TBP-Ps-Dox with 17.2% TBP to HCT-116 cells in the presence or absence of 20-fold excess Tf (1 mg/mL) was determined using MTT assays and the Dox concentrations varied from 0.001 to 40 μg/mL. The half-maximal inhibitory concentration (IC$_{50}$) was derived. Ps-Dox and commercial liposomal doxorubicin (Lipo-Dox) were used as controls. The cytotoxicity of blank Tf@TBP-Ps was similarly conducted with polymer concentrations ranging from 0.1, 0.25, 0.5 and 1 mg/mL after 48 h incubation with HCT-116 cells.

Live/dead assay of the cells was performed using a cell double staining kit (Sigma Aldrich) according to the instruction with slight change. Briefly, 10 μl Solution A and 5 μl Solution B were added to 5 ml PBS to prepare an assay solution. HCT-116 cells on microscope coverslips in 24-well plate (1×10^5 cells/well) were washed (PBS, ×3) to remove residual esterase before addition and incubation with the assay solution (100 μL) for 15 min at 37 ºC. The images were acquired by fluorescence microscopy (Olympus BX41).

2.5 Cellular uptake and intracellular Dox delivery of Tf@TBP-Ps-Dox

The HCT-116 cells in a 6-well plate (3×10^6 cells/well) were cultured for 24 h to achieve 70% confluence. Then, 100 μL of Tf@TBP-Ps-Dox with changeable TBP surface densities (0, 8.6%, 17.2%, 25.8 mol.%) and Ps-Dox were added (10 μg Dox/mL). The cells following 2 h incubation at 37 ºC were digested by trypsin (0.25%, w/v) containing EDTA (0.03%, w/v). The suspensions were centrifuged, re-dispersed in 500 μL PBS following twice PBS washing and analyzed using a BD FACS Calibur flow cytometer (ex. 488 nm, em. 560 nm). The competitive inhibition of the internalization of Tf@TBP-Ps-Dox with 17.2% TBP by HCT-116 cells in the presence of 20-fold excess Tf (1 mg/mL) was further studied.

For confocal laser scanning microscopy (CLSM) observation, HCT-116 cells were cultured on microscope coverslips in 24-well plate (1×10^5 cells/well) for 24 h. 100 µL of Tf@TBP-Ps-Dox with 17.2% TBP was added to 400 µL culture medium (10 µg Dox/mL) and incubated for 2 h at 37 $^\circ$C. The cells were washed with PBS and fixed with 4% paraformaldehyde solution for 15 min followed by washing (PBS, ×3). 4, 6-Diamidino-2-phenylindole (DAPI, 5 µg/mL) was added to stain cell nuclei for 5 min at rt before acquiring the fluorescence images using CLSM (TCS SP5) with 200 Hz speed, 1024 × 1024 resolution and 13% of Argon laser power.

A live-cell imaging system (CELL'R, Olympus) was used for Dox intracellular trafficking to visualize the internalization and intracellular release in HCT-116 cells. Briefly, the cells seeded (2×10^5 cells/well) in a glass petri dish (Φ 35 mm) in 900 µL culture medium were incubated with 100 µL Tf@TBP-Ps-Dox with 17.2 mol.% TBP or Ps-Dox (10 µg Dox/mL). The fluorescent images were captured at excitation wavelengths of 480 nm every minute.

2.6 TfR expression on HCT-116 cells

The expression of TfR on HCT-116 cell lines was evaluated by labelling with antibody CD71-PE (Miltenyi Biotec) using flow cytometry (MDA-MB 231 cells as positive control). Briefly, the cell suspension was centrifuged at 300 ×g for 10 min, and resuspend in PBS at 10^7 cells/100 µL. Then 10 µL of CD71-PE was added to incubate for 10 min in the dark at 4 $^\circ$C. The cells were washed by PBS and centrifuged at 300 ×g for 10 min. The supernatant was removed and the cell pellet was resuspended in 500 µL PBS for flow cytometry analysis.

2.7 The pharmacokinetics, in vivo imaging and biodistribution

All animals were handled under protocols approved by Soochow University Laboratory Animal Center and the Animal Care and Use Committee of Soochow University. For the pharmacokinetic studies, 200 µL of Tf@TBP-Ps-Dox, Ps-Dox or Lipo-Dox (4 mg Dox/kg) was

injected intravenously to healthy Balb/c mice (n = 3). About 50 μL blood was collected from retro-orbital sinus of mice at varied time intervals and 20 μl plasma was used for following study. 500 μL of DMF solution containing 20 mM DTT was added to extract Dox at 25 °C overnight followed by centrifugation. Dox concentration in the supernatant was quantified using fluorometry (ex. 480 nm, em. 560 nm), and was plotted as a function of the time. The circulation half-lives and the area under curve (AUC) were derived by using second-order exponential decay fit (Prism).

Female Balb/c nude mice (5 weeks) were inoculated with 50 μL HCT-116 cells (1×10^6 cell) on the right hind flank to build subcutaneous tumor model. When tumors grew to ca 150-200 mm^3, 200 μL of Cy5-labeled Tf@TBP-Ps or Ps (75 μg Cy5 equiv./kg) were intravenously administrated into the mice via tail veins. The near-infrared images of the mice were acquired at designated time intervals. At 24 h post-injection, the mice were sacrificed, and the major organs and tumors were excised for the *ex vivo* NIR imaging.

For quantification of i*n vivo* biodistribution, the mice bearing HCT-116 tumors of 150 mm^3 were *iv* administrated with Tf@TBP-Ps-Dox and Ps-Dox at 8 mg Dox equiv./kg (n = 3). After 24 h, the major organs and tumors were excised, and 0.1 g of each tissue was homogenized in Triton (1%, 0.5 mL). 1 mL DMF containing 20 mM DTT was added to extract Dox overnight. After centrifugation, the Dox fluorescence in the supernatants was measured using a plate reader (Ex. 480, Em. 560, Varioskan LUX, Thermo scientific) and expressed as injected dose per gram of tissue (%ID/g). The calculation was based on calibration curves of Dox of known concentrations in the corresponding tissues individually.

2.8 *In vivo* treatment efficacy of subcutaneous HCT-116 bearing mice

The treatment was started when the tumor reached about 50 mm^3, and this day was designated as day 0. The mice were divided into five groups randomly (n = 5) and iv injected

with Lipo-Dox (4 mg Dox/kg), Ps-Dox (8 mg Dox/kg), or Tf@TBP-Ps-Dox (8 or 16 mg Dox/kg) and PBS in 200 μL every 4 days with total of 4 injections. Tumor volume and body weight were monitored every two days, both were normalized to their initial values. All mice were sacrificed on day 20 after 2 injection cycles, and major organs and tumors were excised for photographs and histological analyses. The tumor inhibition rate (TIR) was calculated: TIR (%) = (1− tumor weight of treatment group/ tumor weight of PBS group) ×100.

The tumors and organs were fixed with 10% formalin, embedded in paraffin and sliced (thickness: 4 μm), and stained with hematoxylin and eosin (H&E) before observation with a digital microscope. The tumor slices were subjected to terminal deoxynucleotidyl transferase-mediated nick end labeling (TUNEL) before CLSM observation (TCS SP5).

2.9 Statistical analyses

One-way ANOVA with Tukey multiple comparisons tests (Prism) was used to assess the difference between groups, wherein $^*p < 0.05$ was considered significant, $^{**}p < 0.01$ and $^{***}p < 0.001$ were highly significant.

3. Results and discussion

3.1 Formation and characterization of TBP-Ps-Dox and Tf@TBP-Ps-Dox

TBP-Ps-Dox with three different TBP molar surface densities were obtained from co-assembly of PEG-P(TMC-DTC) and 8.6, 17.2 and 25.8 mol.% TBP-PEG-P(TMC-DTC) (referring to the copolymers), followed by Dox·HCl loading using a pH gradient method (**Scheme 1A**). The dynamic light scattering (DLS) revealed that all TBP-Ps-Dox exhibited small sizes around 72 nm with narrow polydispersity indexes (PDI), which were nearly identical to those of Ps-Dox fabricated from PEG-P(TMC-DTC) alone (**Table 1**). Moreover, all three TBP-Ps-Dox displayed a similar drug loading content (DLC = 9.4 - 9.6 wt.%), indicating

that TBP has negligible effect on both size and drug loading. TBP-Ps-Dox was robust against either extensive dilution or in the presence of 10% serum, resulting from disulfide-crosslinking of polymersomal membrane during preparation as reported previously[40, 45].

Table 1. Characterizations of TBP-Ps-Dox with (Theoretical Dox loading content = 16.7 wt.%)

| Entry	TBP molar ratio (%)	Size (nm)[a]	PDI[a]	DLC[b] (wt.%)	DLE[b] (%)	Zeta potential (mV)[c]	
						without Tf	with Tf
1	8.6	73±3	0.15	9.4	52%	-0.30	-0.89
2	17.2	72±2	0.13	9.6	53%	0.41	-0.90
3	25.8	72±3	0.16	9.4	52%	0.56	-1.83

[a] Determined by DLS. [b] Drug loading content (DLC) and Drug loading efficiency (DLE) determined by UV-Vis spectroscopy. [c] Determined by Zetasizer Nano-ZS equipped with a capillary electrophoresis cell before and after Tf coating.

Tf@TBP-Ps-Dox was produced by incubating preformed TBP-Ps-Dox with Tf solutions followed by extensive dialysis to remove unbound Tf. First, the incubation at Tf/TBP = 1/1 (mol/mol) for 1 h led to Tf@TBP-Ps-Dox, and Tf coating had little influence on the size and size distribution (**Figure 1A**). As anticipated, Tf surface contents of Tf@TBP-Ps-Dox accorded well with TBP surface densities (**Figure 1B**). Tf@TBP-Ps with controllable Tf surface density of 1.6, 4.0 and 6.5 mol.% could be fabricated. The Tf binding efficiency was ca. 25%. Due to the low amount of Tf on Tf@TBP-Ps-Dox, they exhibited only slightly more negative surface charge than TBP-Ps-Dox (**Table 1**). Moreover, from static light scattering (SLS) measurements[46], the total molecular weight of average polymersome (1 x 10^7 Da) and

aggregation number (ca. 450) can be calculated. Therefore, ca. 18 Tf located on the surface of Tf@TBP-Ps-Dox (4.0 mol%). But with the increase in TBP surface density from 8.6% to 17.2% the affinity of TBP to Tf increased due to the higher valency of TBP on the polymersome surface (**Figure S1A**). While further increase of TBP density from 17.6% to 25.8% the affinity kept steady. Second, the Tf surface contents at different incubation time of TBP-Ps-Dox with Tf solutions at a concentration of Tf in blood exhibited a rapid adsorption at 10 min, a further increase at 30 min, a decrease to a steady level after 1 h (**Figure S1B**). This behavior was ascribed to the dynamic balance of Tf binding on the surface of TBP-Ps-Dox. Therefore, Tf@TBP-Ps-Dox obtained by 1-hour incubation was applied for the in vitro and in vivo experiments.

To evaluate the stability of Tf binding to TBP-Ps, Tf was labeled with radioactive ^{125}I. The storage stability and exchange studies in Tf containing solutions displayed that over 85% ^{125}I-Tf was retained on the surface of TBP-Ps when stored in PBS for 48 h, in the presence of either 50-fold excess Tf, human serum or mouse whole blood (**Figure 1C**). These results illustrated that the Tf binding was quite stable and could not be exchanged by other Tf or proteins. This is in accordance with ca. 3 fold lower K_d of CGGGHKYLRW peptide binding to Tf (0.90 ± 0.25 μM) as compared to that to BSA (2.61 ± 0.38 μM) as reported by Signore [37].
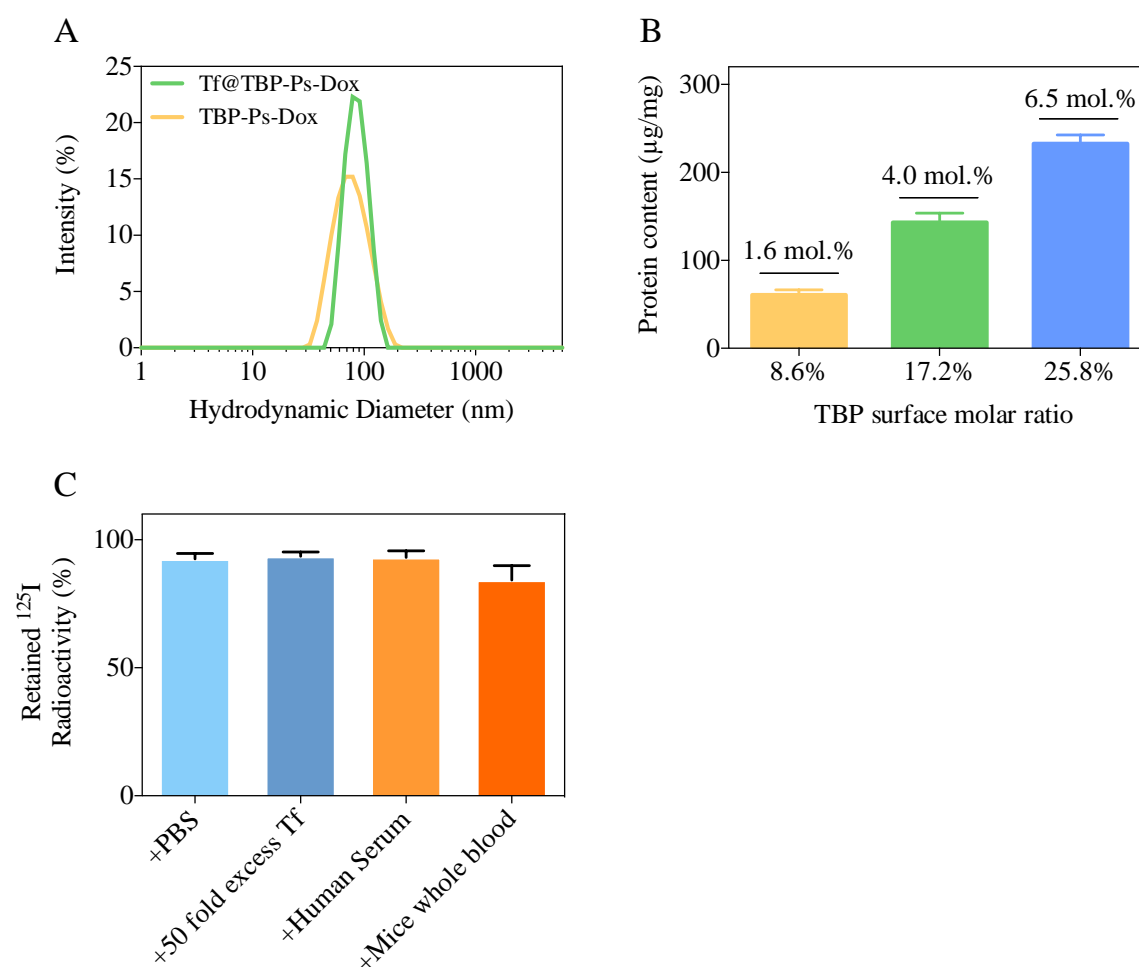
Figure 1. (A) Size and size distribution of TBP-Ps-Dox and Tf@TBP-Ps-Dox determined by DLS. (B) Tf surface density corresponding to varying TBP density at TBP/Tf =1/1 (mol/mol) as a function of TBP surface density. The numbers on top of the bars corresponding to the Tf surface density. (C) The in vitro stability of Tf binding to TBP-Ps using ^{125}I labeled Tf when stored in PBS for 48 h, treated by either 50-fold excess Tf, human serum or mouse whole blood, as compared to the original value.

3.2 TfR targeting and *in vitro* antitumor activity of Tf@TBP-Ps-Dox

Up-regulated TfR expresses on the surface of many cancerous cells like HCT-116 human colorectal cancer cells, MDA-MB 231 breast cancer cells and U87 MG glioblastoma cells[11, 38, 47, 48]. It was reported that the expression of TfR on CRL-1831cells, a normal colon cell line was significantly lower than HCT-116 cells and other cancer cells [38], and those of non-neoplastic breast cells were 4 to 5-fold lower than malignant breast cells [49-51]. The TfR

expression on HCT-116 cells were determined using CD71-PE antibody by flow cytometric analysis, taking MDA-MB 231 cells as positive control. **Figure S3** revealed that very high TfR expression on HCT-116 and MDA-MB 231 cells. Here, we used HCT-116 cell as a model for evaluating the *in vitro* and *in vivo* targeted delivery of Tf@TBP-Ps-Dox. Flow cytometry results indicated that Tf coating greatly enhanced the uptake of Ps-Dox, in which ca. 3-fold higher uptake was observed for Tf@TBP-Ps-Dox with TBP densities of 17.2% and 25.8 mol.% (**Figure 2A**). In comparison, Tf@TBP-Ps-Dox with 8.6% TBP only showed little improvement. Davis *et al.* reported that there was threshold of ligand contents for efficient TfR active targeting, and no significant difference in tumor accumulation was detected for gold nanoparticles with low ligand densities as compared with non-targeting group[52]. Besides, our previous work on Tf modified Ps-Dox revealed a saturation of cellular uptake once Tf surface density beyond 3.9%[53]. Moreover, the cellular uptake of Tf@TBP-Ps-Dox was evidently inhibited by excess free Tf due to the competitive inhibition effect (**Figure 2B**). Live cell imaging measurements displayed that Tf@TBP-Ps-Dox with 17.2% TBP had faster and higher uptake (ca. 2.5-fold) by HCT-116 cells as compared to Ps-Dox (**Figure S4&S5**), supporting the active targeting effect of the Tf coating. CLSM images of HCT-116 cells following 2 h incubation with Tf@TBP-Ps-Dox exhibited clearly more intensive Dox fluorescence than Ps-Dox (**Figure 2C**). The homogenous distribution of Dox fluorescence inside the cells indicated the intracellular Dox release.
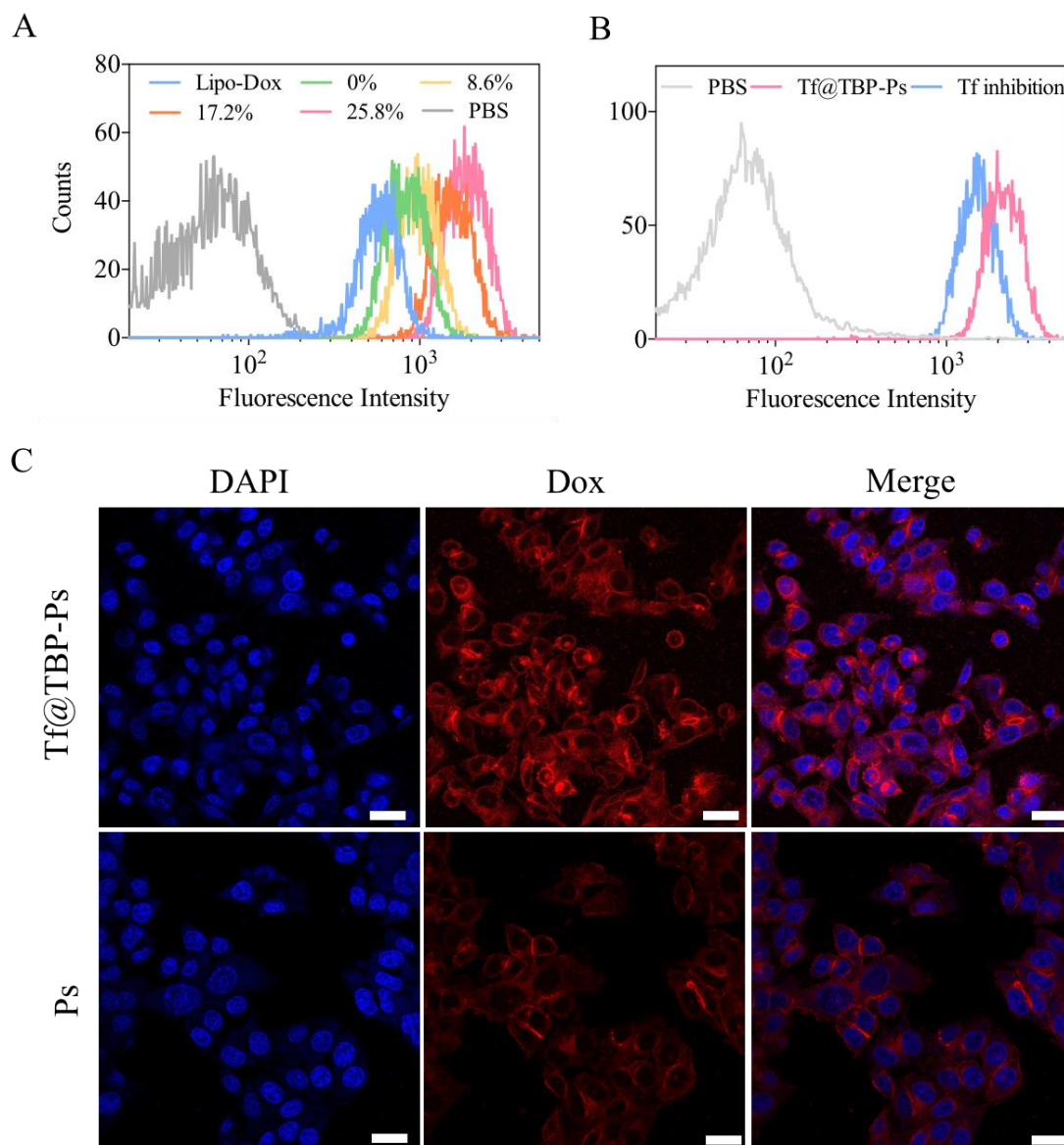
Figure 2. (A) Flow cytometry measurements of HCT-116 cells incubated 2 h with Tf@TBP-Ps-Dox with variable TBP surface densities. Lipo-Dox and PBS were used as controls. (B) HCT-116 cell uptake studies of Tf@TBP-Ps-Dox with or without 0.5 mM free Tf inhibition by flow cytometry. (C) Intracellular Dox release from Tf@TBP-Ps-Dox and Ps-Dox observed by CLSM. Scale Bar: 25 μm.

Of note, MTT assays on HCT-116 cells showed that blank Tf@TBP-Ps is non-toxic at 0.1 -1 mg/mL (**Figure 3A),** and the antitumor effect of Tf@TBP-Ps-Dox was strongly influenced by TBP densities. Tf@TBP-Ps-Dox with TBP densities of 17.2% and 25.8% caused greatly lowered cell viability than Tf@TBP-Ps-Dox with 8.6% TBP, Ps-Dox and Lipo-Dox (**Figure**

3B), which agrees well with the cell uptake results (**Figure 2A)**. The similar cytotoxic effect observed for Tf@TBP-Ps-Dox with TBP densities of 17.2% and 25.8% indicated that further increase in TBP surface density had no beneficial effect. Hence, Tf@TBP-Ps-Dox with 17.2% TBP was selected for further investigations. If not specified, in the following context Tf@TBP-Ps-Dox refers to the one with 17.2% TBP.

The half-maximal inhibitory concentrations of Tf@TBP-Ps-Dox, Ps-Dox and Lipo-Dox were determined to be 1.4 ± 1.08, 3.5 ± 1.13 and 6.4 ± 1.09 µg Dox equiv./mL, respectively (**Figure 3C**). In other words, Tf@TBP-Ps-Dox was ca. 2.5 and 4.5-fold more potent against HCT-116 cells than Ps-Dox and Lipo-Dox, respectively. Of note, Tf-functionalized liposomes, Tf-indocyane green assemblies, and Tf conjugated PLGA nanoparticles showed similar enhancement in cellular uptake and cytotoxicity in HCT-8 colon cancer cells and U87 MG cancer cells[11, 48, 54]. Live/dead assays showed clearly more apoptotic cells caused by Tf@TBP-Ps-Dox than by Ps-Dox (**Figure S6**). In addition, the cytotoxicity of Tf@TBP-Ps-Dox to HCT-116 cells was greatly reduced at co-incubation with free Tf (**Figure 3D**), supporting that the uptake of Tf@TBP-Ps-Dox by HCT-116 cells is mediated by TfR. These results confirm that Tf is stably coated on the surface of polymersomes and can effectively enhance the uptake of polymersomes in TfR over-expressing cancer cells.
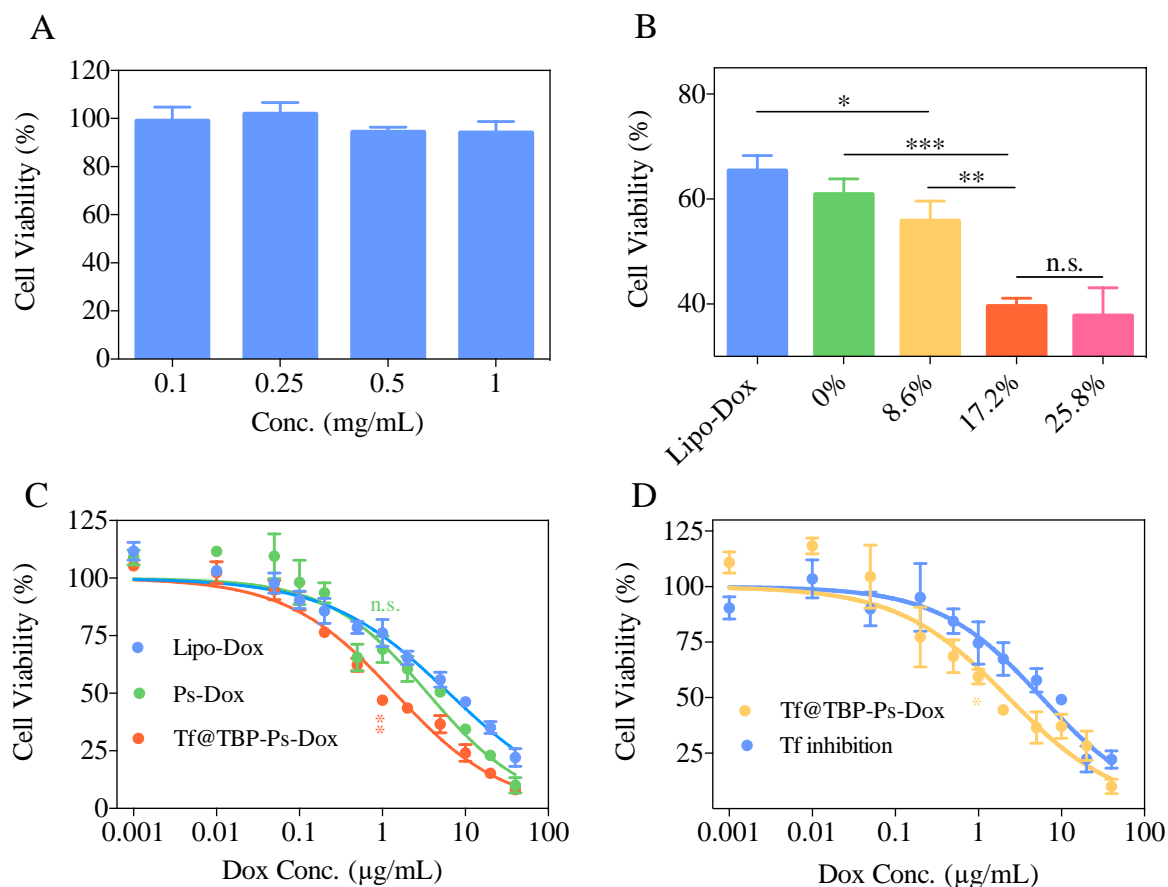
Figure 3. (A) Cytotoxicity of blank Tf@TBP-Ps determined by MTT assays. (B) Viability of HCT-116 cells after 2 h treatment with Tf@TBP-Ps-Dox (2 μg Dox/mL) and 70 h incubation with fresh medium. TBP densities varied from 8.6%, 17.2% to 25.8 mol.%. (C) Dependence of HCT-116 cell viability on concentrations of Tf@TBP-Ps-Dox with 17.2% TBP. Ps-Dox and Lipo-Dox were used as controls. (D) Competitive inhibition experiments performed on Tf@TBP-Ps-Dox in HCT-116 cells by MTT assays. Data are presented as mean ± SD (n = 5). Statistical analyses: one-way Anova Tukey multiple comparisons tests (control: Lipo-Dox) and student t-test, *p< 0.05, **p < 0.01, ***p < 0.001.

3.3 The tumor accumulation and pharmacokinetics of Tf@TBP-Ps

To monitor the biodistribution of Tf@TBP-Ps in the subcutaneous HCT-116 colorectal tumor model using near-infrared imaging (NIR), Cy5 labeled Tf@TBP-Ps and Ps were applied. The *in vivo* imaging results showed fast and high accumulation of Tf@TBP-Ps in the tumor (**Figure 4A**). The tumor exhibited the highest Cy5 fluorescence in the body and tumor Cy5

fluorescence increased from 2 to 8 h after intravenous administration. In contrast, the non-targeting Ps control exhibited much lower tumor accumulation, confirming the active HCT-116 tumor targeting of Tf@TBP-Ps. The ex vivo images of major organs and tumors at 24 h post-injection collaborated with the enhanced tumor accumulation of Tf@TBP-Ps than TBP-Ps (**Figure 4B**). Moreover, the biodistribution study showed that at 24 h Tf@TBP-Ps-Dox accumulated in tumor of 8.5% ID/g which was 2-fold of that Ps-Dox (**Figure 4C**). Furthermore, the *in vivo* pharmacokinetics following intravenous injection with 4 mg Dox/kg displayed that both Tf@TBP-Ps-Dox and Ps-Dox had long circulation time. The elimination half-life and AUC of Tf@TBP-Ps-Dox were determined to be 9.5 h and 10 μg/mL·h, respectively, while those of Ps-Dox were 8.9 h and 8.7 μg/mL·h, respectively (**Figure 4B**). The coating of TBP-Ps-Dox with Tf will not lead to detrimental effect to its stability and circulation *in vivo*. It is generally the case that protein corona forms on the surface of nanoparticles when in vivo injected, and pegylation can reduce the protein nonspecific adsorption. In our formulation, Tf stably bound on the PEG shell of TBP-Ps in the presence of human/mouse serum proteins (**Figure. 1C**) may also shield the protein absorption during circulation preventing the clearance by the MPS and increasing the targeting efficacy.
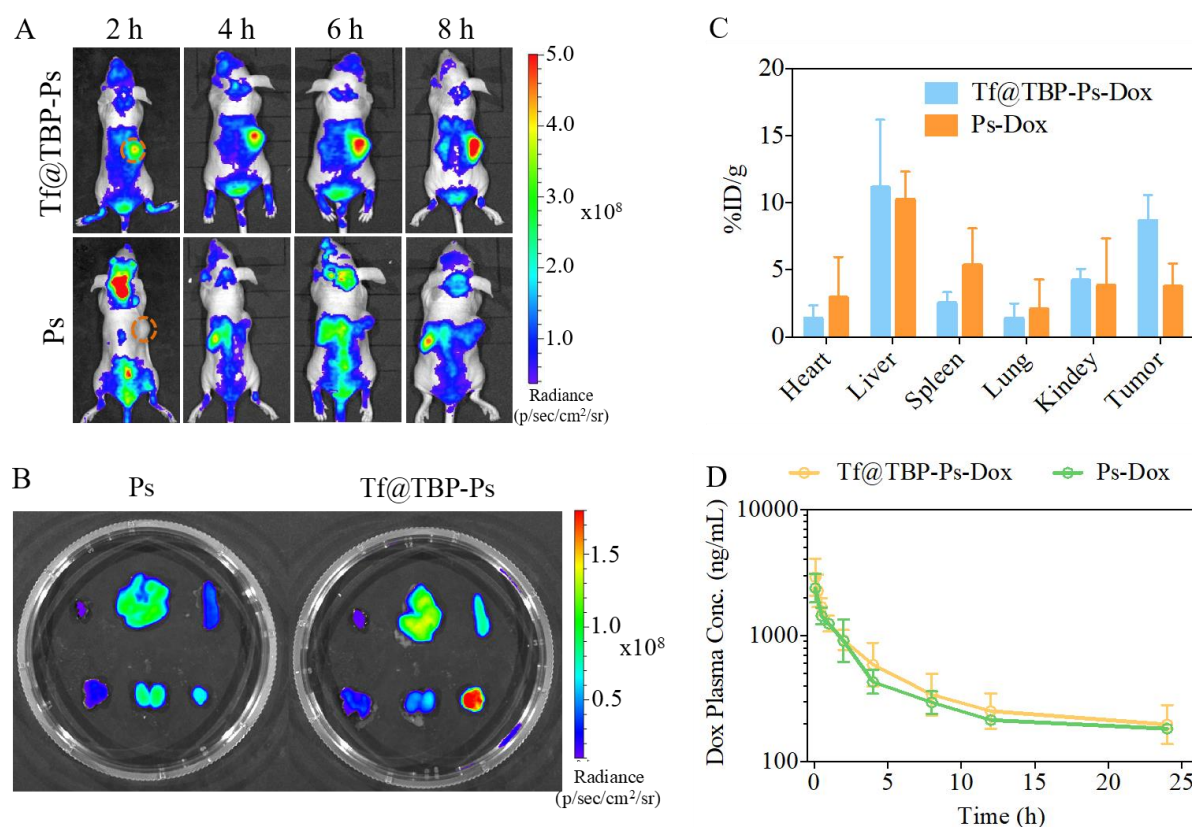
Figure 4. (A) *In vivo* imaging of HCT-116 tumor-bearing mice after *i.v.* injection of Cy5-labeled Tf@TBP-Ps and Ps. The orange circles indicate the tumor regions. (B) The ex vivo images of major organs and tumor of mice at 24 h after injected with Cy5-labeled Tf@TBP-Ps and Ps. (C) The DOX biodistribution in HCT-116 tumor-bearing mice at 24 h after *iv* injected with Tf@TBP-Ps-Dox and Ps-Dox (4 mg Dox/kg). (D) Pharmacokinetics of Tf@TBP-Ps-Dox and Ps-Dox in healthy Balb/c mice (4 mg Dox/kg).

3.4 Targeted treatment of subcutaneous HCT-116 tumor

The antitumor efficacy of Tf@TBP-Ps-Dox was studied in subcutaneous HCT-116 tumor model when tumor volume reached 50 mm^3. Tf@TBP-Ps-Dox was intravenously injected every 4 days at 8 or 16 mg Dox/kg with a total of 4 injections. Ps-Dox (8 mg Dox/kg), Lipo-Dox (4 mg Dox/kg), and PBS were used as controls. Owing to its dose-limiting toxicity, Lipo-Dox was given at 4 mg Dox/kg, which caused systematic toxicity including body weight loss, hand foot syndrome and even death after repeated dosing[53]. **Figure 5A** shows that Tf@TBP-Ps-Dox

instigated significantly more effective tumor inhibition at 8 mg Dox/kg than Ps-Dox, supporting that Tf coating plays an important role in tumor treatment. Notably, tumor inhibition was further enhanced at Tf@TBP-Ps-Dox to 16 mg Dox/kg. Lipo-Dox presented similar tumor inhibition to Tf@TBP-Ps-Dox at 8 mg Dox/kg, which was possibly due to the fast internalization and/or drug release upon cell membrane fusion of Lipo-Dox. However, the mice revealed hand-foot syndrome (HFS) and significant weight loss during the treatment. In contrast, HFS and weight loss did not occur for both Tf@TBP-Ps-Dox groups and Ps-Dox (**Figure 5B**), confirming the low systemic toxicity of Tf@TBP-Ps-Dox. This collaborates well to the high maximum-tolerated dose of Ps-Dox of over 100 mg Dox/kg[40]. Moreover, on day 20 the mice were sacrificed, and the tumors of Tf@TBP-Ps-Dox group at 16 mg Dox/kg were the smallest among all groups (**Figure 5C**). Notably, Tf@TBP-Ps-Dox revealed a tumor inhibition rate (TIR) of respective 89% and 84% at 16 or 8 mg Dox/kg, which were significantly better than Ps-Dox (TIR 66%) and Lipo-Dox (**Figure 5D**). Furthermore, H&E staining of tumor tissues exhibited that the two Tf@TBP-Ps-Dox groups caused massive cell apoptosis: disappeared nuclei and concurrent cell shrinkage showing very dense alkaline staining due to chromosome compression. In comparison, the extent of apoptosis of Lipo-Dox was much lower and more fragmented nuclei were found. Ps-Dox caused significantly less apoptosis (**Figure 5E**). TUNEL assays demonstrated that Tf@TBP-Ps-Dox and Lipo-Dox groups had much less cells and produced more pronounced tumor cell apoptosis than Ps-Dox (**Figure 5E**). No severe side effects in major organs were found from the histological analysis after Tf@TBP-Ps-Dox treatment (**Figure 6**).
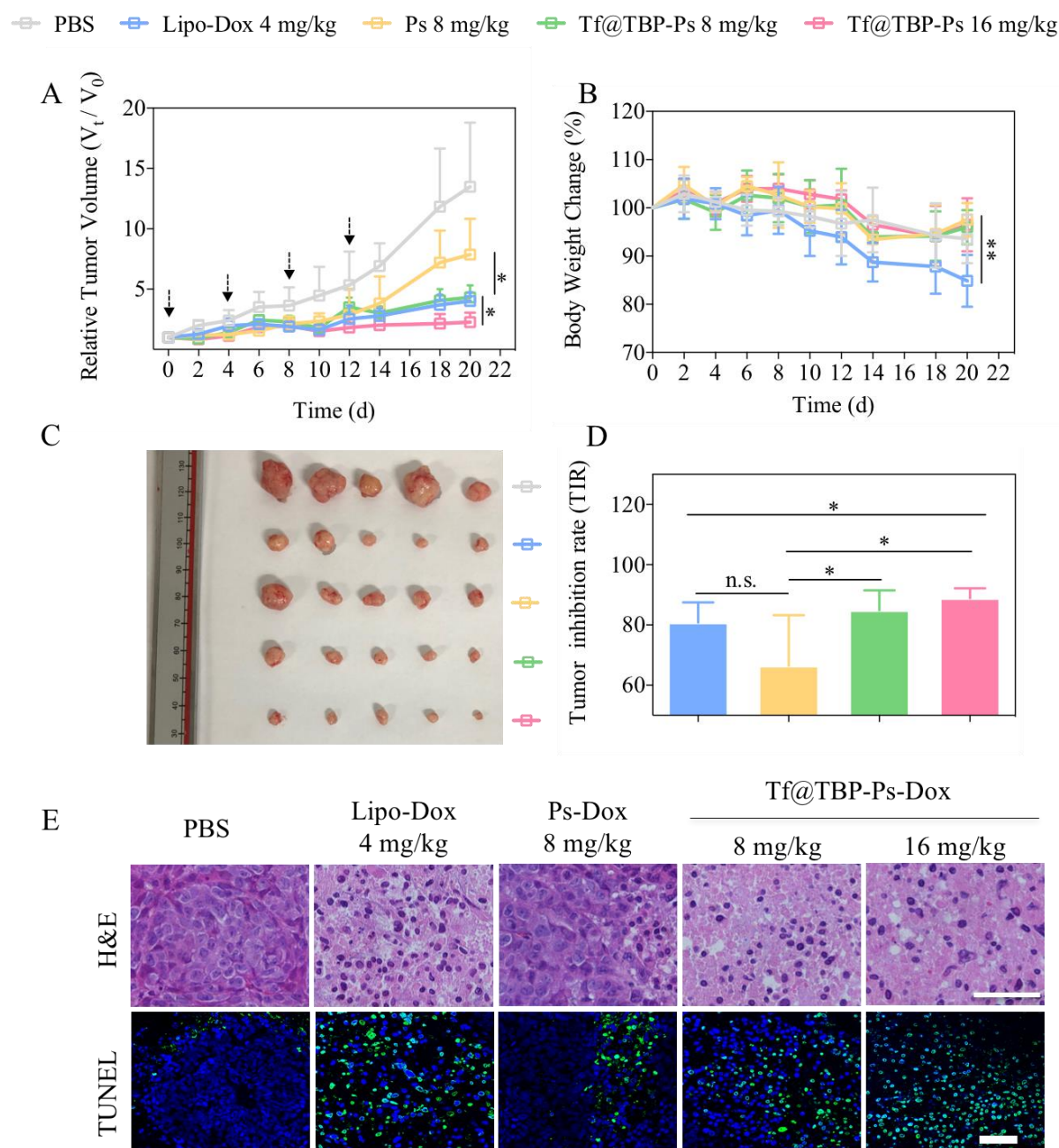
Figure 5. *In vivo* antitumor efficacy of Tf@TBP-Ps-Dox at 8 or 16 mg Dox/kg in HCT-116 tumor-bearing nude mice (n = 5). Ps-Dox (8 mg Dox/kg), Lipo-Dox (4 mg Dox/kg) and PBS were used as controls. The drug was given on day 0, 4, 8, and 12. (A) Tumor volume changes. (B) Body weight changes. (C) Photographs of tumors collected on day 20. (D) Tumor inhibition rates of different groups on day 20. (E) H&E and TUNEL assays of tumor tissues on day 20. Scale bars: 50 μm. For A, B and D, data are presented as mean ± SD (n = 5) and one-way Anova and Tukey multiple comparisons tests was applied, $*p < 0.05$, $**p < 0.01$.
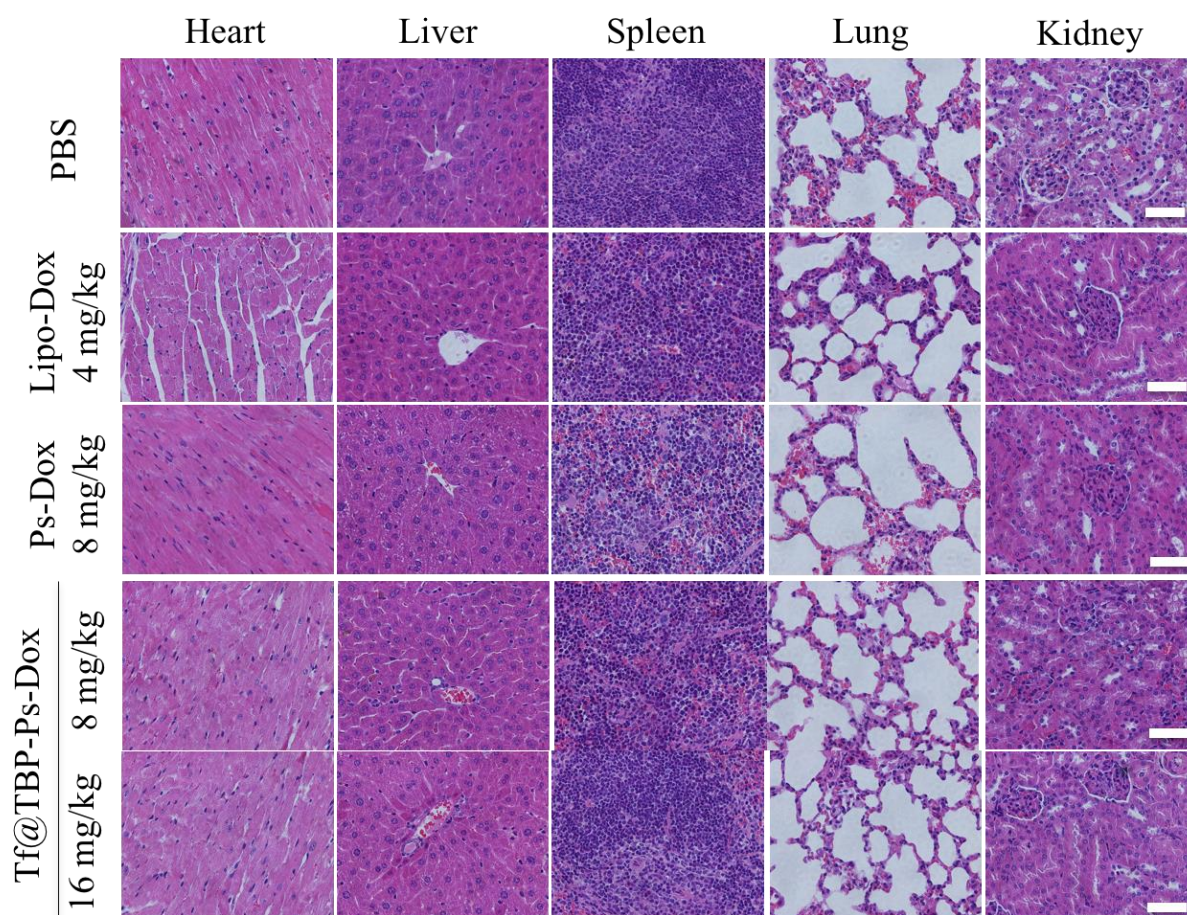
Figure 6. H&E stained heart, liver, spleen, lung and kidney tissues excised from tumor bearing mice following 20 d treatment. Scale bars: 50 μm.

4. Conclusion

We have demonstrated that disulfide-crosslinked polymersomes functionalized with a transferrin-binding peptide (TBP-Ps) can selectively and stably bind transferrin and subsequently mediate targeted Dox delivery to TfR over-expressing HCT-116 colorectal cancer cells *in vitro* and *in vivo*, leading to enhanced tumor suppression and reduced off-target side effects. To the best of our knowledge, this is the first report on the preparation of transferrin-functionalized nanomedicines by selective binding of transferrin. This transferrin-binding strategy is robust and has greatly simplified the production of transferrin-functionalized nanomedicines. Of note, the present study has employed a xenografted HCT-116 colorectal

cancer model. We will investigate the antitumor effect of TBP-Ps-Dox using allograft models, *i.e.* via binding endogenous transferrin in the blood. This proof-of-concept study has shown that Tf-binding peptide provides an appealing strategy in formulating Tf-targeted nanomedicines.

Acknowledgements

References

[1] J.J. Shi, P.W. Kantoff, R. Wooster, O.C. Farokhzad, Cancer nanomedicine: progress, challenges and opportunities, Nat. Rev. Cancer, 17 (2017) 20-37.

[2] Y.Q. Zhu, J. Feijen, Z.Y. Zhong, Dual-targeted nanomedicines for enhanced tumor treatment, Nano Today, 18 (2018) 65-85.

[3] J.L. Markman, A. Rekechenetskiy, E. Holler, J.Y. Ljubimova, Nanomedicine therapeutic approaches to overcome cancer drug resistance, Adv. Drug Deliv. Rev., 65 (2013) 1866-1879.

[4] A. Anitha, S. Maya, A.J. Sivaram, U. Mony, R. Jayakumar, Combinatorial nanomedicines for colon cancer therapy, Wiley Interdiscip. Rev.-Nanomed. Nanobiotechnol., 8 (2016) 151-159.

[5] H.L. Sun, Y.Y. Dong, F.J. Jan, Z.Y. Zhong, Peptide-decorated polymeric nanomedicines for precision cancer therapy, J. Control. Release, 290 (2018) 11-27.

[6] E. Ruoslahti, Tumor penetrating peptides for improved drug delivery, Adv. Drug Deliv. Rev., 110 (2017) 3-12.

[7] J.M. Montenegro, V. Grazu, A. Sukhanova, S. Agarwal, J.M. de la Fuente, I. Nabiev, A. Greiner, W.J. Parak, Controlled antibody/(bio-) conjugation of inorganic nanoparticles for targeted delivery, Adv. Drug Deliv. Rev., 65 (2013) 677-688.

[8] A. Alibakhshi, F.A. Kahaki, S. Ahangarzadeh, H. Yaghoobi, F. Yarian, R. Arezumand, J. Ranjbari, A. Mokhtarzadeh, M. de la Guardia, Targeted cancer therapy through antibody fragments-decorated nanomedicines, J. Control. Release, 268 (2017) 323-334.

[9] M.S. Muthu, R.V. Kutty, Z.T. Luo, J.P. Xie, S.S. Feng, Theranostic vitamin E TPGS micelles of transferrin conjugation for targeted co-delivery of docetaxel and ultra bright gold nanoclusters, Biomaterials, 39 (2015) 234-248.

[10] J. Zhou, M.H. Li, W.Q. Lim, Z. Luo, S.Z.F. Phua, R.L. Huo, L.Q. Li, K. Li, L.L. Dai, J.J. Liu, K.Y. Cai, Y.L. Zhao, A Transferrin-Conjugated Hollow Nanoplatform for Redox-Controlled and Targeted Chemotherapy of Tumor with Reduced Inflammatory Reactions, Theranostics, 8 (2018) 518-532.

[11] Y. Cui, Q. Xu, P.K.-H. Chow, D. Wang, C.-H. Wang, Transferrin-conjugated magnetic silica PLGA nanoparticles loaded with doxorubicin and paclitaxel for brain glioma treatment, Biomaterials, 34 (2013)

8511-8520.

[12] S.K. Sriraman, G. Salzano, C. Sarisozen, V. Torchilin, Anti-cancer activity of doxorubicin-loaded liposomes co-modified with transferrin and folic acid, Eur. J. Pharm. Biopharm., 105 (2016) 40-49.

[13] W. Cheng, J.P. Nie, L. Xu, C.Y. Liang, Y. Peng, G. Liu, T. Wang, L. Mei, L.Q. Huang, X.W. Zeng, pH-Sensitive Delivery Vehicle Based on Folic Acid-Conjugated Polydopamine-Modified Mesoporous Silica Nanoparticles for Targeted Cancer Therapy, ACS Appl. Mater. Interfaces, 9 (2017) 18462-18473.

[14] M. Talelli, M. Barz, C.J.F. Rijcken, F. Kiessling, W.E. Hennink, T. Lammers, Core-crosslinked polymeric micelles: Principles, preparation, biomedical applications and clinical translation, Nano Today, 10 (2015) 93-117.

[15] A. Wicki, D. Witzigmann, V. Balasubramanian, J. Huwyler, Nanomedicine in cancer therapy: Challenges, opportunities, and clinical applications, J. Control. Release, 200 (2015) 138-157.

[16] Y.S. Youn, Y.H. Bae, Perspectives on the past, present, and future of cancer nanomedicine, Adv. Drug Deliv. Rev., 130 (2018) 3-11.

[17] R. van der Meel, L.J.C. Vehmeijer, R.J. Kok, G. Storm, E.V.B. van Gaal, Ligand-targeted particulate nanomedicines undergoing clinical evaluation: Current status, Adv. Drug Deliv. Rev., 65 (2013) 1284-1298.

[18] K.F. Pirollo, J. Nemunaitis, P.K. Leung, R. Nunan, J. Adams, E.H. Chang, Safety and Efficacy in Advanced Solid Tumors of a Targeted Nanocomplex Carrying the p53 Gene Used in Combination with Docetaxel: A Phase 1b Study, Mol. Ther., 24 (2016) 1697-1706.

[19] A. Siefker-Radtke, X.Q. Zhang, C.C. Guo, Y. Shen, K.F. Pirollo, S. Sabir, C. Leung, C. Leong-Wu, C.M. Ling, E.H. Chang, R.E. Millikan, W.F. Benedict, A Phase l Study of a Tumor-targeted Systemic Nanodelivery System, SGT-94, in Genitourinary Cancers, Mol. Ther., 24 (2016) 1484-1491.

[20] R. Singh, M. Norret, M.J. House, Y. Galabura, M. Bradshaw, D.W. Ho, R.C. Woodward, T.G. St Pierre, I. Luzinov, N.M. Smith, L.Y. Lim, K.S. Iyer, Dose-Dependent Therapeutic Distinction between Active and Passive Targeting Revealed Using Transferrin-Coated PGMA Nanoparticles, Small, 12 (2016) 351-359.

[21] S. Ruan, L. Qin, W. Xiao, C. Hu, Y. Zhou, R. Wang, X. Sun, W. Yu, Q. He, H. Gao, Acid-Responsive Transferrin Dissociation and GLUT Mediated Exocytosis for Increased Blood-Brain Barrier

Transcytosis and Programmed Glioma Targeting Delivery, Adv. Funct. Mater., 28 (2018).

[22] F.C. Lam, S.W. Morton, J. Wyckoff, T.L. Vu Han, M.K. Hwang, A. Maffa, E. Balkanska-Sinclair, M.B. Yaffe, S.R. Floyd, P.T. Hammond, Enhanced efficacy of combined temozolomide and bromodomain inhibitor therapy for gliomas using targeted nanoparticles, Nat. Commun., 9 (2018) 1991.

[23] L. Liu, Y. Wei, S. Zhai, Q. Chen, D. Xing, Dihydroartemisinin and transferrin dual-dressed nano-graphene oxide for a pH-triggered chemotherapy, Biomaterials, 62 (2015) 35-46.

[24] S.S. Kim, A. Rait, E. Kim, J. DeMarco, K.F. Pirollo, E.H. Chang, Encapsulation of temozolomide in a tumor-targeting nanocomplex enhances anti-cancer efficacy and reduces toxicity in a mouse model of glioblastoma, Cancer Lett., 369 (2015) 250-258.

[25] S.S. Kim, A. Rait, F. Rubab, A.K. Rao, M.C. Kiritsy, K.F. Pirollo, S. Wang, L.M. Weiner, E.H. Chang, The clinical potential of targeted nanomedicine: delivering to cancer stem-like cells, Mol. Ther., 22 (2014) 278-291.

[26] N.C. Bellocq, S.H. Pun, G.S. Jensen, M.E. Davis, Transferrin-containing, cyclodextrin polymer-based particles for tumor-targeted gene delivery, Bioconjugate Chem., 14 (2003) 1122-1132.

[27] M.E. Davis, J.E. Zuckerman, C.H.J. Choi, D. Seligson, A. Tolcher, C.A. Alabi, Y. Yen, J.D. Heidel, A. Ribas, Evidence of RNAi in humans from systemically administered siRNA via targeted nanoparticles, Nature, 464 (2010) 1067-1070.

[28] N. Senzer, J. Nemunaitis, D. Nemunaitis, C. Bedell, G. Edelman, M. Barve, R. Nunan, K.F. Pirollo, A. Rait, E.H. Chang, Phase I Study of a Systemically Delivered p53 Nanoparticle in Advanced Solid Tumors, Mol. Ther., 21 (2013) 1096-1103.

[29] J.-J. Hu, D. Xiao, X.-Z. Zhang, Advances in Peptide Functionalization on Mesoporous Silica Nanoparticles for Controlled Drug Release, Small, 12 (2016) 3344-3359.

[30] H. Jin, J. Pi, Y. Zhao, J.H. Jiang, T. Li, X.Y. Zeng, P.H. Yang, C.E. Evans, J.Y. Cai, EGFR-targeting PLGA-PEG nanoparticles as a curcumin delivery system for breast cancer therapy, Nanoscale, 9 (2017) 16365-16374.

[31] A.M. Brinkman, G.J. Chen, Y.D. Wang, C.J. Hedman, N.M. Sherer, T.C. Havighurst, S.Q. Gong, W. Xu, Aminoflavone-loaded EGFR-targeted unimolecular micelle nanoparticles exhibit anti-cancer effects in triple negative breast cancer, Biomaterials, 101 (2016) 20-31.

[32] X.W. Cheng, D.R. Yu, G. Cheng, B.C. Yung, Y. Liu, H.W. Li, C. Kang, X.Y. Fang, S.H. Tian, X.J. Zhou, Q.B. Liu, R.J. Lee, T7 Peptide-Conjugated Lipid Nanoparticles for Dual Modulation of Bcl-2 and Akt-1 in Lung and Cervical Carcinomas, Mol. Pharm., 15 (2018) 4722-4732.

[33] Y. Kuang, K.C. Zhang, Y. Cao, X. Chen, K.W. Wang, M. Liu, R.J. Pei, Hydrophobic IR-780 Dye Encapsulated in cRGD-Conjugated Solid Lipid Nanoparticles for NIR Imaging-Guided Photothermal Therapy, ACS Appl. Mater. Interfaces, 9 (2017) 12217-12226.

[34] Q.F. Zhao, H.J. Geng, Y. Wang, Y.K. Gao, J.H. Huang, Y. Wang, J.H. Zhang, S.L. Wang, Hyaluronic Acid Oligosaccharide Modified Redox-Responsive Mesoporous Silica Nanoparticles for Targeted Drug Delivery, ACS Appl. Mater. Interfaces, 6 (2014) 20290-20299.

[35] J. Lee, E.T. Oh, M.H. Choi, H.G. Kim, H.J. Park, C. Kim, Dual-functional cyclic peptide switch on mesoporous nanocontainers for selective CD44 targeting and on-off gatekeeping triggered by conformational transformation, New J. Chem., 42 (2018) 12938-12944.

[36] D.D. Von Hoff, M.M. Mita, R.K. Ramanathan, G.J. Weiss, A.C. Mita, P.M. LoRusso, H.A. Burris, L.L. Hart, S.C. Low, D.M. Parsons, S.E. Zale, J.M. Summa, H. Youssoufian, J.C. Sachdev, Phase I Study of PSMA-Targeted Docetaxel-Containing Nanoparticle BIND-014 in Patients with Advanced Solid Tumors, Clin. Cancer Res., 22 (2016) 3157-3163.

[37] M. Santi, G. Maccari, P. Mereghetti, V. Voliani, S. Rocchiccioli, N. Ucciferri, S. Luin, G. Signore, Rational Design of a Transferrin-Binding Peptide Sequence Tailored to Targeted Nanoparticle Internalization, Bioconjugate Chem., 28 (2017) 471-480.

[38] H. Makwana, F. Mastrotto, J.P. Magnusson, D. Sleep, J. Hay, K.J. Nicholls, S. Allen, C. Alexander, Engineered Polymer-Transferrin Conjugates as Self-Assembling Targeted Drug Delivery Systems, Biomacromolecules, 18 (2017) 1532-1543.

[39] R.L. Siegel, K.D. Miller, S.A. Fedewa, D.J. Ahnen, R.G.S. Meester, A. Barzi, A. Jemal, Colorectal cancer statistics, 2017, CA-Cancer J. Clin., 67 (2017) 177-193.

[40] Y. Zou, F.H. Meng, C. Deng, Z.Y. Zhong, Robust, tumor-homing and redox-sensitive polymersomal doxorubicin: A superior alternative to Doxil and Caelyx?, J. Control. Release, 239 (2016) 149-158.

[41] Y. Fang, W.J. Yang, L. Cheng, F.H. Meng, J. Zhang, Z.Y. Zhong, EGFR-targeted multifunctional polymersomal doxorubicin induces selective and potent suppression of orthotopic human liver cancer

in vivo, Acta Biomater., 64 (2017) 323-333.

[42] N. Zhang, Y.F. Xia, Y. Zou, W.J. Yang, J. Zhang, Z.Y. Zhong, F.H. Meng, ATN-161 Peptide Functionalized Reversibly Cross-Linked Polymersomes Mediate Targeted Doxorubicin Delivery into Melanoma-Bearing C57BL/6 Mice, Mol. Pharm., 14 (2017) 2538-2547.

[43] Y. Zou, Y.F. Xia, F.H. Meng, J. Zhang, Z.Y. Zhong, GE11-Directed Functional Polymersomal Doxorubicin as an Advanced Alternative to Clinical Liposomal Formulation for Ovarian Cancer Treatment, Mol. Pharm., 15 (2018) 3664-3671.

[44] Y. Zhu, J. Zhang, F.H. Meng, C. Deng, R. Cheng, J. Feijen, Z.Y. Zhong, cRGD-functionalized reduction-sensitive shell-sheddable biodegradable micelles mediate enhanced doxorubicin delivery to human glioma xenografts in vivo, J. Control. Release, 233 (2016) 29-38.

[45] W.J. Yang, Y.H. Wei, L. Yang, J. Zhang, Z.Y. Zhong, G. Storm, F.H. Meng, Granzyme B-loaded, cell-selective penetrating and reduction-responsive polymersomes effectively inhibit progression of orthotopic human lung tumor in vivo, J. Control. Release, 290 (2018) 141-149.

[46] L. Ding, W. Gu, Y. Zhang, S. Yue, H. Sun, J.J. Cornelissen, Z.J.B. Zhong, HER2-Specific Reduction-Sensitive Immunopolymersomes with High Loading of Epirubicin for Targeted Treatment of Ovarian Tumor, Biomacromolecules, 20 (2019) 3855-3863.

[47] M.S. Muthu, R.V. Kutty, Z. Luo, J. Xie, S.S. Feng, Theranostic vitamin E TPGS micelles of transferrin conjugation for targeted co-delivery of docetaxel and ultra bright gold nanoclusters, Biomaterials, 39 (2015) 234-248.

[48] M. Zhu, Z. Sheng, Y. Jia, D. Hu, X. Liu, X. Xia, C. Liu, P. Wang, X. Wang, H. Zheng, Indocyanine Green-holo-Transferrin Nanoassemblies for Tumor-Targeted Dual-Modal Imaging and Photothermal Therapy of Glioma, ACS Appl. Mater. Interfaces, 9 (2017) 39249-39258.

[49] H.O. Habashy, D.G. Powe, C.M. Staka, E.A. Rakha, G. Ball, A.R. Green, M. Aleskandarany, E.C. Paish, R.D. Macmillan, R.I. Nicholson, I.O. Ellis, J.M.W. Gee, Transferrin receptor (CD71) is a marker of poor prognosis in breast cancer and can predict response to tamoxifen, Breast Cancer Res. Treat, 119 (2010) 283-293.

[50] S.E. Tonik, J.E. Shindelman, H.H. Sussman, Transferrin Receptor Is Inversely Correlated with Estrogen-Receptor in Breast-Cancer, Breast Cancer Res. Treat, 7 (1986) 71-76.

[51] R.A. Walker, S.J. Day, Transferrin receptor expression in non-malignant and malignant human breast tissue, J. Pathol. , 148 (1986) 217-224.

[52] C.H.J. Choi, C.A. Alabi, P. Webster, M.E. Davis, Mechanism of active targeting in solid tumors with transferrin-containing gold nanoparticles, Proc. Natl. Acad. Sci. U. S. A., 107 (2010) 1235-1240.

[53] Y. Wei, X. Gu, L. Cheng, F. Meng, G. Storm, Z. Zhong, Low-toxicity transferrin-guided polymersomal doxorubicin for potent chemotherapy of orthotopic hepatocellular carcinoma in vivo, Acta Biomater., 92 (2019) 196-204.

[54] I. Leto, M. Coronnello, C. Righeschi, M.C. Bergonzi, E. Mini, A.R. Bilia, Enhanced Efficacy of Artemisinin Loaded in Transferrin-Conjugated Liposomes versus Stealth Liposomes against HCT-8 Colon Cancer Cells, ChemMedChem, 11 (2016) 1745-1751.

Supplementary Data

Table S1. Characterization of PEG-P(TMC-DTC) and MAL-PEG-P(TMC-DTC) copolymers

| Entry	Copolymer	M_n [kg mol^{-1}]		M_w/M_n[b]
		Design	Deter.[a]	
1	PEG-P(TMC-DTC)	5.0-(15.0-2.0)	5.0-14.8-1.9	1.10
2	MAL-PEG-P(TMC-DTC)	7.5-(15.0-2.0)	7.5-15.5-2.2	1.20

[a]Determined by ^{1}H-NMR

[b]Determined by GPC

A

B
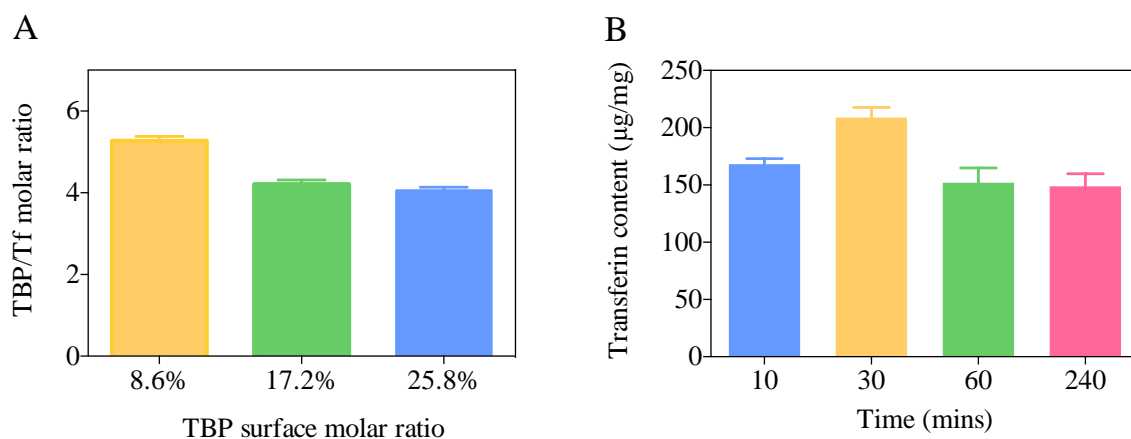
Figure S1. (A) TBP to Tf molar ratio with varied TBP surface density as determined by BCA assays. (B) Tf surface content after the inhibition of TBP-Ps with TBP surface density of 17.2 mol.% with Tf concentration of 2 mg/mL.
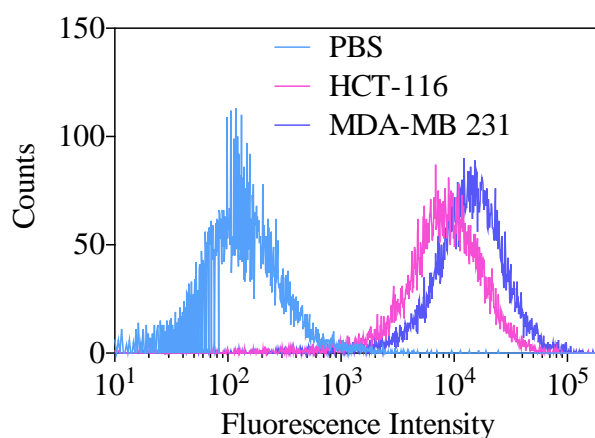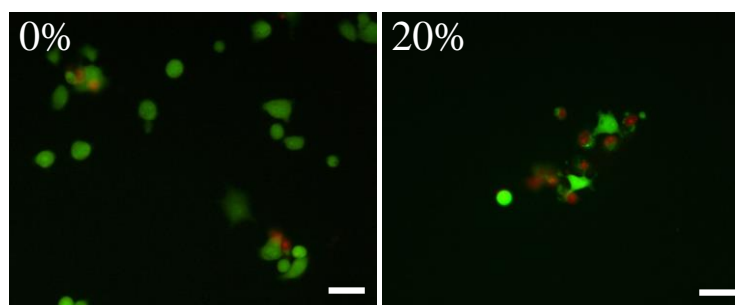

Figure S3. The TfR expression on HCT-116 and MDA-MB 231 cell lines.
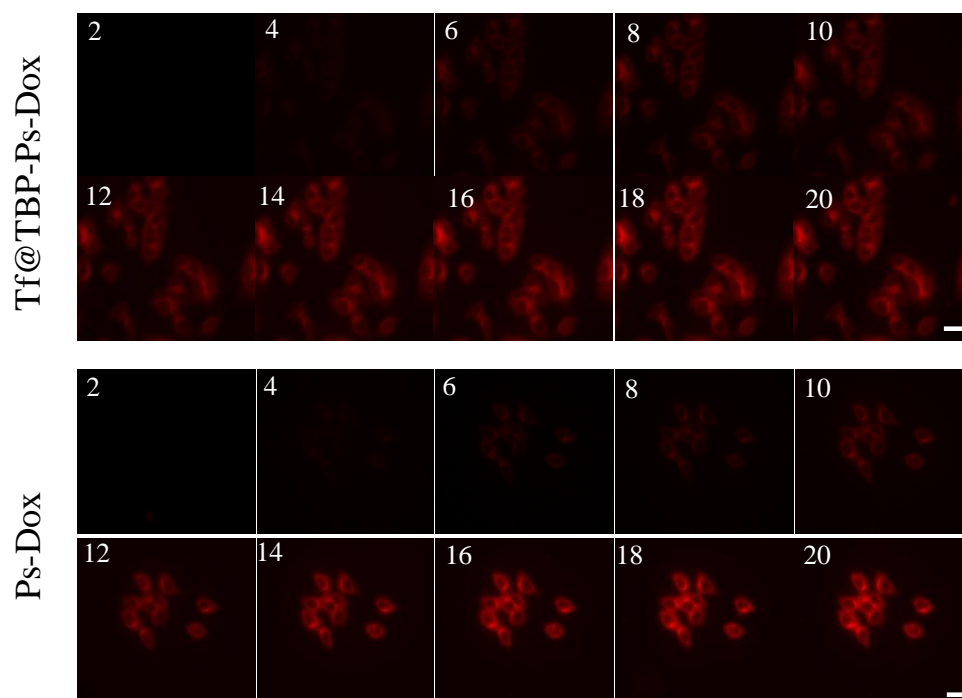
Figure S4. Real-time cellular Dox uptake of Tf@TBP-Ps-Dox and Ps-Dox by HCT-116 cells in 20 mins as tracked by a live-cell imaging system every two mins. Scale bar: 25 μm
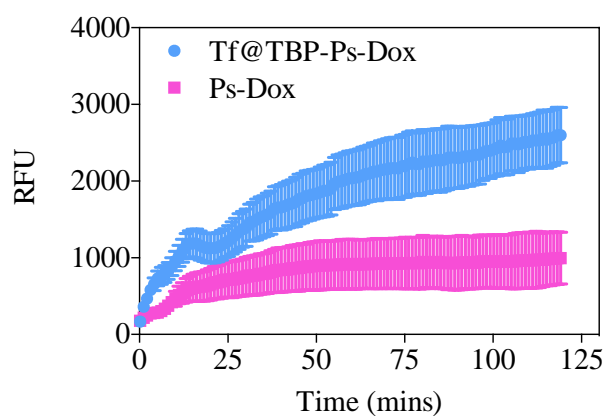
Figure S5. Quantify of Dox fluorescence signal up 120 mins by a live cell imaging system.

Figure S6. Live/dead assay of Ps-Dox and Tf@TBP-Ps-Dox. Scale bar: 50 μm

Chapter 4

Selective Transferrin Coating as a Facile Strategy to Fabricate BBB-Permeable and Targeted Vesicles for Potent RNAi Therapy of Brain Metastatic Breast Cancer *in Vivo**

Yaohua Wei[a,b,] , Yinping Sun[a] , Jingjing Wei[a], Xinyun Qiu[a], Fenghua Meng[a,*], Gert Storm[b,c,d*], and Zhiyuan Zhong[a,*]

[a] Biomedical Polymers Laboratory, College of Chemistry, Chemical Engineering and Materials Science, and State Key Laboratory of Radiation Medicine and Protection, Soochow University, Suzhou, 215123, P. R. China

[b] Department of Biomaterials Science and Technology, MIRA Institute for Biological Technology and Technical Medicine, University of Twente, PO Box 217, 7500AE, Enschede, The Netherlands

[c] Department of Pharmaceutics, Utrecht University, The Netherlands

[d] Department of Surgery, Yong Loo Lin School of Medicine, National University of Singapore, Kent Ridge, Singapore

Corresponding authors: fhmeng@suda.edu.cn (F. Meng); G.Storm@uu.nl (G. Storm); zyzhong@suda.edu.cn (Z. Zhong)

Abstract

Brain metastases are a most disturbing situation for breast cancer patients as there is basically no adequate treatment available. Any potential drug formulation has to be able to cross the blood-brain barrier (BBB) and specific to metastatic brain tumors without causing unacceptable adverse effects. Here, we developed transferrin-functionalized chimeric polymersomes carrying siRNA against polo-like kinase 1 (Tf@TBP-CPs-siPLK1) for treating brain metastatic MDA-MB 231 triple negative breast cancer (TNBC) xenografts in mice. To facilitate the loading of siPLK1, CPs were designed with spermine in the watery core and transferrin-binding peptide (TBP) at the surface, enabling attachment of transferrin after the siRNA loading step and thereby circumventing interference of transferrin with siRNA loading. Tf@TBP-CPs-siPLK1 encapsulating 3.8 wt.% siRNA had a mean size of about 50 nm and a neutral zeta potential in phosphate buffer (PB). By virtue of the presence of transferrin, Tf@TBP-CPs demonstrated greatly (ca. 5-fold) enhanced internalization in MDA-MB 231 cells and transcytosis in the endothelial (bEnd.3) monolayer model *in vitro* as well as markedly improved accumulation in the orthotopically xenografted MDA-MB 231 tumor in the brain *in vivo* compared with control CPs lacking transferrin, supporting that transferrin mediates efficient BBB penetration and high specificity towards MDA-MB 231 cells. As a result, Tf@TBP-CPs-siPLK1 effectively inhibited tumor progression and prolonged the lifespan of the mice significantly. Selective transferrin coating appears to be a particularly facile strategy to fabricate BBB-permeable and targeted vesicles for potent RNAi therapy of brain metastatic breast cancer.

Keywords: Transferrin; polymersomes; brain metastases; RNAi; targeted delivery

1. Introduction

Brain metastases when occurring in cancerous patients with e.g. lung tumor, breast tumor, and melanoma is a most disturbing situation[1-3]. In breast cancer, human epidermal growth factor receptor 2 (HER-2) positive and triple-negative breast cancer (TNBC) patients have exhibited a particularly high risk to develop brain metastases[4, 5]. To date, there is basically no treatment available for brain metastases because few drugs are capable of penetrating the blood-brain barrier (BBB)[6]. One study with over 1400 women observed that the median survival time of TNBC and HER2-positive patients with brain metastases is 12.8 months[7, 8]. In recent years, different approaches have been explored to improve the treatment of breast cancer brain metastases[9, 10]. For example, focused ultrasound was applied to disrupt the BBB and thereby to enhance the delivery of antibodies, antibody-drug conjugates, and nanomedicines to brain metastases[11, 12]. Ligand mediated, BBB-permeable nanosystems that employ low density lipoprotein receptor related protein 1 (LRP1) pathway alone or in combination with receptor targeting antibody were investigated for improved treatment of brain metastatic breast cancers[13-15]. Intravenously administered cell-penetrating peptide-functionalized nanomedicines containing doxorubicin and intracranial delivery of plasmid encoding trastuzumab were also reported to suppress the growth of brain metastases[16, 17]. Notably, most previous receptor-mediated transcytosis (RMT) systems deal with the use of highly toxic drugs, which would most probably also cause serious adverse effects, given the fact that a large part of the administered dose is distributed to other locations in the body than the target.

Different from many chemotherapeutic anticancer drugs, small interfering RNA (siRNA) with a specific target in cancer cells possesses usually low off-target toxicity[18]. A number of siRNA drugs have been studied for treating distinct tumors[19, 20]. siRNA silencing Polo-like kinase 1 (siPLK1), a highly conserved serine-threonine kinase that is overexpressed in diverse

cancer types and correlated with poor prognosis[21], has shown to be able to suppress growth of various tumors including lung and breast tumors *in vivo*[22-24]. The clinical application of siRNA is, however, limited by *in vivo* delivery hurdles like poor tumor cell uptake, rapid degradation by nucleases, and poor endosomal escape[19, 25]. Therefore, the development of efficient delivery vehicles is a challenging task in siRNA applications[26, 27]. In case of brain metastases, the vehicles need to carry siRNA across the BBB. Transferrin is one of the few ligands that have been reported to be capable of penetrating the BBB via transferrin receptor (TfR)-mediated transcytosis (RMT)[28-34]. TfR is also overexpressed by a range of malignant tumor cells including those of glioblastoma and breast tumors[35-37]. Transferrin-drug conjugates and transferrin-functionalized nanomedicines have been explored for glioblastoma and breast tumor RNAi therapy[38, 39]. There are also reports on transferrin-directed siRNA nanocaplet for targeted RNA interference and deep tumor penetration, which generally require dedicated fabrication[40].

Here, we report on facile fabrication of BBB-permeable and targeted vesicles via selective transferrin coating strategy for potent RNAi therapy of brain metastatic breast cancer *in vivo*. Transferrin-functionalized chimeric polymersomes carrying siPLK1 (Tf@TBP-CPs-siPLK1) were simply obtained by treating siPLK1-loaded transferrin binding peptide exposing chimeric polymersomes (TBP-CPs-siPLK1) with transferrin, thus circumventing interference of surface-bound transferrin with siRNA loading (**Scheme 1**). TBP (sequence: CGGGHKYLRW) was reported to specifically bind to transferrin[41]. We have previously shown that transferrin-bound polymersomal doxorubicin hydrochloride prepared by TBP-exposing CPs exhibited transferrin-induced enhanced cellular uptake and antitumor efficacy in a subcutaneous colorectal cancer model[42]. Based on the literature, as cited above, it was hypothesized that Tf@TBP-CPs-siPLK1 would not only cross BBB but also target to brain metastatic TfR-overexpressed TNBC cells, resulting in potent and low toxic RNAi therapy for malignant breast

tumor brain metastases.
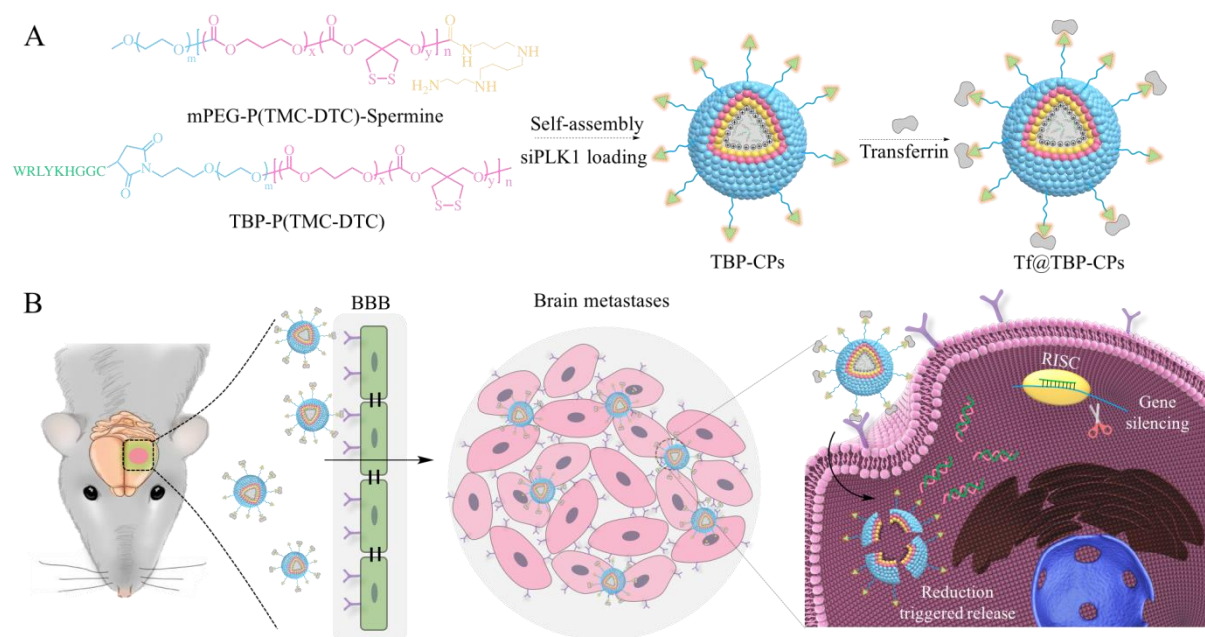
Scheme 1. Illustration of the fabrication of Tf functionalized polymersomal siPLK1 (Tf@TBP-CPs-siPLK1) (A), and the targeted delivery of siPLK1 to brain metastases *in vivo* (B).

2. Experimental section

2.1 Preparation of Tf@TBP-CPs-siRNA

Poly(ethylene glycol)-*b*-poly(trimethylene carbonate-co-dithiolane trimethylene carbonate)-spermine (PEG-P(TMC-DTC)-sp, M_n = 5.0-(15.0-2.0)-0.2 kg/mol) copolymer was synthesized as previously reported[43]. TBP-PEG-P(TMC-DTC) was synthesized via Michael addition between TBP and MAL-PEG-P(TMC-DTC)[42]. siRNA (siPLK1, siEGFP or siScramble) loaded Tf@TBP-CPs were obtained via solvent exchange method. Typically, PEG-P(TMC-DTC)-sp and TBP-PEG-P(TMC-DTC) at weight ratio of 80/20 were dissolved in DMSO at 5 mg/mL. The polymer solution was then added into 900 μL HEPES (5 mM, pH 6.8) containing siRNA and incubated for 2 h without stirring and at 25 °C overnight in an incubator at 100 rpm to allow the formation of TBP-CPs-siPLK1. TBP-CPs-siPLK1 was purified by dialysis (MWCO 350 kDa) in PB (10 mM, pH 7.4) for 6 h. The siRNA loading efficiency was quantified by NanoDrop 2000c spectrophotometer at 260 nm. Tf@TBP-CPs-siPLK1 was

attained by adding Tf solution into TBP-CPs-siPLK1. Briefly, TBP-CPs-siPLK1 with TBP surface density of 17.2% (2 mg/mL, 1 mL) was incubated with 2.7 μM Tf (TBP/Tf = 1/1, mol/mol). BCA assays were used to determine the Tf surface densities. The size and zeta potential of Tf@TBP-CPs-siPLK1 before and after Tf coating were tested.

2.2 Investigation of endocytotic pathway of Tf@TBP-CPs-siPLK1

MDA-MB 231 cells (2 ×10^5 cells/well) were seeded in 6-well plates and cultured for 24 h prior to adding Tf@TBP-CPs-siPLK1(Cy5) (1 μg siRNA/mL). To investigate the energy-dependent process, cells were co-incubated with Tf@TBP-CPs-siPLK1(Cy5) at 4 $^{\circ}$C or in the presence of NaN$_3$ (10 mM) at 37 $^{\circ}$C for 1 h. The cells were washed, harvested and re-suspended in 500 μL PBS for flow cytometry analysis by BD FACS Calibur flow cytometer (Becton Dickinson, USA) based on 10,000 gated events. The endocytic pathway was further investigated by adding inhibitors including chlorpromazine (10 μg/mL), amiloride hydrochloride (1 mg/mL) and β-CD (1 mg/mL) to incubate for 1 h at 37°C prior to addition of Tf@TBP-CPs-siPLK1(Cy5). After 1 h, the cells were similarly treated immediately before flow cytometry analysis. The cells treated with CPs-siPLK1(Cy5) at 37 $^{\circ}$C were used as control.

2.3 Intracellular siPLK1 delivery and *in vitro* gene silencing

MDA-MB 231 cells were seeded in 6-well plates (5×10^5 cells/well) and cultured for 24 h. CPs-siPLK1(Cy5) and Tf@TBP-CPs-siPLK1(Cy5) were added and incubated for 4 h (1 μg siRNA /mL) and the cells were washed, harvested and re-suspended in 500 μL PBS for flow cytometry analyses. For each sample, 10,000 events were collected and MDA-MB 231 cells without any treatment were used as control.

The cellular uptake and intracellular siPLK1(Cy3) delivery were monitored via confocal laser scanning microscopy (CLSM) (Leica TCS SP5). Briefly, MDA-MB 231 cells were seeded

on glass coverslips in 24-well plates (5×10^4 cells/well) and cultured for 24 h at $37\,^{\circ}$C. Tf@TBP-CPs-siPLK1(Cy3) was added and incubated for 12 h at $37\,^{\circ}$C (siPLK1(Cy3): 5 μg/mL). The cells were then washed and fixed with 4% paraformaldehyde for 15 mins. After fixation, the nuclei were stained with DAPI (5 μg/mL) for 5 mins, washed, and finally examined with CLSM using a 63-x oil immersion objective. CPs-siPLK1(Cy3) was used as control.

The gene silencing capacity of siRNA (siEGFP) loaded Tf@TBP-CPs *in vitro* was investigated using MDA-MB 231-EGFP cells. In brief, the cells (5×10^3 cells/well) were cultured in 96-well plates for 24 h, and 10 μL of Tf@TBP-CPs-siEGFP or CPs-siEGFP was added (siRNA: 100 nM) and the cells without treatment were used as control (n = 3). After incubation for 12 h, the culture medium was replaced with 90 μL fresh medium, and the cells were further cultured for 36 h before the observation using fluorescence microscopy (Olympus BX41). The gene silencing efficacy of Tf@TBP-CPs-siEGFP and CPs-siEGFP was calculated by ImageJ in comparison to PBS treated group.

2.4 MTT assays of Tf@TBP-CPs-siPLK1

MDA-MB 231cells were seeded in 96-well plates (3×10^3 cells/well) and after 24 h 20 μL of Tf@TBP-CPs-siPLK1 was added. Following 12 incubation, the medium was replaced with fresh medium, and the cells were further cultured 36 h. Then MTT solution (5 mg/mL) was added and incubated for 4 h at $37\,^{\circ}$C. After removal of the medium, 150 μL DMSO was added to the cells. The absorbance at 492 nm was measured using a microplate reader (Multiskan FC), and the cell viability was expressed as the percentages of the absorbance of the cells treated with different formulations to that of PBS group (n = 5).

2.5 *In vivo* treatment of intracranial MDA-MB 231 metastases model

Mice were handled according to the protocols approved by Soochow University Laboratory

Animal Center and the Animal Care and Use Committee of Soochow University. Intracranial MDA-MB 231 brain metastases model was established using female Balb/c nude mice via implantation of minced breast tumor tissue into the left stratum of the mice, and this day was designated as day 0. On day 10, the mice were imaged and divided into 4 groups ($n = 9$) before the intravenous injection of Tf@TBP-CPs-siPLK1, CPs-siPLK1, Tf@TBP-CPs-siScrambe (2 mg siRNA/kg) or PBS via tail veins on day 10, 12, 14, and 16. The tumor development was tracked on day 13, 16 and 19 using an Lumina IVIS II *in vivo* imaging system. The mice were weighed every two days and the weight was normalized to their initial values. The survival curves of the mice were recorded. On day 20, one mouse of each group was sacrificed and major organs and brain tumors were excised, and prepared for hematoxylin and eosin (H&E) staining and observation with a digital microscope.

2.6 Statistical analyses

One-way analysis of variance (ANOVA) with Tukey multiple comparison test (Prism) was used to determine the significance among groups. Statistical significance was established at *$p < 0.05$, **$p < 0.01$ and ***$p < 0.001$.

3. Results and discussion

3.1 Formation and characterization of Tf@TBP-CPs-siPLK1

Tf@TBP-CPs-siPLK1 were obtained by co-assembly of PEG-P(TMC-DTC)-sp and TBP-PEG-P(TMC-DTC) at a weight ratio of 80/20 in the presence of siPLK1, followed by binding Tf with these preformed polymersomes (**Scheme 1**). The TBP density at the particle surface was set at 17.2 mol.% because that density showed optimal Tf binding and targeting effect to TfR-positive cancer cells earlier [42]. **Table 1** shows that TBP-CPs-siPLK1 obtained at an initial start amount of siPLK1 of 5 wt.% had an encapsulation efficiency of 85% and siPLK1

loading content of 4.1 wt.%. Interestingly, TBP-CPs-siPLK exhibited a small mean size around 50 nm, narrow distribution with mean PDI of 0.10, and neutral zeta potential in the PB (pH 7.4). The incubation of preformed TBP-CPs-siPLK1 was performed with 2.7 μM Tf, which corresponded to a molar ratio of TBP/Tf = 1/1, yielded Tf@TBP-CPs-siPLK1 maintaining similar size distribution, siPLK1 loading and zeta potential (**Table 1**). **Figure 1A** gives a representative hydrodynamic size distribution of Tf@TBP-CPs-siPLK1 as determined by DLS. The little influence of Tf binding on the degree of siPLK1 loading corroborates that siPLK1 is encapsulated in the core of polymersomes. Previously we showed that the chimeric polymersomes based on PEG-P(TMC-DTC)-sp efficiently encapsulated protein drugs in the aqueous core and mediated efficient protein delivery *in vitro* and *in vivo*[44]. To assess the Tf coating stability on the TBP-CPs, Tf was labeled with radioactive ^{125}I and coated on freshly prepared TBP-Ps. The gamma counter results displayed that over 85% ^{125}I-Tf was kept on the surface of TBP-CPs after storage in PBS for 48 h, in the presence of 50-fold excess Tf, mouse whole blood or human serum, indicating that Tf is tightly bound and will not easily be exchanged by excessive Tf or other proteins in the blood[42]. The non-targeted CPs-siPLK1 were formulated with similar siRNA loading, size distribution, and zeta potential (**Table 1**).

Table 1. Characterization of CPs-siPLK1, TBP-CPs-siPLK1 and Tf@TBP-CPs-siPLK1

| Entry	Formulation	Size (nm)[a]	PDI[a]	DLC (wt.%)[b]	DLE (%)[b]	ζ (mV)[c]
1	CPs-siPLK1	52 ± 3	0.12	4.0	83	+ 0.1
2	TBP-CPs-siPLK1	50± 1	0.10	4.1	85	+ 0.4
3	Tf@TBP-CPs-siPLK1	53± 3	0.14	3.8	80	+ 0.2

[a] Determined by dynamic light scattering (DLS) in 5 mM PB (pH 7.4)

[b] Determined by Nanodrop 2000c UV-Vis spectrophotometer at 260 nm

[c] Determined by a zeta potential analyzer in 5 mM PB (pH 7.4)

**3.2** TfR targeting and endocytosis pathways

The targetability and uptake of Tf@TBP-CPs-siPLK1 in MDA-MB 231 breast tumor cells was investigated using Cy5-labeled siPLK1 (siPLK1(Cy5)) as a model by flow cytometry. The results displayed that the presence of Tf on the surface of the CPs enhanced their cellular association, which was about 3-fold better than non-targeted CPs-siPLK1(Cy5) (**Figure 1B**). The internalization of Tf@TBP-CPs-siPLK1(Cy5) by the cells was greatly repressed at 4 °C or in the presence of the ATP inhibitor sodium azide (**Figure 1C**), indicating that Tf@TBP-CPs-siPLK1(Cy5) is internalized by MDA-MB 231 cells via energy-dependent endocytosis process. The internalization pathway of Tf@TBP-CPs-siPLK1(Cy5) was further investigated by treating MDA-MB 231 cells with various endocytic inhibitors such as amiloride hydrochloride, chlorpromazine (CPZ), or methyl-β-cyclodextrins (MβCD). **Figure 1D** displays that the internalization of Tf@TBP-CPs-siPLK1(Cy5) was markedly obstructed by treatment of CPZ, amiloride hydrochloride, and MβCD, indicating that the cellular internalization of Tf@TBP-CPs-siPLK1(Cy5) is mediated not only by clatherin/dynamin but also by caveolae-mediated and macropinocytosis pathways. This result is interesting and different from a previous report that clathrin/dynamin-mediated endocytosis dominates Tf/TfR complex internalization[45].
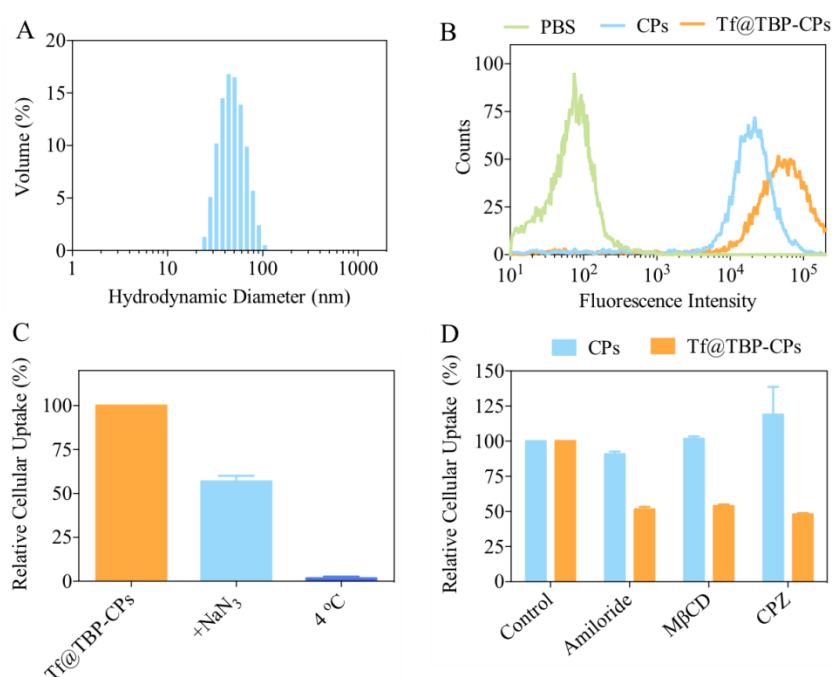
Figure 1. (A) The size distribution of Tf@TBP-CPs-siPLK1 determined by DLS. (B) The association of Tf@TBP-CPs-siPLK1(Cy5) and CPs-siPLK1(Cy5) following 4 h incubation with MDA-MB 231 cells as determined by flow cytometry. (C) The relative cellular uptake of Tf@TBP-CPs-siPLK1(Cy5) in the presence of ATP inhibitor or at 4 °C. (D) The relative cellular uptake of CPs-siPLK1(Cy5) and Tf@TBP-CPs-siPLK1(Cy5) in the presence of various internalization inhibitors.

3.3 *In vitro* BBB permeation

The bEnd.3 (immortalized mouse brain endothelial cell line) monolayers and MDA-MB 231 cells were co-cultured to study BBB passage and subsequent breast cancer cell targeting of Cy5-labeled Tf@TBP-CPs. TfR has been reported to highly express on bEnd.3 endothelial cells and on MDA-MB 231 cells [46, 47]. As shown in **Figure 2A**, the bEnd.3 was seeded as monolayer on the bottom of the upper chamber (TEER over 200 Ω cm^2) to simulate the BBB, and MDA-MB 231 cells were seeded as monolayer on the bottom of the lower chamber. The *in vitro* BBB monolayers were complete after 2 days culturing of bEnd.3 cells and remained intact until the end of the experiment as confirmed by TEER value. The results showed 5-fold enhanced association of Tf@TBP-CPs(Cy5) with MDA-MB 231 cells compared with non-targeted CPs(Cy5) (**Figure 2B**), signifying that Tf@TBP-CPs(Cy5) mediate more effective BBB transcytosis and contact with MDA-MB 231 cells. We further carried out the efflux ratio assays for Tf@TBP-CPs(Cy5) to eradicate the non-specific paracellular permeability of the monolayer (**Figure 2C**). The results revealed that CPs(Cy5) had efflux ratios close to 1.4 in 24 h whereas the efflux ratio of Tf@TBP-CPs(Cy5) increased to 6.2 (**Figure 2C**). The angiopep-2 decorated polymersomes were found an efflux ratio of 2.5 after 24 h incubation [48]. These results confirmed that Tf bounded chimeric polymersomes revealed excellent and selective BBB permeability.
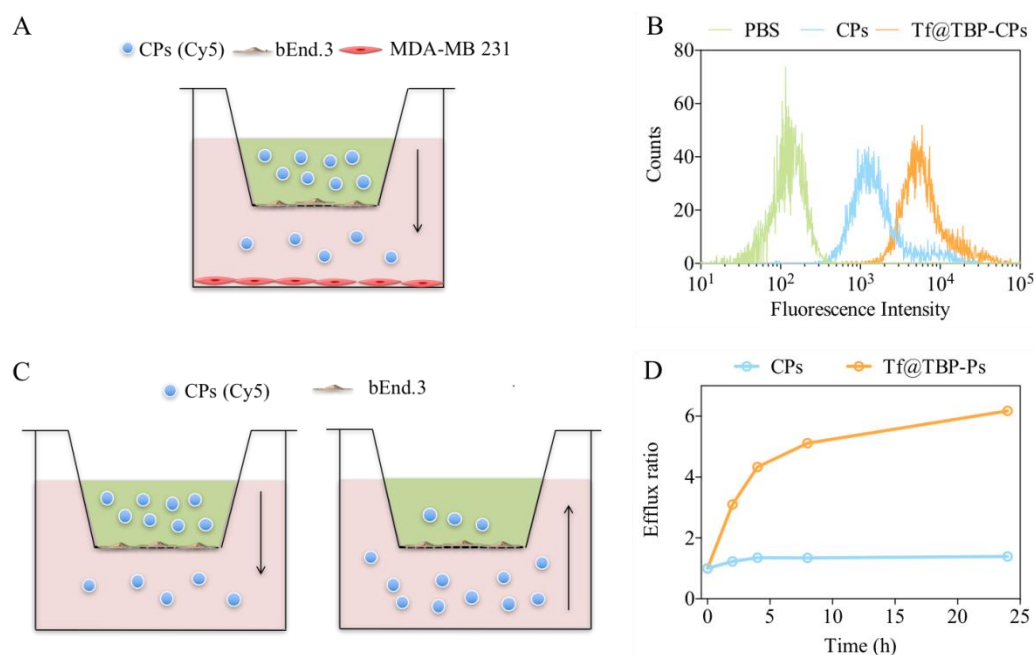
Figure 2. (A) Schematic illustration of bEnd.3 monolayer seeded in the upper chamber and MDA-MB 231 cell monolayer in the lower chamber. (B) The uptake of CPs (Cy5) and Tf@TBP-CPs (Cy5) in MDA-MB 231 cells in the lower chamber measured using flow cytometry. (C) Schematic illustration of efflux ratio assays. (D) The efflux ratios of CPs (Cy5) and Tf@TBP-CPs (Cy5) over time.

3.4 TfR-mediated siRNA delivery and gene silencing *in vitro*

The targetability and intracellular siRNA delivery capability of Tf@TBP-CPs and control CPs were studied by CSLM using siPLK1(Cy3) as a model siRNA in MDA-MB 231 cells by CLSM. The CLSM images of cells after 12 h incubation revealed much stronger intracellular Cy3 fluorescence for Tf@TBP-CPs-siPLK1(Cy3) compared with CPs-siPLK1(Cy3) (**Figure 3A**). The *in vitro* gene silencing experiments performed using siRNA against EGFP (siEGFP) in MDA-MB 231-EGFP cells displayed that the EGFP expression was markedly inhibited by Tf@TBP-CPs-siEGFP while CPs-siEGFP caused little inhibition of EGFP expression (**Figure 3B**). Quantitative fluorescence analysis indicated a strong ligand-mediated gene silencing. Tf@TBP-CPs-siEGFP revealed about 75% fluorescence reduction at 100 nM, in comparison to about 25% for the control CPs-siEGFP (**Figure 3C**).
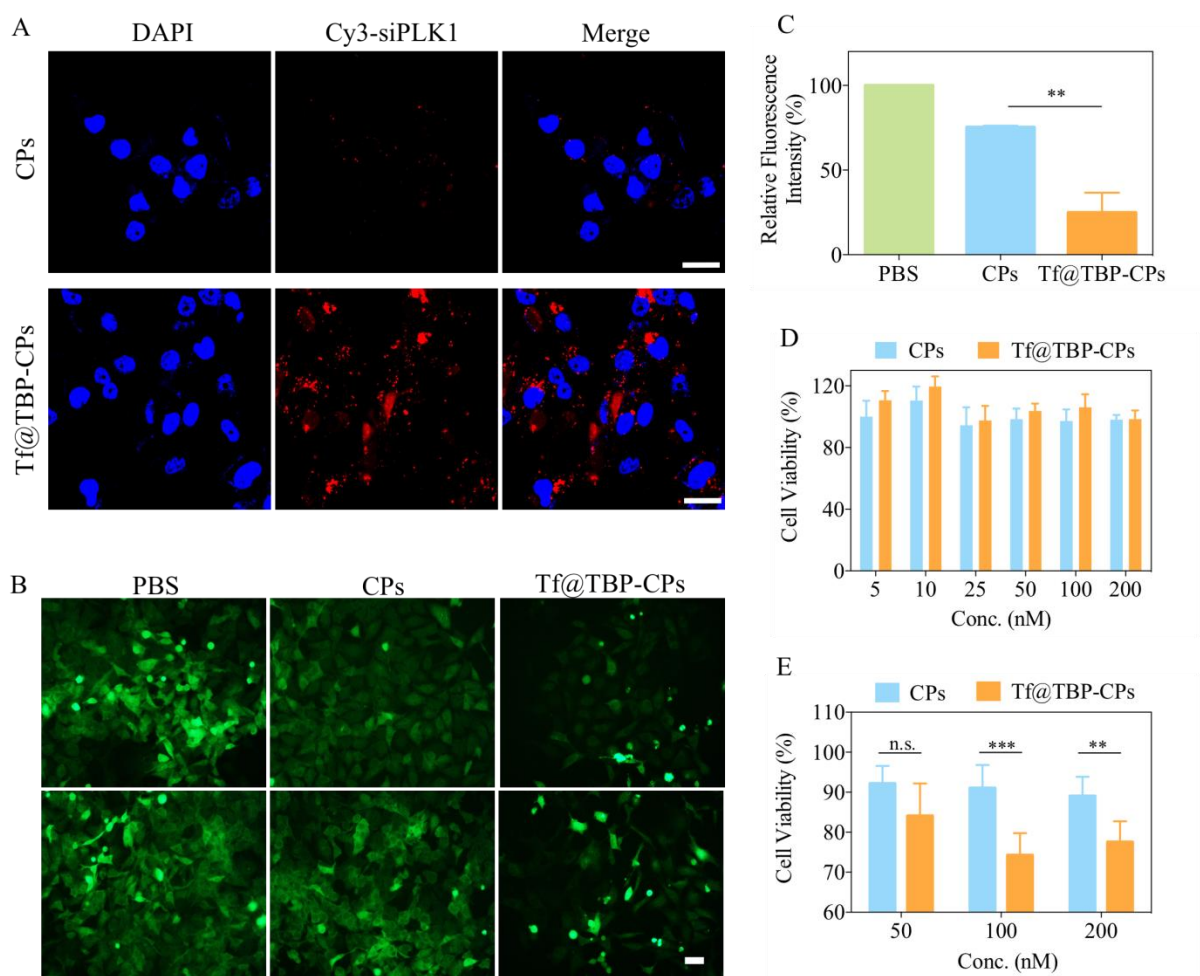
Figure 3. (A) Intracellular siPLK1(Cy3) release from Tf@TBP-CPs-siPLK1(Cy3) and CPs-siPLK1(Cy3) observed by CLSM after 12 h incubation. Scale Bar: 25 μm. (B) *In vitro* silencing of EGFP expression in MDA-MB 231-EGFP cells with siEGFP-loaded CPs or Tf@TBP-CPs (Dosage: 100 nM). The cells incubated for 12 h with siEGFP-loaded CPs or Tf@TBP-CPs were thereafter cultured for another 36 h. Scale Bar: 25 μm. (C) Semi-quantitative fluorescence analysis by software Image J after siEGFP treatment. (D) Viability of MDA-MB 231 cells after treating with siScramble-loaded CPs or siScramble-loaded Tf@TBP-CPs. (E) Viability of MDA-MB 231 cells after treating with 50, 100 or 200 nM CPs-siPLK1 or Tf@TBP-CPs-siPLK1.

The MTT assays were utilized to evaluate the cytotoxicity of Tf@TBP-CPs-siPLK1 and Tf@TBP-CPs-siScramble towards EGFP-overexpressing MDA-MB 231 cells. As anticipated, no obvious cytotoxicity was found for both CPs-siScramble and Tf@TBP-CPs-siScramble

(**Figure 3D**). However, in case of Tf@TBP-CPs-siPLK1, significantly higher cell death was observed at 100 nM compared with CPs-siPLK1 (**Figure 3E**), confirming the targeted silencing effect of Tf@TBP-CPs-siPLK1.

3.5 *In vivo* pharmacokinetics and brain metastases targeting

The accumulation of Tf@TBP-CPs-siPLK1(Cy5) in an intracranial MDA-MB 231-Luc brain metastases model was tracked using *in vivo* NIR imaging system. Notably, Cy5 fluorescence was observed at the intracranial breast tumor at 2 h post-injection of Tf@TBP-CPs-siPLK1(Cy5) and kept strong at 8 h post-injection (**Figure 4A**). Only weak Cy5 fluorescence was detected in the tumor for CPs-siPLK1(Cy5) throughout the entire 8 h period. The *ex-vivo* imaging verified much higher Cy5 fluorescence intensity in intracranial breast tumor for Tf@TBP-CPs-siPLK1(Cy5) than for the non-targeted counterpart (**Figure 4B, tissue number 6**), supporting that Tf@TBP-CPs-siPLK1(Cy5) selectively accumulates in the tumor lesion. The accumulation of CPs-siPLK1(Cy5) in brain metastases was ascribed to the EPR effect, which was reported to increases along with the progression of tumor [49]. Moreover, Tf@TBP-CPs-siPLK1(Cy5) gave less spleen and kidney accumulation than CPs-siPLK1(Cy5), which is possibly related to Tf coating that not only reduces protein corona formation but also prevents siRNA leakage.
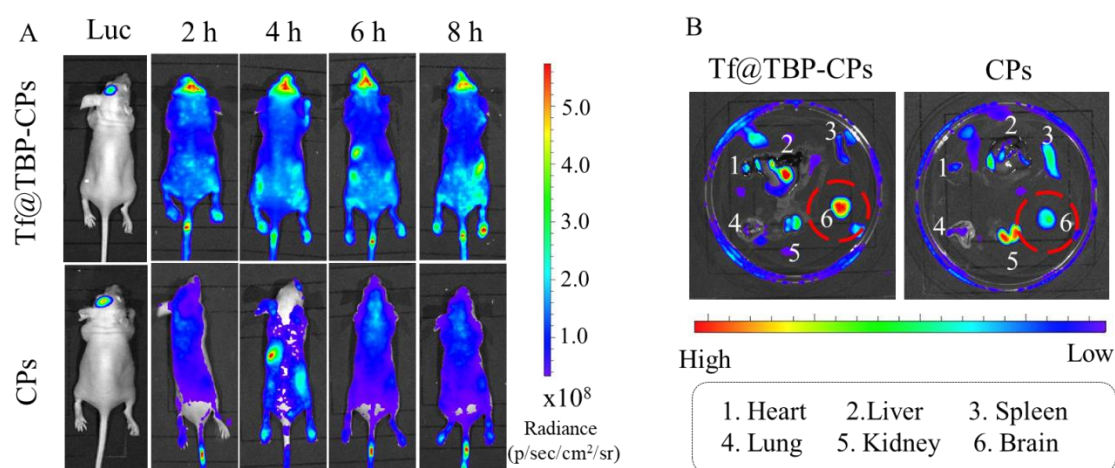

Figure 4. (A) NIR images of the mice bearing intracranial MDA-MB 231 tumor brain metastases at

varying time intervals, and (B) the *ex vivo* imaging of excised major organs and tumors at 8 h after injection of Tf@TBP-CPs-siPLK1(Cy5) or CPs-siPLK1(Cy5).

3.6 Treatment of intracranial MDA-MB 231-Luc tumor

The anti-brain metastases activity of Tf@TBP-CPs-siPLK1 was examined using an intracranial MDA-MB 231-Luc tumor xenografts at 2 mg siPLK1/kg. The *in vivo* bioluminescence images indicated that Tf@TBP-CPs-siPLK1 significantly retarded the tumor progression compared with the non-targeted CPs-siPLK1 and Tf@TBP-CPs-sicramble groups (**Figure 5A**). At day 20, one mouse was sacrificed from each group and the tumor was stained with Evans blue. The photos of stained tumors corroborated effective tumor inhibition by Tf@TBP-CPs-siPLK1 (**Figure 5B**). On the contrary, tumor invaded into the whole brain for the control Tf@TBP-CPs-siScramble and PBS treatments. **Figure 5C** shows clearly that the tumor bioluminescence in the Tf@TBP-CPs-siPLK1 treatment group was significantly weaker than that in CPs-siPLK1, Tf@TBP-CPs-siScramble and PBS groups. In accordance, the body weight of mice after PBS or Tf@TBP-CPs-siScramble treatment dropped rapidly owing to massive tumor invasion and brain disorder. No body weight loss was observed for the Tf@TBP-CPs-siPLK1 treated group, suggesting that effective treatment with Tf@TBP-CPs-siPLK1 leading to retardation of tumor invasion can be realized without inducing unacceptable side effects (**Figure 5D**).
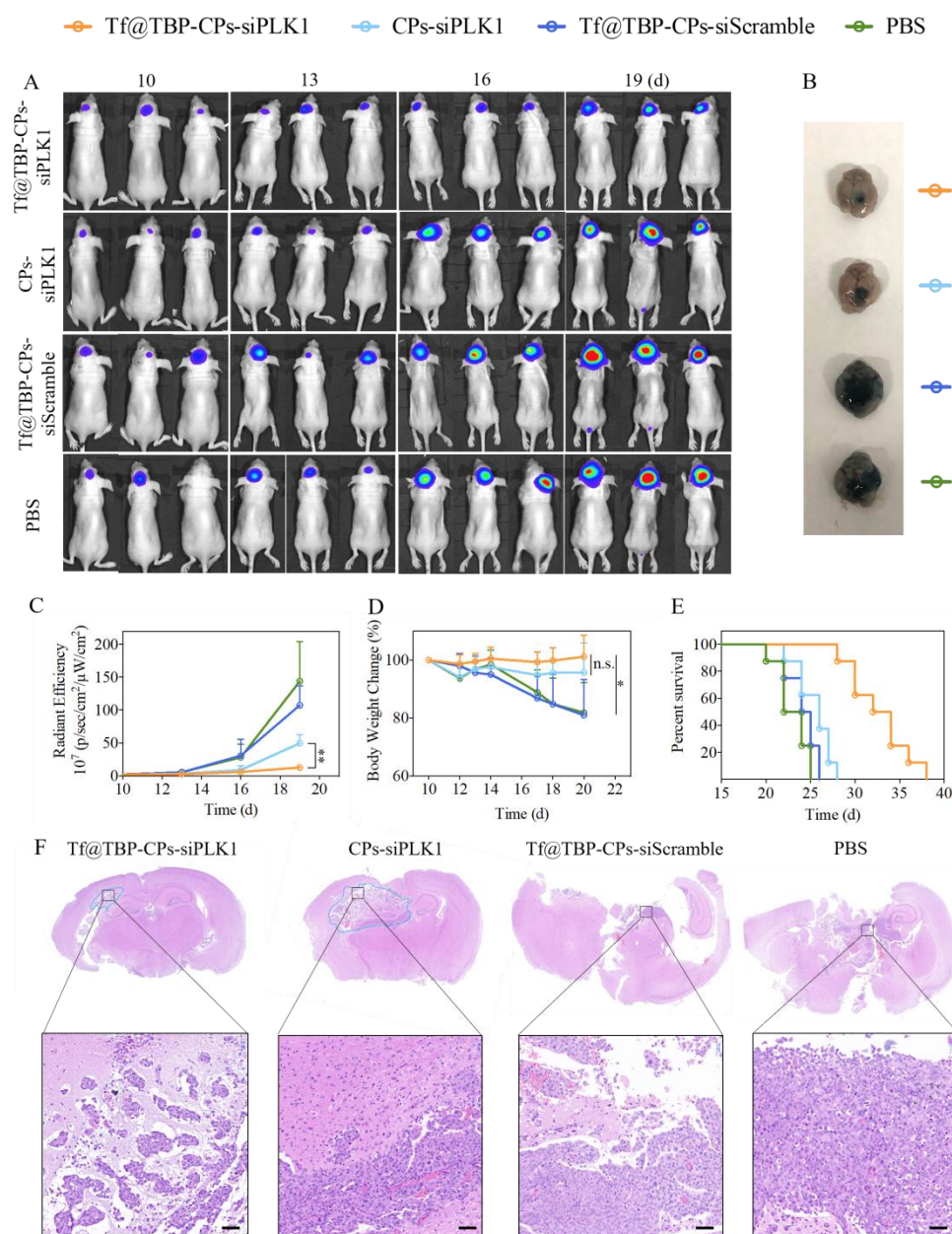
Figure 5. *In vivo* anti-brain metastases efficacy of Tf@TBP-CPs-siPLK1 (dosage: 2 mg/kg) in intracranial MDA-MB 231 breast cancer bearing mice (n=8). (A) Bioluminescence images of mice on day 10, 13, 16 and 19. (B) The photograph of excised brain with Evans Blue staining. (C) Semi-quantitative analysis of mean bioluminescence intensity of MDA-MB 231-Luc in the brain. (D) Body weight changes of mice within 20 days. (E) Survival curves. Kaplan-Meier analysis: Tf@TBP-CPs-siPLK1 *vs* PBS, CPs-siPLK1, or Tf@TBP-CPs-siScrmbale: ***p <0.001; CPs-siPLK1 *vs* PBS: *p <0.05. (F) The whole brain scan using H&E staining (Scar bars: 50 μm).

Kaplan-Meier survival curves disclosed that Tf@TBP-CPs-siPLK1 considerably

prolonged the median survival time of the mice compared with CPs-siPLK1, Tf@TBP-CPs-siScramble and PBS (33 versus 26, 24 and 23 days, respectively) (**Figure 5E**). The H&E staining of the brains confirmed that the animals in the Tf@TBP-CPs-siPLK1 treatment group showed the smallest brain tumor area among all groups (**Figure 5F**). Furthermore, no noticeable tissue damage was observed in the H&E staining images of heart, liver, spleen, lung and kidney, signifying the good safety of Tf@TBP-CPs-siPLK1 (**Figure S1**). The above data strongly suggest that Tf@TBP-CPs-siPLK1 is capable of penetrating the BBB and brings about efficient and targeted gene therapy of breast tumor brain metastases *in vivo*.

4 Conclusion

Transferrin-functionalized polymersomal siPLK1 (Tf@TBP-CPs-siPLK1) has been developed to pass the BBB and elicit specific gene silencing in breast cancer brain metastatic cells, yielding effective inhibition of tumor growth and significant improvement of survival time. Moreover, Tf@TBP-CPs-siPLK1 shows no apparent systemic toxicity, as reflected by the absence of body weight loss during the treatment period and histological analysis. The surface-bound transferrin facilitates BBB transcytosis and subsequently specifically directs polymersomal siPLK1 to intracranial MDA-MB 231 breast tumor cells. This transferrin binding strategy is robust and is based on novel and facile production of transferrin-targeted siRNA nanoformulations via the use of preformed TBP-exposing CPs, avoiding sophisticated chemical procedures to couple Tf and additionally the risk of Tf interfering with siRNA encapsulation. This selective transferrin coating appears to be a particularly facile strategy to fabricate BBB-permeable and targeted vesicles for potent RNAi therapy of breast cancer brain metastases.

References

[1] J.S. Barnholtz-Sloan, A.E. Sloan, F.G. Davis, F.D. Vigneau, P. Lai, R.E. Sawaya, Incidence proportions of brain metastases in patients diagnosed (1973 to 2001) in the metropolitan Detroit cancer surveillance system, J. Clin. Oncol. 22 (2004) 2865-2872.

[2] P.W. Sperduto, S.T. Chao, P.K. Sneed, X.H. Luo, J. Suh, D. Roberge, A. Bhatt, A.W. Jensen, P.D. Brown, H. Shih, J. Kirkpatrick, A. Schwer, L.E. Gaspar, J.B. Fiveash, V. Chiang, J. Knisely, C.M. Sperduto, M. Mehta, Diagnosis-specific prognostic factors, indexes, and treatment outcomes for patients with newly diagnosed brain metastases: a multi-institutional analysis of 4,259 patients, Int. J. Radiat. Oncol. 77 (2010) 655-661.

[3] A.S. Berghoff, S. Schur, L.M. Fureder, B. Gatterbauer, K. Dieckmann, G. Widhalm, J. Hainfellner, C.C. Zielinski, P. Birner, R. Bartsch, M. Preusser, Descriptive statistical analysis of a real life cohort of 2419 patients with brain metastases of solid cancers, Esmo Open 1 (2016) e000024.

[4] H. Nitta, B.D. Kelly, C. Allred, S. Jewell, P. Banks, E. Dennis, T.M. Grogan, The assessment of HER2 status in breast cancer: the past, the present, and the future, Pathol. Int. 66 (2016) 313-324.

[5] T. Bachelot, G. Romieu, M. Campone, V. Dieras, C. Cropet, F. Dalenc, M. Jimenez, E. Le Rhun, J.Y. Pierga, A. Goncalves, M. Leheurteur, J. Domont, M. Gutierrez, H. Cure, J.M. Ferrero, C. Labbe-Devilliers, Lapatinib plus capecitabine in patients with previously untreated brain metastases from HER2-positive metastatic breast cancer (LANDSCAPE): a single-group phase 2 study, Lancet Oncol. 14 (2013) 64-71.

[6] A.M. Hamilton, S. Aidoudi-Ahmed, S. Sharma, V.R. Kotamraju, P.J. Foster, K.N. Sugahara, E. Ruoslahti, B.K. Rutt, Nanoparticles coated with the tumor-penetrating peptide iRGD reduce experimental breast cancer metastasis in the brain, J. Mol. Med. 93 (2015) 991-1001.

[7] M.C. Liu, J. Cortes, J. O'Shaughnessy, Challenges in the treatment of hormone receptor-positive, HER2-negative metastatic breast cancer with brain metastases, Cancer Metast. Rev. 35 (2016) 323-332.

[8] N.D. Arvold, K.S. Oh, A. Niemierko, A.G. Taghian, N.U. Lin, R.F. Abi-Raad, M. Sreedhara, J.R. Harris, B.M. Alexander, Brain metastases after breast-conserving therapy and systemic therapy: incidence and characteristics by biologic subtype, Breast Cancer Res. Tr. 136 (2012) 153-160.

[9] A.S. Mohammad, J.I. Griffith, C.E. Adkins, N. Shah, E. Sechrest, E.L. Dolan, T.B. Terrell-Hall, B.S.

Hendriks, H. Lee, P.R. Lockman, Liposomal irinotecan accumulates in metastatic lesions, crosses the blood-tumor barrier (BTB), and prolongs survival in an experimental model of brain metastases of triple negative breast cancer, Pharm. Res. 35 (2018) 31.

[10] M. Li, K.R. Shi, X. Tang, J.J. Wei, X.L. Cun, Y. Long, Z.R. Zhang, Q. He, Synergistic tumor microenvironment targeting and blood-brain barrier penetration via a pH-responsive dual-ligand strategy for enhanced breast cancer and brain metastasis therapy, Nanomed-Nanotechnol. 14 (2018) 1833-1843.

[11] T. Kobus, I.K. Zervantonakis, Y.Z. Zhang, N.J. McDannold, Growth inhibition in a brain metastasis model by antibody delivery using focused ultrasound-mediated blood-brain barrier disruption, J. Control. Release 238 (2016) 281-288.

[12] C.D. Arvanitis, V. Askoxylakis, Y. Guo, M. Datta, J. Kloepper, G.B. Ferraro, M.O. Bernabeu, D. Fukumura, N. McDannold, R.K. Jain, Mechanisms of enhanced drug delivery in brain metastases with focused ultrasound-induced blood–tumor barrier disruption, Proc. Natl. Acad. Sci. USA 115 (2018) 8717-8726.

[13] C.S. He, J.S. Li, P. Cai, T. Ahmed, J.T. Henderson, W.D. Foltz, R. Bendayan, A.M. Rauth, X.Y. Wu, Two-step targeted hybrid nanoconstructs increase brain penetration and efficacy of the therapeutic antibody trastuzumab against brain metastasis of HER2-positive breast cancer, Adv. Funct. Mater. 28 (2018) 1705668.

[14] Q. Guo, Q.N. Zhu, T.T. Miao, J. Tao, X.F. Ju, Z.L. Sun, H. Li, G.Q. Xu, H.B. Chen, L. Han, LRP1-upregulated nanoparticles for efficiently conquering the blood-brain barrier and targetedly suppressing multifocal and infiltrative brain metastases, J. Control. Release 303 (2019) 117-129.

[15] C.S. He, P. Cai, J. Li, T. Zhang, L. Lin, A.Z. Abbasi, J.T. Henderson, A.M. Rauth, X.Y. Wu, Blood-brain barrier-penetrating amphiphilic polymer nanoparticles deliver docetaxel for the treatment of brain metastases of triple negative breast cancer, J. Control. Release 246 (2017) 98-109.

[16] R.A. Morshed, M.E. Muroski, Q. Dai, M.L. Wegscheid, B. Auffinger, D. Yu, Y. Han, L.J. Zhang, M.J. Wu, Y. Cheng, M.S. Lesniak, Cell-penetrating peptide-modified gold nanoparticles for the delivery of doxorubicin to brain metastatic breast cancer, Mol. Pharm. 13 (2016) 1843-1854.

[17] I. Zafir-Lavie, S. Sherbo, H. Goltsman, F. Badinter, E. Yeini, P. Ofek, R. Miari, O. Tal, A. Liran, T.

Shatil, S. Krispel, N. Shapir, G.A. Neil, I. Benhar, A. Panet, R. Satchi-Fainaro, Successful intracranial delivery of trastuzumab by gene-therapy for treatment of HER2-positive breast cancer brain metastases, J. Control. Release 291 (2018) 80-89.

[18] D. Bumcrot, M. Manoharan, V. Koteliansky, D.W.Y. Sah, RNAi therapeutics: a potential new class of pharmaceutical drugs, Nat. Chem. Biol. 2 (2006) 711-719.

[19] Y. Zhang, A. Satterlee, L. Huang, In vivo gene delivery by nonviral vectors: overcoming hurdles?, Mol. Ther. 20 (2012) 1298-1304.

[20] M.R. Lares, J.J. Rossi, D.L. Ouellet, RNAi and small interfering RNAs in human disease therapeutic applications, Trends Biotechnol. 28 (2010) 570-579.

[21] K. Strebhardt, A. Ullrich, Opinion-targeting polo-like kinase 1 for cancer therapy, Nat. Rev. Cancer 6 (2006) 321-330.

[22] J. Zhao, Y. Mi, S.S. Feng, Targeted co-delivery of docetaxel and siPlk1 by herceptin-conjugated vitamin E TPGS based immunomicelles, Biomaterials 34 (2013) 3411-3421.

[23] S. Dou, X.Z. Yang, M.H. Xiong, C.Y. Sun, Y.D. Yao, Y.H. Zhu, J. Wang, ScFv-decorated PEG-PLA-based nanoparticles for enhanced siRNA delivery to Her2(+) breast cancer, Adv. Healthc. Mater. 3 (2014) 1792-1803.

[24] Y. Zou, M. Zheng, W.J. Yang, F.H. Meng, K. Miyata, H.J. Kim, K. Kataoka, Z.Y. Zhong, Virus-mimicking chimaeric polymersomes boost targeted cancer siRNA therapy in vivo, Adv. Mater. 29 (2017) 1703285.

[25] G. Ozcan, B. Ozpolat, R.L. Coleman, A.K. Sood, G. Lopez-Berestein, Preclinical and clinical development of siRNA-based therapeutics, Adv. Drug Deliv. Rev. 87 (2015) 108-119.

[26] S.J. Tan, P. Kiatwuthinon, Y.H. Roh, J.S. Kahn, D. Luo, Engineering nanocarriers for siRNA delivery, Small 7 (2011) 841-856.

[27] R. Kanasty, J.R. Dorkin, A. Vegas, D. Anderson, Delivery materials for siRNA therapeutics, Nat. Mater. 12 (2013) 967-977.

[28] W.M. Pardridge, Delivery of biologics across the blood–brain barrier with molecular Trojan horse technology, Biodrugs 31 (2017) 503-519.

[29] Y. Uchida, S. Ohtsuki, Y. Katsukura, C. Ikeda, T. Suzuki, J. Kamiie, T. Terasaki, Quantitative

targeted absolute proteomics of human blood-brain barrier transporters and receptors, J. Neurochem. 117 (2011) 333-345.

[30] E.A. Wyatt, M.E. Davis, Method of establishing breast cancer brain metastases affects brain uptake and efficacy of targeted, therapeutic nanoparticles, Bioeng. Transl. Med. 4 (2019) 30-37.

[31] G. Hultqvist, S. Syvanen, X.T. Fang, L. Lannfelt, D. Sehlin, Bivalent brain shuttle increases antibody uptake by monovalent binding to the transferrin receptor, Theranostics 7 (2017) 308-318.

[32] X.N. Song, R. Li, H.L. Deng, Y. Li, Y.N. Cui, H. Zhang, W.B. Dai, B. He, Y. Zheng, X.Q. Wang, Q. Zhang, Receptor mediated transcytosis in biological barrier: The influence of receptor character and their ligand density on the transmembrane pathway of active-targeting nanocarriers, Biomaterials 180 (2018) 78-90.

[33] S. Ayloo, C.H. Gu, Transcytosis at the blood-brain barrier, Curr. Opin. Neurobiol. 57 (2019) 32-38.

[34] D. Yang, D.C. Liu, H.L. Deng, J. Zhang, M.M. Qin, L. Yuan, X.J. Zou, B. Shao, H.P. Li, W.B. Dai, H. Zhang, X.Q. Wang, B. He, X. Tang, Q. Zhang, Transferrin functionization elevates transcytosis of nanogranules across epithelium by triggering polarity-associated transport flow and positive cellular feedback loop, ACS Nano 13 (2019) 5058-5076.

[35] A. Jhaveri, P. Deshpande, B. Pattni, V. Torchilin, Transferrin-targeted, resveratrol-loaded liposomes for the treatment of glioblastoma, J. Control. Release 277 (2018) 89-101.

[36] S.S. Kim, A. Rait, E. Kim, J. DeMarco, K.F. Pirollo, E.H. Chang, Encapsulation of temozolomide in a tumor-targeting nanocomplex enhances anti-cancer efficacy and reduces toxicity in a mouse model of glioblastoma, Cancer Lett. 369 (2015) 250-258.

[37] Y.F. Li, M. Chen, B.W. Yao, X. Lu, X.Q. Zhang, P. He, S.N. Vasilatos, X.M. Ren, W.H. Bian, C. Yao, Transferrin receptor-targeted redox/pH-sensitive podophyllotoxin prodrug micelles for multidrug-resistant breast cancer therapy, J. Mater. Chem. B 7 (2019) 5814-5824.

[38] J.Y. Yhee, S.J. Lee, S. Lee, S. Song, H.S. Min, S.W. Kang, S. Son, S.Y. Jeong, I.C. Kwon, S.H. Kim, K. Kim, Tumor-targeting transferrin nanoparticles for systemic polymerized siRNA delivery in tumor-bearing mice, Bioconjug. Chem. 24 (2013) 1850-1860.

[39] W. Zhang, K. Muller, E. Kessel, S. Reinhard, D.S. He, P.M. Klein, M. Hohn, W. Rodl, S. Kempter, E. Wagner, Targeted siRNA delivery using a lipo-oligoaminoamide nanocore with an influenza peptide

and transferrin shell, Adv. Healthc. Mater. 5 (2016) 1493-1504.

[40] A. Kohata, P.K. Hashim, K. Okuro, T. Aida, Transferrin-appended nanocaplet for transcellular siRNA delivery into deep tissues, J. Am. Chem. Soc. 141 (2019) 2862-2866.

[41] M. Santi, G. Maccari, P. Mereghetti, V. Voliani, S. Rocchiccioli, N. Ucciferri, S. Luin, G. Signore, Rational design of a transferrin-binding peptide sequence tailored to targeted nanoparticle internalization, Bioconjug. Chem. 28 (2017) 471-480.

[42] Y.H. Wei, X.L. Gu, Y.P. Sun, F.H. Meng, G. Storm, Z.Y. Zhong, Transferrin-binding peptide functionalized polymersomes mediate targeted doxorubicin delivery to colorectal cancer in vivo, J. Control. Release 319 (2020) 407-415.

[43] P.L. Yao, Y.F. Zhang, H. Meng, H.L. Sun, Z.Y. Zhong, Smart polymersomes dually functionalized with cRGD and fusogenic GALA peptides enable specific and high-efficiency cytosolic delivery of apoptotic proteins, Biomacromolecules 20 (2019) 184-191.

[44] Y.N. Zhong, F.H. Meng, W. Zhang, B. Li, J.C. van Hest, Z.Y. Zhong, CD44-targeted vesicles encapsulating granzyme B as artificial killer cells for potent inhibition of human multiple myeloma in mice, J. Control. Release 320 (2020) 421-430.

[45] S. Tortorella, T.C. Karagiannis, Transferrin receptor-mediated endocytosis: a useful target for cancer therapy, J. Membrane Biol. 247 (2014) 291-307.

[46] M.S. Muthu, R.V. Kutty, Z.T. Luo, J.P. Xie, S.S. Feng, Theranostic vitamin E TPGS micelles of transferrin conjugation for targeted co-delivery of docetaxel and ultra bright gold nanoclusters, Biomaterials 39 (2015) 234-248.

[47] J. Zhou, M.H. Li, W.Q. Lim, Z. Luo, S.Z.F. Phua, R.L. Huo, L.Q. Li, K. Li, L.L. Dai, J.J. Liu, K.Y. Cai, Y.L. Zhao, A transferrin-conjugated hollow nanoplatform for redox-controlled and targeted chemotherapy of tumor with reduced inflammatory reactions, Theranostics 8 (2018) 518-532.

[48] Y.N. Shi, Y. Jiang, J.S. Cao, W.J. Yang, J. Zhang, F.H. Meng, Z.Y. Zhong, Boosting RNAi therapy for orthotopic glioblastoma with nontoxic brain-targeting chimaeric polymersomes, J. Control. Release 292 (2018) 163-171.

[49] Y. Jiang, W.J. Yang, J. Zhang, F.H. Meng, Z.Y. Zhong, Protein toxin chaperoned by LRP-1-targeted virus-mimicking vesicles induces high-efficiency glioblastoma therapy in vivo, Adv. Mater. 30 (2018)

1800316.

Supplementary Data
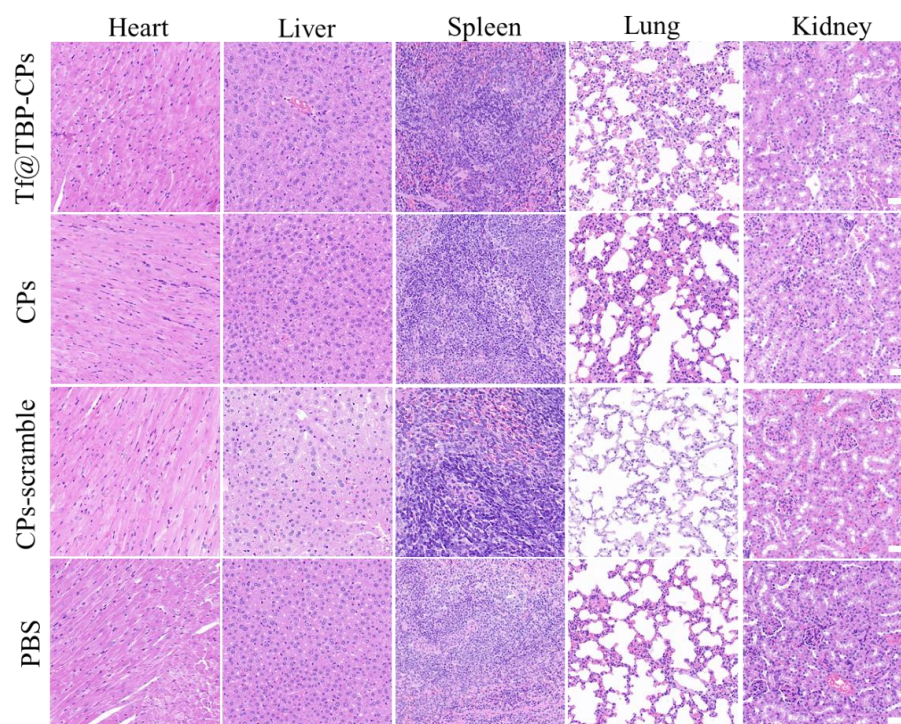
Figure S1. H&E stained tissue slices of heart, liver, spleen, lung and kidney excised from intracranial

MDA-MB 231-Luc bearing nude mice following 19 d treatment. Scale bars: 50 μm.

Chapter 5

Granzyme B-loaded, Cell-selective Penetrating and Reduction-Responsive Polymersomes Effectively Inhibit Progression of Orthotopic Human Lung Tumor *in Vivo**

Weijing Yang[a,#], Yaohua Wei[a,b#], Liang Yang[a], Jian Zhang[a], Zhiyuan Zhong [a,*], Gert Storm[b], Fenghua Menga,*

[a] Biomedical Polymers Laboratory, and Jiangsu Key Laboratory of Advanced Functional Polymer Design and Application, College of Chemistry, Chemical Engineering and Materials Science, Soochow University, Suzhou, 215123, P. R. China

[b] Department of Targeted Therapeutics, MIRA Institute for Biological Technology and Technical Medicine, University of Twente, PO Box 217, 7500AE, Enschede, The Netherlands

[#]W.J. Yang and Y.H. Wei contribute equally to this work.

Abstract

The clinical use of protein therapeutics with intracellular targets is hampered by its in vivo fragility and low cell permeability. Here, we report that cell-selective penetrating and reduction-responsive polymersomes (CPRPs) mediate high-efficiency targeted delivery of granzyme B (GrB) to orthotopic human lung tumor in vivo. Model protein studies using FITC labeled cytochrome C (FITC-CC) revealed efficient and high protein loading up to 17.2 wt.% for CPRPs. FITC-CC-loaded CPRPs exhibited a small size of 82-90 nm, reduction-responsive protein release, as well as greatly enhanced internalization and cytoplasmic protein release in A549 lung cancer cells compared with the non-targeted FITC-CC-loaded RPs control. GrB-loaded CPRPs showed a high potency toward A549 lung cancer cells with a half maximal inhibitory concentration (IC50) of 20.7 nM. Under the same condition, free GrB was essentially non-toxic. Importantly, installing cell-selective penetrating peptide did not alter the circulation time but did enhance tumor accumulation of RPs. Orthotopic A549-Luc lung tumor-bearing nude mice administered with GrB-loaded CPRPs at a dosage of 2.88 nmol GrB equiv./kg showed complete tumor growth inhibition with little body weight loss throughout the treatment period, resulting in significantly improved survival rate over the non-targeted and non-treated controls. These cell-selective penetrating and reduction-responsive polymersomes provide a targeted protein therapy for cancers.

1. Introduction

Proteins have emerged as advanced therapeutics for cancer therapy [1-5]. As compared to cytotoxic chemical drugs, proteins display usually better specificity. The clinical use of protein therapeutics with intracellular targets [6, 7] is, however, hampered by its in vivo fragility and low cell permeability [8-11]. Cell-penetrating peptides (CPPs) such as transactivator of transcription (TAT) have shown to efficiently chaperone functional proteins into various mammal cells [12-14]. Despite a high in vitro efficacy, protein-CPP conjugates reveal a poor protein delivery in vivo because cationic CPPs potentiate non-specific interactions and have low cell selectivity. Moreover, the conjugation of CPP to proteins demands dedicated synthesis and would possibly reduce protein bioactivity.

In the past decade, nanosystems such as polyion complexed micelles [15, 16], nanogels [17-21], nanocapsules [22-24] and polymersomes [25-27] have been exploited to deliver proteins intracellularly. In particular, polymersomes with large aqueous interiors are interesting for physical encapsulation and systemic delivery of proteins [28-32]. Notably, the membrane of polymersomes not only serves to protect cargos from leakage and degradation but also can be explicitly engineered with stimuli-sensitivity to tailor the site and rate of drug release [33-36]. The polymersome surfaces can further be installed with cell-selective ligands like peptides [37], lactoferrin [38], galactose [39] or antibodies [40] to enhance specific cell internalization [41-45]. It should be noted, however, that inefficient intracellular trafficking especially endosomal entrapment is a limiting step for protein delivery nanosystems [46, 47]. Interestingly, Matsushita et al. developed tumor-selective CPP denoted as CPP33 (sequence: RLWMRWYSPRTRAYG) that was reported to selectively penetrate A549 lung cancer cells[48]. We and He's group demonstrated that functionalization of polymersomes and nanoparticles, respectively, with CPP33 peptide significantly improved chemotherapy for A549 lung tumor-bearing mice [49, 50]. Lung cancer is a malignancy with high mortality and

morbidity [51, 52]. Despite significant improvement achieved in the past years, chemotherapy for lung cancer patients remains to be associated with notable adverse effects and drug resistance [53, 54].

Here, we investigated cell-selective penetrating and reduction-responsive polymersomes (CPRPs) for targeted delivery of granzyme B (GrB), a natural and potent apoptotic protein secreted by cytotoxic T cells and NK cells, to orthotopic human lung tumor xenografts (**Scheme 1**). Unlike chemotherapeutics, free GrB is practically non-cytotoxic to cells [39, 55]. However, upon releasing into cancer cells, it induces superior inhibitory effects with a low IC50 in the range of 1.6 nM to 500 nM depending on the intracellular delivery tools [29, 30, 39, 56, 57]. We reported previously that cNGQ peptide (sequence: cNGQGEQc, specific to $\alpha_3 \beta_1$ integrin) functionalized, reversibly-crosslinked chimaeric polymersomes based on poly(ethylene glycol)-*b*-poly(trimethylene carbonate-co-dithiolane trimethylene carbonate)-*b* polyethylenimine (PEG-P(TMC-DTC)-PEI) mediated efficient systemic delivery of siRNA [58]. Remarkably, our results show that GrB-loaded CPRPs (2.88 nmol GrB equiv./kg) induce complete growth inhibition of orthotopic A549-Luc human lung tumor xenografts in nude mice with little side effects throughout the treatment period, significantly improving mice survival rate. CPP33 peptide-guided and reversibly crosslinked polymersomes provide a targeted protein therapy for lung cancers. CPRPs have many unique advantages over previously reported protein delivery nanosystems including easy fabrication, high protein encapsulation, small size, high specificity towards lung cancer cells, and fast cytoplasmic protein release.
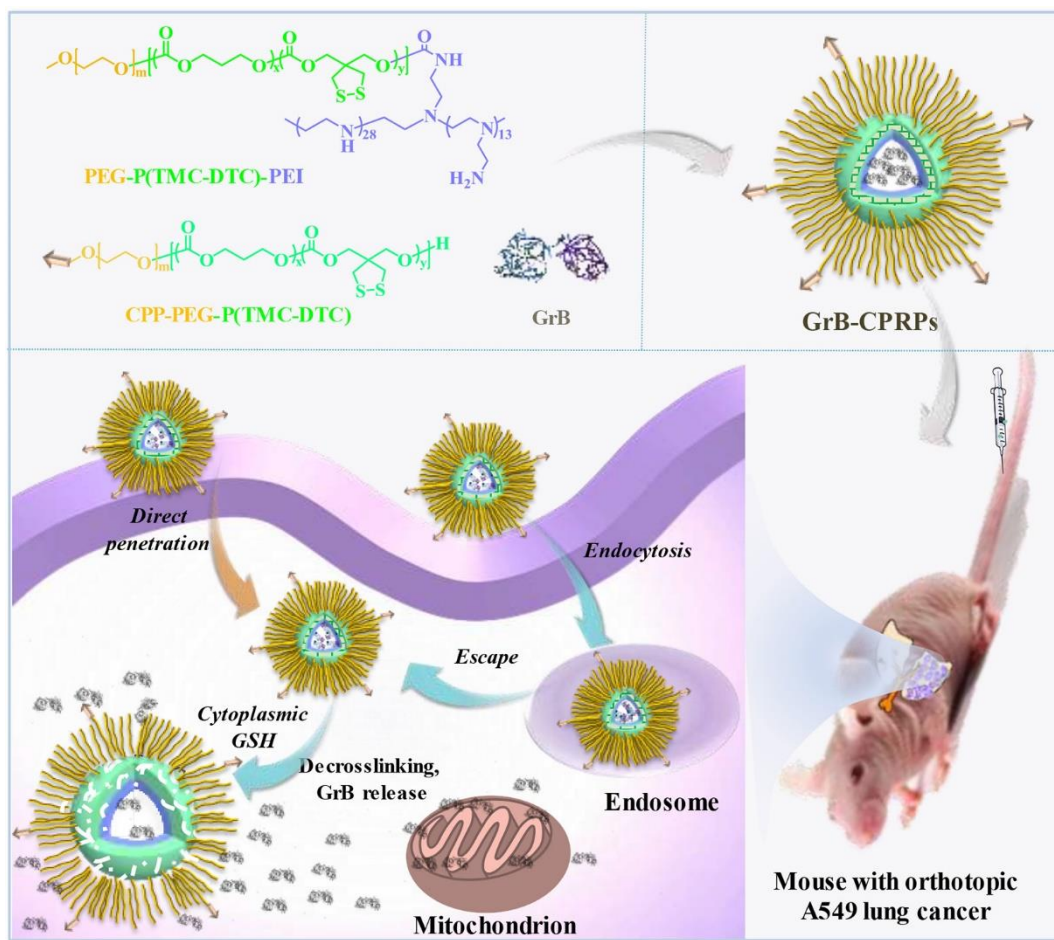
Scheme 1. Schematic of cell-selective penetrating and reduction-responsive polymersomes (CPRPs) for targeted delivery of GrB to orthotopic A549-Luc lung tumor xenograft in nude mice. GrB is efficiently loaded into the lumen of CPRPs which are made from CPP33-PEG-P(TMC-DTC) and PEG-P(TMC-DTC)-PEI. GrB-loaded CPRPs are stable in circulation and selectively home to A549 lung tumor. CPP33 peptide mediates efficient penetration of GrB-loaded CPRPs to A549 lung cancer cells. In the cytoplasm, GrB is quickly released as a result of reduction-triggered de-crosslinking of CPRPs.

2. Experimental section

2.1 Preparation of protein-loaded CPRPs

Cytochrome C was labeled with FITC (FITC-CC) to visualize protein inside the cells, as reported previously [30]. Protein (FITC-CC or GrB)-loaded CPRPs were prepared via self-assembly process by adding 50 μL of CPP33-PEG-P(TMC-DTC) and PEG-P(TMC-DTC)-PEI at predetermined molar ratios in DMSO (10 mg/mL) into 950 μL HEPES buffer (pH 6.8, 5 mM) containing different proteins under stirring. After standing still for 20 min and incubating for 6 h in a shaking bath (200 rpm, 37oC), the polymersomes were extensively dialysized (MWCO 300 KDa) 24 h against phosphate buffer (PB, pH 7.4, 5 mM). Using FITC-CC as a model protein, the protein loading content (PLC) and protein loading efficiency (PLE) were determined with UV-vis (492 nm). The in vitro release of proteins was described in the supporting information.

2.2 MTT assays of GrB-CPRPs

A549 cells were plated in a 96-well plate (5×10^3 cells/well) and cultured for 24 h using RPMI-1640 medium supplemented with 10% fetal bovine serum (FBS), 1% L-glutamine, antibiotics penicillin (100 IU/mL) and streptomycin (100 μg/mL). For determination of the effect of CPP33 contents, GrB-CPRPs with CPP33 molar ratio of 9.1%, 18.5% and 28.0% (GrB concentration = 5 μg/mL) in 20 μL PB buffer were added. The cells were incubated in an atmosphere containing 5% CO at 37 C for 4 h. Then cell culture media were replaced with fresh media and the cells were incubated for 68 h. Then, 10 μL of 3-(4,5-dimethylthiazol-2-yl)-2,5-diphenyl-tetrazoliumbromide (MTT) solution in PBS (5.0 mg/mL) was added. MTT assays were performed as described in our previous report [30].

Similarly, for determination of half-maximal inhibitory concentration (IC50), GrB-CPRPs

(CPP33 molar ratio of 18.5%), GrB-RPs and free GrB (GrB concentrations varying from 0.0038 to 45.6 nM) in 20 μL PBS were added to A549 cells.

To determine the cytotoxicity of empty polymersomes, A549 cells were incubated with CPRPs or RPs (final polymersome concentration = 0.1, 0.3 or 0.5 mg/mL) at 37 °C for 48 h.

2.3 Cellular uptake and Intracellular Release of FITC-CC

A549 cells were cultured on microscopic coverslips in 24-well plates (5.0×104 cells/well), and incubated with FITC-CC-CPRPs, FITC-CC-RPs, or free FITC-CC (FITC-CC dosage: 3.85 μM, FITC: 7.20 nmol equiv./mL) in 100 μL PB at 37 oC for 12 h. The culture medium was removed and the cells on coverslips were washed with PBS (x3), fixed with 4% formaldehyde for 15 min and washed with PBS (x3). The cell nuclei were stained with 4-6-diamidino-2-phenylindole (DAPI) for 10 min followed by PBS washing (x3). Fluorescence images of cells were obtained using confocal laser scanning microscope (CLSM, TCS SP5).

To investigate the cell entry and endosomal escape, A549 cells cultured on coverslips in 24-well plates were incubated with FITC-CC-CPRPs (FITC-CC dosage: 3.85 μM, FITC: 7.20 nmol equiv./mL) for 0.5, 1 or 2 h. Then the cells on microscope coverslips were treated with lysotracker-red (100 μL, 150 nM) for 50 min to stain the endosomes, followed by fixation (4% formaldehyde, 15 min), DAPI staining and CLSM observation. The cells were washed with PBS (x3) between each step.

To quantify the cellular uptake, A549 cells in a 6-well plate (1 × 106 cells/well) after incubation with FITC-CC-CPRPs, FITC-CC-PS or free FITC-CC in 0.2 mL PBS (FITC-CC dosage: 3.85 μM, FITC: 7.20 nmol equiv./mL) at 37 oC for 2 h. PBS treated cells were taken as a blank. The cells were digested by 0.25 w/v% trypsin/0.03 w/v% EDTA, as reported earlier [30], by immediately recording the fluorescence histograms with a BD FACS Calibur flow

cytometer and analysis using Cell Quest. 10,000 Gated events were analyzed to generate each histogram and the gate was arbitrarily set for the detection of FITC fluorescence.

2.4 Blood circulation of CPRPs-Cy5 in mice

All animal experiments were approved by the Animal Care and Use Committee of Soochow University (P.R. China), and all protocols of animal studies conformed to the Guide for the Care and Use of Laboratory Animals.

For pharmacokinetic studies, CPRPs-Cy5 or PS-Cy5 (0.25 mg Cy5 equiv./kg) in 200 μL PB was intravenously injected into Balb/c mice (18-22 g) via the tail vein (n = 3). At prescribed time points post injection, ca. ~30 μL of blood was withdrawn from the orbit of mice. The blood samples upon withdrawing were immediately dissolved in 0.1 mL of Triton X-100 with brief sonification. Drug was extracted by incubating blood samples in 0.6 mL of extraction solution (DMSO containing 20 mM DTT) in a shaking bath (37°C, 200 rpm) overnight followed by centrifugation (14.8 krpm, 30 min). The Cy5 fluorescence intensity of the supernatant was determined using a fluorometer. Cy5 levels were expressed as injected dose per gram of blood (% ID/g). The blood circulation curves were obtained and the half-lives of two phases ($t_{1/2}$, α and $t_{1/2}$, β) were determined by fitting the experimental data using Software Origin 8 exponential decay 2 model: $y = A_1 \times \exp(-x/t_1) + A_2 \times \exp(-x/t_2) + y_0$, taking $t_{1/2}$, α = 0.693 t_1 and $t_{1/2}$, β = 0.693 t_2.

2.5 The in vivo imaging of CPRPs-Cy5

The mice bearing orthotopic A549-luc lung tumors were established as described in our early report [58]. Briefly, 0.1 mL of A549-Luc cell suspension (1×10^7 cells) was injected into the left lung parenchyma of nude mice (18-22 g). The bioluminescence of mouse lung and tumor volume was monitored using imaging system in live animals. After 2 weeks when tumors

reached 1.0×10^7 p/s/cm^2/sr, the tumor-bearing mice were randomly grouped and intravenously injected with Cy5-labeled polymersomes (CPRPs-Cy5 or CPs-Cy5) in 0.2 mL PB (pH 7.4, 5 mM) via the tail veins (0.25 mg Cy5 equiv./kg). The mice were scanned at 2, 4, 8, 12 and 24 h post-injection using IVIS II fluorescence imaging system.

2.6 In vivo antitumor efficacy of GrB-CPRPs

The mice bearing orthotopic A549-luc lung tumors (1.0×10^7p/s/cm^2/sr) were weighed and randomly divided into four groups (n = 6), and this day was designated as day 0. GrB-CPRPs and GrB-RPs (75 μg GrB equiv./kg) were injected via tail vein every 4 days. CPRPs and PBS were used as controls. The treatment efficacy of mice was evaluated by monitoring tumor bioluminescence intensity. The relative body weight of the mice was normalized to their initial weight. On day 20, one mouse of each group was sacrificed by cervical vertebra dislocation. The heart, liver, spleen, lung and kidney were excised, fixed with 10% formalin and embedded in paraffin. The sliced organ tissues (thickness: 4 μm) mounted on the glass slides were stained by hematoxylin and eosin (H&E) and observed by a Leica digital microscope (Olympus BX41) at magnification (400×).

The Kaplan-Meier survival curve was determined within 60 days (n = 5). Mice in each cohort were considered to be dead either when the mice died during treatment or when the body weight decreased by 15% compared with initial value.

2.7 Statistical Analysis

Data were expressed as mean ±SD. Differences between groups were assessed by one-way ANOVA with Tukey multiple comparison tests. Kaplan-Meier survival curves were analyzed by one-way ANOVA with a log-rank test for comparisons using GraphPad Prism 7. *$p<0.05$ was considered significant, and **$p <0.01$, ***$p <0.001$ were considered highly significant.

3. Results and discussion

3.1 Preparation and characterization of protein-loaded CPRPs

Cell-selective penetrating and reduction-responsive polymersomes (CPRPs) were fabricated from co-self-assembly of CPP33-PEG-P(TMC-DTC) and PEG-P(TMC-DTC)-PEI copolymers (**Table S1**). Notably, proteins were conveniently loaded into the lumen of CPRPs by adding copolymer solution in DMSO into a protein-containing HEPES buffer (pH 6.8, 5 mM). Model protein studies using FITC-labeled cytochrome C (FITC-CC) and CPRPs with CPP33 peptide surface density of 18.5 mol.% revealed that protein loading efficiency (PLE) was 95.1% at theoretical protein loading contents (PLC) of 1-5 wt.% (**Table 1**). Even at a theoretical PLC of 20 wt.%, a high PLE of 83.2%, which corresponded to a PLC of 17.2 wt.%, was obtained. This high-efficacy protein loading is most probably owing to electrostatic interactions and hydrogen bonding of proteins with PEI in the lumen, as previously reported for different chimaeric polymersomes [49, 58]. FITC-CC-loaded CPRPs (FITC-CC-CPRPs) exhibited slightly increased size from 82 to 90 nm with increase in PLC from 1.0 wt.% to 17.2 wt.% (**Table 1**). The non-targeted control, reduction-responsive polymersomes (RPs), revealed similar loading of FITC-CC. The size of FITC-CC-loaded RPs (FITC-CC-RPs) was somewhat smaller than that of FITC-CC-CPRPs, ranging from 67 to 78 nm with increase in PLC from 1.0 wt.% to 17.8 wt.% (**Table 1**). Notably, all FITC-CC-CPRPs displayed slightly positive surface charges (+1.9 ~ +3.5 mV), which were similar to FITC-CC-RPs, suggesting that decorating RPs with CPP33 peptide has little influence on their surface properties. Minimal positive surface charge is an important prerequisite for long circulation and cell selectivity [59]. In a similar way, GrB-loaded CPRPs (GrB-CPRPs) were fabricated at a low theoretical PLC of 1.8 wt.%, given its high potency. **Figure 1A** shows that GrB-CPRPs had a good distribution and a hydrodynamic size of 88 nm. GrB-loaded RPs (GrB-RPs, non-targeted control) displayed a smaller size of 75 nm. As for FITC-CC-CPRPs, GrB-CPRPs also had a close to neutral surface

charges (**Table 2**). The similar biophysical properties (size, distribution and surface charge) observed for protein-loaded and blank polymersomes, indicating that loading of proteins has little influence on their structure. TEM micrograph confirmed that FITC-CC-CPRPs retained a vesicular structure (**Figure S1**).

**Table 1.** Characteristics of FITC-CC-CPRPsa and FITC-CC-RPs.

Polymersomes	PLC (wt%)		PLE[b] (%)	Size[c] (nm)	PDI[c]	ζ[d] (mV)
	Theory	Deter[b]				
FITC-CC–CPRPs	0	–	–	80	0.17	+1.9
	1	1.0	~100	82	0.17	+3.5
	2	2.0	99.1	83	0.15	+3.4
	5	4.8	95.1	85	0.19	+1.9
	10	8.8	86.4	87	0.18	+2.1
	20	17.2	83.2	90	0.21	+2.3
FITC-CC-RPs	0	–	–	65	0.16	+1.8
	1	1.0	~100	67	0.19	+2.4
	2	2.0	98.5	70	0.18	+1.9
	5	4.8	94.5	72	0.19	+2.5
	10	9.1	90.0	74	0.13	+2.2
	20	17.8	86.4	78	0.20	+2.3

[a] CPP33 molar content: 18.5%; [b] Determined by UV-vis; [c] Determined by DLS in PB (pH 7.4, 5 mM); [d] Determined by electrophoresis in PB (pH 7.4, 5 mM).

Using FITC-CC as a model protein, in vitro release studies demonstrated that protein release from CPRPs was less than 13% in PBS within 24 h while ca. 88% FITC-CC was released in 24 h under conditions containing 10 mM dithiothreitol (DTT) (**Figure 1B**). FITC-CC RPs exhibited an identical protein release profile. Circular dichroism (CD) measurements

revealed that CC released from CC-CPRPs had the same spectrum to native CC (**Figure 1C**), indicating that proteins well preserved their secondary structure. We further evaluated the proteolytic activity of GrB released from GrB-CPRPs using a fluorescent Ac-IETD-AFC as a substrate. **Figure 1D** shows that released GrB, similar to native GrB, efficiently cleaved the substrates resulting in complete fluorescence shift from 440 nm (Ac-IETD-AFC) to 490 nm (AFC). These results support that proteins encapsulated in CPRPs maintain their structure and bioactivity.
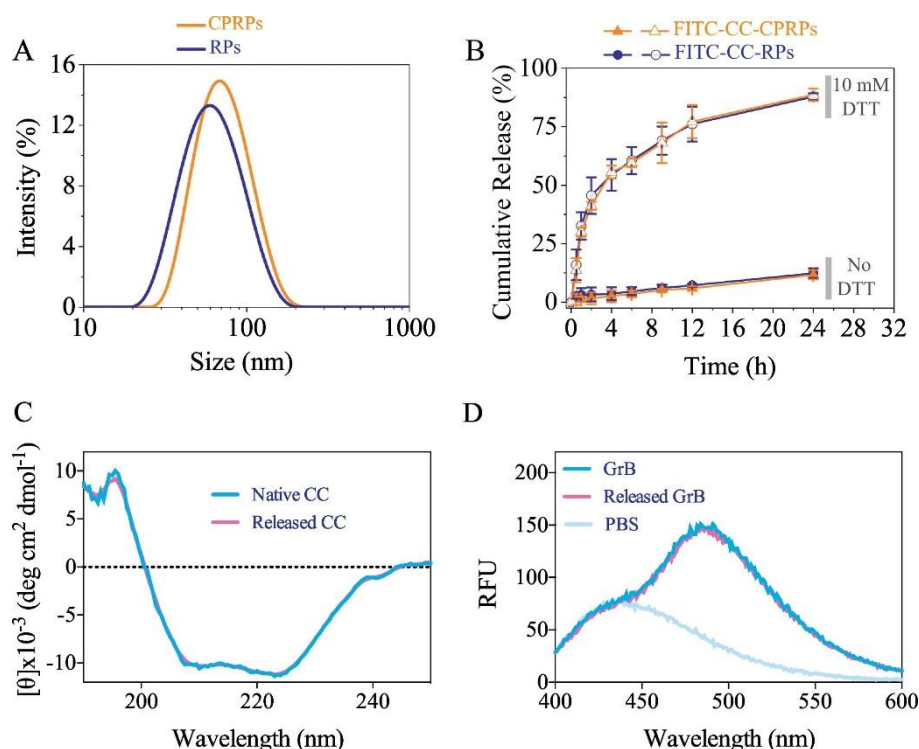
Figure 1. (A) Size distribution of GrB-CPRPs (CPP33 content: 18.5%) and GrB-RPs determined by DLS. (B) In vitro FITC-CC release in PBS (pH 7.4, 10 mM, 150 mM NaCl) with or without 10 mM DTT at 37℃ (Polymersome concentration = 100 μg/mL, FITC-CC concentration = 17.2 μg/mL, n = 3). (C) CD spectra of CC released from CC-CPRPs and native CC at 100 μg/mL. (D) The fluorescence spectra of the substrate Ac-IETD-AFC following 1 h treatment with GrB released from GrB-CPRPs, native GrB and PBS, respectively, at 37 ℃.

Table 2. Characteristics of GrB-CPRPsa at a theoretical protein loading content of 1.8 wt.%.

| Entry	Polymersomes	Size[b](nm)	PDI[b]	ζ[c] (mV)
1	GrB-CPRPs	88	0.18	+ 3.2
2	GrB-RPs	75	0.17	+ 2.1

[a] CPP33 molar content: 18.5%; [b] Determined by DLS in PB (pH 7.4, 5 mM); [c] Determined by electrophoresis in PB (pH 7.4, 5 mM).

3.2 Intracellular protein delivery by CPRPs

GrB is a serine protease secreted by cytotoxic T cells and NK cells. As reported previously [21], free GrB caused little toxicity to A549 cells (Fig. 2A), owing to its inferior cellular uptake. Notably, GrB following loading into CPRPs exhibited significantly enhanced inhibitory effect to A549 cells, in which optimal CPP33 peptide molar content appeared to be 18.5 mol.%. If not otherwise specified, CPRPs refer to the ones with CPP33 peptide molar content of 18.5 mol.%. The IC$_{50}$ of GrB-loaded CPRPs to A549 cells was determined to be 20.7 nM, which was ca. 2-fold lower than that of non-targeting GrB-RPs (**Figure 2B**). Both empty polymersomes, CPRPs and RPs, were essentially non-toxic to A549 cells (cell viability > 85%) even at a concentration of 0.5 mg/mL and 48 h incubation (**Figure S2**). GrB-CPRPs with 40 nM GrB corresponded to a CPRPs concentration of 0.05 mg/mL. It is clear that the enhanced antitumor activity of GrB-CPRPs over GrB-RPs is not due to direct cytotoxic effects of CPP33 peptide. To further investigate whether the observed killing effects of GrB-CPRPs is due to the specific pro-apoptotic effects of GrB, we conducted apoptosis assays using Annexin V-FITC/PI FACS analyses and caspase 3/7 activation in A549 cells using Apo-ONE homogeneous caspase3/7 assays. **Figure S3A** demonstrates that after treatment with 7.5 nM GrB-CPRPs, 29.6% and 8.0% A549 cells underwent late and early apoptosis, respectively. In comparison, non-targeted GrB-RPs caused 15.2% late apoptosis and 6.7% early apoptosis. **Figure S3B** displays that GrB-

CPRPs induced pronounced caspase 3/7 activation with 5.5-fold higher caspase 3/7 activity in cleaving Z-DEVD-R110 substrate than empty CPRPs.
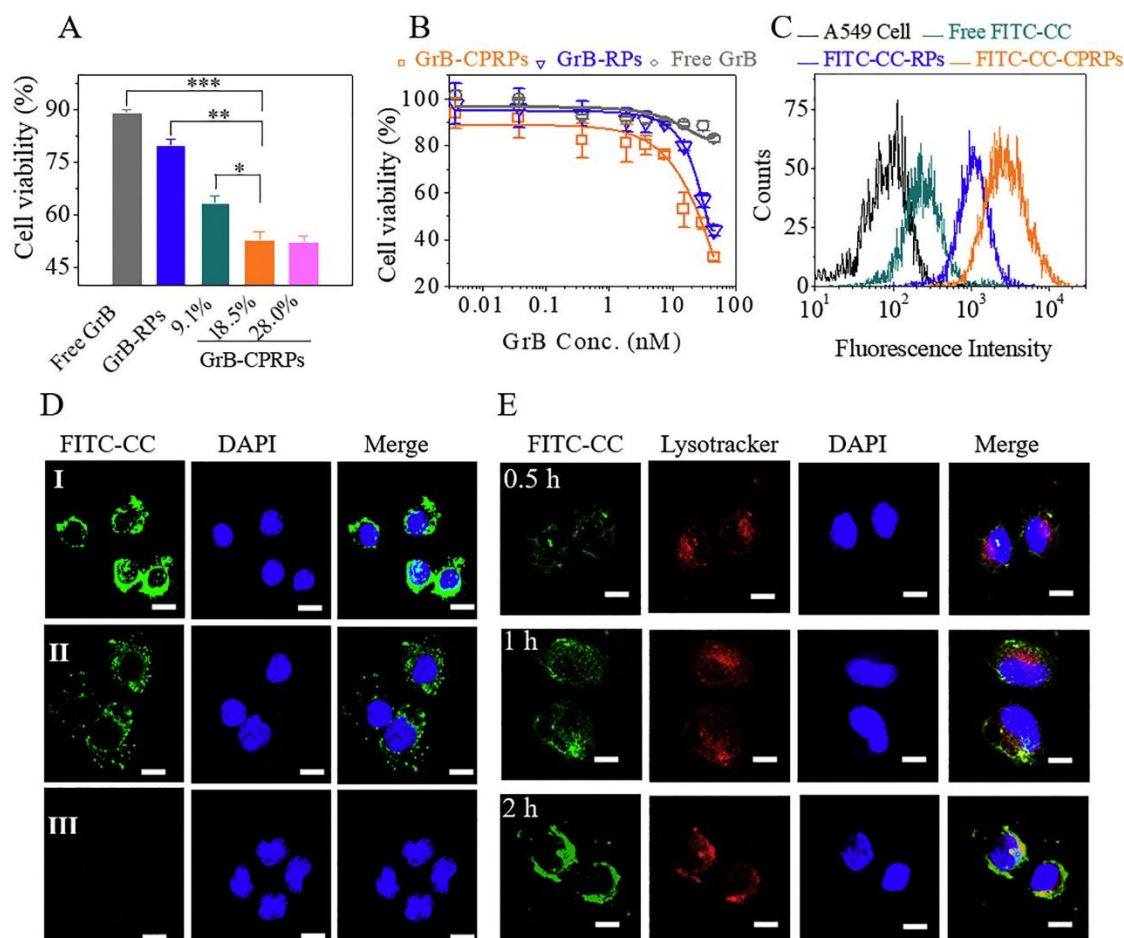
Figure 2. (A) Influence of CPP33 peptide surface density (ranging from 9.1 mol.%, 18.5 mol.% to 28.0 mol.%) on antitumor activity of GrB-CPRPs to A549 cells determined by MTT assays (dosage: 15.2 nM GrB). One-way ANOVA with Tukey multiple comparison tests, $*p < 0.05$, $**p < 0.01$, $***p < 0.001$. (B) Antitumor activity of GrB-CPRPs and RPs to A549 cells determined using MTT assays. For both A and B, the cells following 4 h incubation with different formulations were further cultured in fresh medium for 68 h. Free GrB was used as a control. Data are presented as mean ± SD (n = 4). (C) Flow cytometric analyses of A549 cells incubated 2 h with FITC-CC-CPRPs, FITC-CC-RPs and free FITC-CC, respectively (dosage: 50 μg FITC-CC /mL). (D) CLSM images of A549 cells following 12 h incubation with FITC-CC-CPRPs (I), FITC-CC-RPs (II) or free FITC-CC (III). (E) CLSM images of A549 cells following 0.5, 1, or 2 h incubation with FITC-CC-CPRPs. FITC-CC dose: 3.85 μM, FITC: 7.20 nmol equiv./mL. Scale bars: 15 μm.

The cellular uptake and intercellular trafficking of proteins were investigated using FITC-CC as a model protein. **Figure 2C** shows that installation of CPP33 peptide significantly enhanced cellular uptake, in which A549 cells treated with FITC-CC-CPRPs demonstrated 2.1 and 11.4-fold higher FITC-CC levels than cells with non-targeted FITC-CC-RPs and free FITC-CC controls, respectively. CLSM observation revealed that FITC-CC distributed all over the cells treated with FITC-CC-CPRPs (**Figure 2D**). In comparison, significantly weaker FITC fluorescence was observed in A549 cells incubated with FITC-CC-RPs or free FITC-CC controls. These results support that CPP33 peptide greatly improves intracellular protein delivery.

We further stained the endo/lyso-somes of A549 cells with lysotracker red. Interestingly, significant amount of FITC-CC was delivered to the cytosol of A549 cells after incubation with FITC-CC-CPRPs for 1 h (**Figure 2E**). This fast cytoplasmic delivery of proteins could be due to either direct transduction of FITC-CC-CPRPs or receptor-mediated endocytosis followed by endosomal escape.

3.3 The in vivo pharmacokinetics and biodistribution of Cy5-labeled CPRPs

Pharmacokinetics studies demonstrated that Cy5-labeled polymersomes CPRPs-Cy5 had long blood circulation time in mice with elimination half-life (t1/2,) of 6.75 h, similar to that of non-targeted RPs-Cy5 (6.67 h) (**Figure 3A**), indicating cell-selective penetrating peptide did not alter the blood circulation. To study in vivo tumor targetability of polymersomes, nude mice inoculated with orthotopic A549-Luc lung tumor were injected with CPRPs-Cy5 or RPs-Cy5 via tail veins of mice which showed similar initial Luc bioluminescence intensity in the lungs. In vivo NIR imaging results displayed that Cy5 fluorescence intensity in the lung enhanced from 2 to 8 h and reduced from 8 to 24 h (**Figure 3B**). It is noteworthy that mice treated by CPRPs-Cy5 had obviously better lung tumor accumulation than RPs-Cy5 treated ones, and

strong fluorescence could still be seen at 24 h. The improved tumor accumulation of CPRPs is mainly attributed to the targeting effect of CPP33 peptide to A549 lung tumor, which leads to not only better cellular uptake but also enhanced tumor retention [48-50].
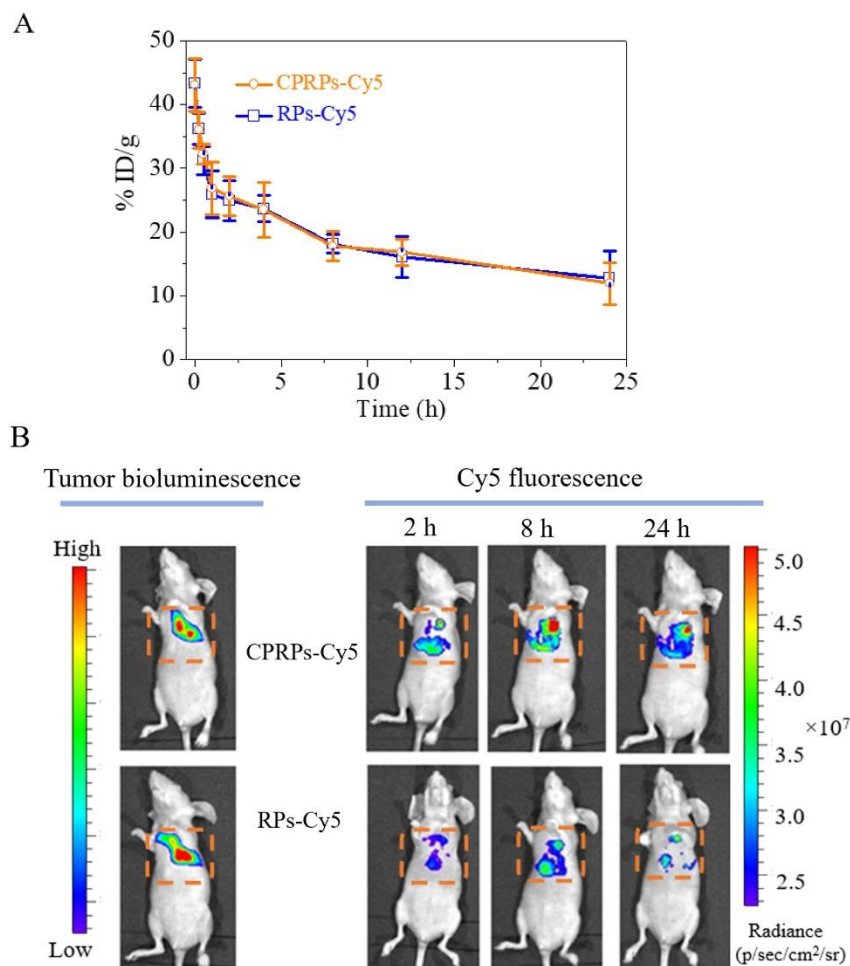

Figure 3. (A) Blood circulation of CPRPs-Cy5 and RPs-Cy5 in nude mice (n = 3). (B) In vivo imaging of mice bearing orthotopic A549-Luc tumor treated with CPRPs-Cy5 and RPs-Cy5. The left photo shows the bioluminescence of A549-Luc tumor in the mouse lung before treatment. Dosage: 0.25 mg Cy5 equiv./kg.

3.4 Antitumor activity of GrB-CPRPs

The antitumor activity of GrB-CPRPs was assessed using orthotopic A549-Luc tumor-bearing nude mice. The mice were i.v. injected with GrB-CPRPs every four days and for four times at a low GrB dosage of 2.88 nmol/kg. The non-targeted GrB-RPs and blank CPRPs were

used as controls. Notably, Fig. 4A shows that mice treated with GrB-CPRPs had little change of A549-Luc bioluminescence within 20 days, indicating effective inhibition of tumor growth. GrB-RPs could also slow down tumor growth though obviously less effective than GrB-CPRPs (**Figure 4B**). By contrast, tumor grew rapidly for mice administered with blank CPRPs and PBS (**Figure 4C and D**). Semi-quantitative bioluminescence analyses exhibited that tumor growth was nearly completely subdued by GrB-CPRPs (**Figure 5A**). GrB-CPRPs brought about significantly more effective inhibition of A549-Luc tumor growth than the non-targeted GrB-RPs. The ex vivo bioluminescence images of lung tumor excised on day 20 revealed aggressive invasion of A549-Luc cancer cells to the lung of mice treated with blank CPRPs or PBS and GrB-CPRPs inducing clearly the best inhibition (**Figure 5B**).
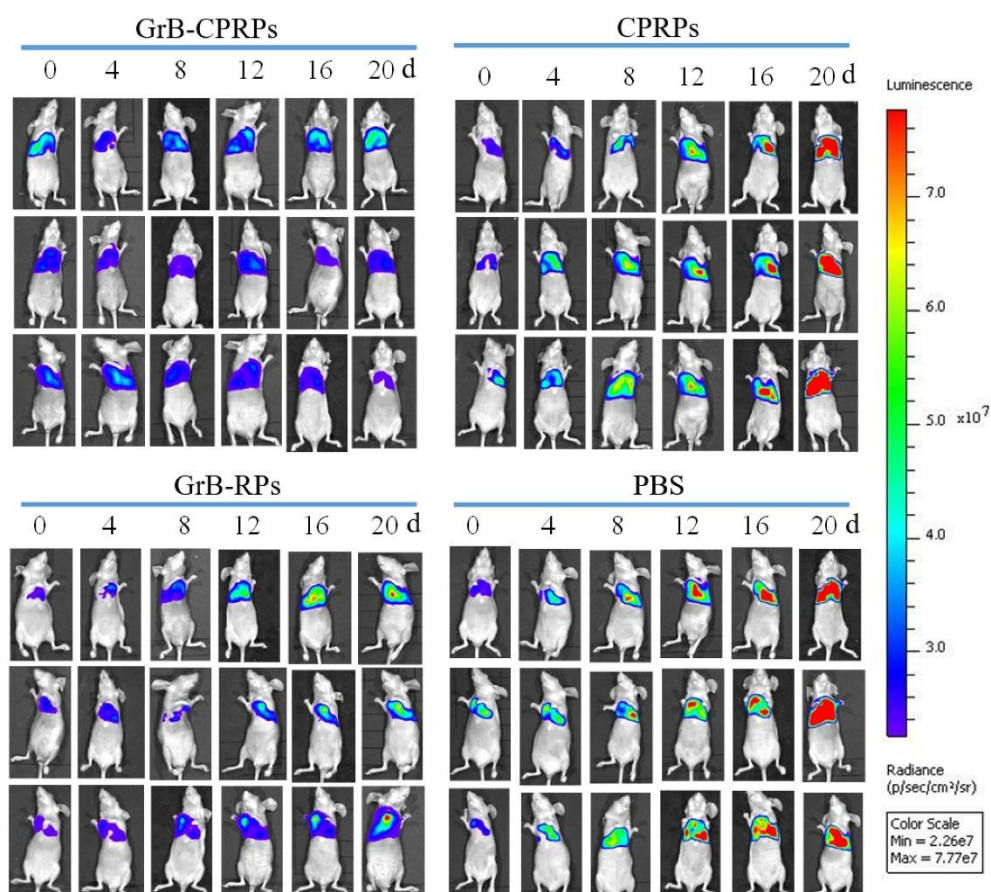
Figure 4. Bioluminescence images of orthotopic A549-Luc lung tumor-bearing mice treated with GrB-CPRPs. GrB-RPs, CPRPs and PBS were used as controls. The mice were via i.v. injected at a dosage of 2.88 nmol GrB /kg on day 0, 4, 8 and 12.

Figure 5C displays that mice treated with blank CPRPs or PBS had significant body weight loss (more than 20% in 20 days), due to the fact that the invasion of A549-Luc tumor to lung would cause lung malfunction. On the contrary, little body weight loss was shown for the mice treated with GrB-CPRPs or GrB-RPs within 20 days, which on one hand supports their effective inhibition of tumor invasion into the lung, and on the other hand indicates that they have a low systemic toxicity. Remarkably, GrB-RPs (non-targeted control) significantly improved mice survival rate over the PBS control (median survival time: 35 versus 21 days) (**Figure 5D**). GrB-CPRPs further improved median survival time to 48 days, which was a significant improvement compared with GrB-RPs. Blank CPRPs caused no change of survival rate relative to PBS, indicating that CPRPs do not induce adverse or therapeutic effects. Rosenblum et al. reported that GrB/scFvMEL fusion protein at a dosage of 288 nmol GrB/kg, which was 100-fold higher than GrB-CPRPs used in this study, could efficiently inhibit growth of human melanoma A375 xenograft tumors in nude mice [60]. Histological analyses illustrated that GrB-CPRPs and GrB-RPs treated mice had nearly no tumor tissue in the lung similar as unaffected lung tissue. However, large tumor tissues were present in mouse lungs treated with PBS or CPRPs (**Figure 5E**). No noticeable damage to other major organs like heart, liver, spleen or kidney was observed for all groups (**Figure S4**).
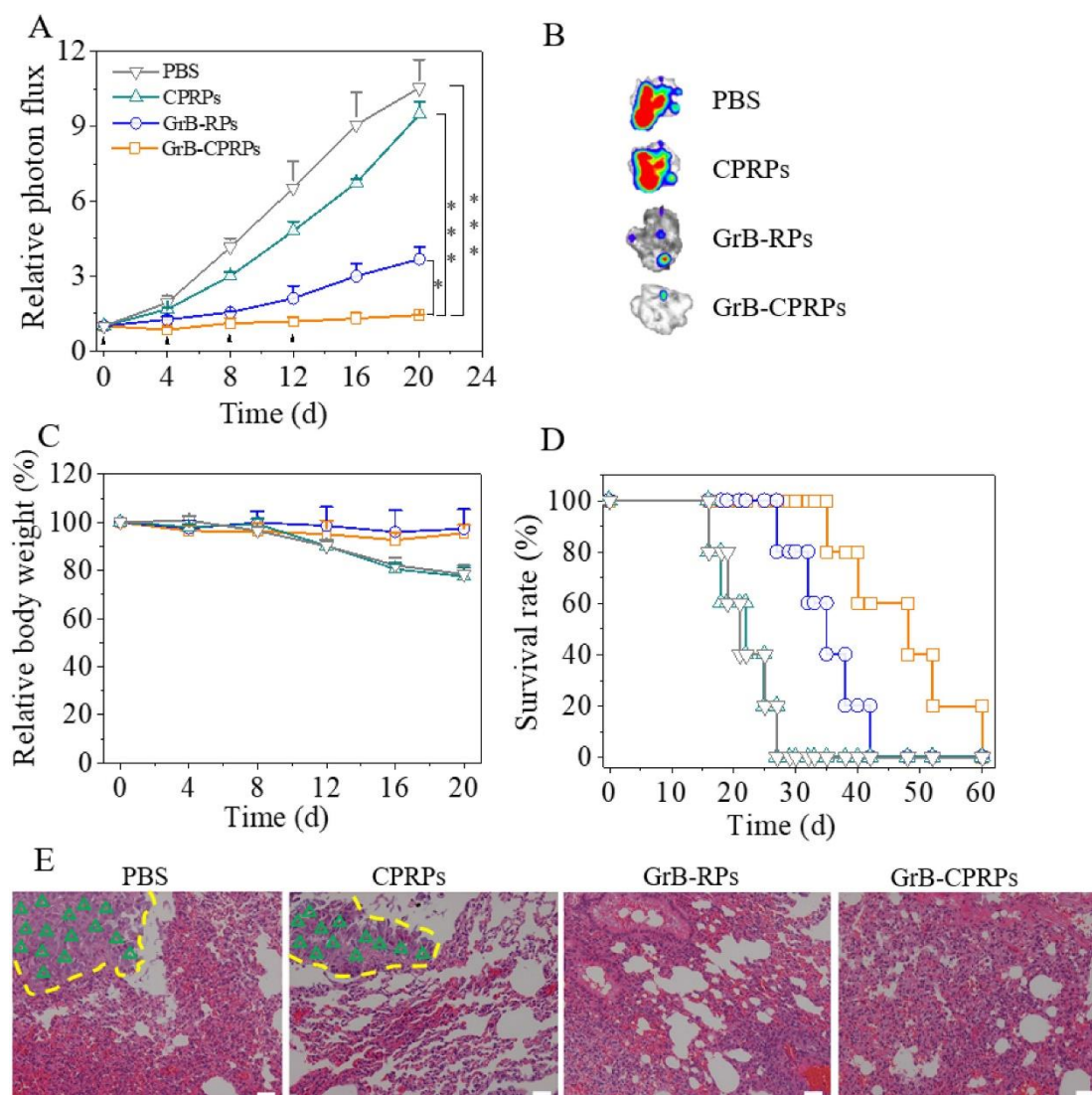
Figure 5. In vivo therapeutic efficacy of GrB-CPRPs toward orthotopic A549-Luc lung tumor-bearing mice. The mice were i.v. injected with 2.88 nmol GrB/kg on day 0, 4, 8 and 12. GrB-RPs, CPRPs and PBS were used as controls. (A) Dependence of A549-Luc bioluminescence levels in the lung of mice on time (n = 6). One-way ANOVA with Tukey multiple comparison tests, *p < 0.05, ***p < 0.001. (B) Ex vivo images of mouse lungs on day 20. (C) Body weight changes of mice (n = 6). (D) Survival rates of mice (n = 5). Kaplan-Meier analysis (log-rank test for comparison): GrB-CPRPs vs. GrB-RPs: *p < 0.05; GrB-CPRPs vs. CPRPs and PBS: **p < 0.01; GrB-RPs vs. CPRPs and PBS: *p < 0.05. (E) Histological analyses of mouse lungs (magnification: 400×). Circles and green arrows indicate the tumor region and cells, respectively. Scale bar: 100 μm.

4. Conclusion

We have demonstrated that cell-selective penetrating and reduction-responsive polymersomes (CPRPs) mediate high-efficiency targeted delivery of granzyme B (GrB) to orthotopic human lung tumor in vivo, leading to complete suppression of tumor growth, little body weight loss throughout the treatment period, and significantly improved survival rate over the non-targeted and non-treated controls. GrB-CPRPs are unique for targeted protein therapy for lung tumor in that they show highly efficient protein loading, small size, sufficient in vivo stability, good targetability to A549 cells, strong tumor accumulation and tumor tissue penetration. Considering their biodegradability, biocompatibility and facile preparation, CPRPs are promising for constructing artificial killer cells for targeted protein therapy of non-small cell lung cancer.

References

[1] C.J. Eun, S. Tan, S.J. Gao, Y. Nunnarpas, K.S. Hee, L.J. Heon, C.H. Soo, Y. Hirohisa, L. Zhuo, K. Motoichi, Self-assembled micellar nanocomplexes comprising green tea catechin derivatives and protein drugs for cancer therapy, Nat. Nanotechnol. 9 (2014) 907-912.

[2] D.W. Stuckey, K. Shah, TRAIL on trial: preclinical advances for cancer therapy, Trends Mol. Med. 19 (2013) 685-694.

[3] D. Li, C.F. van Nostrum, E. Mastrobattista, T. Vermonden, W.E. Hennink, Nanogels for intracellular delivery of biotherapeutics, J. Controlled Release 259 (2017) 16-28.

[4] C.D. Spicer, C. Jumeaux, B. Gupta, M.M. Stevens, Peptide and protein nanoparticle conjugates: versatile platforms for biomedical applications, Chem. Soc. Rev. 47 (2018) 3574-3620.

[5] Y. Lu, W. Sun, Z. Gu, Stimuli-responsive nanomaterials for therapeutic protein delivery, 194 (2014) 1.

[6] M. Okada, N.I. Smith, A.F. Palonpon, H. Endo, S. Kawata, M. Sodeoka, K. Fujita, Label-free Raman observation of cytochrome c dynamics during apoptosis, Proc. Natl. Acad. Sci. USA. 109 (2012) 28-32.

[7] A.V. Follis, J.E. Chipuk, J.C. Fisher, M.K. Yun, C.R. Grace, A. Nourse, K. Baran, L. Ou, L. Min, S.W. White, D.R. Green, R.W. Kriwacki, PUMA binding induces partial unfolding within BCL-xL to disrupt p53 binding and promote apoptosis, Nat. Chem. Biol. 9 (2013) 163-168.

[8] B. Leader, Q.J. Baca, D.E. Golan, Protein therapeutics: a summary and pharmacological classification, Nat. Rev. Drug Discov. 7 (2008) 21-39.

[9] D.S. Pisal, M.P. Kosloski, S.V. Balu-Iyer, Delivery of therapeutic proteins, J. Pharm. Sci. 99 (2010) 2557-2375.

[10] P. Zhang, D. He, P.M. Klein, X. Liu, R. Röder, M. Döblinger, E. Wagner, Enhanced intracellular protein transduction by sequence defined tetra-oleoyl oligoaminoamides targeted for cancer therapy, Adv. Funct. Mater. 25 (2016) 6627-6636.

[11] M. Wang, K. Alberti, S. Sun, C.L. Arellano, Q. Xu, Combinatorially designed lipid-like nanoparticles for intracellular delivery of cytotoxic protein for cancer therapy, Angew Chem. Int. Ed. 53 (2014) 2893–2898.

[12] J.S. Wadia, S.F. Dowdy, Transmembrane delivery of protein and peptide drugs by TAT-mediated transduction in the treatment of cancer, Adv. Drug Deliver. Rev. 57 (2005) 579-596.

[13] H. He, J. Ye, Y. Wang, Q. Liu, H.S. Chung, Y.M. Kwon, M.C. Shin, K. Lee, V.C. Yang, Cell-penetrating peptides meditated encapsulation of protein therapeutics into intact red blood cells and its application, J. Controlled Release 176 (2014) 123-132.

[14] N. Nischan, H.D. Herce, F. Natale, N. Bohlke, N. Budisa, M.C. Cardoso, C.P. Hackenberger, Covalent Attachment of Cyclic TAT Peptides to GFP Results in Protein Delivery into Live Cells with Immediate Bioavailability, Angew. Chem. Int. Ed., 54 (2015), p. 1950.

[15] Y. Lee, T. Ishii, H. Cabral, H.J. Kim, J.H. Seo, N. Nishiyama, H. Oshima, K. Osada, K. Kataoka, Charge-conversional polyionic complex micelles-efficient nanocarriers for protein delivery into cytoplasm, Angew Chem. Int. Ed. 121 (2009) 5413-5416.

[16] Y. Lee, T. Ishii, H.J. Kim, N. Nishiyama, Y. Hayakawa, K. Itaka, K. Kataoka, Efficient delivery of bioactive antibodies into the cytoplasm of living cells by charge-conversional polyion complex micelles, Angew Chem. Int. Ed. 122 (2010) 2606-2609.

[17] Q. Hu, W. Sun, Y. Lu, H.N. Bomba, Y. Ye , T. Jiang, A.J. Isaacson, Z. Gu, Tumor microenvironment-mediated construction and deconstruction of extracellular drug-delivery depots, Nano Lett. 16 (2016) 1118-1126.

[18] X. Wu, C. He, Y. Wu, X. Chen, J. Cheng, Nanogel-incorporated physical and chemical hybrid gels for highly effective chemo-protein combination therapy, Adv. Funct. Mater. 25 (2015) 6744-6755.

[19] T. Nochi, Y. Yuki, H. Takahashi, S. Sawada, M. Mejima, T. Kohda, N. Harada, I.G. Kong, A. Sato, N. Kataoka, D. Tokuhara, S. Kurokawa, Y. Takahashi, H. Tsukada, S. Kozaki, K. Akiyoshi, H. Kiyono, Nanogel antigenic protein-delivery system for adjuvant-free intranasal vaccines, Nat. Mater. 9 (2010) 572-578.

[20] Q. Zhu, X. Chen, X. Xu, Y. Zhang, C. Zhang, R. Mo, Tumor-specific self-degradable nanogels as potential carriers for systemic delivery of anticancer proteins, Adv. Funct. Mater. 28 (2018) 1707371.

[21] J. Chen, Y. Zou, C. Deng, F. Meng, J. Zhang, Z. Zhong, Multifunctional click hyaluronic acid nanogels for targeted protein delivery and effective cancer treatment in vivo, Chem. Mater. 28 (2016) 8792-8799.

[22] M. Zhao, Y. Liu, R.S. Hsieh, N. Wang, W. Tai, K.I. Joo, P. Wang, Z. Gu, Y. Tang, Clickable protein nanocapsules for targeted delivery of recombinant p53 protein, J. Am. Chem. Soc. 136 (2014) 15319-15325.

[23] J. Wen, S.M. Anderson, J. Du, M. Yan, J. Wang, M. Shen, Y. Lu, T. Segura, Controlled protein delivery based on enzyme-responsive nanocapsules, Adv. Mater. 23 (2011) 4549-4553.

[24] E.A. Prasetyanto, A. Bertucci, D. Septiadi, R. Corradini, P. Castrohartmann, C.L. De, Breakable hybrid organosilica nanocapsules for protein delivery, Angew Chem. Int. Ed. 55 (2016) 3323-3327.

[25] D.A. Christian, S. Cai, D.M. Bowen, Y. Kim, J.D. Pajerowski, D.E. Discher, Polymersome carriers: From self-assembly to siRNA and protein therapeutics, Eur. J. Pharm. Biopharm. 71 (2009) 463-474.

[26] R.J.R.W. Peters, M. Marguet, S. Marais, M.W. Fraaije, J.C.M. van Hest, S. Lecommandoux, Cascade Reactions in Multicompartmentalized Polymersomes, Angew. Chem. Int. Edit. 53 (2014) 146-150.

[27] L.K.E.A. Abdelmohsen, M. Nijemeisland, G.M. Pawar, G.-J.A. Janssen, R.J.M. Nolte, J.C.M. van Hest, D.A. Wilson, Dynamic Loading and Unloading of Proteins in Polymeric Stomatocytes: Formation of an Enzyme-Loaded Supramolecular Nanomotor, ACS Nano 10 (2016) 2652-2660.

[28] C.K. Wong, A.J. Laos, A.H. Soeriyadi, J. Wiedenmann, P.M. Curmi, J.J. Gooding, C.P. Marquis, M.H. Stenzel, P. Thordarson, Polymersomes prepared from thermoresponsive fluorescent protein-polymer bioconjugates: capture of and report on drug and protein payloads, Angew Chem. Int. Ed. 54 (2015) 5317-5322.

[29] L. Xiang, W.J. Yang, Z. Yan, F.H. Meng, D. Chao, Z.Y. Zhong, Efficacious delivery of protein drugs to prostate cancer cells by PSMA-targeted pH-responsive chimaeric polymersomes, J. Controlled Release 220 (2015) 704-714.

[30] W.J. Yang, Y. F. Xia, Y. Zou, F.H. Meng, J. Zhang, Z.Y. Zhong, Bioresponsive chimaeric nano-polymersomes enable targeted and efficacious protein therapy for human lung cancers in vivo, Chem. Mater. 29 (2017) 8757-8765.

[31] X. Hu, J. Yu, C. Qian, Y. Lu, A.R. Kahkoska, Z. Xie, X. Jing, J.B. Buse, Z. Gu, H O -responsive vesicles integrated with transcutaneous patches for glucose-mediated insulin delivery, ACS Nano 11 (2017) 613-620.

[32] C. Martino, S.H. Kim, L. Horsfall, A. Abbaspourrad, S.J. Rosser, J. Cooper, D.A. Weitz, Protein expression, aggregation, and triggered release from polymersomes as artificial cell-like structures, Angew Chem. Int. Ed. 51 (2012) 6416-6420.

[33] H. Che, S. Cao, J.H. Van, Feedback-induced temporal control of "breathing" polymersomes to create self-adaptive nanoreactors, J. Am. Chem. Soc. 140 (2018) 5356-5359.

[34] G. Liu, X. Wang, J. Hu, G. Zhang, S. Liu, Self-immolative polymersomes for high efficiency triggered release and programmed enzymatic reactions, J. Am. Chem. Soc. 136 (2014) 7492-7497.

[35] S. Haas, N. Hain, M. Raoufi, S. Handschuh-Wang, T. Wang, X. Jiang, H. Schoenherr, Enzyme Degradable Polymersomes from Hyaluronic Acid-block-poly(epsilon-caprolactone) Copolymers for the Detection of Enzymes of Pathogenic Bacteria, Biomacromolecules 16 (2015) 832-841.

[36] A. Feng, J. Liang, J. Ji, J. Dou, S. Wang, J. Yuan, CO2-breathing and piercing polymersomes as tunable and reversible nanocarriers, Sci. Rep. 6 (2016) 23624.

[37] Y. Zou, Y.H. Wei, G.L. Wang, F.H. Meng, M.Y. Gao, G. Storm, Z.Y. Zhong, Nanopolymersomes with an Ultrahigh Iodine Content for High-Performance X-Ray Computed Tomography Imaging In Vivo, Adv. Mater. 29 (2017) 201603997.

[38] Z. Pang, L. Feng, R. Hua, J. Chen, H. Gao, S. Pan, X. Jiang, P. Zhang, Lactoferrin-conjugated biodegradable polymersome holding doxorubicin and tetrandrine for chemotherapy of glioma rats, Mol. Pharm 7 (2010) 1995-2005.

[39] X. Wang, H. Sun, F. Meng, R. Cheng, C. Deng, Z. Zhong, Galactose-decorated reduction-sensitive degradable chimaeric polymersomes as a multifunctional nanocarrier to efficiently chaperone apoptotic proteins into hepatoma cells, Biomacromolecules 14 (2013) 2873-2882.

[40] J. Chen, Q. Liu, J. Xiao, J. Du, EpCAM-Antibody-Labeled Noncytotoxic Polymer Vesicles for Cancer Stem Cells-Targeted Delivery of Anticancer Drug and siRNA, Biomacromolecules 16 (2015) 1695-1705.

[41] N. Kamaly, Z. Xiao, P.M. Valencia, A.F. Radovic-Moreno, O.C. Farokhzad, Targeted polymeric therapeutic nanoparticles: design, development and clinical translation, Chem. Soc. Rev. 41 (2012) 2971-3010.

[42] J.A. Kemp, M.S. Shim, C.Y. Heo, Y.J. Kwon, "Combo" nanomedicine: Co-delivery of multi-modal therapeutics for efficient, targeted, and safe cancer therapy, Adv. Drug Deliver. Rev. 98 (2016) 3-18.

[43] M. Srinivasarao, C.V. Galliford, P.S. Low, Principles in the design of ligand-targeted cancer therapeutics and imaging agents, Nat. Rev. Drug Discov. 14 (2015) 203-219.

[44] Y.-C. Chen, C.-F. Chiang, L.-F. Chen, S.-C. Liao, W. -Y. Hsieh, W.-L. Lin, Polymersomes conjugated with des-octanoyl ghrelin for the delivery of therapeutic and imaging agents into brain tissues, Biomaterials 35 (2014) 2051-2065.

[45] W.J. Yang, Y. Zou, F.H. Meng, J. Zhang, R. Cheng, C. Deng, Z.Y. Zhong, Efficient and targeted suppression of human lung tumor xenografts in mice with methotrexate sodium encapsulated in all-function-in-one chimaeric polymersomes Adv. Mater. 28 (2016) 8234-8239.

[46] Z. Gu, A. Biswas, M. Zhao, Y. Tang, Tailoring nanocarriers for intracellular protein delivery, Chem. Soc. Rev. 40 (2011) 3638-3655.

[47] A. ila, A. S nche , M. ob , P. Calvo, M.J. Alonso, Design of biodegradable particles for protein delivery, J. Controlled Release 78 (2002) 15-24.

[48] E. Kondo, K. Saito, Y. Tashiro, K. Kamide, S. Uno, T. Furuya, M. Mashita, K. Nakajima, T. Tsumuraya, N. Kobayashi, M. Nishibori, M. Tanimoto, M. Matsushita, Tumour lineage-homing cell-penetrating peptides as anticancer molecular delivery systems, Nat. Commun. 3 (2012) 951.

[49] W.J. Yang, Y. F. Xia, Y. Fang, F.H. Meng, J. Zhang, R. Cheng, C. Deng, Z.Y. Zhong, Selective cell penetrating peptide-functionalized polymersomes mediate efficient and targeted delivery of methotrexate disodium to human lung cancer in vivo, Adv. Healthc. Mater. 7 (2018) 1701135.

[50] H. Gao, Q. Zhang, Y. Yang, X. Jiang, Q. He, Tumor homing cell penetrating peptide decorated nanoparticles used for enhancing tumor targeting delivery and therapy, Int. J. Pharmaceut. 478 (2015) 240-250.

[51] R.L. Siegel, K.D. Miller, A. Jemal, Cancer statistics, 2017, CA-Cancer J. Clin. 67 (2017) 7-30.

[52] W. Chen, R. Zheng, P.D. Baade, S. Zhang, H. Zeng, F. Bray, A. Jemal, X.Q. Yu, J. He, Cancer statistics in China, 2015, CA-Cancer J. Clin. 66 (2016) 115-132.

[53] P.A. Janne, J.C. Yang, D.W. Kim, D. Planchard, Y. Ohe, S.S. Ramalingam, M.J. Ahn, S.W. Kim, W.C. Su, L. Horn, D. Haggstrom, E. Felip, J.H. Kim, P. Frewer, M. Cantarini, K.H. Brown, P.A. Dickinson, S. Ghiorghiu, M. Ranson, AZD9291 in EGFR inhibitor-resistant non-small-cell lung cancer, N. Engl. J. Med. 372 (2015) 1689-1699.

[54] J.L. Markman, A. Rekechenetskiy, E. Holler, J.Y. Ljubimova, Nanomedicine therapeutic approaches to overcome cancer drug resistance, Adv. Drug Deliver. Rev. 65 (2013) 1866-1879.

[55] J. Zhao, L.H. Zhang, L.T. Jia, L. Zhang, Y.M. Xu, Z. Wang, C.J. Yu, W.D. Peng, W.H. Wen, C.J. Wang, S.Y. Chen, A.G. Yang, Secreted antibody/granzyme B fusion protein stimulates selective killing of HER2-overexpressing tumor cells, J. Biol. Chem. 279 (2004) 21343-21348.

[56] K.A. Mohamedali, Y. Cao, L.H. Cheung, W.N. Hittelman, M.G. Rosenblum, The functionalized human serine protease granzyme B/VEGF121 targets tumor vasculature and ablates tumor growth, Mol. Cancer Ther. 12 (2013) 2055-2066.

[57] L. Lu, Y. Zou, W.J. Yang, F.H. Meng, C. Deng, R. Cheng, Z.Y. Zhong, Anisamide-Decorated pH-Sensitive Degradable Chimaeric Polymersomes Mediate Potent and Targeted Protein Delivery to Lung Cancer Cells, Biomacromolecules 16 (2015) 1726-1735.

[58] Y. Zou, M. Zheng, W.J. Yang, F.H. Meng, K. Miyata, H.J. Kim, K. Kataoka, Z.Y. Zhong, Virus-mimicking chimaeric polymersomes boost targeted cancer siRNA therapy in vivo, Adv. Mater. 29 (2017) 1703285.

[59] E. Blanco, H. Shen, M. Ferrari, Principles of nanoparticle design for overcoming biological barriers to drug delivery, Nat. Biotechnol. 33 (2015) 941-951.

[60] Y. Liu, W. Zhang, T. Niu, L.H. Cheung, A. Munshi, R.E. Meyn, M.G. Rosenblum, Targeted apoptosis activation with GrB/scFvMEL modulates melanoma growth, metastatic spread, chemosensitivity, and radiosensitivity, Neoplasia 8 (2006) 125-135.

## Supplementary Data

Table S1. Characteristics of copolymers.

| Entry | Copolymers | M_n (kg/mol) | | GPC[b] | |
		Design	^{1}H NMR[a]	M_n (kg/mol)	M_w/M_n
1	PEG-P(TMC-DTC)	5.0-(15.0-2.0)	5.0-(14.5-1.8)	31.3	1.1
2	PEG-P(TMC-DTC)-PEI	5.0-(15.0-2.0)-1.8	5.0-(14.5-1.8)-1.8	--	--
3	Mal-PEG-P(TMC-DTC)	7.5-(15.0-2.0)	7.5-(13.8-2.1)	32.5	1.2

[a] Calculated from ^{1}H NMR by comparing the intensities of signals at δ 3.51, 2.05 to 3.02, respectively.

[b] Polymers analyzed by GPC measurements using DMF as an eluent at a flow rate of 1.0 mL/min

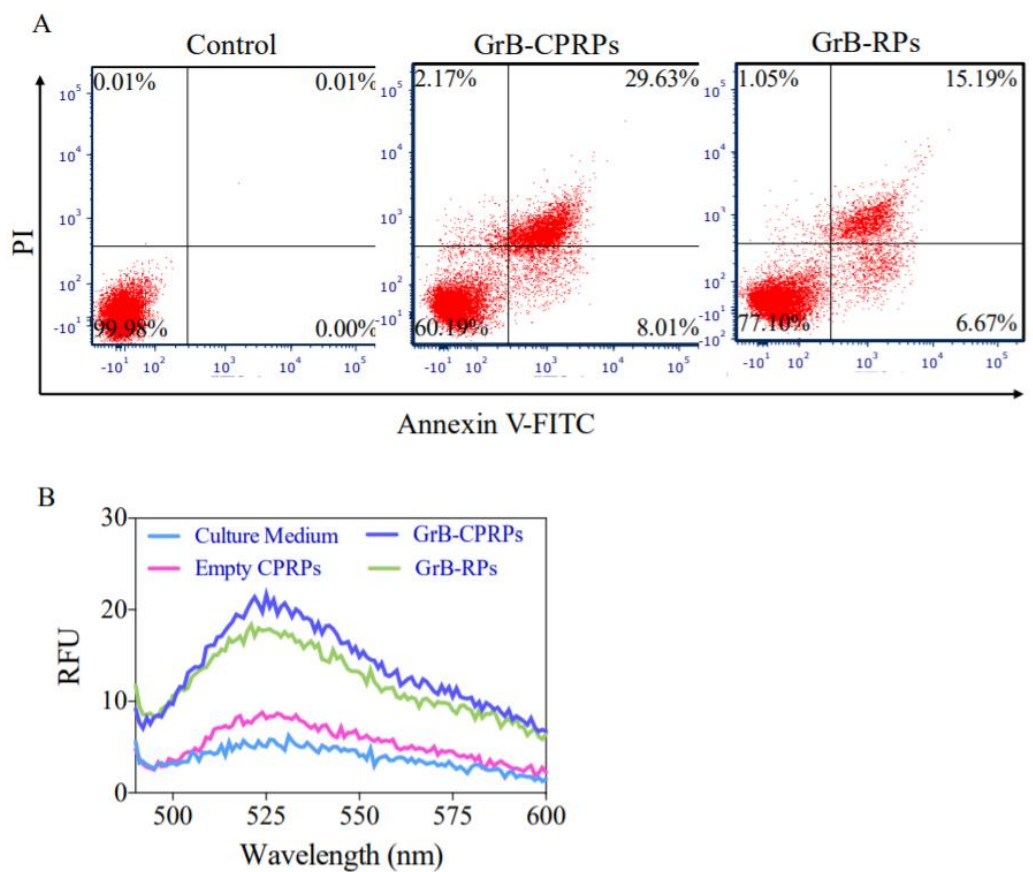(standards: polystyrene, 30 oC).
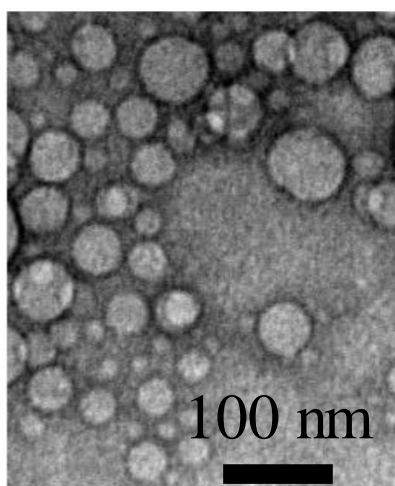

Figure S1. TEM micrograph of FITC-CC-CPRPs.
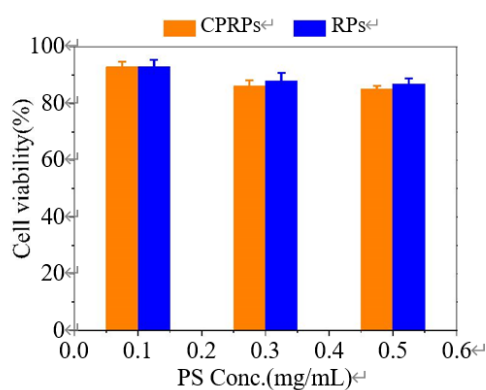
Figure S2. The viability of A549-luc cells following 48 h incubation with blank CPRPs and RPs.

Data are presented as the average ± SD (n = 4).

Figure S3. The proapoptotic activity of GrB-CPRPs. (A) Annexin V-FITC/PI apoptosis assays of A549 cells following 4 h treatment with GrB-CPRPs or GrB-RPs at 7.5 nM GrB and another 44 h culture in fresh medium. (B) The activation of caspase 3/7 in A549 cells following treatment with GrB-CPRPs, GrB-RPs or empty CPRPs using Apo-ONE homogeneous caspase3/7 assays.
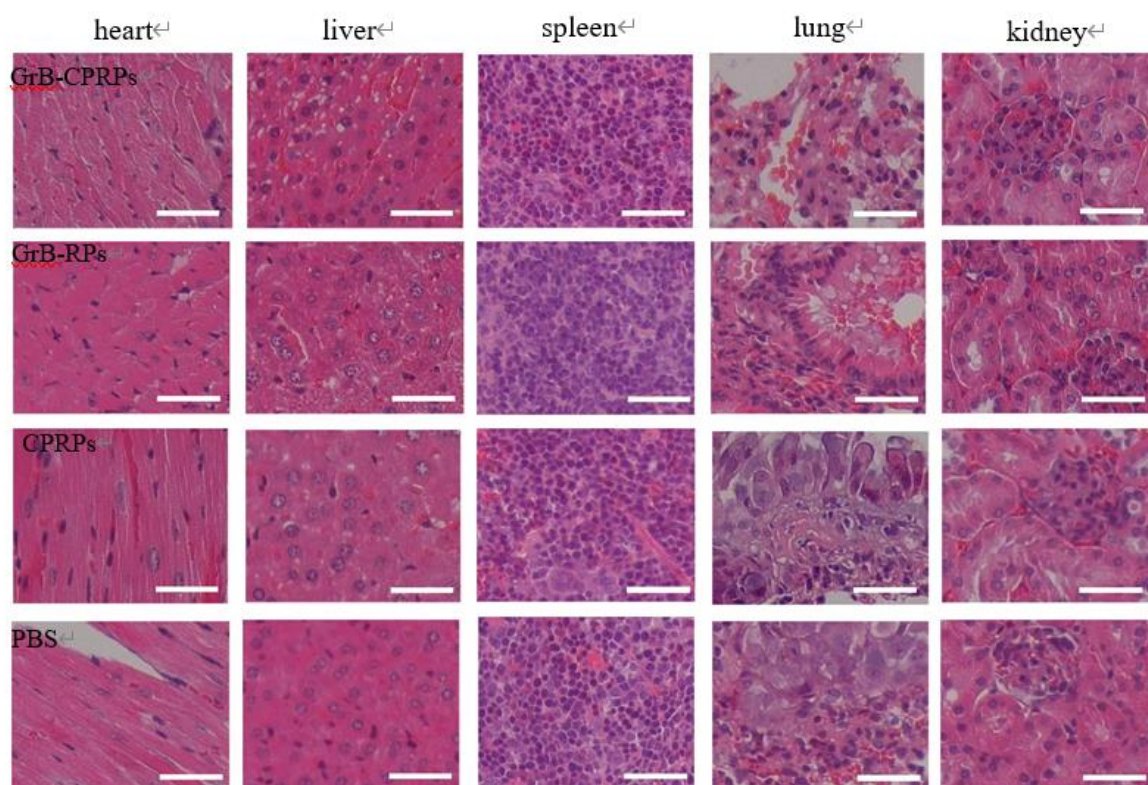
Figure S4. The histological analyses of H&E stained sections of tumor and major organs excised from A549 orthotopic tumor model nude mice on day 20. The images of tumor and major organs were obtained by a Leica microscope at magnification (400×). Scale bars: 100 μm.

Chapter 6

Nano-Polymersomes with an Ultrahigh Iodine Content for High-Performance X-Ray Computed Tomography Imaging *In Vivo**

Yan Zou[a], Yaohua Wei[a,c], Guanglin Wang[b], Fenghua Meng[a,*], Mingyuan Gao[b], Gert Storm[a,c] and Zhiyuan Zhong[a,*]

[a] Biomedical Polymers Laboratory, College of Chemistry, Chemical Engineering and Materials Science, Soochow University, Suzhou, 215123, P.R. China.

[b] Center for Molecular Imaging and Nuclear Medicine, School for Radiological and Interdisciplinary Sciences, Soochow University, Suzhou, 215123, P.R. China.

[c] Department of Targeted Therapeutics, MIRA Institute for Biological Technology and Technical Medicine, University of Twente, PO Box 217, 7500AE, Enschede, The Netherlands

Y. Zou and Y.H. Wei contributed equally.

X-Ray computed tomography (CT) owing to its high resolution, deep tissue penetration, low cost and wide availability has become one of the clinically most used non-invasive diagnostic tools[1]. To better visualize soft tissues and pathological regions, CT contrast agents based on iodinated small molecules (iohexol, iodixanol) are typically applied in the clinics[2]. It should be noted, however, that current iodinated small molecule contrast agents encounter several challenges such as swift blood clearance, high osmolality and viscosity, potential renal failure risk, and possible iodine hypersensitivity[3]. To this end, various nanoparticulate contrast agents in particular inorganic nanoparticles based on gold[4-7], bismuth[8-12], tungsten[13, 14], rare earth[15-17] and iodine-containing organic nanoparticles including nano-emulsions[18, 19], liposomes[20, 21], nanoparticulate[22, 23], nanogels[24], and dendritic polymers[25, 26] have recently been designed and explored for *in vivo* CT imaging. These nano-sized contrast agents showed significant improvements over iodinated small molecule contrast agents including prolonged blood-pool residence time, potential for targeted imaging application and cell tracking[27, 28]. However, in spite of their superior X-ray attenuation coefficient, clinical translation of inorganic CT contrast agents is challenged by their potential toxicity and high cost concerns.

Interestingly, a couple of iodine-containing organic nanoparticles like Fenstra[®] and ExiTronP[®] have been commercialized as small animal micro-CT contrast agents[29, 30]. The clinical application of nano-sized iodine contrast agents, however, remains formidable. Iodinated nano-emulsions, liposomes, micelles, nanogels and nanoparticles have typically a reduced iodine content as compared to clinical small molecule contrast agents, which requires a large dose and high concentration for *in vivo* CT imaging[31]. Iodinated dendrimers besides complex synthesis and high cost are challenged with high viscosity[32]. Importantly, potential nano-sized contrast agents shall also be nonfouling, biocompatible, biodegradable, and nontoxic.

Here, we have designed and developed biodegradable nano-polymersomes with an ultrahigh iodine content for high-performance CT imaging *in vivo* (**Figure 1a**). Notably, these novel radiopaque nano-polymersomes display excellent colloidal stability and biocompatibility, low viscosity, iso-osmolality, a small size of ca. 100 nm, as well as an unprecedented iodine content of 60.4 wt.%. We show that iodine-rich nano-polymersomes (IPs) can significantly enhance the *in vivo* imaging of blood pool, reticuloendothelial system (RES) and several malignant tumors as compared to iohexol, a clinically used iodinated small molecule.
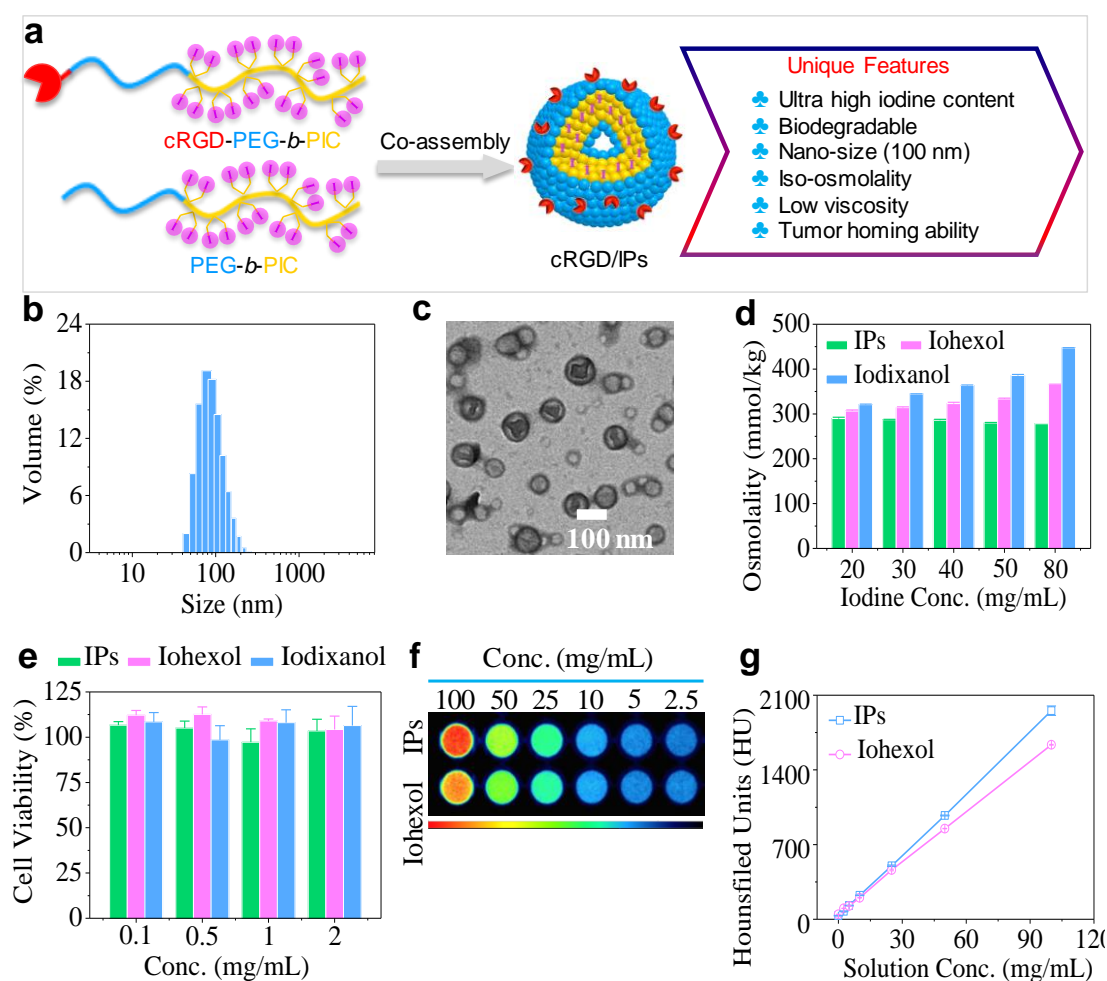
Figure 1. a) Self-assembled nano-structure of iodine-rich nano-polymersomes. b) Size distribution of IPs measured by DLS. c) Size and structure of IPs visualized by TEM. d) Osmolality of IPs, Iodixanol and Iohexol at varying concentrations. e) MTT assays of IPs, Iohexol and Iodixanol at varying concentrations in L929 cells following 48 h incubation (n=4). f) CT images of IPs and iohexol at varying concentrations. g) dependence of X-ray attenuation efficacy of IPs and iohexol on concentrations.

To obtain iodine-rich nano-polymersomes, we devised and prepared a new iodine-functionalized trimethylene carbonate (IC) monomer in two straight steps with an overall yield of 25% by Finkelstein reaction (**Scheme S1**, Supporting Information)[33]. The chemical structure of IC was verified by elemental analysis, ^{1}H- and ^{13}C-NMR (**Figure S1**, Supporting Information). The ring-opening polymerization of IC using MeO-PEG-OH (M_n = 5.0 kg/mol) and zinc bis[bis(trimethylsilyl) amide] at an [M]/[I] ratio of 130/1 yielded poly(ethylene glycol)-*b*-poly(iodine trimethylene carbonate) (PEG-*b*-PIC) with a controlled M_n of 5.0-49.4 kg/mol, as revealed by ^{1}H NMR (**Scheme S2 & Figure S2**, Supporting Information). Gel permeation chromatography displayed a unimodal distribution with a moderate M_w/M_n of 1.40, confirming successful synthesis of PEG-*b*-PIC. Interestingly, PEG-*b*-PIC had an ultra-high iodine content of 60.4 wt.%, which is significantly higher than iohexol (46.4 wt.%) and all reported iodinated nanoparticle platforms[20].

Remarkably, PEG-*b*-PIC diblock copolymer was readily self-assembled into stable nano-polymersomes. Dynamic light scattering (DLS) showed a small hydrodynamic size of ~ 100 nm with a low polydispersity index (PDI = 0.10) (**Figure 1b**). TEM image confirmed their small size and vesicle structure (**Figure 1c**). Notably, iodine-rich nano-polymersomes demonstrated superb stability over dilution and 10% serum (**Figure S3**, Supporting Information), likely due to their thick membrane and inherent PEG stealth[34, 35]. The stability of iodine conjugated with aliphatic chain is usually weaker than that conjugated with aromatic derivatives. However, unlike traditional small molecules, all iodine atoms in IPs are sequestered in the hydrophobic membrane of polymersomes, which would effectively protect iodine from leakage. To study their *in vitro* and *in vivo* stability, IPs were labeled with radioactive iodine (^{125}I) by iodine exchange reaction. The results (**Figure S4**, Supporting Information) confirmed little iodine leakage in both PBS and 10% FBS over 48 h. The *in vivo* SPECT/CT images (**Figure S5**, Supporting Information) showed that in sharp contrast to Na^{125}I

which mainly accumulated in the thyroid and bladder, ^{125}I-labeled IPs had a long circulation time and predominantly accumulated in the reticuloendothelial system (RES) like spleen and liver, further corroborating that IPs are stable in circulation and iodine leakage is negligible. Moreover, osmolality measurements revealed that IPs had an iso-osmotic pressure similar to PBS (10 mM, pH 7.4) over an iodine concentration range from 20 to 80 mg I/mL (**Figure 1d**). In contrast, commercial iodine contrast agents like iodixanol and iohexol clearly showed hyper-osmolality (366 and 447 mmol/kg at an iodine concentration of 80 mg/mL), which is a key factor for their systemic adverse effects[36]. The iso-osmolality of IPs makes them a unique CT contrast agent. Figure 1e shows that IPs were non-toxic to L929 mouse fibroblast cells at a high concentration of 2 mg/mL, indicating that they are non-cytotoxic.

To investigate their X-ray attenuation effects, we performed CT imaging of IPs dispersions over a broad range of concentrations. **Figure 1f**, g shows clearly that IPs dispersions resulted in obviously better signal enhancement than iohexol at the same concentration, as a result of their high iodine content. The attenuation coefficient of IPs was ca. 1.2-fold higher than iohexol. The ultra-high iodine content of IPs may significantly reduce their injection volume and concentration needed for *in vivo* imaging. The feasibility of IPs as a contrast agent was verified by *in vivo* CT imaging. IPs dispersion was intravenously administered at a dosage of 500 mg I/kg to C57BL/6 mice followed by CT imaging at different time intervals. The images observed a clear signal enhancement of both aorta and vena cava either from coronal section or transversal section (**Figure 2a**). The quantitative analysis indicated that the enhancement of aorta is 220 HU by the region of interest (ROI) and last for at least 80 mins (**Figure 2b**).

It is known that nanoparticles with size over 20 nm would be uptaken by RES[37, 38]. Hence, nano-contrast agent can be potentially used for RES imaging[39]. To verify this, IPs were intravenously injected into Balb/c mice and CT images were gained at 2, 4, 6, and 8 h after injection. Notably, greatly enhanced CT images were observed for both liver and spleen (**Figure 2c**). Up to 120 HU enhancement was found at liver till 8 h and 280 HU enhancement

at spleen (**Figure 2d**). The *in vivo* pharmacokinetics studies using Cy5-labled IPs confirmed that they have a prolonged circulation time with an elimination half-life of 2.5 h (**Figure S6**, Supporting Information). The long circulation time and tissue retention observed for IPs would not only facilitate scheduling of the imaging instrument in the clinical settings but also enable targeted imaging of tissues of interest.
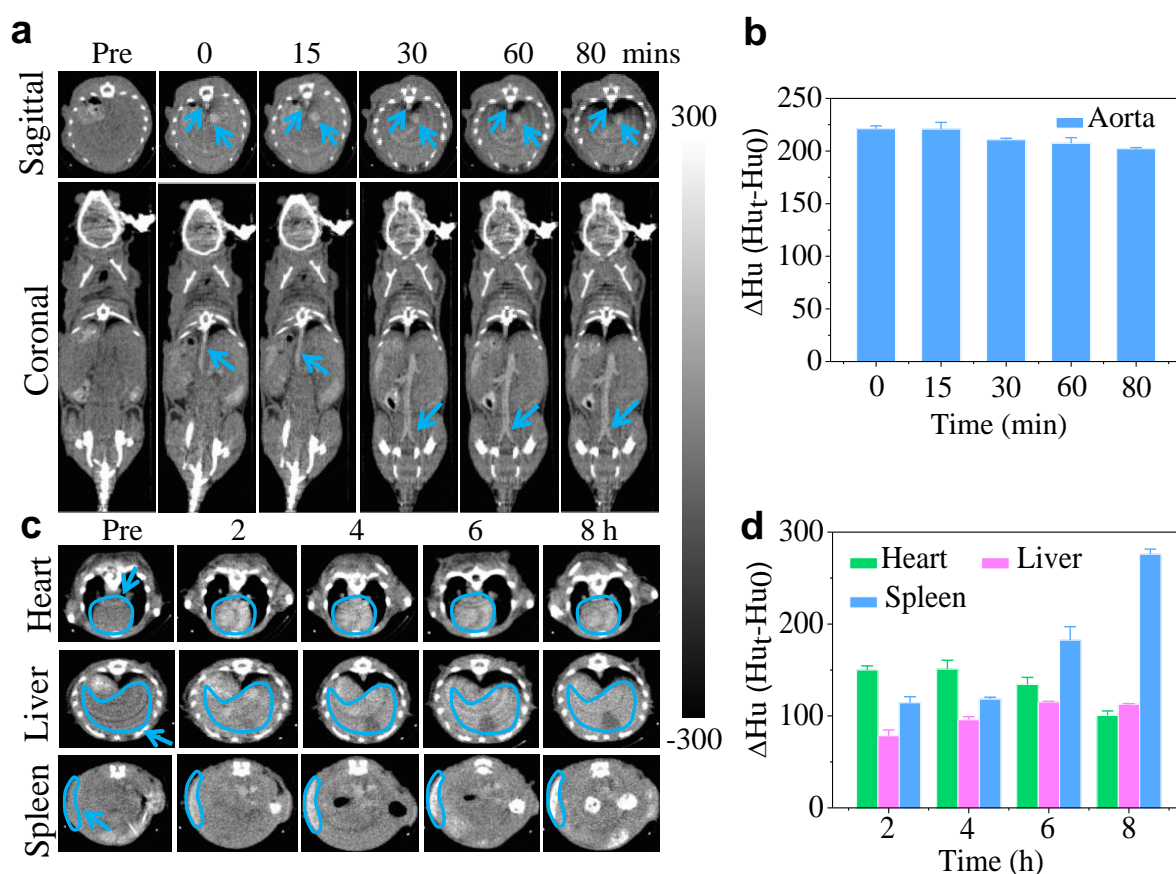

Figure 2. a) Sagittal and coronal sections and b) dynamic contrast enhanced density (ΔHu) of aorta of C57BL/6 mice after *i.v.* injection of IPs (500 mg I/kg). c) *In vivo* CT images and d) dynamic contrast enhanced density (ΔHu) of several major organs at C57BL/6 mice after *i.v.* injection of IPs at different time intervals.

To investigate whether these iodine-rich nano-polymersomes can be used for targeted CT imaging, we have decorated IPs with cRGDfK cyclic peptide (cRGD-IPs) and applied for *in vivo* imaging of several different tumor models. cRGD peptide is well known for its neovascular and $\alpha_v\beta_3$ integrin targeting ability[40-42]. cRGD-IPs were readily prepared from

cRGD-PEG-*b*-PIC and PEG-*b*-PIC (20/80, w/w). We have established $\alpha_v\beta_3$ integrin-overexpressing B16 melanoma xenografts as well as MCF-7 breast tumor with a low expression of $\alpha_v\beta_3$ integrins. **Figures 3a** and **3c** show that cRGD-IPs yielded sufficient contrast to provide good CT images of both tumors in mice at 6-8 h following *i.v.* injection, which was significantly better than the non-targeted IPs groups (**Figure S7**, Supporting Information). Notably, B16 melanoma at a small tumor volume of 50 mm^3 revealed a significant contrast enhancement of up to 90 HU (**Figure 3b**). The enhanced contrast of MCF-7 tumor is mainly attributed to neovasculature targeting. Remarkably, intratumoral injection of cRGD-IPs showed approximately 17-fold contrast enhancement of tumor after 4 h likely owing to the prolonged retention time of targeted IPs (**Figure 3d**). More interestingly, cRGD-IPs showed also clear contrast enhancement of the orthotopic A549 lung tumor after *i.v.* injection (**Figure 3e,f**). These results indicate that cRGD-IPs is highly promising as a tumor-homing CT contrast agent for early diagnosis of various malignancies.
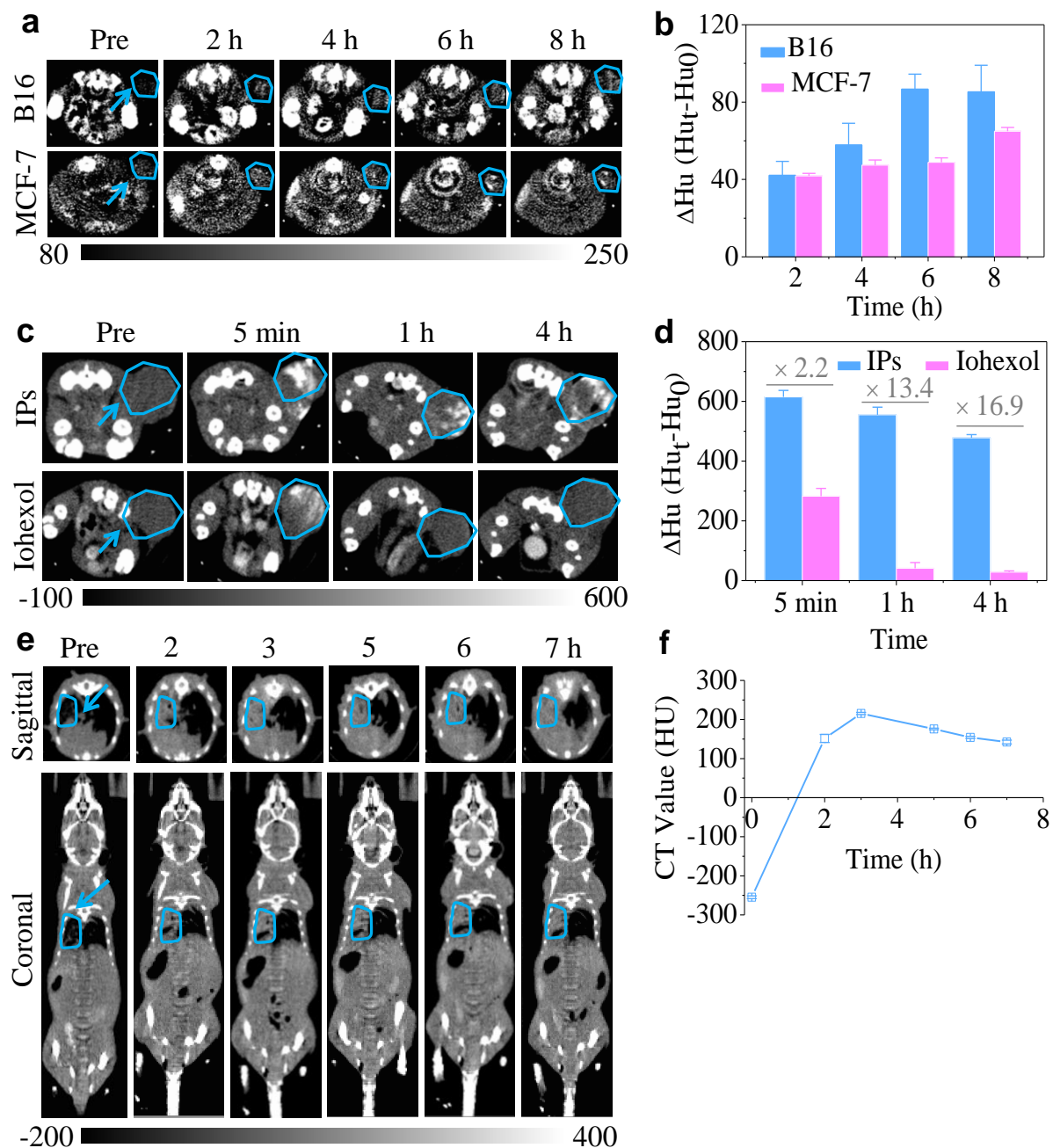
Figure 3. a) *In vivo* CT images and b) dynamic contrast enhanced density (ΔHu) of mice bearing subcutaneous B16 mouse melanoma or MCF-7 human breast tumor following intravenous injection of cRGD-IPs (500 mg I equiv./kg) at different time intervals. c) CT images and d) enhanced density (ΔHu) of B16 melanoma tumor bearing C57BL/6 mice following *i.t.* injection of 50 μL of IPs at 500 mg I/kg. Images were taken before injection as well as 5 mins, 1 h and 4 h post injection. e) CT images and f) dynamic contrast of A549 orthotopic mouse model after injection of cRGD-IPs (500 mg I equiv./kg) at different time intervals. For pictures a, c, e, blue circled areas indicate the enhanced contrast regions in the tumor bed.

Systematic toxicity is a big concern for the clinical translation of CT contrast agents[43, 44]. Here, we performed blood and histological analysis on Balb/c mice following *i.v.* injection of 500 mg I equiv./kg. Histological analyses displayed that IPs did not cause damage of healthy organs like heart, liver, spleen, lung, and kidney (**Figure S10A**, Supporting Information). Blood biochemistry studies indicated no obvious hepatic and kidney disorders. Blood routine examinations showed that IPs had little influence on the white blood cells, red blood cells, hemoglobin, and platelet (**Figure S10B**, Supporting Information). We further studied the biodegradability of PEG-*b*-PIC polymer. Notably, PEG-*b*-PIC films exhibited a fast weight loss and an eroded porous morphology in the presence of lipase (**Figures S8 and S9**, Supporting Information), confirming that PEG-*b*-PIC is prone to enzymatic degradation. IPs appear to be a safe CT contrast agent.

In summary, we have developed iodine-rich biodegradable nano-polymersomes as a novel high-performance contrast agent for CT imaging *in vivo*. These radiopaque nano-polymersomes have shown several unique features such as an ultra-high iodine content, a small size, excellent stability, iso-osmolality, low viscosity, and non-toxicity. The *in vivo* imaging demonstrates that they have a prolonged circulation time and can be used for blood pool as well as reticuloendothelial system imaging over a few hours. Furthermore, iodine-rich nano-polymersomes can readily be decorated with tumor homing peptides achieving early diagnosis of various malignancies. Iodine-rich nano-polymersomes have appeared as a superior contrast agent to commercial iodinated small molecules including Iohexol for CT imaging. It should further be noted that these nano-polymersomes can load different diagnostic and therapeutic agents, which renders them a truly multifunctional system for emerging multimodality imaging as well as nano-theranostics.

Supporting Information

Supporting Information is available from the Wiley Online Library or from the author.

References

[1] H. Lusic, M.W. Grinstaff, X-ray-computed tomography contrast agents, Chem. Rev. 113 (2013) 1641-1666.

[2] Y. Liu, K. Ai, L. Lu, Nanoparticulate X-ray computed tomography contrast agents: from design validation to in vivo applications, Accounts Chem. Res. 45 (2012) 1817-1827.

[3] N. Lee, S.H. Choi, T. Hyeon, Nano-sized CT contrast agents, Adv. Mater. 25 (2013) 2641-2660.

[4] R. Popovtzer, A. Agrawal, N.A. Kotov, A. Popovtzer, J. Balter, T.E. Carey, R. Kopelman, Targeted gold nanoparticles enable molecular CT imaging of cancer, Nano Lett. 8 (2008) 4593-4596.

[5] D. Kim, Y.Y. Jeong, S. Jon, A drug-loaded aptamer-gold nanoparticle bioconjugate for combined CT imaging and therapy of prostate cancer, ACS nano 4 (2010) 3689-3696.

[6] M. Chen, S. Tang, Z. Guo, X. Wang, S. Mo, X. Huang, G. Liu, N. Zheng, Core-shell Pd@ Au nanoplates as theranostic agents for in-vivo photoacoustic imaging, CT imaging, and photothermal therapy, Adv. Mater. 26 (2014) 8210-8216.

[7] H. Deng, F. Dai, G. Ma, X. Zhang, Theranostic gold nanomicelles made from biocompatible comb-like polymers for thermochemotherapy and multifunctional imaging with rapid clearance, Adv. Mater. 27 (2015) 3645-3653.

[8] O. Rabin, J.M. Perez, J. Grimm, G. Wojtkiewicz, R. Weissleder, An X-ray computed tomography imaging agent based on long-circulating bismuth sulphide nanoparticles, Nat. Mater. 5 (2006) 118-122.

[9] G. Song, C. Liang, H. Gong, M. Li, X. Zheng, L. Cheng, K. Yang, X. Jiang, Z. Liu, Core–shell MnSe@ Bi2Se3 fabricated via a cation exchange method as novel nanotheranostics for multimodal imaging and synergistic thermoradiotherapy, Adv. Mater. 27 (2015) 6110-6117.

[10] D. Pan, E. Roessl, J.P. Schlomka, S.D. Caruthers, A. Senpan, M.J. Scott, J.S. Allen, H. Zhang, G. Hu, P.J. Gaffney, Computed tomography in color: NanoK-enhanced spectral CT molecular imaging, Angew. Chem. Int. Ed. 49 (2010) 9635-9639.

[11] K. Ai, Y. Liu, J. Liu, Q. Yuan, Y. He, L. Lu, Large-scale synthesis of Bi2S3 nanodots as a contrast agent for in vivo X-ray computed tomography imaging, Adv. Mater. 23 (2011) 4886-4891.

[12] J.M. Kinsella, R.E. Jimenez, P.P. Karmali, A.M. Rush, V.R. Kotamraju, N.C. Gianneschi, E. Ruoslahti, D. Stupack, M.J. Sailor, X-ray computed tomography imaging of breast cancer by using targeted peptide-labeled bismuth sulfide nanoparticles, Angew. Chem. Int. Ed. 50 (2011) 12308-12311.

[13] L. Cheng, J. Liu, X. Gu, H. Gong, X. Shi, T. Liu, C. Wang, X. Wang, G. Liu, H. Xing, PEGylated WS2 nanosheets as a multifunctional theranostic agent for in vivo dual-modal CT/Photoacoustic imaging guided photothermal therapy, Adv. Mater. 26 (2014) 1886-1893.

[14] L. Wen, L. Chen, S. Zheng, J. Zeng, G. Duan, Y. Wang, G. Wang, Z. Chai, Z. Li, M. Gao, Ultrasmall biocompatible WO3-x nanodots for multi-modality imaging and combined therapy of cancers, Adv. Mater. (2016).

[15] Y. Liu, K. Ai, J. Liu, Q. Yuan, Y. He, L. Lu, A high-performance ytterbium-based nanoparticulate contrast agent for in vivo X-ray computed tomography imaging, Angew. Chem. Int. Ed. 51 (2012) 1437-1442.

[16] Y. Wu, Y. Sun, X. Zhu, Q. Liu, T. Cao, J. Peng, Y. Yang, W. Feng, F. Li, Lanthanide-based nanocrystals as dual-modal probes for SPECT and X-ray CT imaging, Biomaterials 35 (2014) 4699-4705.

[17] Z. Liu, K. Dong, J. Liu, X. Han, J. Ren, X. Qu, Anti-biofouling polymer-decorated lutetium-based nanoparticulate contrast agents for in vivo high-resolution trimodal imaging, Small 10 (2014) 2429-2438.

[18] X. Li, N. Anton, G. Zuber, M. Zhao, N. Messaddeq, F. Hallouard, H. Fessi, T.F. Vandamme, Iodinated α-tocopherol nano-emulsions as non-toxic contrast agents for preclinical X-ray imaging, Biomaterials 34 (2013) 481-491.

[19] M.F. Attia, N. Anton, M. Chiper, R. Akasov, H. Anton, N. Messaddeq, S. Fournel, A.S. Klymchenko, Y. Mély, T.F. Vandamme, Biodistribution of X-ray iodinated contrast agent in nano-emulsions is controlled by the chemical nature of the oily core, ACS Nano 8 (2014) 10537-10550.

[20] F. Hallouard, N. Anton, P. Choquet, A. Constantinesco, T. Vandamme, Iodinated blood pool contrast media for preclinical X-ray imaging applications-a review, Biomaterials 31 (2010) 6249-6268.

[21] X. Li, N. Anton, G. Zuber, T. Vandamme, Contrast agents for preclinical targeted X-ray imaging, Adv. Drug Deliv. Rev. 76 (2014) 116-133.

[22] E. Jin, Z.-R. Lu, Biodegradable iodinated polydisulfides as contrast agents for CT angiography, Biomaterials 35 (2014) 5822-5829.

[23] F. Hyafil, J.-C. Cornily, J.E. Feig, R. Gordon, E. Vucic, V. Amirbekian, E.A. Fisher, V. Fuster, L.J. Feldman, Z.A. Fayad, Noninvasive detection of macrophages using a nanoparticulate contrast agent for computed tomography, Nat. Med. 13 (2007) 636-641.

[24] Q. Yin, F.Y. Yap, L. Yin, L. Ma, Q. Zhou, L.W. Dobrucki, T.M. Fan, R.C. Gaba, J. Cheng, Poly (iohexol) nanoparticles as contrast agents for in vivo X-ray computed tomography imaging, J. Am. Chem. Soc. 135 (2013) 13620-13623.

[25] A.T. Yordanov, A.L. Lodder, E.K. Woller, M.J. Cloninger, N. Patronas, D. Milenic, M.W. Brechbiel, Novel iodinated dendritic nanoparticles for computed tomography (CT) imaging, Nano Lett. 2 (2002) 595-599.

[26] S. You, H.-y. Jung, C. Lee, Y.H. Choe, J.Y. Heo, G.-T. Gang, S.-K. Byun, W.K. Kim, C.-H. Lee, D.-E. Kim, High-performance dendritic contrast agents for X-ray computed tomography imaging using potent tetraiodobenzene derivatives, J. Control. Release 226 (2016) 258-267.

[27] P. Chhour, P.C. Naha, S.M. O'Neill, H.I. Litt, M.P. Reilly, V.A. Ferrari, D.P. Cormode, Labeling monocytes with gold nanoparticles to track their recruitment in atherosclerosis with computed tomography, Biomaterials 87 (2016) 93-103.

[28] R. Meir, K. Shamalov, O. Betzer, M. Motiei, M. Horovitz-Fried, R. Yehuda, A. Popovtzer, R. Popovtzer, C.J. Cohen, Nanomedicine for cancer immunotherapy: tracking cancer-specific T-cells in vivo with gold nanoparticles and CT imaging, ACS Nano 9 (2015) 6363-6372.

[29] N.R.B. Boase, I. Blakey, B.E. Rolfe, K. Mardon, K.J. Thurecht, Synthesis of a multimodal molecular imaging probe based on a hyperbranched polymer architecture, Polymer Chemistry 5 (2014) 4450-4458.

[30] A. de Vries, E. Custers, J. Lub, S. van den Bosch, K. Nicolay, H. Grüll, Block-copolymer-stabilized iodinated emulsions for use as CT contrast agents, Biomaterials 31 (2010) 6537-6544.

[31] H. Aviv, S. Bartling, F. Kieslling, S. Margel, Radiopaque iodinated copolymeric nanoparticles for X-ray imaging applications, Biomaterials 30 (2009) 5610-5616.

[32] Y. Fu, D.E. Nitecki, D. Maltby, G.H. Simon, K. Berejnoi, H.-J. Raatschen, B.M. Yeh, D.M. Shames, R.C. Brasch, Dendritic iodinated contrast agents with PEG-cores for CT imaging: synthesis and preliminary characterization, Bioconjugate Chem. 17 (2006) 1043-1056.

[33] L. Li, W. Liu, H. Zeng, X. Mu, G. Cosa, Z. Mi, C.-J. Li, Photo-induced Metal-Catalyst-Free Aromatic Finkelstein Reaction, J. Am. Chem. Soc. 137 (2015) 8328-8331.

[34] E. Mabrouk, D. Cuvelier, F. Brochard-Wyart, P. Nassoy, M.-H. Li, Bursting of sensitive polymersomes induced by curling, P. Natl. Acad. Sci. USA 106 (2009) 7294-7298.

[35] B.M. Discher, Y.-Y. Won, D.S. Ege, J.C.M. Lee, F.S. Bates, D.E. Discher, D.A. Hammer, Polymersomes: tough vesicles made from diblock copolymers, Science 284 (1999) 1143-1146.

[36] E. Seeliger, M. Sendeski, C.S. Rihal, P.B. Persson, Contrast-induced kidney injury: mechanisms, risk factors, and prevention, Eur. Heart J. 33 (2012) 2007-2015.

[37] D.E. Owens, N.A. Peppas, Opsonization, biodistribution, and pharmacokinetics of polymeric nanoparticles, Int. J. Pharm. 307 (2006) 93-102.

[38] J. Xie, C. Xu, N. Kohler, Y. Hou, S. Sun, Controlled PEGylation of monodisperse Fe_3O_4 nanoparticles for reduced non-specific uptake by macrophage cells, Adv. Mater. 19 (2007) 3163-3166.

[39] J. Huang, L. Bu, J. Xie, K. Chen, Z. Cheng, X. Li, X. Chen, Effects of nanoparticle size on cellular uptake and liver MRI with polyvinylpyrrolidone-coated iron oxide nanoparticles, ACS Nano 4 (2010) 7151-7160.

[40] Y.H. Kim, J. Jeon, S.H. Hong, W.K. Rhim, Y.S. Lee, H. Youn, J.K. Chung, M.C. Lee, D.S. Lee, K.W. Kang, Tumor targeting and imaging using cyclic RGD-PEGylated gold nanoparticle probes with directly conjugated iodine-125, Small 7 (2011) 2052-2060.

[41] Y. Miura, T. Takenaka, K. Toh, S. Wu, H. Nishihara, M.R. Kano, Y. Ino, T. Nomoto, Y. Matsumoto, H. Koyama, Cyclic RGD-linked polymeric micelles for targeted delivery of platinum anticancer drugs to glioblastoma through the blood–brain tumor barrier, ACS Nano 7 (2013) 8583-8592.

[42] N. Nasongkla, X. Shuai, H. Ai, B.D. Weinberg, J. Pink, D.A. Boothman, J. Gao, cRGD-functionalized polymer micelles for targeted doxorubicin delivery, Angew. Chem. Int. Ed. 116 (2004) 6483-6487.

[43] H. Maeda, H. Nakamura, J. Fang, The EPR effect for macromolecular drug delivery to solid tumors: Improvement of tumor uptake, lowering of systemic toxicity, and distinct tumor imaging in vivo, Adv. Drug Deliv. Rev. 65 (2013) 71-79.

[44] K. Peynshaert, B.B. Manshian, F. Joris, K. Braeckmans, S.C. De Smedt, J. Demeester, S.J. Soenen, Exploiting intrinsic nanoparticle toxicity: the pros and cons of nanoparticle-induced autophagy in biomedical research, Chem. Rev. 114 (2014) 7581-7609.
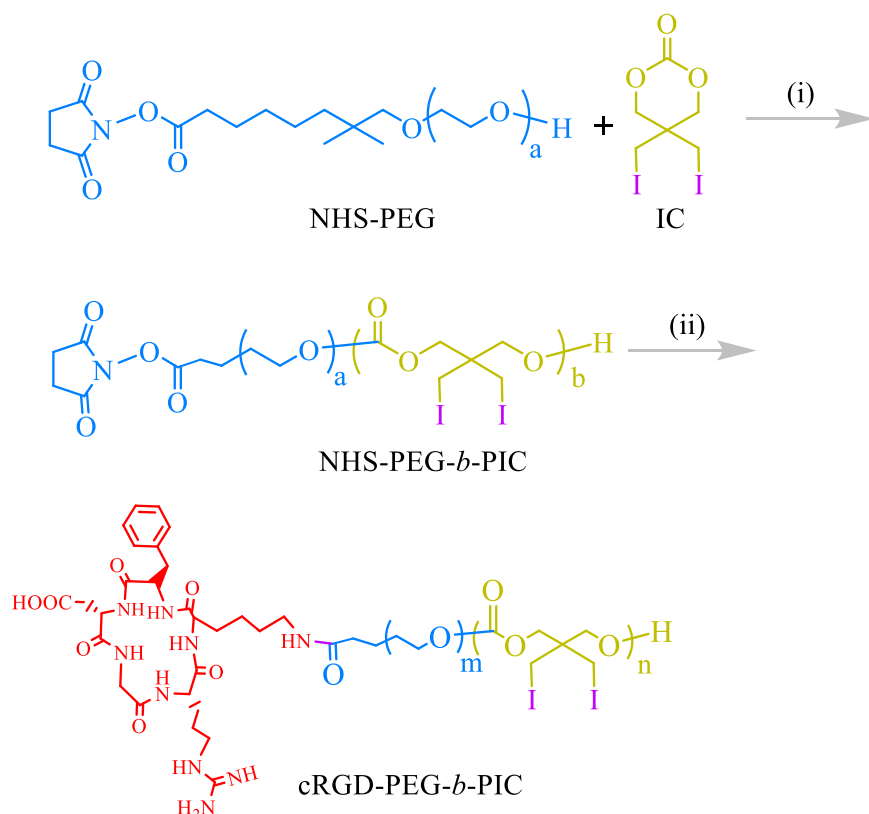
Supplementary Data
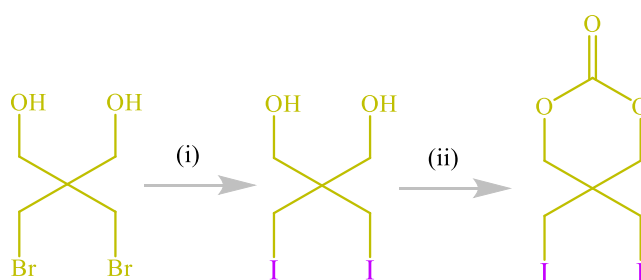
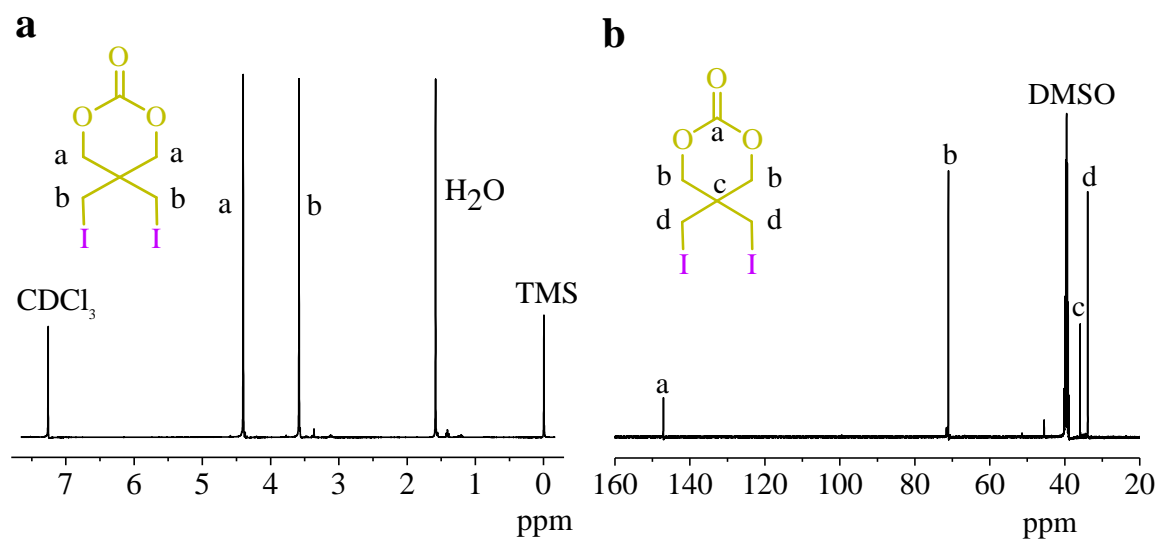**Scheme 1.** Synthesis of IC monomer. Conditions: (i) acetone, 55 °C, 24 h; (ii) THF, 0 °C, 4 h.
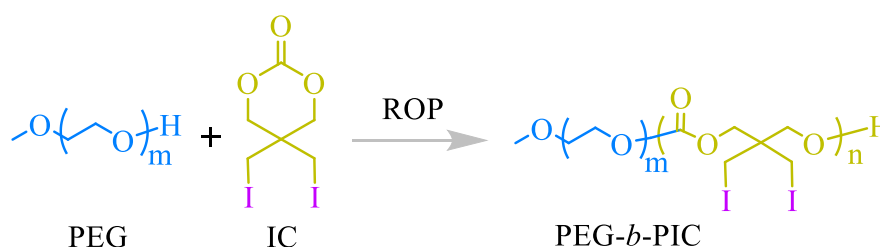
Scheme S2. Synthesis of PEG-*b*-PIC block polymer. Conditions: zinc bis[bis(trimethylsilyl) amide], CH$_2$Cl$_2$, 40 °C, 4 d.
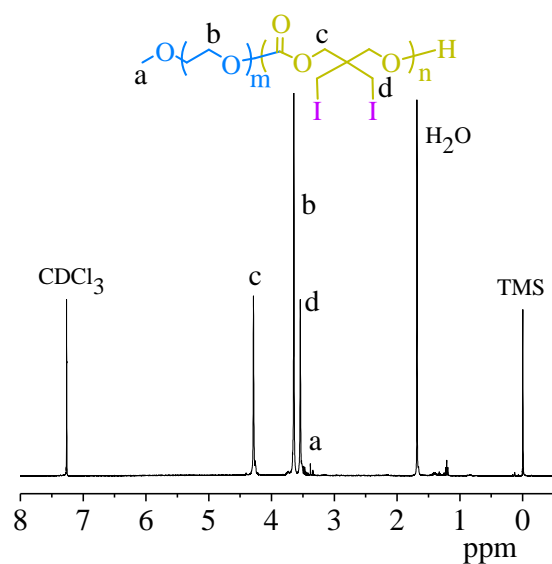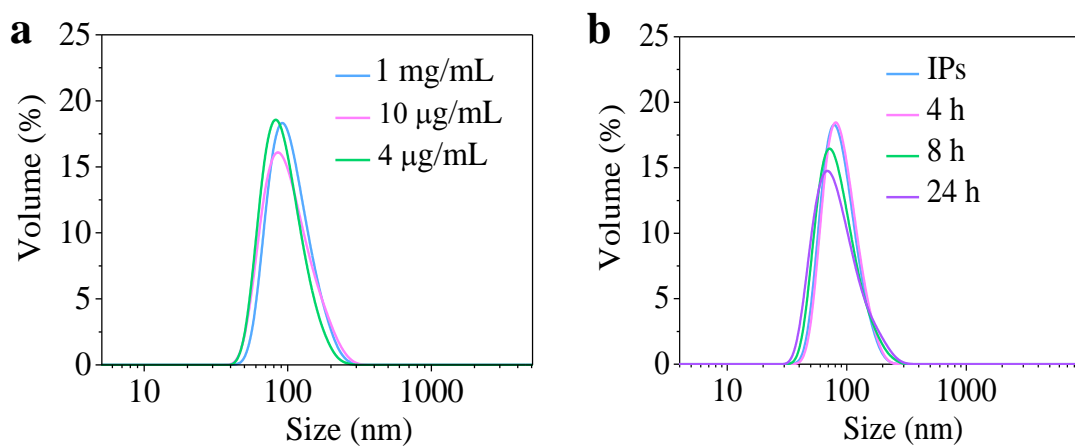
Scheme S3. Synthesis of cRGD-PEG-*b*-PIC. (i) zinc bis[bis(trimethylsilyl) amide], CH₂Cl₂, 40 °C, 4 d; (ii) c(RGDfK), r.t., 48 h.
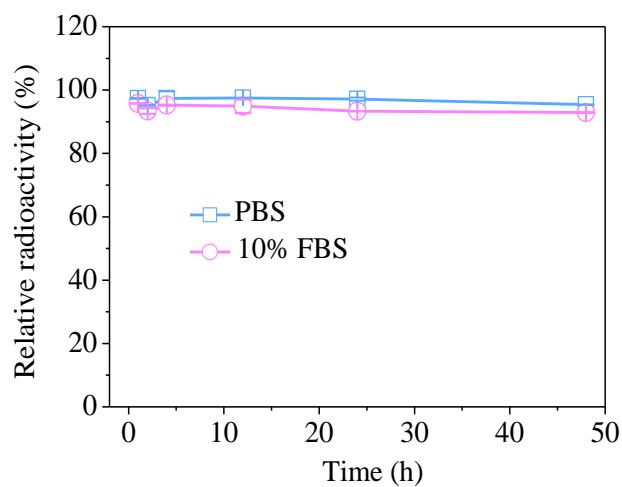

Figure S1. ^{1}H NMR (400 MHz,CDCl₃) (a) and ^{13}C NMR (100 MHz, DMSO-d_6) (b) of IC monomer.
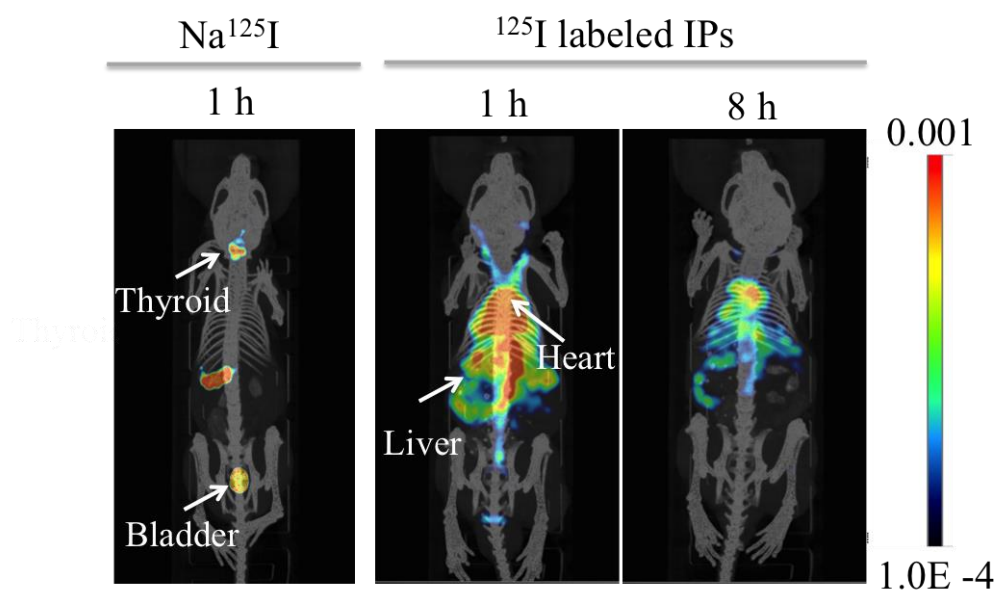
Figure S2. ^{1}H NMR (400 MHz, CDCl$_3$) of PEG-*b*-PIC.
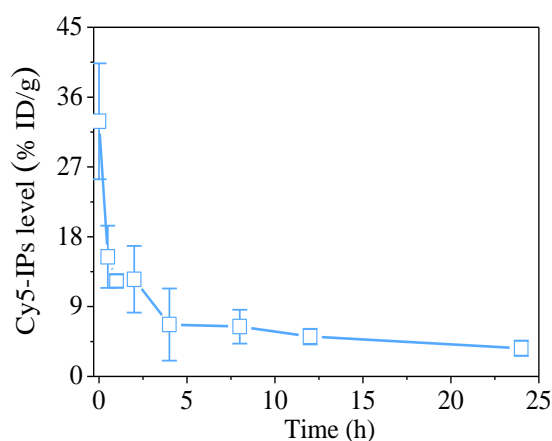

Figure S3. Colloidal stability of IPs against extensive dilution (a) and 10% FBS (b) determined by DLS.

Figure S4. Relative radioactivity of ^{125}I-labeled IPs following 48 h dialysis in PBS or 10% FBS.

Figure S5. SEPCT/CT images of mice following *i.v.* injection of ^{125}I-labeled IPs or Na^{125}I (control).

Figure S6. *In vivo* pharmacokinetics of Cy5-labeled IPs in the healthy Balb/c mice.
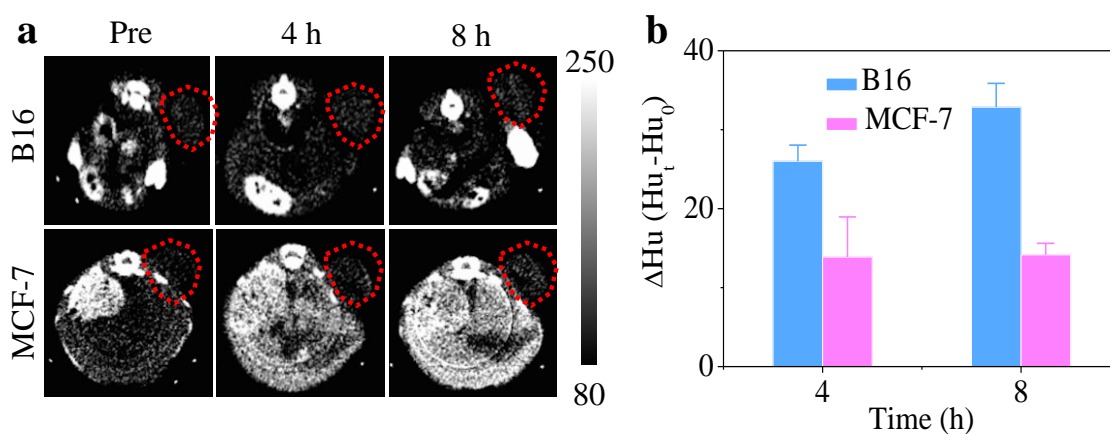
Figure S7. Dynamic contrast enhanced density (ΔHu) of different tumor models at 4 or 8 h post injection of IPs. Mice bearing MCF-7 human breast tumor or B16 mouse melanoma tumor were intravenously injected with 500 mg I equiv./kg of IPs.
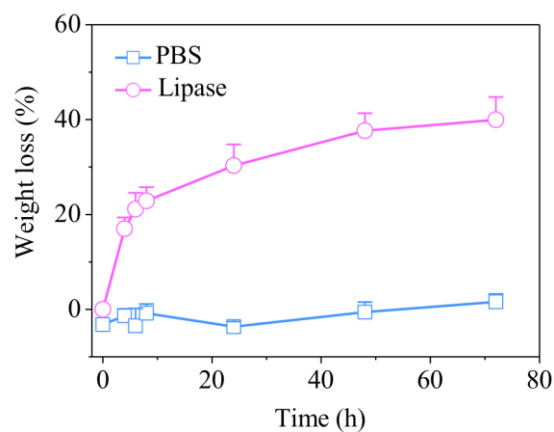
Figure S8. Weight loss percentage of PEG-PIC films as a function of degradation time in PBS with or without lipase (500 units/mL) at 37 °C. and 150 rpm.
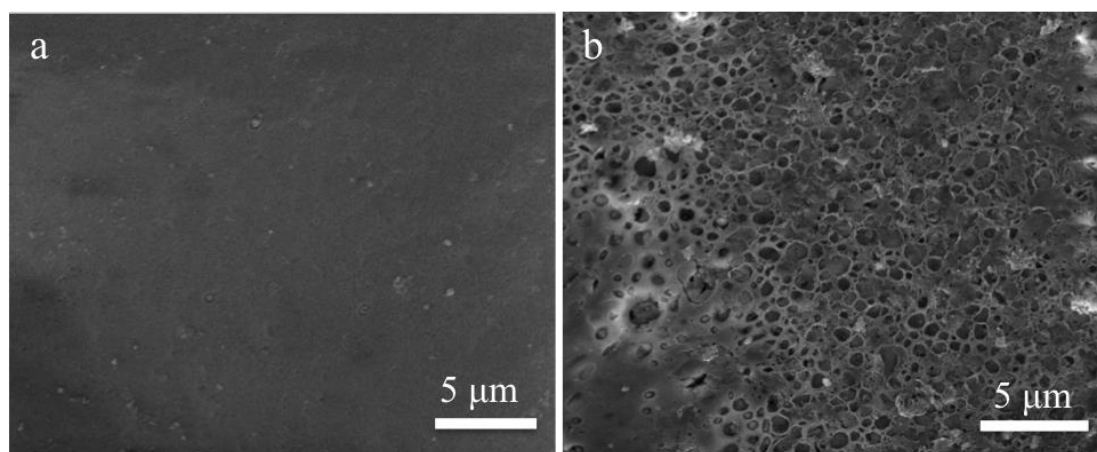
Figure S9. SEM micrographs of PEG-*b*-PIC films following 3 d incubation at 37 °C in PBS (a) and PBS containing lipase (500 units/mL) (b).
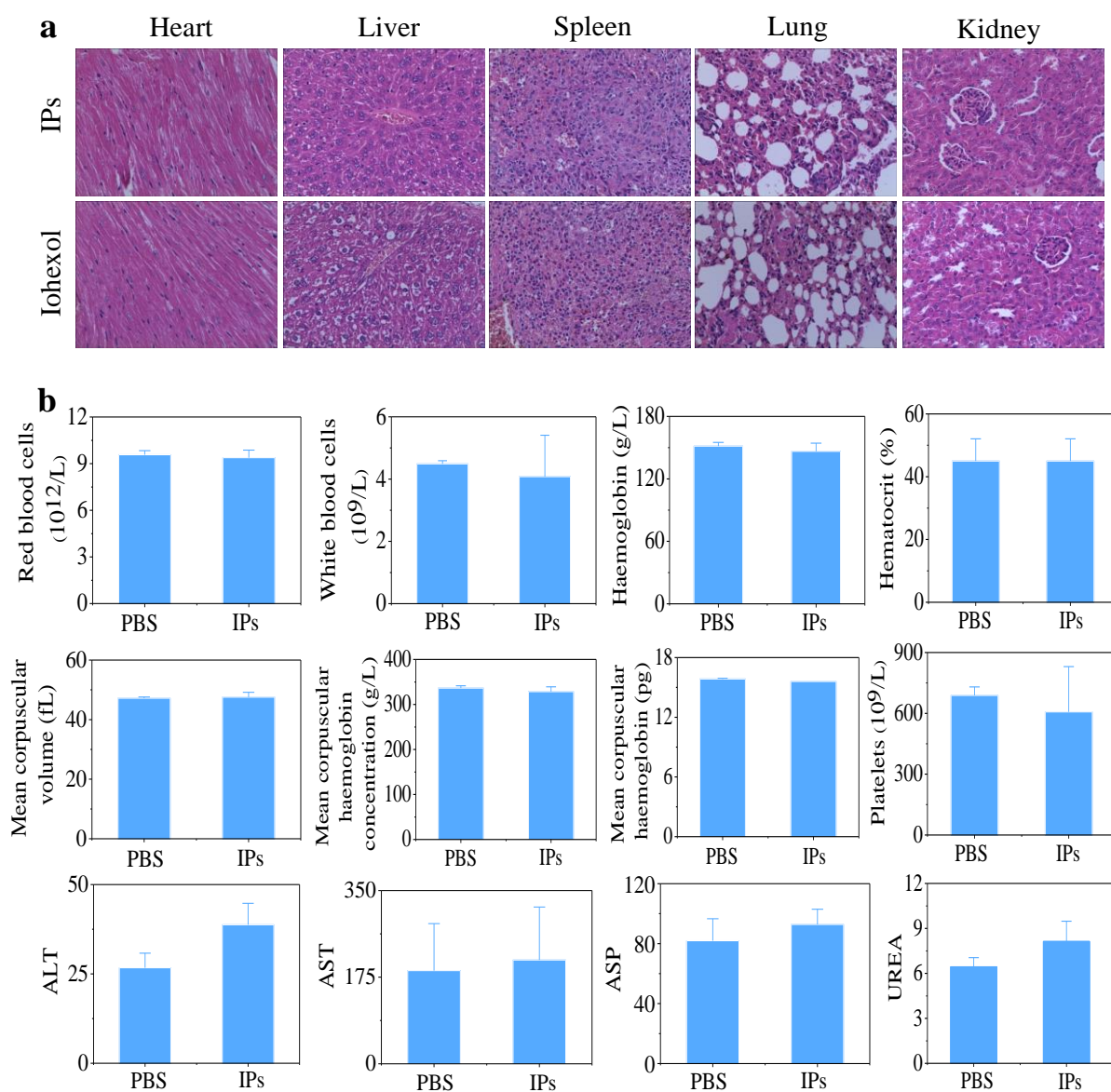
Figure S10. a) H&E stained heart, liver, spleen, lung, and kidney sections excised from Balb/c mice 2 d after *i.v.* injection of IPs (500 mg I equiv./kg). Mice treated with PBS were used as a control. The images of organs were obtained by microscope at 400X magnification. b) Blood analysis and blood biochemistry analysis of healthy Balb/c mice treated with IPs at a dose of 500 mg I equiv./kg at 24 h post injection. PBS treated healthy mice were used as a control.

Chapter 7

Cyclic RGD-Functionalized and Disulfide-Crosslinked Iodine-Rich Polymersomes as a Robust and Smart Theranostic Agent for Targeted CT Imaging and Chemotherapy of Tumor*

Yan Zou[a,b,#], Yaohua Wei[a,c,#], Yinping Sun[a], Jie Bao[d], Feirong Yao[d], Zekun Li[a], Fenghua Meng[a,*], Chunhong Hu[d], Gert Storm[c] and Zhiyuan Zhong[a,*]

[a] Biomedical Polymers Laboratory, and Jiangsu Key Laboratory of Advanced Functional Polymer Design and Application, College of Chemistry, Chemical Engineering and Materials Science, and State Key Laboratory of Radiation Medicine and Protection, Soochow University, Suzhou, 215123, P. R. China

[b] International Joint Centre for Biomedical Innovation, School of Life Sciences, Henan University, Jin Ming Avenue, Kaifeng, Henan, 475004, P. R. China

[c] Department of Targeted Therapeutics, MIRA Institute for Biological Technology and Technical Medicine, University of Twente, PO Box 217, 7500AE, Enschede, The Netherlands

[d] Imaging Center, the First Affiliated Hospital of Soochow University, Suzhou, Jiangsu, 215006, P.R. China

[#] These authors contributed equally to this work

Abstract

There is tremendous interest in integrating CT imaging with chemotherapy; however, reported iodine-based nanosystems such as nanogels and nano-emulsions display typically reduced contrast coefficient, low drug loading and stability, and poor targetability. Here, cRGD-functionalized disulfide-crosslinked iodine-rich polymersomes (cRGD-XIPs) were designed as a novel, robust and smart theranostic agent and investigated for targeted CT imaging and chemotherapy of malignant tumors.

Methods: cRGD-XIPs were prepared from co-self-assembly of poly(ethylene glycol)-*b*-poly(dithiolane trimethylene carbonate-*co*-iodinated trimethylene carbonate) (PEG-P(DTC-IC)) and cRGD-PEG-P(DTC-IC) block copolymers. *In vitro* and *in vivo* CT contrast effect of cRGD-XIPs was studied using $\alpha_v\beta_3$-overexpressing B16 melanoma as a tumor model in comparison with clinical agent iohexol. The therapeutic efficacy of doxorubicin-loaded cRGD-XIPs (cRGD-XIPs-Dox) to B16 melanoma was investigated and compared with XIPs-Dox (non-targeted), cRGD-IPs-Dox (non-crosslinked) and free Dox.

Results: cRGD-XIPs were formed with 55.5 wt.% iodine and ca. 90 nm in diameter. cRGD-XIPs-Dox with a Dox loading of 15.3 *wt.*% bared superior colloidal stability and reduction-responsive drug release. Notably, blank cRGD-XIPs showed a maximum-tolerated dose (MTD) > 400 mg iodine equiv./kg while cRGD-XIPs-Dox had an MTD > 150 mg Dox equiv./kg, ca. 15-fold improvement over free Dox. cRGD-XIPs revealed superior CT contrast effect and achieved 46.5- and 24.0-fold better enhancement of CT imaging of B16 melanoma than iohexol at 4 h following intratumoral and intravenous injection, respectively. cRGD-XIPs-Dox displayed an elimination half-life of 6.5 h and an elevated accumulation of 6.68% ID/g in the tumors. Furthermore, cRGD-XIPs-Dox was significantly more effective than XIPs-Dox and cRGD-XPs-Dox in inhibiting growth of B16 melanoma model.

Conclusion: This proof-of-concept study demonstrates that cRGD-XIPs are a robust,

non-toxic and smart polymeric theranostic agent that can not only significantly enhance CT imaging of tumors but also mediate efficient tumor-targeted chemotherapy. XIPs offer a unique and safe platform for theranostic polymersomes that pre-select patients using CT imaging prior to targeted chemotherapy with the same system.

Keywords: Targeted delivery, polymersomes, reduction-sensitive, solid tumor, CT imaging

Introduction

Theranostics that integrates diagnostics and therapy into a single system provides an emerging treatment modality for diseases like cancers [1-7]. X-ray computed tomography (CT) is a frequently applied clinical diagnostic tool [8-12]. To enhance CT imaging of soft tissues like tumors in patients, iodine-containing compounds such as iohexol, iodixanol and iopromide are typically used [13-15]. In the past years, great interest has put on the development of novel nano-CT contrast agents that are able to overcome the problems of small molecular contrast agents, such as fast elimination, high doses needed, low tumor selectivity, potential renal toxicity, and possible iodine hypersensitivity [16-18], to achieve dual and multi-modal imaging [19-21], and to combine CT with various therapies [22]. For example, inorganic nanoparticles based on gold [23, 24], copper chalcogenides [25], transition-metal dichalcogenides [26], rare earth [27], and iodinated organic nanosystems including liposomes [28], nanogels [29], nanoemulsions [30], nanoparticles [31], and dendritic polymers [32] have been investigated for simultaneous tumor CT imaging and therapy. These nanotheranostic systems demonstrate not only enhanced imaging but also potent anti-tumor efficacy. However, despite their excellent X-ray attenuation coefficient, the clinical translation of inorganic nanoparticles is limited by their safety and high cost concerns. While iodinated nanosystems typically possess inadequate CT contrast coefficients, mainly due to low iodine contents. In addition to complicated synthesis process, high viscosity of iodinated dendritic polymers stands as a critical shortcoming against their utilization. In our previous work, nanopolymersomes containing high iodine based on poly(ethylene glycol)-*b*-poly(iodinate trimethylene carbonate) (PEG-*b*-PIC) exhibited significant CT imaging enhancement of the blood pool and malignant tumors in contrast with iohexol [33]. Moreover, low *in vivo* stability and slow drug release inside tumor cells are additional problems for nano-CT contrast agents to be applied for therapeutic purposes. We and others

verified that disulfide crosslinked nanoparticles show superb *in vivo* stability and accelerated intracellular drug release [34-36].

Here, cyclic RGD directed, disulfide crosslinked iodine-rich polymersomes (cRGD-XIPs) were designed based on biodegradable poly(ethylene glycol)-*b*-poly(dithiolane trimethylene carbonate-*co*-iodinated trimethylene carbonate) copolymer (PEG-P(DTC-IC)) and cRGD-PEG-P(DTC-IC) for targeted CT imaging of an $\alpha_v\beta_3$-integrin positive B16 melanoma model (**Fig. 1**). We further examined the anti-tumor efficacy of doxorubicin-loaded cRGD-XIPs (cRGD-XIPs-Dox) in mice bearing B16 melanoma. cRGD has been extensively explored as an active targeting ligand to $\alpha_v\beta_3$ integrin over-expressing cancer cells including B16 cells [37-41]. It should be noted that even for the same type of tumor, different patients might have vastly different responses to targeted therapies, owing to the differences in tumor physical, pathological and biological properties. The screening of patients is thus of critical importance to targeted nanomedicines [42-44]. This study aimed to develop theranostic polymersomes that pre-select patients using CT imaging prior to targeted chemotherapy with the same system. Interestingly, these novel theranostic polymersomes exhibited small size (90 nm), high iodine content of 55.5 *wt.%*, iso-osmolality, high Dox loading content (15.3 *wt.%*), superior colloidal stability, and fast intracellular drug release. cRGD-XIPs could greatly improve the *in vivo* CT imaging via intratumoral or intravenous injection compared with iohexol. Moreover, cRGD-XIPs-Dox was far more potent in retarding the growth of B16 tumor than non-targeted XIPs-Dox and non-crosslinked cRGD-IPs-Dox controls.
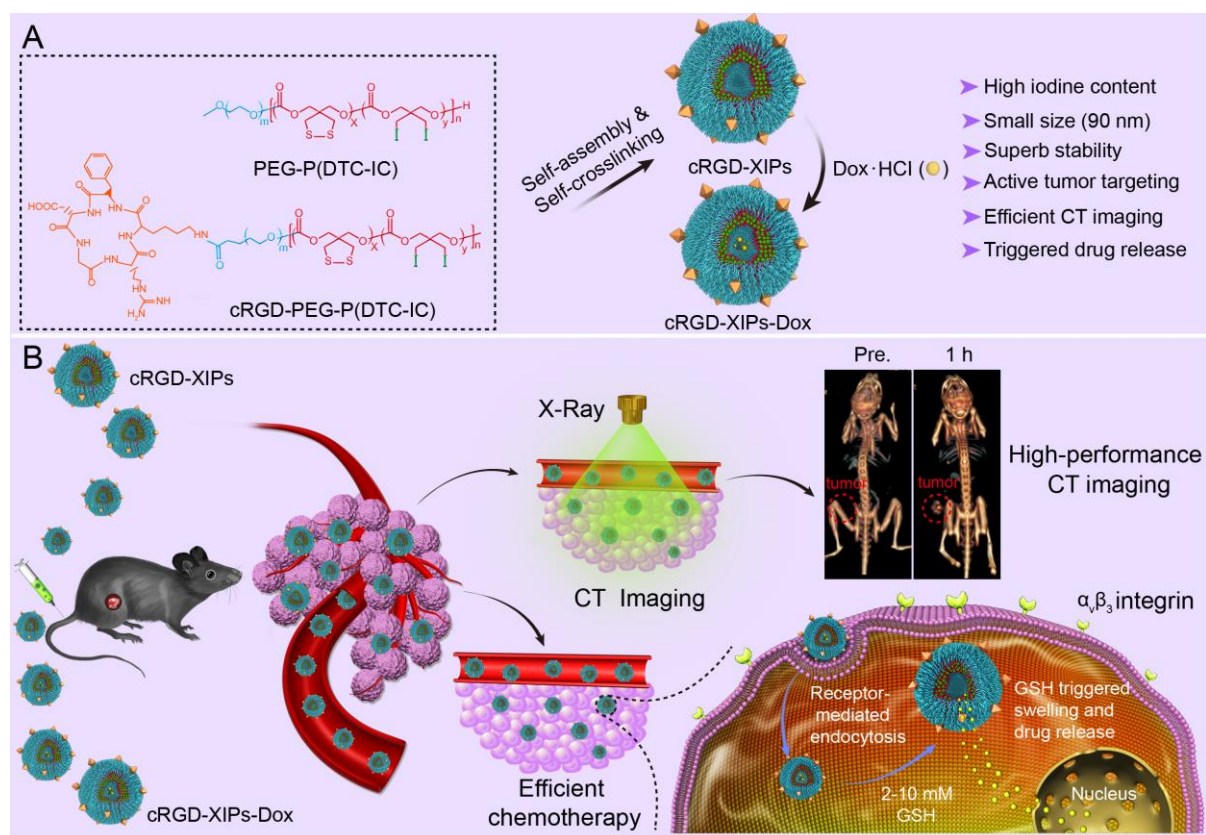
Figure 1. Illustration of the fabrication and properties of cRGD-functionalized disulfide-crosslinked iodine-rich polymersomes (cRGD-XIPs) and Dox-loaded cRGD-XIPs (cRGD-XIPs-Dox) (**A**), and cRGD-XIPs as robust nano-CT contrast agents for enhanced CT imaging of tumor and cRGD-XIPs-Dox as smart nanomedicines for targeted chemotherapy (**B**).

2. Materials and methods

2.1 Synthesis of PEG-P(DTC-IC) and cRGD-PEG-P(DTC-IC) block copolymers

Briefly, under a nitrogen atmosphere, MeO-PEG-OH (M_n 5.0 kg/mol, 0.1 g, 20 μmol), DTC (0.1 g, 0.52 mmol), IC (1.0 g, 2.62 mmol) and DCM (5.0 mL) was charged into a schlenk bottle and stirred to dissolve using a magnetic stirrer. To the solution, zinc bis[bis(trimethylsilyl)amide] (29 mg, 75 μmol) was quickly added. The ring opening polymerization (ROP) proceeded at 40 °C for 48 h before termination, and the resulting

copolymer was precipitated in cold diethyl ether, filtrated and dried in vacuo for 24 h. Yield: 84.2%. Similarly, NHS-PEG-P(DTC-IC) was synthesized using NHS-PEG (M_n = 6.5 kg/mol) as an initiator. Yield: 82.1%. Then, cyclic cRGDfK (16 mg, 2.62 mmol) was conjugated to NHS-PEG-P(DTC-IC) (0.5 g, 1.31 mmol) yielding cRGD-PEG-P(DTC-IC) similarly as reported [40]. Yield: 85.6%. The degree of cRGD conjugation was 92% as determined by micro BCA protein assays. Briefly, 10 μL DMF solution of cRGD-PEG-P(DTC-IC) (10 mg/mL) was diluted to 0.1 mg/mL in water. A 20 μL aliquot was added into a 96-well plate and mixed with 100 μL of working reagent of micro BCA (Reagent A and B = 50/1). The plate was mixed well and kept at 37 °C for 60 min and measured the absorbance at 570 nm using a microplate reader. The absorbance of Mal-PEG-P(DTC-IC) solution prepared similarly was subtracted. The cRGD conjugation was calculated from the standard curve of cRGD peptide of known concentrations.

2.2 Preparation of cRGD-XIPs and cRGD-XIPs-Dox

Typically, 900 μL of phosphate buffer (PB, 10 mM, pH 7.4) was added dropwise to 100 μL DMF solution (10.0 mg/mL) of PEG-P(DTC-IC) and cRGD-PEG-P(DTC-IC) (4/1, w/w) under stirring. After 20 min, the mixture was dialyzed against PB for 12 h (Spectra/Pore, MWCO 7000), placed in a shaking-bed at 37 °C for 24 h yielding self-crosslinked polymersomes cRGD-XIPs. The colloidal stability at low concentration (50 mg/L) and in the presence of 10% serum or 10 mM GSH was investigated using DLS.

cRGD-XIPs-Dox was fabricated by loading Dox into preformed cRGD-XIPs via a pH-gradient method. Briefly, 2.7 mL citrate buffer (10 mM, pH 4.0) was dropwise adding into 0.3 mL DMF solution of PEG-P(DTC-IC) and cRGD-PEG-P(DTC-IC) (10 mg/mL).

After stirring for 15 min, the pH was adjusted to 8.0 with disodium hydrogen phosphate (4 M). Then, 60, 120, or 180 µL Dox·HCl solution (5 mg/mL), corresponding theoretical DLC of 9.7, 16.7, or 23.1 wt.%, respectively) was added and stirred at 37 °C for 5 h in dark. cRGD-IPs-Dox was obtained via dialysis procedure similar as above. Dox loading content (DLC) and loading efficiency (DLE) was quantified using fluorescence (Agilent Cary Eclipse) measurement (ex. 480 nm and em. 560 nm) [40, 45] using the following formula:

DLC (wt.%) = weight of loaded drug/total weight of polymer and loaded drug) × 100

DLE (%) = (weight of loaded drug/weight of drug in feed) × 100

2.3 In vivo pharmacokinetics and biodistribution

The mice were handled under protocols approved by Soochow University Laboratory Animal Center and the Animal Care and Use Committee of Soochow University. cRGD-XIPs-Dox, XIPs-Dox, cRGD-IPs-Dox and free Dox (10 mg Dox/kg) in PBS were injected into C57BL/6 mice (18-20 g) via the tail veins (n = 3), and ca. ~50 µL blood was taken from the eye socket of the mice at prescribed time post injection. The blood samples upon withdrawing were mixed with 100 µL Triton X-100 solution (1%) with brief sonication. 500 µL DMF (containing 20 mM DTT) was introduced to extract Dox. The samples were stored at -20 °C overnight, centrifuged, and Dox in the supernatant was determined by fluorometry based on a calibration curve of Dox solution of known concentrations (supporting information). Dox expressed as percent injected dose per gram (%ID/g) was plotted as a function of time. The half-lives of two phases ($t_{1/2,\alpha}$ and $t_{1/2,\beta}$) and area under the curve (AUC) were derived using Origin 8.

For biodistribution studies in female C57BL/6 mice (18-20 g), 50 µL of B16 cells (1 × 10^6) were subcutaneously injected in the right hind flank. When the tumors grew to *ca.* 200 mm^3 after around 10 days, cRGD-XIPs-Dox, XIPs-Dox and free Dox (10 mg Dox/kg, 200 µL)

was intravenously (*iv*) injected via tail veins (n = 3). After 4 h, the tumors and major organs were excised, washed, weighed, and homogenized in 500 μL Triton X-100 (1%). Subsequently, 1 mL DMF (containing 20 mM DTT) was added to extract Dox, and the samples were treated as above based on calibration curves of Dox of known concentrations in different tissue individually (supporting information).

2.4 Maximum-tolerated dose (MTD) determination

The healthy C57BL/6 mice were randomly divided into 6 groups (n = 3) and a single dose of cRGD-XIPs (300 or 400 mg I equiv./kg), cRGD-XIPs-Dox (100 or 150 Dox/kg), or free Dox (5 or 10 mg Dox/kg) were *iv* injected. Body weight, behavior and survival of mice were examined for 10 days. MTD was defined as the dose that causes neither mouse death due to the toxicity, nor >15% of body weight loss, nor other remarkable changes in the general appearance within 10 days.

2.5 CT imaging of mice with intratumoral (it) and intravenous (iv) injection of cRGD-XIPs

B16 tumor-bearing C57BL/6 mice were used as a $\alpha_v\beta_3$ integrin over-expressing tumor model to evaluate the targeted CT contrast enhancement of tumors in vivo. The mice were randomly divided into two groups (n = 3), and treated with cRGD-XIPs and iohexol at 350 mg I equiv./kg (50 μL) via *it* injection. Before and 5 min, 1 h and 4 h after *it* injection, the CT scan was carried out using a GE discovery CT750 HD (GE Healthcare, WI) setting parameters as follows: beam collimation = 64 ×0.625 mm; table speed = 27 mm per rotation; beam pitch = 1.25; gantry rotation time = 1.0 s.

The tumor bearing mice were also *iv* injected with cRGD-XIPs, XIPs or iohexol (350 mg I equiv./kg) in 200 μL PB. The CT images were obtained before and 40 min, 2 h, 4 h and 6 h post *iv* injection as described above.

2.6 In vivo antitumor efficacy of cRGD-XIPs-Dox

The female B16 tumor-bearing mice (tumor volume: 50-100 mm^3) were randomly

divided into six groups (n = 5): cRGD-XIPs-Dox (5 or 10 mg Dox/kg), XIPs-Dox (10 mg Dox/kg), cRGD-IPs-Dox (10 mg Dox/kg), free Dox (5 or 10 mg Dox/kg), and PBS. The formulations were *iv* injected every 2 days. The first day of the injection was labeled as day 0. The tumor size was measured every two days and the volume was calculated according to the formula $V = 0.5 \times L \times W^2$, wherein L and W are the tumor dimension at the longest and widest point, respectively. Mice were weighed and normalized to the initial weights. On day 10, the tumors were excised, weighed and photographed. Heart, liver, spleen, lung and kidney were sliced and prepared for H&E and then observed with a digital microscope (Leica QWin, Germany). The tumor inhibition rate (TIR) was calculated:

TIR (%) = (1− tumor weight of treatment group/ tumor weight of PBS group) ×100.

2.7 Statistics

All data are presented as the mean ± standard deviation (SD). One-way analysis of variance (ANOVA) was used to determine significance among groups, after which post-hoc tests with the Bonferroni correction were used for comparison between individual groups. Statistical significance was established at $*p < 0.05$, $**p < 0.01$ and $***p < 0.001$.

3. Results and discussion

3.1 Fabrication of cRGD-XIPs and cRGD-XIPs-Dox

cRGD-XIPs were co-self-assembled from PEG-P(DTC-IC) and cRGD-PEG-P(DTC-IC). The ROP of IC and DTC monomers using MeO-PEG-OH (M_n = 5.0 kg/mol) as a macro-initiator afforded PEG-P(DTC-IC) (**Fig. S1**), similar to our previous report [33]. ^{1}H NMR analyses (**Fig. S2**) revealed that the P(DTC-IC) block had an M_n of 52.9 kg/mol and DTC/IC weight ratio of 8.7/91.3 (**Table S1**). GPC measurement revealed that the molecular weight distribution of PEG-P(DTC-IC) was unimodal (M_w/M_n = 1.31), and M_n was 63.2 kg/mol, close to that determined by ^{1}H NMR (57.9 kg/mol) and the theoretical value (60.0

kg/mol) (**Table S1**), endorsing controlled synthesis of PEG-P(DTC-IC). Likewise, NHS-PEG-P(DTC-IC) was obtained with similar P(DTC-IC) block molecular weight (M_n = 53.9 kg/mol) and composition (DTC/IC = 8.7/91.3, w/w) by copolymerization of DTC and IC initiated by NHS-PEG-OH (M_n = 6.5 kg/mol) (**Fig. S3**). The conjugation of cRGDfK to NHS-PEG-P(DTC-IC) by carbodiimide chemistry yielded cRGD-PEG-P(DTC-IC). Micro BCA protein assay results showed a cRGD functionality of 92% (**Fig. S4**). Notably, the molecular weight of PEG in cRGD-PEG-P(DTC-IC) was longer than that in PEG-P(DTC-IC) (6.5 *vs.* 5.0 kg/mol) to achieve better exposure of cRGD for optimal targeting. Differential scanning calorimetry (DSC) measurements confirmed the amorphous structure of PEG-P(DTC-IC) and cRGD-PEG-P(DTC-IC) with glass transition temperatures (T_g) of -25.3 and -21.5 °C, respectively (**Table S1**), indicating that they are rubbery and flexible at body temperature.

The co-self-assembly of PEG-P(DTC-IC) and cRGD-PEG-P(DTC-IC) (w/w, 8/2) in water yielded cRGD-XIPs of ca. 90 nm in diameter and a size distribution (PDI) of 0.10 (**Fig. 2A**) via a solvent exchange method. The addition of PB into a DMF solution of amphiphilic block copolymers increased the interfacial tension between P(DTC-IC) segment and water, rendering P(DTC-IC) segment insoluble thus triggering copolymer self-assembly into polymersomes. A cRGD density of 20% in polymersomes was investigated as nanoparticles of this density displayed the best targetability [36, 38]. TEM micrograph verified a spherical hollow structure (**Fig. 2B**). UV-Vis measurements displayed that the characteristic absorbance of dithiolane ring at 320 nm disappeared after polymersome work-up procedure (**Fig. S5**), revealing the spontaneous dithiolanes crosslinking in the polymersome membrane. As a result, no critical aggregation concentration (CAC) could be detected. Interestingly, cRGD-XIPs displayed excellent colloidal stability during two-month storage at room temperature and against dilution or in the presence of 10% serum for 48 h (**Fig. S6**), due to the spontaneous

disulfide-crosslinking of the membrane as reported for other DTC-containing polymersomes [35, 40]. Accordingly, cRGD-XIPs could undergo fast destabilization in 10 mM GSH as determined by both DLS and TEM measurements (**Fig. S7**), owing to disulfide cleavage and de-crosslinking. Notably, cRGD-XIPs exhibited an iso-osmotic pressure of 280 mmol kg^{-1} at iodine contents ranging from 20 to 80 mg I/mL (**Fig. 2C**), while the osmolality of iohexol increased with concentration, reaching 366 mmol kg^{-1} at 80 mg I/mL. XIPs self-assembled from PEG-P(DTC-IC) only displayed almost the same biophysical properties and were used as a non-targeted control.
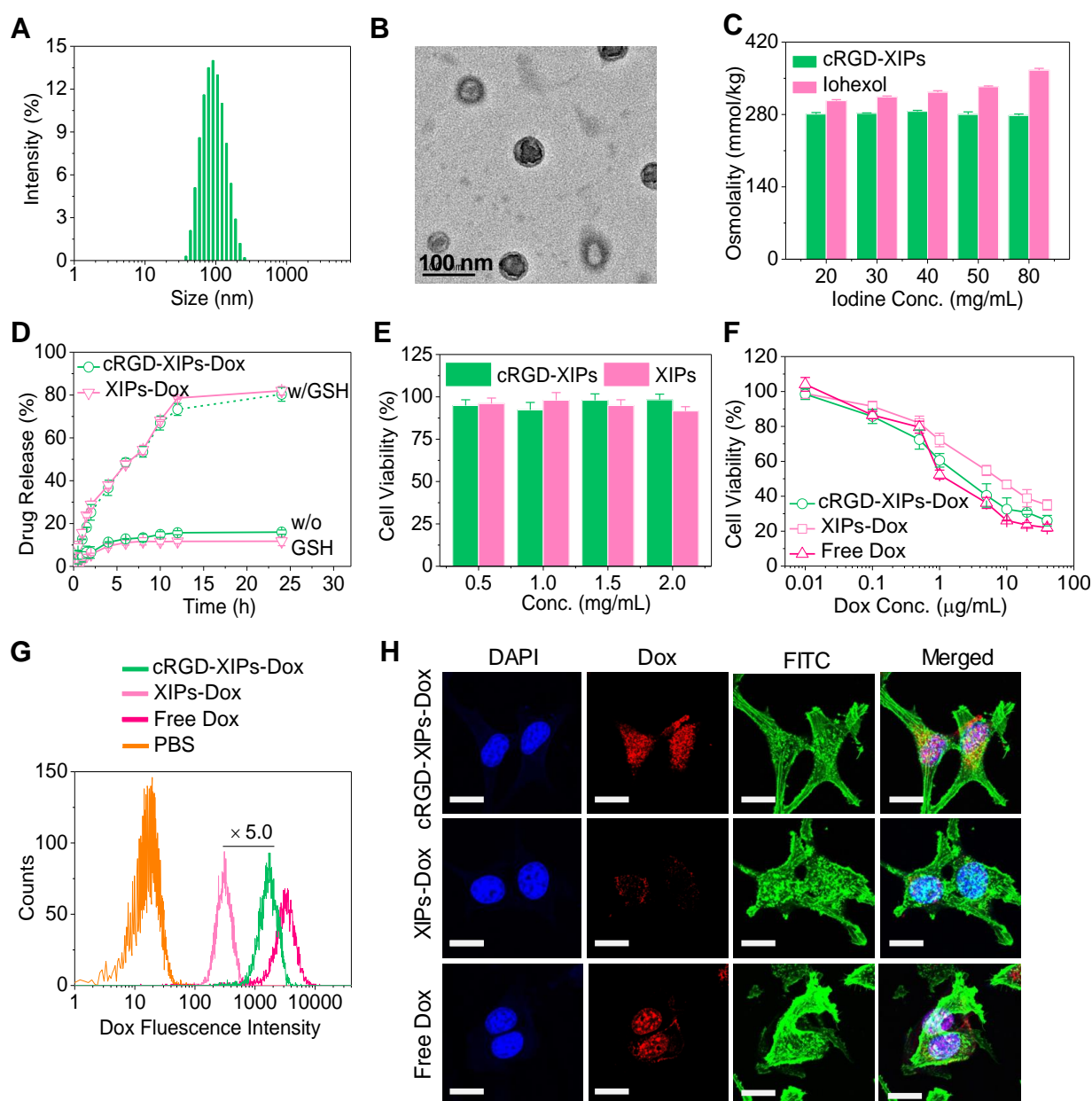
Table 1. Characterizations of cRGD-XIPs-Dox and XIPs-Dox

Polymersomes	TLC[a] (wt.%)	DLC[b] (wt.%)	DLE[b] (%)	Size[c] (nm)	PDI[c]	Zeta potential (mV)[c]
cRGD-XIPs-Dox	9.1	6.6	71.2	80	0.10	+ 0.3
	16.7	12.0	68.3	84	0.06	+ 1.6
	23.1	15.3	60.3	92	0.10	+ 0.9
XIPs-Dox	9.1	6.6	70.4	82	0.09	+ 1.2
	16.7	11.8	66.9	87	0.11	+ 0.5
	23.1	15.2	59.8	89	0.07	+ 0.8

[a] Theoretical drug loading content. [b] Determined using UV spectrometer. [c] Determined with a Zetasizer Nano ZS equipped with a DLS and an electrophoresis cell in PB at 1 mg/mL.

Doxorubicin hydrochloride (Dox) could be efficiently loaded into cRGD-XIPs and XIPs via pH-gradient method, in which the pH values of inner and outer of the polymersomes were 4.0 and 8.0, respectively. The drug loading content (DLC) increased with increasing theoretical DLC and cRGD-XIPs-Dox achieved a high DLC of 15.3 *wt.*%. cRGD-XIPs-Dox enlarged from 80, 84, to 92 nm with increasing DLC from 6.6, 12.0, to 15.3 wt.% (**Table 1**). Notably, all cRGD-XIPs-Dox presented a low PDI (0.06-0.10) and close to neutral surface charge. XIPs-Dox had nearly identical size distribution, drug loading, and zeta potential to cRGD-XIPs-Dox (**Table 1**), indicating little influence of cRGD peptide on polymersomal

Dox. **Fig. 2D** shows that at a polymersome concentration of 50 mg/L, Dox release from XIPs-Dox and cRGD-XIPs-Dox was less than 16% in 24 h. Importantly, under an intracellular mimicking condition (10 mM GSH), cRGD-XIPs-Dox dumped more than 80% Dox within 24 h (**Fig. 2D**). In contrast, within 12 h over 40% Dox leaked out of the non-crosslinked counterparts, IPs-Dox and cRGD-IPs-Dox, which were based on PEG-PIC and cRGD-PEG-PIC/PEG-PIC, respectively (**Fig. S8**). The results demonstrate the important role of disulfide crosslinking in preventing drug leakage at physiological condition and in triggering fast drug release intracellularly.

Figure 2. Characterizations of cRGD-XIPs and cRGD-XIPs-Dox. Size distribution (**A**), TEM image (**B**), and osmolality as a function of concentration (iohexol as control) (**C**) of cRGD-XIPs. (**D**) *In vitro* Dox release study of cRGD-XIPs-Dox and XIPs-Dox in PB with or without 10 mM GSH at 37 °C. Polymersomes concentration was 50 mg/L. (**E**) Cytotoxicity of empty XIPs and cRGD-XIPs to B16 cells following 48 h incubation. (**F**) Antitumor activity of cRGD-XIPs-Dox to B16 cells. The cells following 4 h incubation with Dox formulations were further cultured for 44 h. Flow cytometric analyses (**G**) and CLSM observation (**H**) of B16 cells following 4 h incubation with cRGD-XIPs-Dox (Dox: 10.0 µg/mL). The images from left to right are cell nuclei stained by DAPI (blue), Dox (red), cytoskeleton stained by phalloidin-FITC (green), and the merged images. Scale bars: 20 µm. XIPs-Dox and free Dox were used as controls in **F, G, H.**

3.2. In vitro cytotoxicity and targetability of cRGD-XIPs-Dox

cRGD is widely used as a targeting motif toward $\alpha_v\beta_3$ integrin over-expressing tumor cells including B16 melanoma cells [46, 47]. Here, we evaluated the cytotoxicity of blank cRGD-XIPs and cRGD-XIPs-Dox in B16 cell model using MTT assays. **Fig. 2E** shows that XIPs and cRGD-XIPs had no toxicity at concentrations ≤ 2.0 mg/mL, as reported for non-crosslinked polymersomes [33], confirming their excellent biocompatibility. In comparison, cRGD-XIPs-Dox showed high potency to B16 cells with an IC_{50} (half-maximal inhibitory concentration) of 2.33 µg Dox/mL, which was comparable to free Dox and 3.3-fold lower than XIPs-Dox (**Fig. 2F**).

Flow cytometric analyses displayed that cRGD-XIPs-Dox reveal ca. 5.0-fold higher cellular uptake by B16 cells than XIPs-Dox following 4 h incubation (**Fig. 2G**). Interestingly, both cRGD-XIPs-Dox and XIPs-Dox had low cellular uptake by L929 fibroblasts, further verifying their specific targetability (**Fig. S9**). CLSM images showed that Dox fluorescence in the nuclei of cells treated with cRGD-XIPs-Dox accumulated gradually from 0.5 h to 2 h and mostly in the nuclei at 4 h, which was considerably more intensive than those of XIPs-Dox treated cells and free cRGD pretreated B16 cells (**Fig. 2H & Fig. S10**). The above results

corroborate that cRGD-XIPs-Dox can be efficiently internalized by B16 cells via receptor-mediated endocytosis mechanism [48, 49], and Dox releases quickly intracellularly.
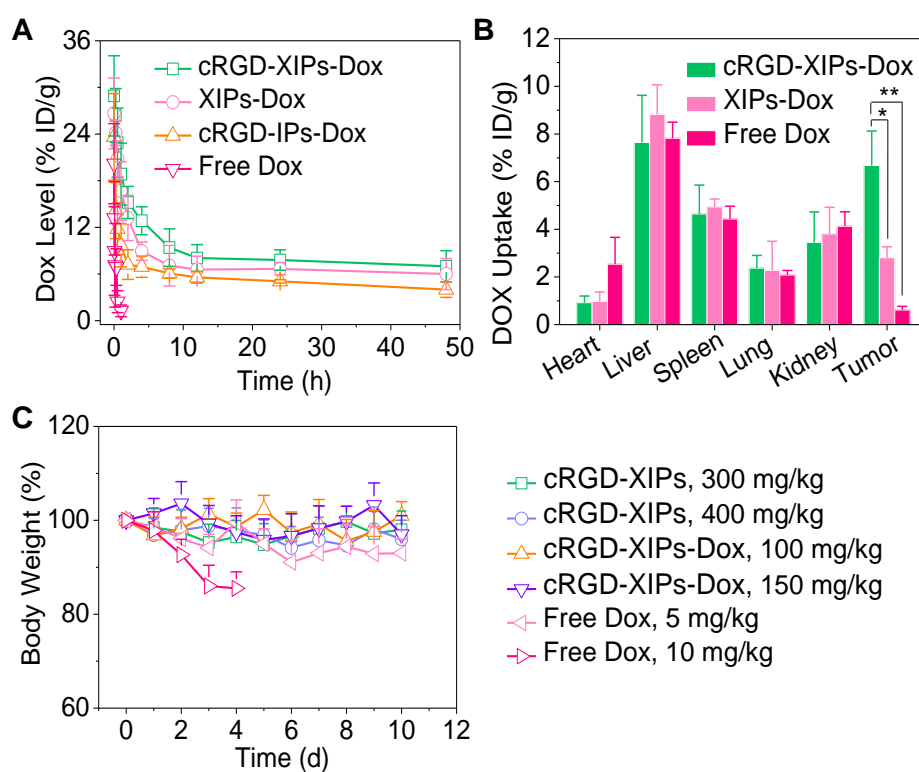
3.3. Pharmacokinetics, biodistribution and safety in vivo

The pharmacokinetics studies demonstrated that the blood circulation followed a typical two-compartment model: a rapid decline in distribution phase and long period elimination phase, and the circulation of Dox was significantly extended by loading into cRGD-XIPs and XIPs as calculated from the calibration curve of Dox of known concentrations in the presence of blood (**Table S2**). cRGD-XIPs-Dox and XIPs-Dox showed an elimination half-life ($t_{1/2,\beta}$) of about 6.5 h, which was ca. 50- and 1.8-fold longer than free Dox (0.13 h) and cRGD-IPs-Dox (non-crosslinked control, 3.61 h), respectively (**Fig. 3A**). Notably, commercial contrast agent iohexol has a short $t_{1/2,\beta}$ of 24.6 min [50, 51]. The AUC (area under the curve) of cRGD-XIPs-Dox was 97.76 h·µg/mL, which was 1.8- and 26.4-time bigger than that of cRGD-IPs-Dox and free Dox, respectively.

The quantitative biodistribution of Dox in cRGD-XIPs-Dox treated mice 4 h following *iv* injection was determined from calibration curves of Dox in the presence of individual tissue (**Table S2**), and demonstrated that Dox accumulation in the tumors was 6.68% of injected dose per gram of tissue (% ID/g). The accumulation was ca. 2.4- and 11.0-fold higher than that of XIPs-Dox (2.81% ID/g) and free Dox (0.61% ID/g), respectively (**Fig. 3B**). **Table S3** shows clearly that cRGD-XIPs-Dox had higher tumor-to-normal tissue (T/N) ratios in all major organs than free Dox and XIPs-Dox. Notably, cRGD-XIPs-Dox treated mice showed T/N ratios of Dox in the heart was ca. 30 times higher than free Dox treated ones, signifying the possibly significant reduction of cardiotoxicity, which is a dose-limiting side effect for Dox [52, 53].

To explore their theranostic window, we assessed the safety of blank cRGD-XIPs and

cRGD-XIPs-Dox in C57BL/6 tumor-free mice. Remarkably, a single dose of cRGD-XIPs at 300 and 400 mg I equiv./kg, or cRGD-XIPs-Dox at 100 and 150 mg Dox/kg did not provoke obvious loss in body weight or change of behavior of the mice within the experiment period of 10 days (**Fig. 3C**). In contrast, dramatic body weight loss was caused by free Dox at 10 mg/kg, indicating over 15-fold better toleration of cRGD-XIPs-Dox than free Dox. Safety profile is one of the critical requirements for clinical translation of theranostic agents [54, 55]. This high MTD of cRGD-XIPs-Dox was ascribed to the excellent biocompatibility of the materials, reduced non-specific uptake by normal organs resulting from cRGD active targeting effect, and high stability preventing Dox leakage and damage of the normal tissues from the crosslinked polymersomal structure.

Figure 3. *In vivo* pharmacokinetics, biodistribution and toleration studies of cRGD-XIPs-Dox in mice (n = 3). (**A**) Pharmacokinetics of cRGD-XIPs-Dox in healthy C57BL/6 mice (10 mg Dox/kg). XIPs-Dox (non-targeted), cRGD-IPs-Dox (non-crosslinked) and free Dox were used as controls. (**B**) Biodistribution of free Dox and Dox delivered by cRGD-XIPs or XIPs in C57BL/6 mice bearing B16 tumor 4 h post *iv* injection. (**C**) Toleration studies of tumor-free C57BL/6 mice towards cRGD-XIPs, cRGD-XIPs-Dox and free Dox. *$p < 0.05$ and **$p < 0.01$

(one-way Anova and Tukey multiple comparisons tests).

3.4. CT imaging performance of cRGD-XIPs in vivo

Despite its wide use in the clinics, CT imaging of soft tissues like tumors is challenging. To improve the CT imaging contrast, nano-contrast agents containing elements of high atomic numbers (e.g. iodine, gold) have been explored [56, 57]. Here, we investigated cRGD-XIPs for CT imaging of subcutaneous B16 melanoma as a model tumor. Melanoma is a very aggressive type of skin cancer and has high risk of lymphatic metastasis [58, 59]. **Fig. 4A** displays that cRGD-XIPs presented good CT contrast. The calculated CT attenuation as a function of iodine concentrations (measured in Hounsfield units (HU) revealed that cRGD-XIPs had even better attenuation coefficient than iohexol (**Fig. 4B**).

For *in vivo* CT imaging, 50 μL of cRGD-XIPs or iohexol (350 mg I equiv./kg) was intratumorally (*it*) administered into C57BL/6 mice bearing B16 tumors, and then scanned by CT. At 1 h after injection, CT images of cRGD-XIPs treated mice showed strong tumor contrast, and the CT attenuation increased from 35.4 ± 4.8 HU before injection to 221.9 ± 8.7 HU (**Fig. 4C**). The CT images acquired at different time intervals following *it* injection further showed that strong CT signals were observed in the tumors from 5 min to 4 h post *it* injection of cRGD-XIPs (**Fig. 4D**). In comparison, from 1 h post *it* injection of iohexol, no CT contrast could be discerned. **Fig. 4E** displays that the tumors of cRGD-XIPs group had about 10.5- and 46.5-fold higher ΔHU than iohexol group at 1 and 4 h post-injection, respectively. It is noted that very sharp CT signals could be detected in the bladder of iohexol group, which accorded well with the fast renal clearance of small molecular contrast agents [60, 61]. The results of *it* injection illustrate the clear benefit of utilizing stable cRGD-XIPs over iohexol for prolonged retention in the region of interest for CT imaging.

We further studied the CT imaging of B16 tumors in mice following intravenous (*iv*) injection of cRGD-XIPs, XIPs and iohexol (350 mg I equiv./kg). **Fig. 4F** shows that

cRGD-XIPs afforded the best CT images of the tumors in 3D reconstruction mode or axial mode. The quantification of CT attenuation revealed that ΔHU in the tumors of cRGD-XIPs group increased from 40 min to 4 h (**Fig. 4G**). Notably, cRGD-XIPs gave 2.7- and 24.0-fold higher contrast than XIPs and iohexol at 4 h, respectively. It is interesting to note that cRGD-XIPs did not show a high CT signal in liver (**Fig. 4F** & **Fig. S11**), in contrast to cRGD-XIPs-Dox that revealed a high liver accumulation besides a high tumor accumulation (**Fig. 3B**). The difference between biodistribution and CT imaging results most probably comes from liver saturation effect, *i.e.* liver uptake of cRGD-XIPs was saturated above certain level. CT imaging was performed at over 7.7-fold higher cRGD-XIPs dosage than for biodistribution studies. The high tumor contrast and low liver contrast of cRGD-XIPs renders CT imaging a particularly interesting tool for validating their tumor-targetability.
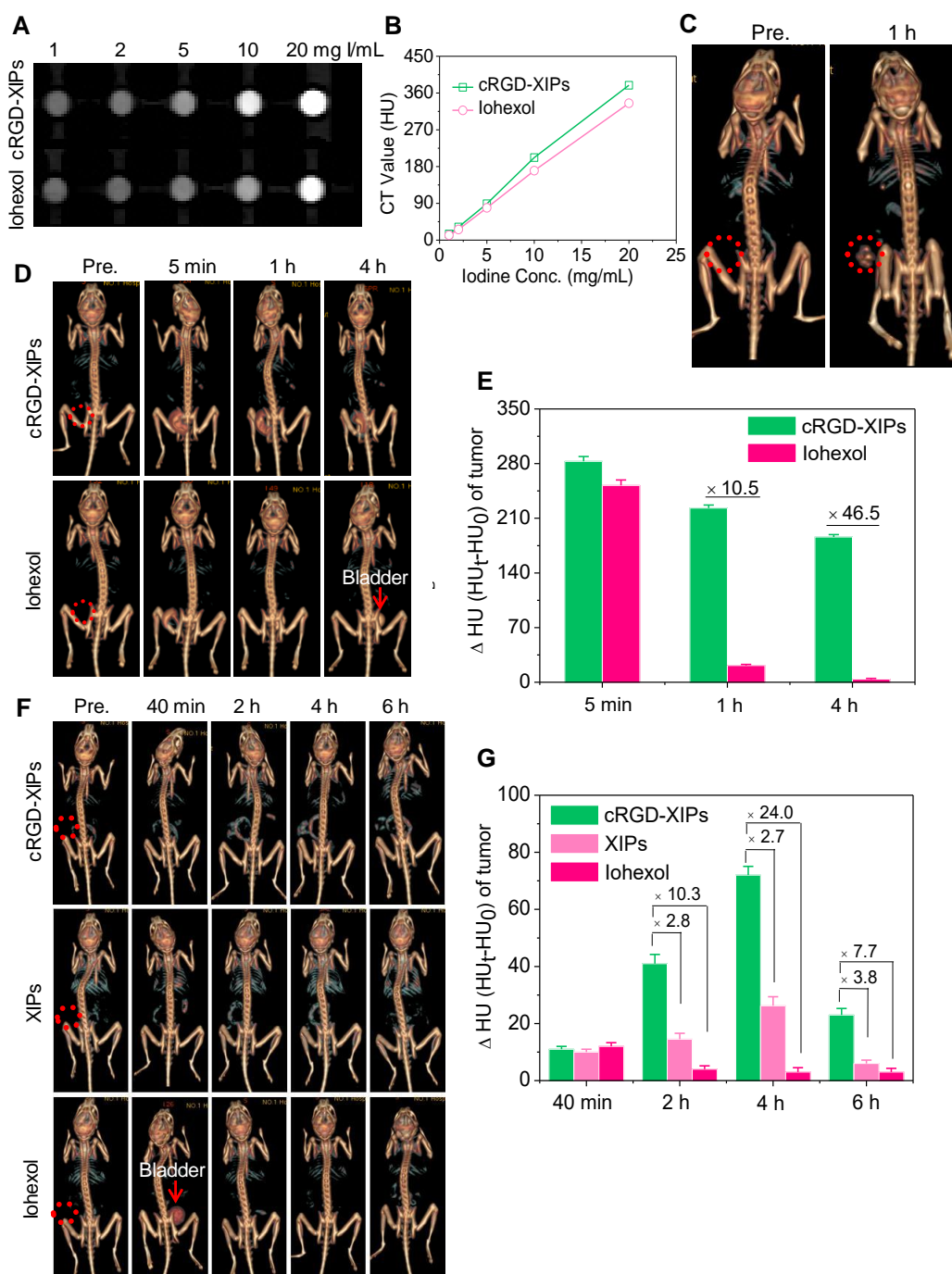
Figure 4. CT images (**A**) and X-ray attenuation (**B**) of iohexol and cRGD-XIPs solutions as a function of iodine concentrations. (**C**) 3D reconstruction CT images of tumors in mice before and 1 h after *it* administration of cRGD-XIPs or iohexol. 3D reconstruction CT images (**D**) and enhanced CT attenuation (ΔHU) (**E**) of the tumors before and at 5 min, 1 h or 4 h after *it* injection of cRGD-XIPs or iohexol. 3D reconstruction CT images (**F**) and ΔHU (**G**) of the tumors before and at different time post *iv* injection of cRGD-XIPs, XIPs or iohexol. The red dotted circles in **B, D** and **F** indicate the tumor areas. The iodine dose was set at 350 mg I equiv./kg for **C-G**.

3.5. The anti-tumor activity of cRGD-XIPs-Dox in mice bearing B16 tumor

With validated targetability of cRGD-XIPs to $\alpha_v\beta_3$-integrin over-expressing B16 melanoma by CT imaging, the *in vivo* antitumor activity of cRGD-XIPs-Dox to B16 tumor was then studied and compared with XIPs-Dox (non-targeted), cRGD-IPs-Dox (non-crosslinked) and free Dox formulation. B16 tumor was highly aggressive and grew from 52 mm^3 to 2197.0 mm^3 in 10 days (PBS group, **Fig. 5A**). Notably, cRGD-XIPs-Dox at 10 mg Dox/kg displayed the best tumor inhibition, being significantly more effective than XIPs-Dox and cRGD-IPs-Dox controls at the same dosage, certifying the pivotal roles of both cRGD targeting and disulfide crosslinking. In consideration of its dose-limiting effect, free Dox was given at 5 mg/kg. The results showed that free Dox was less potent in tumor inhibiting than cRGD-XIPs-Dox at 5 mg Dox/kg. The photographs of tumors collected on day 10 were consistent with tumor volumes (**Fig. 5B**). Moreover, cRGD-XIPs-Dox, XIPs-Dox and cRGD-IPs-Dox treated mice showed little body weight loss (**Fig. 5C**), in collaborating with the high MTD of these polymersomal formulations. **Fig. 5D** reveals a remarkable tumor inhibition rate (TIR) of 87.8% for cRGD-XIPs-Dox at 10 mg Dox/kg, and this was significantly higher than other groups. H&E staining showed that cRGD-XIPs-Dox did not induce significant damage to major organs (**Fig. S12**). Free Dox, however, induced obvious damage of liver, kidney and heart. Hence, despite of slightly better tumor suppression ability of cRGD-XIPs-Dox at 5 mg/kg than free Dox, further increase of the dose to 10 mg/kg produced excellent tumor inhibition with little adverse effects. cRGD-XIPs-Dox can thus be used as a safe and efficient therapeutic agent showing not only improved safety but also active targetability and better therapeutic efficacy toward B16 tumor in mice.
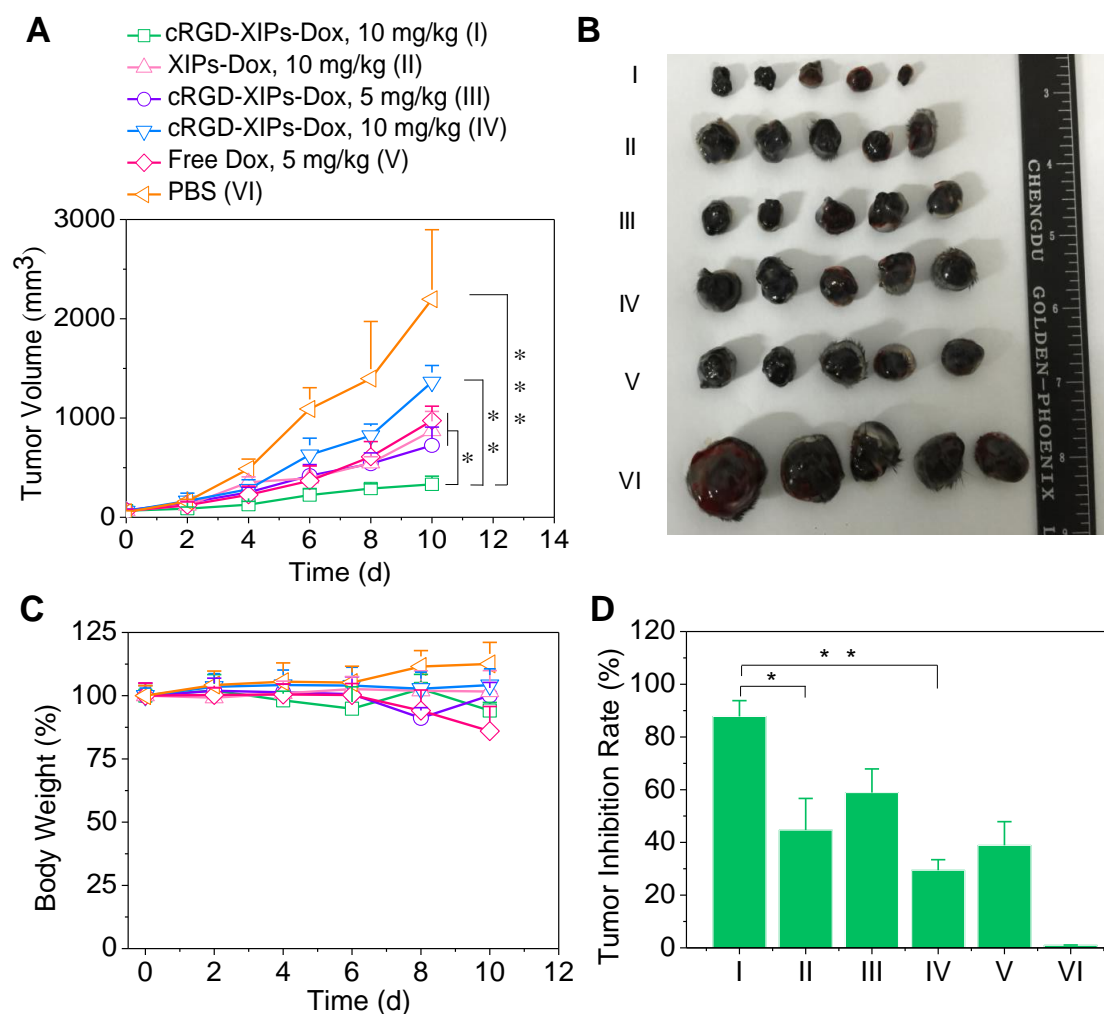
Figure 5. *In vivo* evaluation of the therapeutic efficacy of cRGD-XIPs-Dox using B16 tumor-bearing mice. XIPs-Dox, cRGD-IPs-Dox, free Dox and PBS were used as controls. The drugs were administrated on day 0, 2, 4, 6 and 8 (5 or 10 mg Dox/kg). (**A**) Tumor volume changes. (**B**) Photographs of tumors collected on day 10. (**C**) Body weight changes. (**D**) Tumor inhibition rates on day 10. Data are presented as mean ± SD (n = 5). *$p < 0.05$, **$p < 0.01$, and ***$p < 0.001$ (one-way Anova and Tukey multiple comparisons tests).

Conclusion

We have demonstrated that cRGD-functionalized, disulfide-crosslinked, biodegradable iodine-rich polymersomes (cRGD-XIPs) bare small size, low toxicity and superior CT imaging of $\alpha_v\beta_3$ integrin overexpressed tumors to clinical agent iohexol *in vivo*. Importantly, cRGD-XIPs can efficiently load Dox. Dox-loaded cRGD-XIPs (cRGD-XIPs-Dox) possess several appealing features like high stability, reduction-triggered drug release, prolonged

circulation time and active targetability to B16 melanoma, resulting in elevated tumor accumulation and significantly more effective suppression of B16 melanoma than XIPs-Dox (non-targeted), cRGD-IPs-Dox (non-crosslinked) and free Dox controls. This proof-of-concept study reveals that cRGD-XIPs are a robust, non-toxic and smart polymer theranostic agent that can not only significantly enhance CT imaging of $\alpha_v\beta_3$ integrin overexpressing tumors but also mediate efficient tumor-targeted chemotherapy. XIPs offer a unique and safe platform for theranostic polymersomes that pre-select patients using CT imaging prior to targeted chemotherapy with the same system.

Acknowledgements

Supplementary Material

Supplementary figures, tables and materials and methods.

Abbreviations

cRGD: cyclic RGD; CT: computed tomography; PEG-P(DTC-IC): poly(ethylene glycol)-*b*-poly(dithiolane trimethylene carbonate-*co*-iodinated carbonate); cRGD-PEG-P(DTC-IC): cRGD-poly(ethylene glycol)-*b*-poly(dithiolane trimethylene carbonate-*co*-iodinated carbonate); PEG-PIC: poly(ethylene glycol)-*b*-poly(iodinated carbonate); DLS: dynamic light scanning; Dox: doxorubicin hydrochloride; DSC: differential scanning calorimetry; TEM: transmission electron microscopy; DTT: dithiothreitol; GSH: glutathione; MTD: maximum tolerated dosage; RES: reticulaendothelial system; MTT:

3-(4,5-dimethylthiazol-2-yl)-2,5-diphenyl tetrazoliumbromide; PBS: phosphate buffer saline; DAPI: 4,6-diamidino-2-phenylindole; CLSM: confocal laser scanning microscopy; T/N: tumor-to-normal tissue; H&E: hematoxylin-eosin staining; HU: Hounsfield units.

Competing Interests

The authors declare no competing financial interest.

References

[1] Y. Cong, H. Xiao, H. Xiong, Z. Wang, J. Ding, C. Li, X. Chen, X.-J. Liang, D. Zhou, Y. Huang, Dual drug backboned shattering polymeric theranostic nanomedicine for synergistic eradication of patient-derived lung cancer, Adv. Mater. 30 (2018) 1706220.

[2] G. Yu, S. Yu, M.L. Saha, J. Zhou, T.R. Cook, B.C. Yung, J. Chen, Z. Mao, F. Zhang, Z. Zhou, Y. Liu, L. Shao, S. Wang, C. Gao, F. Huang, P.J. Stang, X. Chen, A discrete organoplatinum(II) metallacage as a multimodality theranostic platform for cancer photochemotherapy, Nat. Commun. 9 (2018) 4335.

[3] S.M. Dadfar, K. Roemhild, N.I. Drude, S. von Stillfried, R. Knüchel, F. Kiessling, T. Lammers, Iron oxide nanoparticles: Diagnostic, therapeutic and theranostic applications, Adv. Drug Deliver. Rev. 138 (2019) 302-325.

[4] T. Lammers, S. Aime, W.E. Hennink, G. Storm, F. Kiessling, Theranostic Nanomedicine, Accounts Chem. Res. 44 (2011) 1029-1038.

[5] A.G. Arranja, V. Pathak, T. Lammers, Y. Shi, Tumor-targeted nanomedicines for cancer theranostics, Pharmacol. Res. 115 (2017) 87-95.

[6] F. Wang, J. Xiao, S. Chen, H. Sun, B. Yang, J. Jiang, X. Zhou, J. Du, Polymer vesicles: Modular platforms for cancer theranostics, Adv. Mater. 30 (2018) 1705674.

[7] M.S. Muthu, D.T. Leong, L. Mei, S.-S. Feng, Nanotheranostics - application and further development of nanomedicine strategies for advanced theranostics, Theranostics 4 (2014) 660-677.

[8] H.K. Gaikwad, D. Tsvirkun, Y. Ben-Nun, E. Merquiol, R. Popovtzer, G. Blum, Molecular imaging of cancer using X-ray computed tomography with protease targeted iodinated activity-based probes, Nano Lett. 18 (2018) 1582-1591.

[9] X. Chen, J. Song, X. Chen, H. Yang, X-ray-activated nanosystems for theranostic applications, Chem. Soc. Rev. 48 (2019) 3073-3101.

[10] S. Kunjachan, J. Ehling, G. Storm, F. Kiessling, T. Lammers, Noninvasive imaging of nanomedicines and nanotheranostics: Principles, progress, and prospects, Chem. Rev. 115 (2015) 10907-10937.

[11] Z. Zhou, Z.-R. Lu, Molecular imaging of the tumor microenvironment, Adv. Drug

Deliver. Rev. 113 (2017) 24-48.

[12] Z.-R. Lu, Theranostics: fusion of therapeutics and diagnostics, Pharm. Res. 31 (2014) 1355-1357.

[13] Q. Yin, F.Y. Yap, L. Yin, L. Ma, Q. Zhou, L.W. Dobrucki, T.M. Fan, R.C. Gaba, J. Cheng, Poly(iohexol) nanoparticles as contrast agents for in vivo X-ray computed tomography imaging, J. Am. Chem. Soc. 135 (2013) 13620-13623.

[14] M.M. Lubbers, M. Kock, A. Niezen, T. Galema, M. Kofflard, T. Bruning, H.S. Kooij, H. van Valen, M. Dijkshoorn, R. Booij, A. Padmos, A. Vogels, R.P.J. Budde, K. Nieman, Iodixanol versus iopromide at coronary CT angiography: Lumen opacification and effect on heart rhythm—the randomized isoCOR trial, Radiology 286 (2017) 71-80.

[15] J.W. Lambert, Y. Sun, C. Stillson, Z. Li, R. Kumar, S. Wang, P.F. FitzGerald, P.J. Bonitatibus, R.E. Colborn, J.C. Roberts, P.M. Edic, M. Marino, B.M. Yeh, An intravascular tantalum oxide–based CT contrast agent: Preclinical evaluation emulating overweight and obese patient size, Radiology 289 (2018) 103-110.

[16] Y. Dou, Y. Guo, X. Li, X. Li, S. Wang, L. Wang, G. Lv, X. Zhang, H. Wang, X. Gong, J. Chang, Size-tuning ionization to optimize gold nanoparticles for simultaneous enhanced CT imaging and radiotherapy, ACS Nano 10 (2016) 2536-2548.

[17] P. Dogra, N.L. Adolphi, Z. Wang, Y.-S. Lin, K.S. Butler, P.N. Durfee, J.G. Croissant, A. Noureddine, E.N. Coker, E.L. Bearer, V. Cristini, C.J. Brinker, Establishing the effects of mesoporous silica nanoparticle properties on in vivo disposition using imaging-based pharmacokinetics, Nat. Commun. 9 (2018) 4551.

[18] W. He, K. Ai, L. Lu, Nanoparticulate X-ray CT contrast agents, Sci. China Chem. 58 (2015) 753-760.

[19] L. Cheng, J. Liu, X. Gu, H. Gong, X. Shi, T. Liu, C. Wang, X. Wang, G. Liu, H. Xing, W. Bu, B. Sun, Z. Liu, PEGylated WS2 nanosheets as a multifunctional theranostic agent for in vivo dual-modal CT/photoacoustic imaging guided photothermal therapy, Adv. Mater. 26 (2014) 1886-1893.

[20] B. Wu, S.-T. Lu, H. Yu, R.-F. Liao, H. Li, B.V. Lucie Zafitatsimo, Y.-S. Li, Y. Zhang, X.-L. Zhu, H.-G. Liu, H.-B. Xu, S.-W. Huang, Z. Cheng, Gadolinium-chelate functionalized bismuth nanotheranostic agent for in vivo MRI/CT/PAI imaging-guided photothermal cancer

therapy, Biomaterials 159 (2018) 37-47.

[21] J. Wang, L. Liu, Q. You, Y. Song, Q. Sun, Y. Wang, Y. Cheng, F. Tan, N. Li, All-in-one theranostic nanoplatform based on hollow MoS(x) for photothermally-maneuvered oxygen self-enriched photodynamic therapy, Theranostics 8 (2018) 955-971.

[22] R. Meir, K. Shamalov, O. Betzer, M. Motiei, M. Horovitz-Fried, R. Yehuda, A. Popovtzer, R. Popovtzer, C.J. Cohen, Nanomedicine for cancer immunotherapy: Tracking cancer-specific T-cells in vivo with gold nanoparticles and CT imaging, ACS Nano 9 (2015) 6363-6372.

[23] Z. Liu, Y. Li, W. Li, C. Xiao, D. Liu, C. Dong, M. Zhang, E. Mäkilä, M. Kemell, J. Salonen, J.T. Hirvonen, H. Zhang, D. Zhou, X. Deng, H.A. Santos, Multifunctional nanohybrid based on porous silicon nanoparticles, gold nanoparticles, and acetalated dextran for liver regeneration and acute liver failure theranostics, Adv. Mater. 30 (2018) 1703393.

[24] H. Deng, Y. Zhong, M. Du, Q. Liu, Z. Fan, F. Dai, X. Zhang, Theranostic self-assembly structure of gold nanoparticles for NIR photothermal therapy and X-Ray computed tomography imaging, Theranostics 4 (2014) 904-918.

[25] J. Cui, R. Jiang, C. Guo, X. Bai, S. Xu, L. Wang, Fluorine grafted Cu7S4–Au heterodimers for multimodal imaging guided photothermal therapy with high penetration depth, J. Am. Chem. Soc. 140 (2018) 5890-5894.

[26] B. Yang, Y. Chen, J. Shi, Material chemistry of two-dimensional inorganic nanosheets in cancer theranostics, Chem 4 (2018) 1284-1313.

[27] T.I. Kostelnik, C. Orvig, Radioactive main group and rare earth metals for imaging and therapy, Chem. Rev. 119 (2019) 902-956.

[28] H. Xu, T.Y. Ohulchanskyy, A. Yakovliev, R. Zinyuk, J. Song, L. Liu, J. Qu, Z. Yuan, Nanoliposomes co-encapsulating CT imaging contrast agent and photosensitizer for enhanced, imaging guided photodynamic therapy of cancer, Theranostics 9 (2019) 1323-1335.

[29] Y. Zhu, X. Wang, J. Chen, J. Zhang, F. Meng, C. Deng, R. Cheng, J. Feijen, Z. Zhong, Bioresponsive and fluorescent hyaluronic acid-iodixanol nanogels for targeted X-ray computed tomography imaging and chemotherapy of breast tumors, J. Control. Release 244 (2016) 229-239.

[30] N. Lee, S.H. Choi, T. Hyeon, Nano-sized CT contrast agents, Adv. Mater. 25 (2013) 2641-2660.

[31] Y. Liu, K. Ai, L. Lu, Nanoparticulate X-ray computed tomography contrast agents: From design validation to in vivo applications, Acc. Chem. Res. 45 (2012) 1817-1827.

[32] Y. Ma, Q. Mou, D. Wang, X. Zhu, D. Yan, Dendritic polymers for theranostics, Theranostics 6 (2016) 930-947.

[33] Y. Zou, Y. Wei, G. Wang, F. Meng, M. Gao, G. Storm, Z. Zhong, Nanopolymersomes with an ultrahigh iodine content for high-performance X-ray computed comography imaging in vivo, Adv. Mater. 29 (2017) 1603997.

[34] Y. Jiang, J. Zhang, F. Meng, Z. Zhong, Apolipoprotein E peptide-directed chimeric polymersomes mediate an ultrahigh-efficiency targeted protein therapy for glioblastoma, ACS Nano 12 (2018) 11070-11079.

[35] Y. Zou, Y. Fang, H. Meng, F. Meng, C. Deng, J. Zhang, Z. Zhong, Self-crosslinkable and intracellularly decrosslinkable biodegradable micellar nanoparticles: A robust, simple and multifunctional nanoplatform for high-efficiency targeted cancer chemotherapy, J. Control. Release 244 (2016) 326-335.

[36] D.P. Donnelly, M.G. Dowgiallo, J.P. Salisbury, K.C. Aluri, S. Iyengar, M. Chaudhari, M. Mathew, I. Miele, J.R. Auclair, S.A. Lopez, R. Manetsch, J.N. Agar, Cyclic thiosulfinates and cyclic disulfides selectively cross-link thiols while avoiding modification of lone thiols, J. Am. Chem. Soc. 140 (2018) 7377-7380.

[37] M. Qiu, X. Wang, H. Sun, J. Zhang, C. Deng, Z. Zhong, Cyclic RGD-peptide-functionalized polylipopeptide micelles for enhanced loading and targeted delivery of monomethyl auristatin E, Mol. Pharmaceutics 15 (2018) 4854-4861.

[38] P. Zhong, H. Meng, J. Qiu, J. Zhang, H. Sun, R. Cheng, Z. Zhong, αvβ3 Integrin-targeted reduction-sensitive micellar mertansine prodrug: Superb drug loading, enhanced stability, and effective inhibition of melanoma growth in vivo, J. Control. Release 259 (2017) 176-186.

[39] Y. Liang, S. Li, X. Wang, B. He, B. He, W. Dai, H. Zhang, X. Wang, Y. Wang, D. Zhou, Q. Zhang, A nanosystem of amphiphilic oligopeptide-drug conjugate actualizing both αvβ3 targeting and reduction-triggered release for maytansinoid, Theranostics 7 (2017) 3306-3318.

[40] Y. Zou, J. Wei, Y. Xia, F. Meng, J. Yuan, Z. Zhong, Targeted chemotherapy for subcutaneous and orthotopic non-small cell lung tumors with cyclic RGD-functionalized and disulfide-crosslinked polymersomal doxorubicin, Signal Transduction and Targeted Ther. 3

(2018) 32.

[41] B.T. Luk, R.H. Fang, L. Zhang, Lipid- and polymer-based nanostructures for cancer theranostics, Theranostics 2 (2012) 1117-1126.

[42] S.C. Baetke, T. Lammers, F. Kiessling, Applications of nanoparticles for diagnosis and therapy of cancer, Brit. J. Radiol. 88 (2015) 20150207.

[43] N. Schleich, C. Po, D. Jacobs, B. Ucakar, B. Gallez, F. Danhier, V. Préat, Comparison of active, passive and magnetic targeting to tumors of multifunctional paclitaxel/SPIO-loaded nanoparticles for tumor imaging and therapy, J. Control. Release 194 (2014) 82-91.

[44] L. Li, C. Chen, H. Liu, C. Fu, L. Tan, S. Wang, S. Fu, X. Liu, X. Meng, H. Liu, Multifunctional carbon–silica nanocapsules with gold core for synergistic photothermal and chemo-cancer therapy under the guidance of bimodal imaging, Adv. Funct. Mater. 26 (2016) 4252-4261.

[45] Y. Zou, F. Meng, C. Deng, Z. Zhong, Robust, tumor-homing and redox-sensitive polymersomal doxorubicin: A superior alternative to Doxil and Caelyx?, J. Control. Release 239 (2016) 149-158.

[46] Z. Guo, B. He, H. Jin, H. Zhang, W. Dai, L. Zhang, H. Zhang, X. Wang, J. Wang, X. Zhang, Q. Zhang, Targeting efficiency of RGD-modified nanocarriers with different ligand intervals in response to integrin $\alpha v \beta 3$ clustering, Biomaterials 35 (2014) 6106-6117.

[47] S. Zhu, L. Qian, M. Hong, L. Zhang, Y. Pei, Y. Jiang, RGD-modified PEG-PAMAM-DOX conjugate: In vitro and in vivo targeting to both tumor neovascular endothelial cells and tumor cells, Adv. Mater. 23 (2011) 84-89.

[48] C. Chen, Z. Duan, Y. Yuan, R. Li, L. Pang, J. Liang, X. Xu, J. Wang, Peptide-22 and cyclic RGD functionalized liposomes for glioma targeting drug delivery overcoming BBB and BBTB, ACS Appl. Mater. Interfaces 9 (2017) 5864-5873.

[49] K. Miyano, H. Cabral, Y. Miura, Y. Matsumoto, Y. Mochida, H. Kinoh, C. Iwata, O. Nagano, H. Saya, N. Nishiyama, K. Kataoka, T. Yamasoba, cRGD peptide installation on cisplatin-loaded nanomedicines enhances efficacy against locally advanced head and neck squamous cell carcinoma bearing cancer stem-like cells, J. Control. Release 261 (2017) 275-286.

[50] W. Cheng, F. Zhao, C.-Y. Tang, X.-W. Li, M. Luo, S.-B. Duan, Comparison of iohexol

and iodixanol induced nephrotoxicity, mitochondrial damage and mitophagy in a new contrast-induced acute kidney injury rat model, Arch. Toxicol. 92 (2018) 2245-2257.

[51] L. Zhuang, J. Gao, Y. Zeng, F. Yu, B. Zhang, M. Li, H. Derendorf, C. Liu, HPLC method validation for the quantification of lomustine to study pharmacokinetics of thermosensitive liposome-encapsulated lomustine containing iohexol for CT imaging in C6 glioma rats, Eur. J. Drug Metab. Ph. 36 (2011) 61-69.

[52] M. Cagel, E. Grotz, E. Bernabeu, M.A. Moretton, D.A. Chiappetta, Doxorubicin: nanotechnological overviews from bench to bedside, Drug Discov. Today 22 (2017) 270-281.

[53] C. Mamot, R. Ritschard, A. Wicki, G. Stehle, T. Dieterle, L. Bubendorf, C. Hilker, S. Deuster, R. Herrmann, C. Rochlitz, Tolerability, safety, pharmacokinetics, and efficacy of doxorubicin-loaded anti-EGFR immunoliposomes in advanced solid tumours: a phase 1 dose-escalation study, Lancet Oncol. 13 (2012) 1234-1241.

[54] C. Li, Y. Wang, Y. Du, M. Qian, H. Jiang, J. Wang, N. Murthy, R. Huang, Side effects-avoided theranostics achieved by biodegradable magnetic silica-sealed mesoporous polymer-drug with ultralow leakage, Biomaterials 186 (2018) 1-7.

[55] M.A. O'Reilly, R.M. Jones, E. Barrett, A. Schwab, E. Head, K. Hynynen, Investigation of the safety of focused ultrasound-induced blood-brain barrier opening in a natural canine model of aging, Theranostics 7 (2017) 3573-3584.

[56] T. Kim, N. Lee, D.R. Arifin, I. Shats, M. Janowski, P. Walczak, T. Hyeon, J.W.M. Bulte, In vivo micro-CT imaging of human mesenchymal stem cells labeled with gold-poly-l-lysine nanocomplexes, Adv. Funct. Mater. 27 (2016) 1604213.

[57] B. Sun, J. Wu, S. Cui, H. Zhu, W. An, Q. Fu, C. Shao, A. Yao, B. Chen, D. Shi, In situ synthesis of graphene oxide/gold nanorods theranostic hybrids for efficient tumor computed tomography imaging and photothermal therapy, Nano Res. 10 (2017) 37-48.

[58] C.M. Deroose, A. De, A.M. Loening, P.L. Chow, P. Ray, A.F. Chatziioannou, S.S. Gambhir, Multimodality imaging of tumor xenografts and metastases in mice with combined small-animal PET, small-animal CT, and bioluminescence imaging, J. Nucl. Med. 48 (2007) 295-303.

[59] K. Strobel, R. Dummer, D.B. Husarik, M. Pérez Lago, T.F. Hany, H.C. Steinert, High-risk melanoma: Accuracy of FDG PET/CT with added CT morphologic information for

detection of metastases, Radiology 244 (2007) 566-574.

[60] J. Qi, Y. Fang, R.T.K. Kwok, X. Zhang, X. Hu, J.W.Y. Lam, D. Ding, B.Z. Tang, Highly stable organic small molecular nanoparticles as an advanced and biocompatible phototheranostic agent of tumor in living mice, ACS Nano 11 (2017) 7177-7188.

[61] H. Wei, O.T. Bruns, M.G. Kaul, E.C. Hansen, M. Barch, A. Wiśniowska, O. Chen, Y. Chen, N. Li, S. Okada, J.M. Cordero, M. Heine, C.T. Farrar, D.M. Montana, G. Adam, H. Ittrich, A. Jasanoff, P. Nielsen, M.G. Bawendi, Exceedingly small iron oxide nanoparticles as positive MRI contrast agents, P. Natl. Acad. Sci. USA 114 (2017) 2325-2330.

Supplementary Data

Table S1. Characteristics of block copolymers

| Entry | copolymer | M_n (kg/mol) | | | M_w/M_n[b] (GPC) | T_g[c] (°C) |
		Design	^{1}H NMR[a]	GPC[b]		
1	PEG-P(DTC-IC)	5-(5-50)	5-(4.6-48.3)	63.2	1.31	-25.3
2	cRGD-PEG-P(DTC-IC)	6.5-(5-50)	6.5-(4.7-49.2)	68.3	1.23	-21.5

[a] Determined by ^{1}H NMR by comparing the integrals of signals at δ 3.04 (methylene proton of PDTC) with that of PEG methylene protons at δ 3.65 for MW of PDTC; and for MW of PIC, the integrals of signals e, f, b, c, and d in **Fig. S2** were compared and calculated according to the following equation: Ie/Ib = [(Ie+Ic)-Id]/{(Ib+If)- [(Ie+Ic)-Id]. [b] Determined by GPC (eluent: DMF, flow rate: 1 mL/min, standards: polystyrene, 30 °C). [c] Determined by DSC.

**Table S2.** Calibration curves of free Dox in the presence of blood or each tissue

Tissue	Standard Curves	Linear range (µg/mL)	R^2
---	$Y = 2.662 \times X + 1.005$	0.01-20	0.9911
Plasma	$Y = 4.344 \times X + 0.673$	0.1-10	0.9963
Heart	$Y = 3.808 \times X - 0.194$	0.5-20	0.9998
Liver	$Y = 4.387 \times X - 2.101$	0.1-20	0.9975
Spleen	$Y = 2.448 \times X + 1.614$	0.1-20	0.9956
Lung	$Y = 3.008 \times X - 1.748$	0.1-20	0.9877
Kidney	$Y = 4.668 \times X + 0.360$	0.1-20	0.9889
Tumor	$Y = 2.892 \times X - 0.591$	0.1-20	0.9858

Table S3. Tumor-to-normal tissue (T/N) ratios of Dox at 4 h after *i.v.* injection

	Heart	Liver	Spleen	Lung	Kidney
cRGD-XIPs-Dox	7.27 ± 1.57	0.87 ± 0.19	1.44 ± 0.31	2.82 ± 0.61	1.94 ± 0.42
XIPs-Dox	2.88 ± 0.47	0.32 ± 0.05	0.57 ± 0.09	1.23 ± 0.20	0.74 ± 0.12
Free Dox	0.24 ± 0.06	0.08 ± 0.02	0.14 ± 0.03	0.29 ± 0.07	0.15 ± 0.04
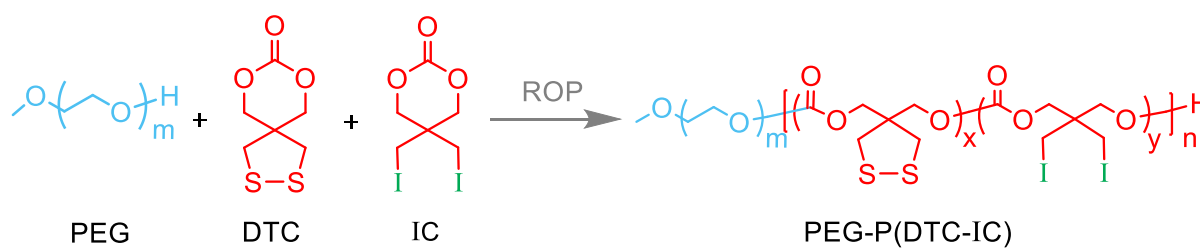
Figure S1. Synthesis of PEG-P(DTC-IC) by ring-opening polymerization. Conditions: zinc bis[bis(trimethylsilyl)amide], CH_2Cl_2, 40 °C, 3 days.
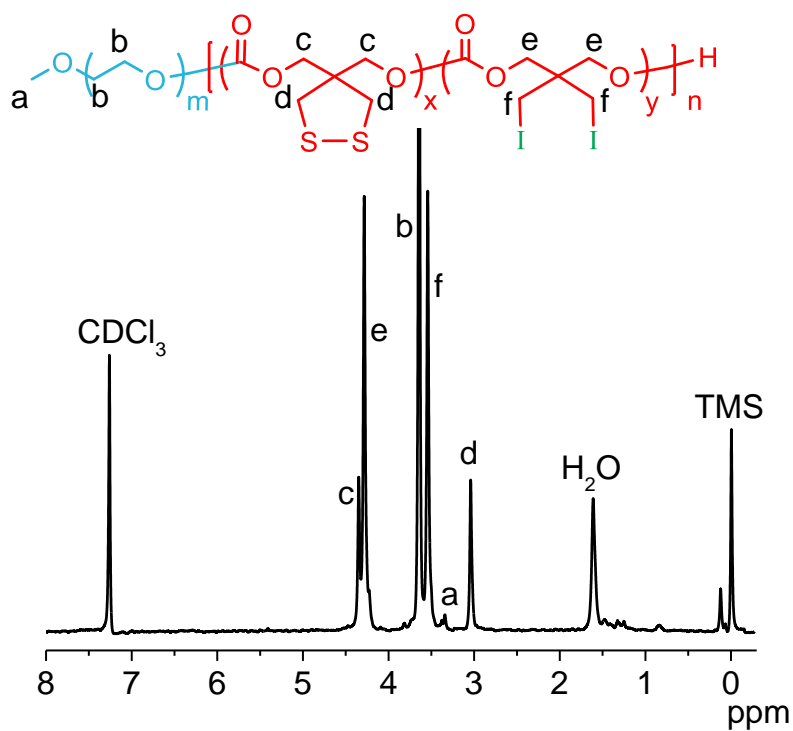
Figure S2. ^{1}H NMR spectrum (400 MHz, CDCl$_3$) of PEG-P(DTC-IC).
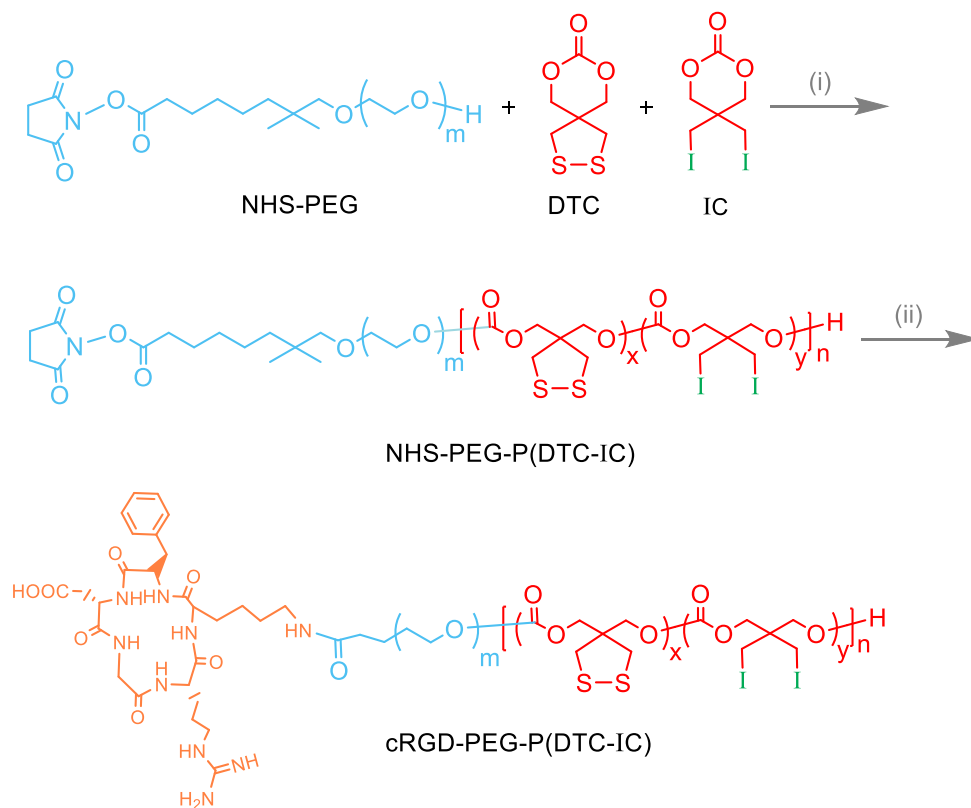
Figure S3. Synthesis of cRGD-PEG-P(DTC-IC). Conditions: (i) zinc bis[bis(trimethylsilyl)amide], CH$_2$Cl$_2$, 40 °C, 3 days; (ii) C(RGDfK), r.t, 48 h.
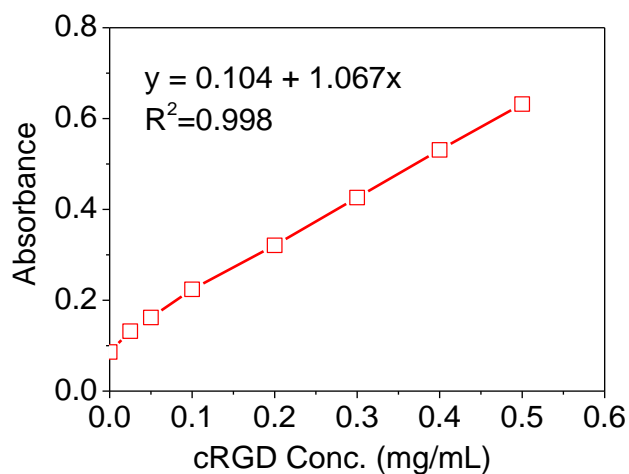
Figure S4. Standard curve of free cRGD peptide determined with the micro-BCA protein assay.
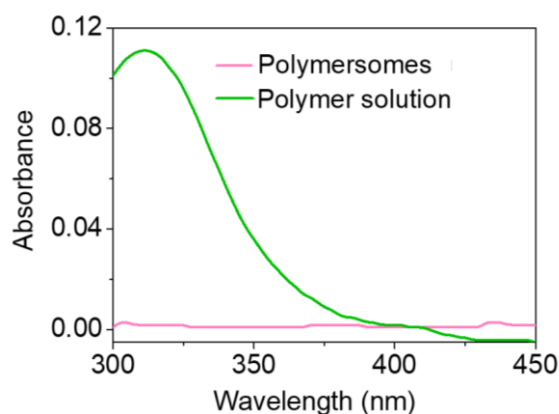
Figure S5. UV spectra of PEG-P(DTC-IC)/cRGD-PEG-P(DTC-IC) (8/2, mol/mol) polymer solution in DMSO and cRGD-XIPs dispersion at polymer concentration of 10 mg/mL.
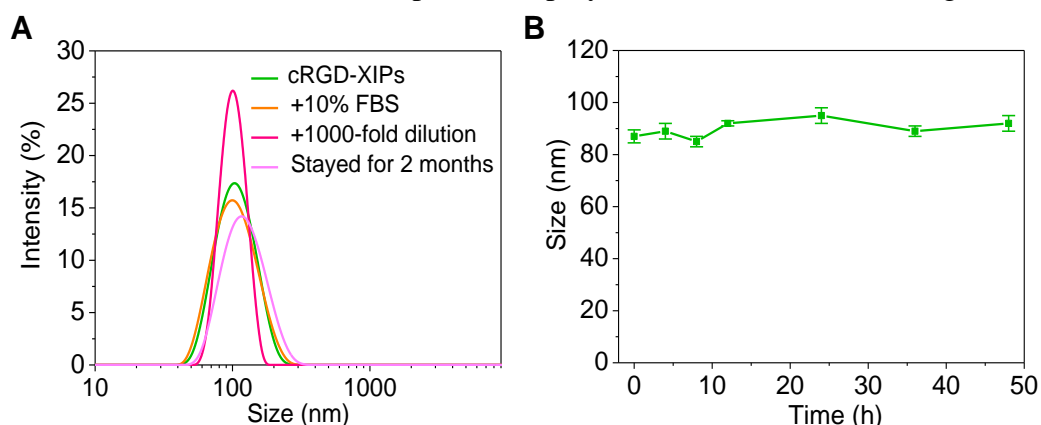
Figure S6. Size changes of cRGD-XIPs against 10% FBS, 1000-fold dilution and storage (**A**) and colloidal stability of cRGD-XIPs incubated in 10% FBS with time (**B**).
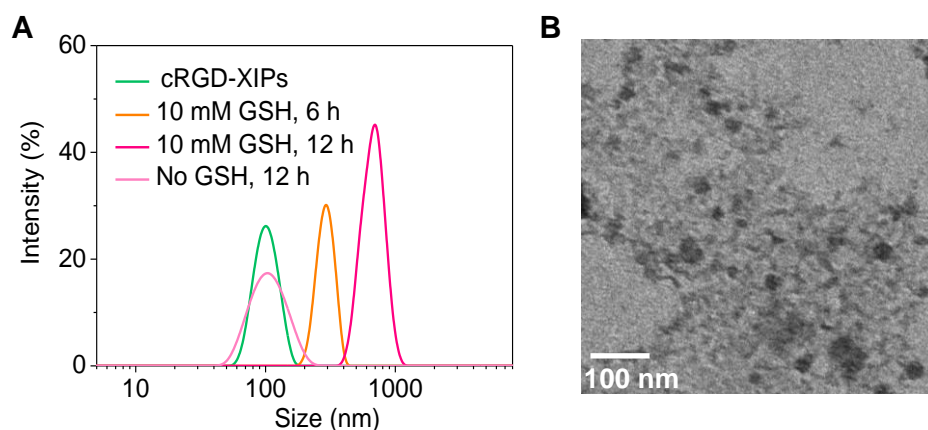
Figure S7. Size change of cRGD-XIPs in PB (pH 7.4, 10 mM) with or without 10 mM GSH at 37 °C (A) and TEM image of cRGD-XIPs treated with 10 mM GSH for 24 h (B).
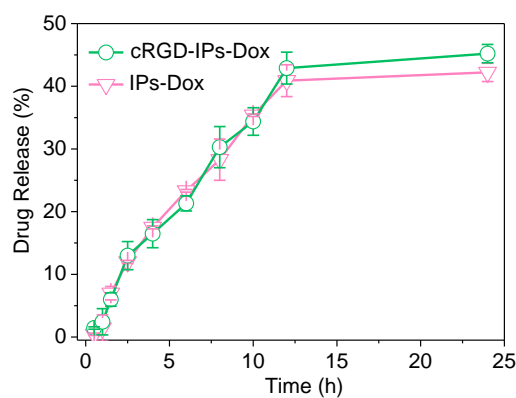
Figure S8. *In vitro* Dox release study of cRGD-IPs-Dox and IPs-Dox (non-crosslinked controls) in PB at 37 °C. Polymersome concentration was set 50 µg/mL.
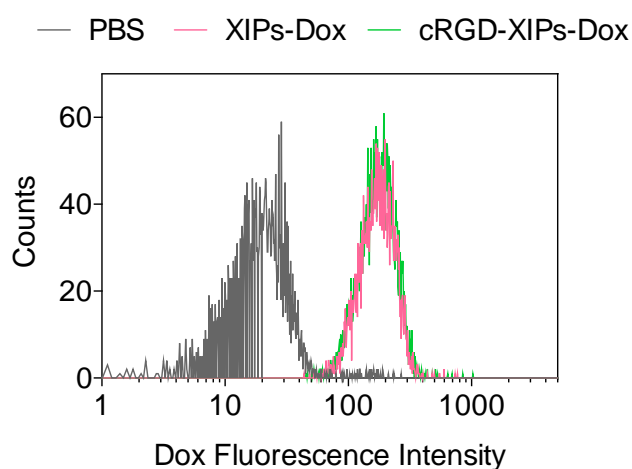
Figure S9. Flow cytometric analyses of L929 fibroblasts following 4 h incubation with cRGD-XIPs-Dox and XIPs-Dox (Dox: 10.0 µg/mL).
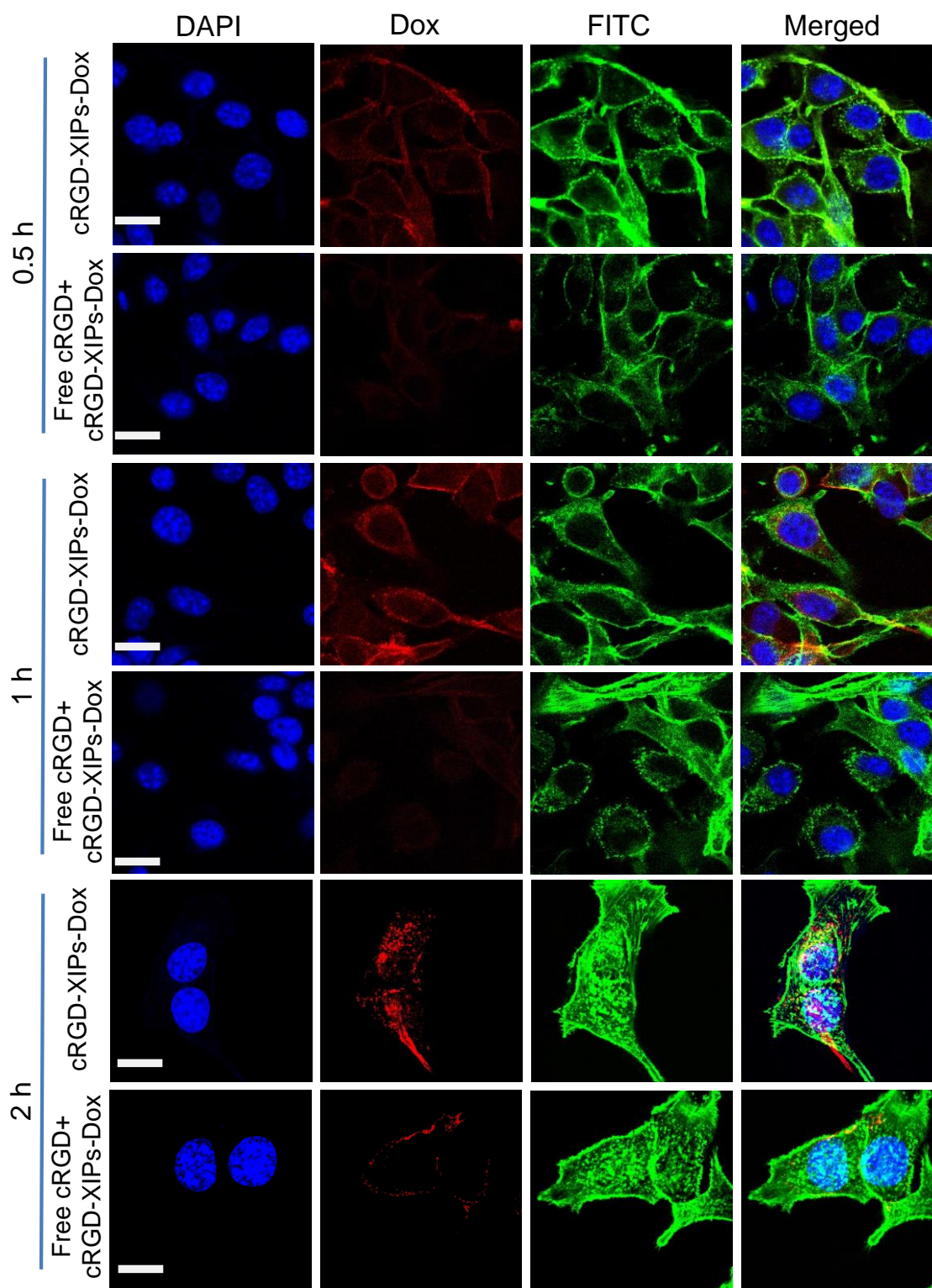
Figure S10. CLSM images of B16 cells following 0.5, 1 and 2 h incubation with cRGD-XIPs-Dox (Dox: 10.0 µg/mL). The inhibitive experiments were performed by pre-treating B16 cells with 200 µg/mL free cRGD for 2 h prior to adding cRGD-XIPs-Dox. The images from left to right are cell nuclei stained by DAPI (blue), Dox (red), cytoskeleton stained by phalloidin (green), and the merged images. Scale bars: 20 µm.
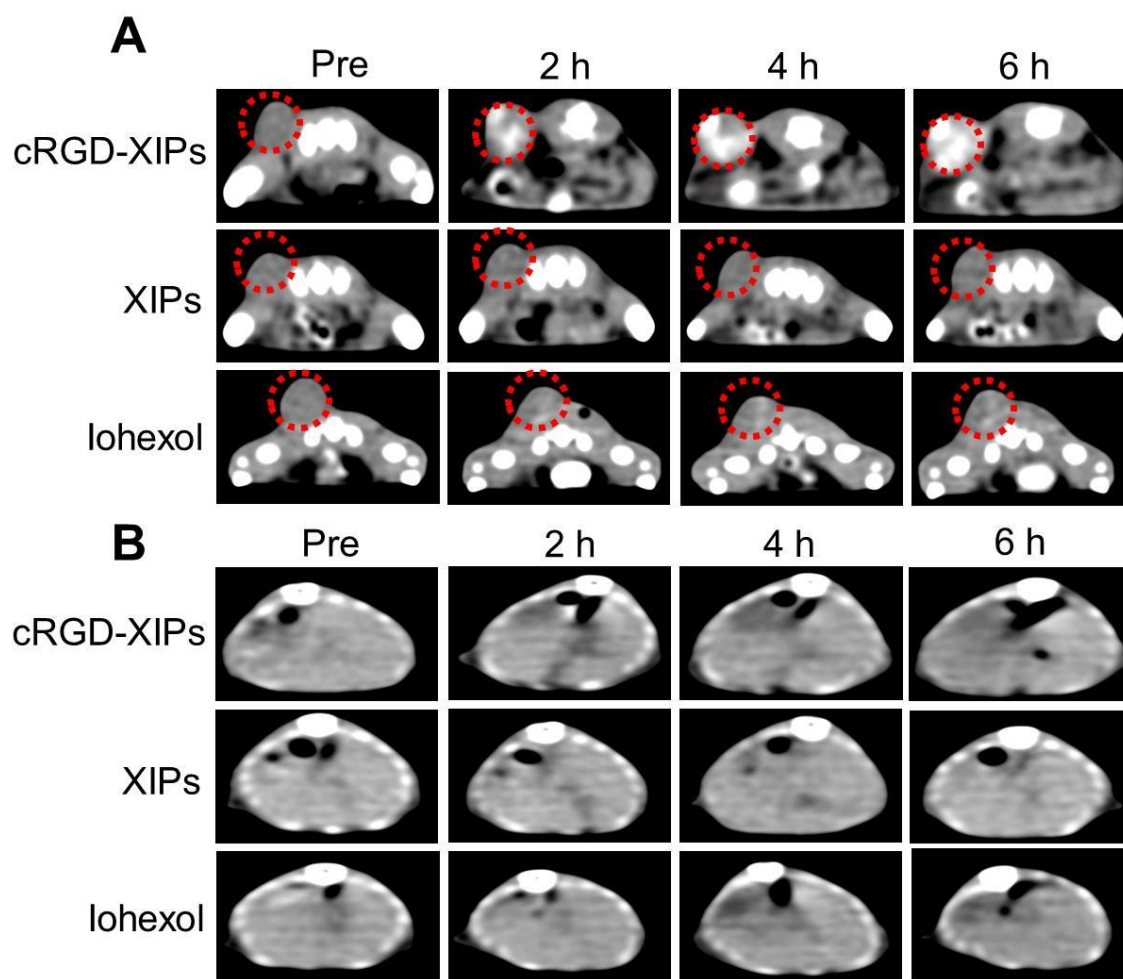
Figure S11. The axial CT images of the tumor (**A**) and liver (**B**) region of the mice before and at different time post *iv* injection of cRGD-XIPs, XIPs or iohexol. The red dotted circles indicate the tumor areas. The iodine dose was set at 350 mg I equiv./kg.
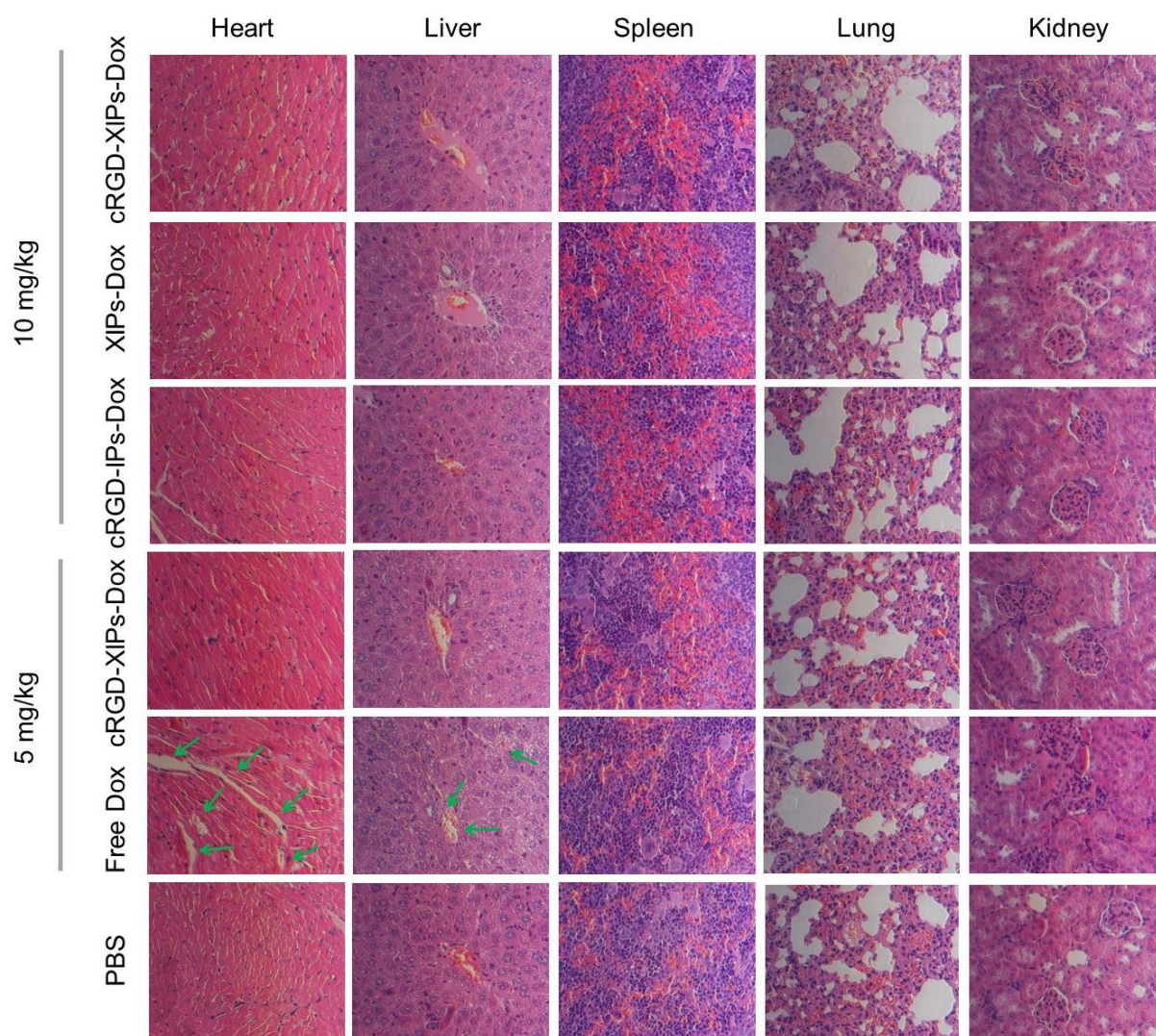
Figure S12. H&E stained organ slices of B16 tumor-bearing mice following 10 d treatment with cRGD-XIPs-Dox, XIPs-Dox, cRGD-IPs-Dox, free Dox or PBS. The images were obtained by a Leica microscope at 400× magnification.

Chapter 8

1. Summary

Polymersomes (Ps) are structures self-assembled from various amphiphilic block copolymers and exhibit a nano-vesicular architecture that enables encapsulation of hydrophilic or hydrophobic molecules in the internal aqueous compartment or the surrounding polymeric bilayer, respectively (**Scheme 1**, Chapter 1)[1, 2]. In comparison to the safety concerns of inorganic nanoparticulates for clinical translation, the biocompatibility and/or biodegradability of Ps promise to result in lower or no toxicity *in vivo*[3]. Actively targeted reduction-responsive Ps were developed exhibiting the following features: high stability in the blood circulation, significant tumor accumulation, enhanced tumor cell uptake and fast intracellular drug release[4, 5]. Besides, Ps also enable the possibility of image-guided drug delivery for optimized and personalized treatment (theranostics)[6, 7]. In this thesis, we designed and evaluated Ps systems based on either PEG-disulfide polycarbonate and/or PEG-iodinated polycarbonate for targeted tumor imaging and therapy.

Chapter 1 provides a general introduction to Ps, with emphasis on the necessity of stabilization achieved by disulfide crosslinking, the use of the active targeting approach, and the potential therapeutic and theranostic applications. The chapter ends with the aim of the thesis research and an outline of the research topics and contents presented in the subsequent chapters.

In **Chapter 2**, we report on potent transferrin-targeted polymersomal doxorubicin (Tf-Ps-Dox) for the treatment of transferrin receptor (TfR)-positive human liver tumor SMMC-7721[8]. Tf-Ps-Dox was efficiently prepared by utilizing post-modification of maleimide-functionalized Ps-Dox with thiolated transferrin. The observed inhibited cellular uptake, reduced intracellular Dox level, and reduced anticancer efficacy of Tf-Ps-Dox in SMMC-7721 cell cultures after supplementing the medium with additional free transferrin, points to cellular uptake of Tf-Ps-

Dox by TfR mediated endocytosis. The life span of orthotopic SMMC-7721 tumor-bearing mice was extended to 82, 88 to 96 days after intravenous administration with Tf-Ps-Dox at Dox doses from 8, 12 to 16 mg/kg, respectively, which was significantly longer than Ps-Dox at 8 mg/kg (58 days) and Lipo-Dox at 4 mg/kg (48 days) or PBS (36 days). Lipo-Dox was administered at a lower dose owing to its low maximum tolerated dose (MTD) in this model being around 15 mg/kg, so much lower than the 100 mg/kg MTD in case of Ps-Dox[4]. Notably, unlike Lipo-Dox, body weight loss and damage to major organs were not observed in case of all Tf-Ps-Dox groups, suggesting lower systemic toxicity of Tf-Ps-Dox.

Though the Tf-targeted nanotherapeutics exhibited potent anti-tumor efficacy *in vivo* with no problematic toxicity signs observed, the post-modification procedure to couple the Tf protein to the Ps surface is a challenging step during production processes. Besides, an additional risk is the impairment of the targeting capacity of the Tf ligand by intermolecular crosslinking between thiolated Tf and the maleimide group. Therefore, to avoid this potential intermolecular crosslinking problem, we report in **Chapter 3** on the use of Tf-binding peptide (TBP) (CGGGHKYLRW) modified polymersomes (TBP-Ps) that are able to selectively and stably bind Tf in a non-covalent way for tumor-targeted Dox delivery *in vivo*[9]. The Tf surface density could be tailored by tuning the surface TBP density. Indeed, Dox-loaded TBP-Ps binding Tf present in the culture medium showed significantly increased cellular uptake by and inhibitory effects towards HCT-116 colorectal cancer cells *in vitro*. More importantly, *i.v.* administered Dox-loaded TBP-Ps binding Tf (Tf@TBP-Ps-Dox) exhibited enhanced antitumor efficacy in subcutaneous HCT-116 -bearing mice compared to control Dox-Ps without TBP modification. Thus, the use of TBP surface modification provides significant advantages over the use of traditional Tf protein coupling and is therefore an attractive strategy when formulating Tf-targeted nanomedicines.

Patients with brain metastases, particularly those in case of triple-negative breast cancer

(TNBC), exhibit very short overall survival time as effective treatment modalities are lacking[10]. The inefficient blood-brain barrier (BBB) penetration limits the brain bio-availability of most drugs, especially for biopharmaceuticals with larger molecular weights, like proteins and nucleic acids[11, 12]. siRNAs offer the advantages of being highly potent and hardly toxic as compared to conventional small therapeutic molecules[13]. In **Chapter 4**, we report on Tf-targeted polymersomes loaded with the biotherapeutic siPLK1 (Tf@TBP-CPs-siPLK1). Interestingly, in the *in vitro* BBB mimic model used, up to 5-fold enhanced tumor cell uptake was observed as compared to control groups, suggesting the occurrence of Tf-ligand mediated enhanced cellular transcytosis through the BBB endothelial cells and subsequent receptor-mediated endocytosis by the tumor cells. *In vivo*, the animal group injected with Tf@CPs-siPLK1(Cy5) showed a higher degree of accumulation in the brain metastases (intracranial model) as compared to CPs-siPLK1 without targeting ligand as assessed by *in vivo* NIR imaging. Furthermore, the life-span of the intracranial brain metastases bearing mice was extended to 33 days in case of the Tf-targeted Ps treatment, in contrast to 26 and 23 days for the non-targeted Ps group and PBS control group, respectively.

In case of biomacromolecules, like siRNA and proteins, cytosolic delivery is often crucial for achieving their activity. Trans-acting activator of transcription (TAT) peptides have been widely used for transduction into cells of diverse origins but do not show selectivity between neoplastic and non-neoplastic cells[14]. Apart from TAT, artificial cell-penetrating peptide-CPP33 is of interest as targeting ligand, as it have shown high specificity to A549 lung cancer cells[15]. In **Chapter 5**, we report on CPP33-targeted reduction-responsive polymersomes (CPRPs) for granzyme B (GrB) delivery to orthotopic human lung tumor cells *in vivo*[16]. GrB is a natural and potent apoptotic protein secreted by cytotoxic T cells and NK cells[17]. CPRPs loaded with GrB characterized by a high protein loading (up to 17.2 wt%) and mean small size in the 80-90 nm range exhibited ca. 3-fold enhanced internalization and ca. 7-fold reduction

responsive cytoplasmic protein release *in vitro* compared with non-targeted control Ps. Remarkably, the presence of the surface-exposed CPP did not have an impact on the circulation time but did promote tumor accumulation, when compared to proper Ps control formulations. After treatment with GrB-loaded CPRPs at a single dosage of 2.88 nmol GrB equiv./kg, mice bearing orthotopic A549-Luc lung tumor cells showed complete tumor growth inhibition (vs. nontargeted Ps loaded with GrB) determined by bioluminescence intensity with little body weight loss throughout the treatment period of 20 days. Hence, further research is warranted on GrB-loaded CPRPs for providing targeted cytotoxic protein therapy of cancers.

Tumor accumulation of nanoparticles has been confirmed by clinical studies albeit with high inter- and intraindividual variability. Patient stratification prior treatment determined by noninvasive imaging techniques assessing the degree of tumor accumulation is vital to increase the response rate of nanomedicines. Iodinated small molecules (iohexol, iodixanol) are typically used in clinical computed tomography (CT) imaging to visualize pathological regions. However, their use is not without problems, as reflected by their swift blood clearance, high osmolality and viscosity, risk for renal damage and iodine hypersensitivity[18]. In **Chapter 6**, we report on the design and development of biodegradable Ps with an ultrahigh iodine content (60.4 wt%) for high-performance CT imaging *in vivo*[19]. Notably, these novel radiopaque Ps display excellent colloidal stability and biocompatibility, low viscosity, iso-osmolality, as well as a small size of about 100 nm. We show in this thesis that iodine-rich polymersomes (IPs) can improve the *in vivo* imaging of the blood pool, reticuloendothelial system (RES) and several malignant tumors as compared to iohexol, the clinically used iodinated small molecule.

Although integration of CT imaging in nano-chemotherapy protocols is attracting high interest of academic scientists, the currently iodinated based nanoparticle studies typically still suffer from a low contrast coefficient, low drug loading, and poor targetability. In **Chapter 7**, we report on cRGD-functionalized disulfide-crosslinked iodine-rich polymersomes (cRGD-

XIPs) as a novel, robust and 'smart' theranostic agent for targeted CT imaging and chemotherapy of malignant tumors[20]. 'Empty' cRGD-XIPs (without drug) could be used for pre-selection of patients by CT imaging prior to targeted chemotherapy. Our novel theranostic Ps exhibited a small mean size (90 nm), high iodine content of 55.5 wt.%, low iso-osmolality, high Dox loading content (15.3 wt.%), superior colloidal stability, and fast intracellular drug release. cRGD-XIPs greatly improve the quality of *in vivo* CT imaging after intratumoral or intravenous injection compared with iohexol. Moreover, cRGD-XIPs-Dox was far more potent in retarding the growth of a subcutaneous B16 tumor than non-targeted XIPs-Dox and non-crosslinked cRGD-IPs-Dox (lack of disulfide carbonate) controls.

Finally, **Chapter 8** summarizes the results described in this thesis and provides perspectives for Ps-based nanomedicines regarding clinical translation and commercial development.

2. Final Considerations and Perspectives

Reduction-responsive Ps have a "liposomes-like" structure and potentially can share some of the advantages liposomes can offer for targeted drug delivery (e.g. mitigated toxicity, fast intracellular drug release etc.) An additional advantage offered by reduction-responsive Ps is the possibility of stimuli-triggered drug release resulting from the versatile polymer chemistry and thereby enable improved antitumor therapy (i.e. increased therapeutic index) as compared to cytotoxic agents administered in free form. Coupling of targeting ligands (e.g. antibodies, peptides, aptamers etc.) to Ps can provide the reduction-responsive Ps with the possibility to directly bind to and internalized by the actual target cells in the tumor and achieve cellular internalization. In addition, noninvasive imaging technologies can be applied for patient stratification and drug targeting optimization. Several actively-targeted polymeric nanomedicines have entered into clinic trials during the past decade (**Table 1**)[21]. The problem is that there is never a comparison with the nanomedicine system without surface-exposed

targeting ligand and only comparison with the clinical standard-of-care. So, the role of targeting ligand attachment in active targeting strategies with nanomedicines is still unclear, despite numerous preclinical articles. Also, actively targeted nanoparticles often heavily depend on the possibility of the EPR effect to occur, particularly if one wants to reach target cells (e.g. tumor cells, fibroblasts) in solid tumor tissue. Targeting of endothelial cells in tumor tissue does not require EPR, and is therefore also a strategy under investigation but so far not yielding any product on the market. In general, there is a big gap between the many successful outcomes reported in preclinical papers and the in fact slow clinical translation as discussed in several recent opinion papers[22, 23]. Factors underlying this gap involve for example the difference between animals and human beings, safety concerns, scale-up manufacturing challenges, the attitude of large pharma companies, high costs associated with clinical translation, and the difficulty academic scientists may experience in starting clinical translation activities (e.g. regarding the need to involve investors and clinicians).

Table 1. Well-known ligand-decorated polymeric nanomedicines which have been or are in clinical development

Polymer-based nanomedicines							
Product Name	Company	Approx. Size (nm)	Payload	Ligand	Target	Clinical Indication	Clinical Phase
BIND-014	BIND Biosciences	100	Docetaxel	Small molecule	Prostate specific membrane antigen	Solid tumors	Phase II
CALAA-01	Calando Pharmaceuticals	50–70	RRM2 siRNA	Protein	Transferrin receptor	Solid tumors	Phase I
SEL-068	Selecta Biosciences	150–250	Nicotine antigen, T-helper cell peptide, TLR agonist	Small molecule	Antigen presenting cells	Smoking cessation vaccine	Phase I

Several strategies have been proposed to accelerate the clinical translation and exploitation of nanomedicine. **1) Choose the right patient**: The major clinical benefit from targeted nanomedicines containing antitumor drugs is often improved safety. A major problem encountered is the high variability of the EPR effect and therefore in tumor localization in the clinical setting. Hence, patient stratification via the application of non-invasive imaging modalities to monitor tumor accumulation of the nanocarrier system in individual patients is vital to increase antitumor response rates. **2) Choose the right drug**: Drug selection is important in realizing both clinical and commercial success. The advantages of nanomedicinal delivery should be fully considered (e.g. passive targeting/active targeting, mitigated toxicity) in the selection of the right payload. Nowadays, the need for efficient targeted drug delivery systems is bigger than ever with the arrival of biopharmaceuticals, like nucleic acids and proteins suffering from rapid degradation and short half-life *in vivo* and lack of capability to enter the cells. **3) Choose the right combination of drugs**: Combination therapies are commonly applied in clinical cancer care. And nanomedicines are and will be used in such combination settings, rather than being used as monotherapy. Also, combination with physical approaches (e.g. HIFU to trigger drug release at target sites) should be high on the tumor management agenda. **4) Choose the right therapeutic approach**: Immunotherapy is likely to become a game changer in terms of cancer treatment: to use nanomedicine to boost the immune system's ability to fight cancer and/or to improve the efficacy of existing immunotherapies while mitigating some of their side effects.

Finally, when clinical translation is pursued, the KISS (Keep it simple, stupid) and BIS (It's biology, stupid) principles should be taken into account to enhance the chance for clinical and commercial success[24]. In the end, the polymer scientist should learn from marketed products (in case of drug targeting: right now mainly liposome products) and seriously take into account opportunities but also limitations which biology brings to the table of nanomedicine designers.

References

[1] J. Leong, J.Y. Teo, V.K. Aakalu, Y.Y. Yang, H. Kong, Engineering polymersomes for diagnostics and therapy, Adv. Healthc. Mater. 7 (2018) 1701276.

[2] F. Meng, Z. Zhong, J. Feijen, Stimuli-responsive polymersomes for programmed drug delivery, Biomacromolecules 10 (2009) 197-209.

[3] A.C. Anselmo, S. Mitragotri, A review of clinical translation of inorganic nanoparticles, AAPS J. 17 (2015) 1041-1054.

[4] Y. Zou, F. Meng, C. Deng, Z. Zhong, Robust, tumor-homing and redox-sensitive polymersomal doxorubicin: A superior alternative to Doxil and Caelyx?, J. Control. Release 239 (2016) 149-158.

[5] Y. Zou, M. Zheng, W. Yang, F. Meng, K. Miyata, H.J. Kim, K. Kataoka, Z. Zhong, Virus-mimicking chimaeric polymersomes boost targeted cancer siRNA therapy in vivo, Adv. Mater. 29 (2017) 1703285.

[6] J. Thevenot, H. Oliveira, S. Lecommandoux, Polymersomes for theranostics, J. Drug Deliv. Sci. Tec. 23 (2013) 38-46.

[7] C. Sanson, O. Diou, J. Thevenot, E. Ibarboure, A. Soum, A. Brûlet, S. Miraux, E. Thiaudière, S. Tan, A. Brisson, Doxorubicin loaded magnetic polymersomes: theranostic nanocarriers for MR imaging and magneto-chemotherapy, ACS nano 5 (2011) 1122-1140.

[8] Y. Wei, X. Gu, L. Cheng, F. Meng, G. Storm, Z. Zhong, Low-toxicity transferrin-guided polymersomal doxorubicin for potent chemotherapy of orthotopic hepatocellular carcinoma in vivo, Acta Biomater. 92 (2019) 196-204.

[9] Y. Wei, X. Gu, Y. Sun, F. Meng, G. Storm, Z. Zhong, Transferrin-binding peptide functionalized polymersomes mediate targeted doxorubicin delivery to colorectal cancer in vivo, J. Control. Release (2020).

[10] A.S. Achrol, R.C. Rennert, C. Anders, R. Soffietti, M.S. Ahluwalia, L. Nayak, S. Peters, N.D. Arvold, G.R. Harsh, P.S. Steeg, Brain metastases, Nat. Rev. Dis. Primers 5 (2019) 1-26.

[11] Y. Jiang, J. Zhang, F. Meng, Z. Zhong, Apolipoprotein E peptide-directed chimeric polymersomes mediate an ultrahigh-efficiency targeted protein therapy for glioblastoma, ACS nano 12 (2018) 11070-11079.

[12] D. Liu, Y. Cheng, R. Cai, W. Wang, H. Cui, M. Liu, Q. Mei, S. Zhou, The enhancement of siPLK1 penetration across BBB and its anti glioblastoma activity in vivo by magnet and transferrin co-modified

nanoparticle, Nanomed-Nanotechnol 14 (2018) 991-1003.

[13] J.K. Lam, M.Y. Chow, Y. Zhang, S.W. Leung, siRNA versus miRNA as therapeutics for gene silencing, Mol. Ther. Nucleic Acids 4 (2015) e252.

[14] I. Nakase, A. Tadokoro, N. Kawabata, T. Takeuchi, H. Katoh, K. Hiramoto, M. Negishi, M. Nomizu, Y. Sugiura, S. Futaki, Interaction of arginine-rich peptides with membrane-associated proteoglycans is crucial for induction of actin organization and macropinocytosis, Biochemistry 46 (2007) 492-501.

[15] E. Kondo, K. Saito, Y. Tashiro, K. Kamide, S. Uno, T. Furuya, M. Mashita, K. Nakajima, T. Tsumuraya, N. Kobayashi, Tumour lineage-homing cell-penetrating peptides as anticancer molecular delivery systems, Nat. Commun. 3 (2012) 951.

[16] W. Yang, Y. Wei, L. Yang, J. Zhang, Z. Zhong, G. Storm, F. Meng, Granzyme B-loaded, cell-selective penetrating and reduction-responsive polymersomes effectively inhibit progression of orthotopic human lung tumor in vivo, J. Control. Release 290 (2018) 141-149.

[17] S.J. Lord, R.V. Rajotte, G.S. Korbutt, R.C. Bleackley, Granzyme B: a natural born killer, Immunol. Rev. 193 (2003) 31-38.

[18] N. Lee, S.H. Choi, T. Hyeon, Nano-sized CT contrast agents, Adv. Mater. 25 (2013) 2641-2660.

[19] Y. Zou, Y. Wei, G. Wang, F. Meng, M. Gao, G. Storm, Z. Zhong, Nanopolymersomes with an ultrahigh iodine content for high-performance X-ray computed tomography imaging in vivo, Adv. Mater. 29 (2017) 1603997.

[20] Y. Zou, Y. Wei, Y. Sun, J. Bao, F. Yao, Z. Li, F. Meng, C. Hu, G. Storm, Z. Zhong, Cyclic RGD-functionalized and disulfide-crosslinked iodine-rich polymersomes as a robust and smart theranostic agent for targeted CT imaging and chemotherapy of tumor, Theranostics 9 (2019) 8061.

[21] R. van der Meel, L.J. Vehmeijer, R.J. Kok, G. Storm, E.V. van Gaal, Ligand-targeted particulate nanomedicines undergoing clinical evaluation: current status, Adv. Drug Deliv. Rev. 65 (2013) 1284-1298.

[22] K. Park, The drug delivery field at the inflection point: Time to fight its way out of the egg, J. Control. Release 267 (2017) 2-14.

[23] K. Park, Transcending nanomedicine to the next level: Are we there yet?, J. Control. Release 298 (2019) 213.

[24] D.J. Crommelin, P. van Hoogevest, G. Storm, The role of liposomes in clinical nanomedicine development. What now? Now what?, J. Control. Release 318 (2020) 256-263.

Samenvatting

Polymersomen (Ps) zijn zelf-geassembleerde structuren opgebouwd uit verschillende amfifiele blokcopolymeren en vertonen een nano-vesiculaire architectuur die inkapseling van hydrofiele of hydrofobe moleculen in respectievelijk het interne waterige compartiment of de omringende polymere dubbellaag mogelijk maakt (**Schema 1, Hoofdstuk 1**). De biocompatibiliteit en biologische afbreekbaarheid van Ps beloven een lage-tot-geen toxiciteit *in vivo*. In dit proefschrift werden Ps ontwikkeld met de volgende kenmerken: hoge stabiliteit in de bloedcirculatie, aanzienlijke tumorophoping, goede opname door tumorcellen en snelle intracellulaire afgifte van ingesloten farmaca. Bovendien is ook de mogelijkheid van beeldgestuurde farmaconafgifte onderzocht om in de toekomst te komen tot een geoptimaliseerde en gepersonaliseerde behandeling van patiënten (theranostics). In dit proefschrift zijn Ps-systemen ontworpen en geëvalueerd op basis van PEG-disulfide polycarbonaat en/of PEG-gejodeerd polycarbonaat voor gerichte beeldvorming en therapie van tumoren.

Hoofdstuk 1 geeft een algemene inleiding tot Ps, met de nadruk op de noodzaak van stabilisatie bereikt door disulfide crosslinking, het gebruik van de active targeting benadering (d.w.z. het gebruik van targeting liganden op het oppervlak van nanodeeltjes), en de mogelijke therapeutische en theranostische toepassingen. Het hoofdstuk eindigt met het doel van het proefschriftonderzoek en een overzicht van de onderzoeksinhoud die in de volgende hoofdstukken wordt aan bod komt.

Hoofdstuk 2 richt zich op de evaluatie van doxorubicine-bevattende Ps met transferrine als targeting ligand op het oppervlak (Tf-Ps-Dox) voor de behandeling van transferrinereceptor

(TfR)-positieve humane levertumorcellen (SMMC-7721). De waargenomen geremde cellulaire opname, verminderde intracellulaire Dox-spiegel en verminderde antikankerwerkzaamheid van Tf-Ps-Dox in SMMC-7721-celculturen na aanvulling van het medium met extra vrij transferrine, wijst op cellulaire opname van Tf-Ps-Dox door TfR-gemedieerde endocytose. De levensduur van orthotope SMMC-7721-tumordragende muizen werd verlengd met 82, 88 en 96 dagen na intraveneuze (i.v.) toediening met Tf-Ps-Dox in Dox-doseringen van respectievelijk 8, 12 tot 16 mg/kg, wat significant langer was dan in geval van Ps-Dox bij 8 mg/kg (58 dagen) en Lipo-Dox bij 4 mg/kg (48 dagen) en PBS (36 dagen). Lipo-Dox werd in een lagere dosis toegediend omdat de lage maximaal te verdragen dosis (MTD) in dit diermodel ongeveer 15 mg/kg was, dus veel lager dan de 100 mg/kg MTD in het geval van Ps-Dox. Anders dan met Lipo-Dox, werd in geval van Tf-Ps-Dox geen verlies van lichaamsgewicht en orgaanschade waargenomen, wat duidt op een lagere systemische toxiciteit van Tf-Ps-Dox.

Ondanks de positieve resultaten in Hoofdstuk 2, is de gebruikte post-modificatieprocedure om het Tf-eiwit te koppelen aan het Ps-oppervlak een problematische stap tijdens het bereidingsproces. Bovendien is een bijkomend risico dat de targeting eigenschappen van het Tf-ligand worden verminderd door intermoleculaire verknoping van gethioleerd Tf met de maleïmidegroepen. Om dit potentiële risico van intermoleculaire verknoping te vermijden, bestudeerden we in **Hoofdstuk 3** het gebruik van Tf-bindende peptide (TBP) (CGGGHKYLRW) gemodificeerde polymersomen (TBP-Ps) die in staat zijn om in de bloedbaan selectief en stabiel Tf te binden op niet-covalente wijze. De Tf-oppervlaktedichtheid bleek te kunnen worden aangepast via de oppervlakte-TBP-dichtheid. Dox-beladen TBP-Ps bonden Tf aanwezig in kweekmedium en vertoonden daarom een significant verhoogde

cellulaire opname door en remmende effecten op HCT-116 colorectale kankercellen *in vitro*. Wat nog belangrijker is, i.v. toegediende Dox-beladen TBP-Ps die *in* vivo Tf binden (Tf @ TBP-Ps-Dox) vertoonden een grotere antitumor activiteit in subcutane HCT-116-dragende muizen in vergelijking met controle Dox-Ps zonder TBP-modificatie. Het gebruik van TBP-oppervlaktemodificatie biedt dus aanzienlijke voordelen ten opzichte van het gebruik van traditionele Tf-eiwitkoppeling en is daarom een aantrekkelijke strategie bij het formuleren van op Tf gerichte nanomedicijnen.

Patiënten met hersenmetastasen, vooral die in het geval van triple-negatieve borstkanker (TNBC), kennen een korte levensduur omdat effectieve behandelingsmodaliteiten ontbreken. De bloed-hersenbarrière (BBB) kan worden omschreven als een natuurlijke beveiliging waardoor allerlei stoffen niet zomaar vanuit het bloed naar de hersenen kunnen diffunderen en omgekeerd evenmin, met name voor biofarmaceutica met een hoger molecuulgewicht, zoals eiwitten en nucleïnezuren. Smal interfering RNA's (siRNA's) bieden het voordelen dat ze zeer krachtig kunnen werken en nauwelijks toxisch zijn in vergelijking met conventionele kleine therapeutische moleculen. In **Hoofdstuk 4** rapporteren we over Tf-gerichte Ps beladen met siPLK1 (Tf @ TBP-CPs-siPLK1). Bemoedigend was dat in het *in vitro* BBB-nabootsingsmodel dat werd gebruikt, een tot 5-voudige verbeterde opname van Tf@TBP-CPs-siPLK1 door de tumorcellen werd waargenomen in vergelijking met controlegroepen, wat suggereert dat Tf-ligand-gemedieerde verbeterde cellulaire transcytose door de BBB-endotheelcellen en daaropvolgende receptor-gemedieerde endocytose door de tumorcellen optreedt. *In vivo* vertoonde de diergroep geïnjecteerd met Tf@TBP-CPs-siPLK1 (Cy5) een hogere mate van accumulatie in de hersenmetastasen (intracranieel model) in vergelijking met CPs-siPLK1

zonder targeting ligand, zoals waargenomen met behulp van *in vivo* near-infrared (NIR) beeldvorming. Bovendien werd de levensduur van de muizen met intracraniële hersenmetastasen verlengd tot 33 dagen in het geval van de Tf-gerichte Ps-behandeling, in tegenstelling tot respectievelijk 26 en 23 dagen voor de controlegroepen niet-Tf gericht Ps en PBS.

In het geval van biomacromoleculen, zoals siRNA en eiwitten, is het bereiken van het cytosol vaak cruciaal voor het realiseren van hun activiteit. In **Hoofdstuk 5** rapporteren we over ons onderzoek naar de cytosolaire aflevering van granzyme B (GrB) aan orthotope menselijke longtumorcellen *in vivo*. GrB is een natuurlijk en krachtig apoptotisch eiwit dat wordt uitgescheiden door cytotoxische T-cellen en NK-cellen. We koppelden daartoe het zgn. TAT peptide CPP33 aan het oppervlak van GrB beladen Ps. CPP33 bezit een hoge specificiteit voor binding aan A549-longkankercellen. Een ongeveer 3-voudige verbeterde internalisatie en 7-voudige reductie-responsieve cytoplasmatische eiwitafgifte werd waargenomen *in vitro* in vergelijking met niet-getargette controle Ps. Opmerkelijk was dat de aanwezigheid van CPP33 op het oppervlak geen invloed had op de circulatietijd van de Ps, maar wel de tumor accumulatie bevorderde, vergeleken met de Ps-controleformuleringen. Na behandeling met een enkelvoudige dosering van 2,88 nmol GrB equiv./kg, vertoonden muizen met orthotope A549-Luc-longtumorcellen een volledige remming van de tumorgroei (vs. niet-gerichte Ps beladen met GrB). Verder onderzoek is gerechtvaardigd naar de mogelijkheden die Ps kunnen bieden voor het cytosolair afleveren van cytotoxische eiwitten aan kankercellen.

Tumorophoping van nanodeeltjes is bevestigd in klinisch onderzoek, zij het met een hoge inter- en intra-individuele variabiliteit. Patiëntstratificatie met betrekking tot de mate van

tumoraccumulatie, voorafgaande aan de behandeling met behulp van niet-invasieve beeldvormingstechnieken die de mate van tumorophoping vaststellen, is van vitaal belang om de klinische activiteit van nanogeneesmiddelen te verhogen. Gejodeerde kleine moleculen (iohexol, iodixanol) worden gebruikt in klinische computertomografie (CT) beeldvorming om pathologische gebieden te visualiseren. Het gebruik ervan is echter niet zonder problemen, zoals blijkt uit hun snelle bloedklaring, hoge osmolaliteit en viscositeit, risico op nierbeschadiging en overgevoeligheid voor jodium. **Hoofdstuk 6** richt zich op het ontwerp en de ontwikkeling van biologisch afbreekbare Ps met een ultrahoog jodiumgehalte (60,4 gew.%) ten behoeve van hoogwaardige CT-beeldvorming *in vivo*. De nieuw ontwikkelde radiopake Ps vertoonden een uitstekende colloïdale stabiliteit en biocompatibiliteit, lage viscositeit, iso-osmolaliteit en een kleine afmeting van ongeveer 100 nm. We laten in dit proefschrift zien dat de jodiumrijke Ps de *in vivo* beeldvorming van het bloed, het reticulo-endotheliale systeem (RES) en verschillende kwaadaardige tumoren kunnen verbeteren in vergelijking met iohexol, het klinisch gebruikte gejodeerde kleine molecuul.

Hoewel de integratie van CT-beeldvorming in protocollen voor nano-chemotherapie grote belangstelling trekt van academische wetenschappers, hebben de momenteel op jodium gebaseerde nanodeeltjesstudies doorgaans nog steeds last van een lage contrastcoëfficiënt, een lage farmacon belading en onbevredigende targeting efficiëntie. In **Hoofdstuk 7** beschrijven we cRGD-gefunctionaliseerde disulfide-gecrosslinked jodium-bevattende Ps (cRGD-XIPs) als een nieuw, robuust en 'slim' theranostisch middel voor gerichte CT-beeldvorming en chemotherapie van kwaadaardige tumoren. 'Lege' cRGD-XIP's (zonder farmacon) zouden kunnen worden gebruikt voor voorselectie van patiënten door middel van CT-beeldvorming

voorafgaand aan de nano-chemotherapeutische behandeling. Onze nieuwe theranostische Ps vertoonde een kleine gemiddelde grootte (90 nm), hoog jodiumgehalte van 55,5 gew.%, lage iso-osmolaliteit, en een hoog farmacon (doxorubicine)-beladingsgehalte (15,3 gew.%), uitstekende colloïdale stabiliteit en snelle intracellulaire farmaconafgifte. cRGD-XIP's verbeterden de kwaliteit van *in vivo* CT-beeldvorming na intratumorale of intraveneuze injectie aanzienlijk in vergelijking met iohexol. Bovendien was cRGD-XIPs-Dox veel krachtiger in het vertragen van de groei van een subcutane B16-tumor in vergelijking met de getestte doxorubicine-bevattende controleformuleringen.

Tot slot vat **Hoofdstuk 8** de resultaten samen die in dit proefschrift worden beschreven en beschrijft het perspectieven voor Ps-gebaseerde nanomedicijnen met betrekking tot klinische translatie en commerciële ontwikkeling.

Acknowledgements

My Ph.D. study have undoubtedly been the biggest undertaking that I have ever pursued. The years of Ph.D. study not only improved my academic capabilities, but also greatly influenced my personal development. I really appreciated University of Twente and Soochow University provide me such a platform to study in different laboratories in both China and the Netherlands. My PhD study began at Suzhou back to 2015. All the time in Suzhou seems to be still in sight. I still remember when I first came to Suzhou, I felt that everything was new, and I was full of curiosity to explore everything about Suzhou and the time in Suzhou is also memorable and fulfilling. I flew to the Netherlands after few years study in Suzhou to fulfil the last part of my Ph.D. Study. One year in the Netherlands is fleeting. The biggest regret for me is that I have no chance to enjoy the scenery and explore the beauty of the Netherlands due to the pandemic. The Ph.D. study is definitely inseparable from the help of too many people.

I would like to start with thanking my promotor and supervisor, Prof. Dr. Zhiyuan Zhong. Thank you for giving me such an opportunity to join this special program. I really admire your rigorous and pioneering spirit towards scientific research. Moreover, your inspiration and intellectual insights really give me great help in my research. In addition, I really appreciate your comments and suggestions on my monthly routine report, manuscript and thesis as well.

Secondly, I would like to thank Prof. Dr. Gert Storm. Thank you for giving me the opportunity to join BST. Every time after discussing with you, I will gain a lot and have a better understanding of my research. It is a great honor to me to have two supervisors with different backgrounds who can guide me from different perspectives. Thank you for your suggestions on the manuscripts and also the thesis. Meanwhile, I would like to thank you for taking care of me during my stay in the Netherlands, especially during the pandemic. I still remember that we went to the cinema together to watch a movie, and have lunch together by the canal in Utrecht.

I would also like to give my special thanks to Prof. Dr. Fenghua Meng. The manuscript could not be published without Prof. Meng. All my papers are indispensable for Prof. Meng guidance. It was Prof. Meng who taught me how to revise the manuscript and how to respond to reviewers' comments. I really admire Prof. Meng's patience, professionalism towards work and also enthusiasm towards life.

I would to thank the people from Biomaterials Science and Technology (BST) group. Prof. Dr. Dirk Grijpma and Dr. Andreas Poot, thank you for letting me to join the group meeting and offering me a chance to do research in BST group. I also would like to thank Prof. Dr. Piet Dijkstra. Thank you for helping me to get the used bike, which made life much easier in Enschede. Dear Karin, thank you for your kind help during the administration and also the defense preparation. At the same time, I would like to thanks to my Chinese colleagues in BST Jia Liang, Tao Lu, Zhengchao Guo and Rong Wang. Thanks for your kind help when I first arrived which make me use to the life in the Netherlands quickly.

And I want to thank my friends and colleagues from Biomedical Polymers (BMP) lab from Soochow university. I would like to thanks to Dr. Yan Zou, Dr. Weijing Yang, Dr. Yaqin Zhu, Dr. Yinan Zhong, Dr. Yu Jiang, Dr. Xiuxiu Wang, Dr. Min Qiu, Dr. Xiaolei Gu, Jinsong Cao, Yinping Sun. I really miss the happy days we spent in Suzhou. I wish you all a happy life and bright future.

Last but not the least, I would to thank my parents for their endless love, support and help over the years. Thank you.

Yaohui Wei

Mar. 2021

Beijing

List of Publications

Publications from this thesis:

Y.H. Wei, X.L. Gu, L. Cheng, F.H. Meng, G. Storm, Z.Y. Zhong, Low toxicity of transferrin-guided polymersomal doxorubicin for potent chemotherapy of orthotopic hepatocellular carcinoma in vivo, Acta Biomater. 2019, 92, 196-204　(Chapter 2)

Y.H. Wei, X.L. Gu, Y.P. Sun, F.H. Meng, G. Storm, Z.Y. Zhong, Transferrin-binding peptide functionalized polymersomes mediate targeted doxorubicin delivery to colorectal cancer in vivo, J. Control. Release 2020, 319，407-415　(Chapter 3)

Y.H. Wei, Y.P. Sun, J.J. Wei, X.Y. Qiu, F.H. Meng, G. Storm, Z.Y. Zhong, Selective transferrin coating as a facile strategy to fabricate BBB-permeable and targeted vesicles for potent RNAi therapy of brain metastatic breast cancer *in vivo*, J. Control. Release, in revision (Chapter 4)

W.J. Yang‡, **Y.H. Wei‡** (co-first author), L. Yang, J. Zhang, Z.Y. Zhong, G. Storm, F.H. Meng, Granzyme B-loaded, cell-selective penetrating and reduction-responsive polymersomes effectively inhibit progression of orthotopic human lung tumor in vivo, J. Control. Release 2018, 290, 141-149 (Chapter 5)

Y. Zou‡, **Y.H. Wei‡** (co-first author), G.L. Wang, F.H. Meng, M.Y. Gao, G. Storm, Z.Y. Zhong, Nano-polymersomes with an ultrahigh iodine content for high-performance X-ray computed tomography imaging in vivo, Adv. Mater. 2017, 29, 1603997 (Chapter 6)

Y. Zou‡, **Y.H. Wei‡** (co-first author), Y.P. Sun, J. Bao, F.Y. Yao, Z.K. Li, F.H. Meng, C.H. Hu, G. Storm. Z.Y. Zhong, Cyclic RGD-functionalized and disulfide-crosslinked iodine-rich polymersomes as a robust and smart theranostic agent for targeted CT imaging and chemotherapy of tumor, Theranostics 2019, 9, 8061-8072 (Chapter 7)

Other selected publications:

Y.H. Wei, Y.P. Sun, X.L. Gu, F.H. Meng, G. Storm, Z.Y. Zhong, Endogenous transferrin installed polymersomal toxin for breast cancer brain metastases therapy, Manuscript in preparation

Y.H. Wei, F.H. Meng, G. Storm, Z.Y. Zhong, Transferrin Receptor-targeted anticancer nanomedicines: from rational design, fabrication strategies, proof-of-concept studies to clinical trials, To be submitted

C. Zhou，Y.F. Xia, **Y.H. Wei**，L. Cheng，J.J Wei，B.B. Guo，F.H. Meng，S.P. Cao，van H. Jan, Z.Y. Zhong, GE11 peptide-installed chimaeric polymersomes tailor-made for high-efficiency EGFR-targeted protein therapy of orthotopic hepatocellular carcinoma, Acta Biomaterialia, 2020, 113, 512-521

Y.W. Li, J.J. Wei, **Y.H. Wei**, L. Cheng, B.B. Guo, F.H. Meng, F. Li, Z.Y. Zhong, Apolipoprotein E peptide-guided disulfide-crosslinked micelles for targeted delivery of sorafenib to hepatocellular carcinoma, Biomacromolecules, 2019, 21, 716-724

X.L. Gu, Z.H. Zhu, Q.Y. Fan, **Y.H. Wei**, G.L. Wang, F.H. Meng, Z.Y. Zhong, C. Deng, Nanoagents based on poly(ethylene glycol)-b-poly(I-thyroxine) block copolypeptide for enhanced dual-modality imaging and targeted tumor radiotherapy, Small, 2019, DOI: 10.1002/smll.201902577

Y. Zou, Y.P. Sun, **Y.H. Wei**, Y.F. Xia, Z.Y. Huangfu, F.H. Meng, van H. Jan, Z.Y. Zhong, Integrin-targeting polymersomal docetaxel as an advanced nanotherapeutics for non-small cell lung cancer treatment, ACS Appl. Mater. & Inter. 2020, 12, 14905-14913

M. Qiu, J. Ouyang, **Y.H. Wei**, J. Zhang, Q. Lan, C. Deng, Z.Y. Zhong, Selective cell penetrating peptide-functionalized envelope-type chimaeric lipopepsomes boost systemic RNAi therapy for lung tumor, Adv. Healthcare Mater. 2019, 24, 1900500

X.L. Gu, **Y.H. Wei**, Q.Y. Fan, H.L. Sun, R. Cheng, Z.Y. Zhong, C. Deng, cRGD-decorated biodegradable polytyrosine nanoparticles for robust encapsulation and targeted delivery of doxorubicin to colorectal cancer in vivo J. Control. Release 2019, 301, 110-118

J.S. Cao, **Y.H. Wei**, Y.X. Zhang, G.L. Wang, X. Ji, Z.Y. Zhong, Iodine-rich polymersomes enable versatile SPECT/CT imaging and potent radioisotope therapy for tumor in vivo, ACS Appl. Mater. & Inter. 2019, 11, 18953-18959

M. Qiu, Z.Q. Zhang, **Y.H. Wei**, H.L. Sun, F.H. Meng, C. Deng, Z.Y. Zhong, Small-sized and robust chimaeric lipopepsomes: a simple and functional platform with high protein loading for targeting intracellular delivery of protein toxin in vivo, Chem. Mater. 2018, 30, 6831-6838

M. M. Fettis‡, **Y.H. Wei‡** (co-first author), A. Restuccia, J. J. Kurian, S.M. Wallet, G. A. Hudalla, Microgels with tunable affinity-controlled protein release via desolvation of self-assembled peptide nanofibers, J. Mater. Chem. B 2016, 18, 3054-3064

C.X. Li, T. Wang, L.H. Hu, **Y.H. Wei**, J.N. Liu, X.Y. Mu, J. Nie, D.Z. Yang, Photocrosslinkable bioadhesive based on dextran and PEG derivatives, Mater. Sci. Eng., C 2014, 35, 300-306

Y.F. Ai, **Y.H. Wei**, J. Nie, D.Z. Yang*, Study on the synthesis and properties of mussel mimetic poly (ethylene glycol) bioadhesive, J. Photochem. Photobiol. B 2013, 120, 183-190